INFORMATION TO USERS

This manuscript has been reproduced from the microfilm master. UMI films the text directly from the original or copy submitted. Thus, some thesis and dissertation copies are in typewriter face, while others may be from any type of computer printer.

The quality of this reproduction is dependent upon the quality of the copy submitted. Broken or indistinct print, colored or poor quality illustrations and photographs, print bleedthrough, substandard margins, and improper alignment can adversely affect reproduction.

In the unlikely event that the author did not send UMI a complete manuscript and there are missing pages, these will be noted. Also, if unauthorized copyright material had to be removed, a note will indicate the deletion.

Oversize materials (e.g., maps, drawings, charts) are reproduced by sectioning the original, beginning at the upper left-hand corner and continuing from left to right in equal sections with small overlaps. Each original is also photographed in one exposure and is included in reduced form at the back of the book.

Photographs included in the original manuscript have been reproduced xerographically in this copy. Higher quality 6" x 9" black and white photographic prints are available for any photographs or illustrations appearing in this copy for an additional charge. Contact UMI directly to order.

UMI

A Bell & Howell Information Company
300 North Zeeb Road, Ann Arbor MI 48106-1346 USA
313/761-4700 800/521-0600

STAR FORMATION IN CAMELOPARDALIS: Cam OB1

by

David Anthony Lyder
B.Sc., University of Alberta 1982
B.Sc., University of Alberta 1987
M.Sc., University of Alberta 1989

A Dissertation Submitted in Partial Fulfillment of the
Requirements for the Degree of

DOCTOR OF PHILOSOPHY

in the Department of Physics and Astronomy

We accept this thesis as conforming
to the required standard

Dr. A. C. Gower, Supervisor (Department of Physics and Astronomy)

Dr. C. R. Purton, Co-Supervisor (Dominion Radio Astrophysical Observatory)

Dr. C. D. Scarfe, Departmental Member (Department of Physics and Astronomy)

Dr. F. D. Hartwick, Departmental Member (Department of Physics and Astronomy)

Dr. G. Miller, Outside Member (Department of Mathematics and Statistics)

Dr. J. M. MacLeod, External Examiner (James Clerk Maxwell Telescope)

Supervisors: Drs. A. C. Gower and C. R. Purton

ABSTRACT

Star formation in the Cam OB1 region is investigated. Star formation, in general, is considered in terms of three elements: a) the structural relationship between the parent molecular clouds and newly formed stars, b) the temporal evolution of the parent molecular clouds, and c) the probability of the occurrence of star formation. Star formation in Cam OB1, over the range in l and b considered in this work, is concentrated in the vicinity of Cam R1 and appears to have led to the formation of three distinct stellar groups: a) Group I, formed $\sim 1 - 50 \times 10^6$ yr ago, and located spatially and kinematically between two CO complexes, b) Group II, formed $\sim 1 - 3 \times 10^6$ yr ago, and coincident with one of the previously mentioned complexes, and c) Group III, the youngest group, formed $\sim 1 - 20 \times 10^4$ yr ago, and located at the current point of intersection between the two complexes in (a). The mass function (MF) for Groups I and II is similar to the cloud mass function of the parent molecular clouds, i.e., a power-law with exponent $\alpha \sim 2$. A similar analysis for the Group III stars and associated molecular clouds cannot be performed due to the relatively small numbers in both samples. The star forming efficiency (SFE) in all cases is $\sim$ 1%. It is proposed that cloud-cloud collisions between the CO complexes in the region triggered the formation of Groups I and III, while Group II was produced by a shock induced by the radiation pressure and stellar winds from the stars in Group I. An analysis of the molecular cloud structure in Cam OB1 and the background Perseus arm also shows that the clouds in both regions are turbulent, and typical of clouds seen elsewhere in the Galaxy. However, the clouds in Cam OB1 show a large dispersion in the degree with which they are self-gravitating, with the

larger, warmer clouds being gravitationally bound.

The principal data set for this work comprises fully sampled ^{12}CO (J=1-0) observations of the western half of Cam OB1, which were obtained at the Center for Astrophysics during the winter of 1992-1993. These data have an effective resolution of 10′, a velocity resolution of 0.65 km s^{-1}, and a sensitivity of 0.115 K. High resolution (20″) observations of the ^{12}CO (J=2-1) transition of the most active star forming region were obtained with the James Clerk Maxwell Telescope during the winter of 1994-1995. These observations led to the discovery of a second outflow, AFGL 490 – iki, associated with IRAS 03234+5843, in the immediate vicinity of the very well-studied molecular outflow AFGL 490. Additional observations of the CH_3OH maser ($5_1 - 6_0A^+$), taken with the 26m telescope at the Dominion Radio Astrophysical Observatory during the fall of 1994, did not reveal any such maser-ing activity in the Cam OB1 region, but did lead to the discovery of a new maser, associated with IRAS 02455+6034, in the background Perseus arm.

ABSTRACT cont.

Dr. A. C. Gower, Supervisor (Department of Physics and Astronomy)

Dr. C. R. Purton, Co-Supervisor (Dominion Radio Astrophysical Observatory)

Dr. C. D. Scarfe, Departmental Member (Department of Physics and Astronomy)

Dr. E. D. Hartwick, Departmental Member (Department of Physics and Astronomy)

Dr. G. Miller, Outside Member (Department of Mathematics and Statistics)

Dr. J. M. MacLeod, External Examiner (James Clerk Maxwell Telescope)

Table of Contents

List of Tables

List of Figures

Acknowledgments

I started this adventure so many years ago that I am sure I have run into people who I will forget to thank but who really did help me very much. Please forgive my poor memory.

When I started out in Victoria I was fortunate enough to make the acquaintance of some good friends and darn good astrophysicists including Ana, Roberto, Luc, Joanne, Steven, Pat, all of the Davids, and John, et al. I enjoyed your company very much and learned a lot from you. I should also like to say a special thank you to Jeremy Tatum for standing up for me when I first landed in Victoria and was adjusting to my new surroundings.

I also would like to thank the folks in Victoria outside of U. Vic. who were so very kind to me during my stay there: Russ and Margie and the kids for many nice dinners and a chance to play, the Ewings for their very kind hospitality, great dinners and good company. I would be remiss if I didn't say a special thank you to Samantha (Sam) for being so good to me. You were really such a good friend to me Sam, I wish you all the joy and happiness in the World. I would also like to thank Sharon and Alex from SVdP, who allowed me to help out and keep my feet planted firmly on the ground and think about what is really important in this World.

On my way to Penticton I had the chance to make a six-month detour in Boston. This was a great opportunity for me to study at the CfA and meet many great astronomers. I must thank Pat Thaddeus, Tom Dame and Sam Palmer for allowing me the opportunity to use such a great instrument and just allowing me a chance to talk to them about CO, etc. I must also send a very special thank you to Seth Digel (and his wife Jeanne) who was a great colleague and friend, and gave me a lot of support when I was desperately trying to get this project underway. I do not think I could have done this without you Seth. Oh yes, lest I forget, thanks to my

crazy cousin, Ann-Lee, for letting me stay with her during my stay at the CfA – it was a very interesting experience.

Landing in Penticton I quickly learned that DRAO was made up of a great group of people. Tom Landecker and Lloyd Higgs were very kind in making sure I had all the resources I needed to complete this thesis. I have to thank everyone for many interesting conversations I had with them over the years and all of the help they have given me. In particular, I must thank Ken Tapping for teaching me about SIS junctions, Lewis Knee for corrections to an earlier version of this thesis and his thoughts on star formation, and Tom Burgess for his editorial comments.

I have many good memories of my days at DRAO and a (large) number of them have to do with dancing. Many thanks to little Dianeski for her little red number, to Colleen and Tara et al. for the many fun nights cutting a rug. Many thanks to Peter for the enjoyable fishing trips, and also to Tom and Karen for their excellent wine and and their good company (I hope we still get to play bridge together someday). I must also thank Chris and Sandra for their kind hospitality during my stay in Penticton and Hawai'i - I am a rather large stray! A special thanks must also go to Ricky, one of the kindest men I have met in my life and a good friend.

My stay in Penticton would not have been complete/right without being able to work for SVdP. So many friends I met and enjoyed through my work with the Society. I would like to first remember those who have gone before us - Donna and Margaret - we still think about you and pray for you. I must say a special thanks to Rose who is very in tune with the World and taught me how to pray, and Margeurite who taught me how to organize (delegate) and enjoy my right brain. I also would like to thank Cecil (Papa Bear) and Marguerite for their good company many a night playing scrabble. Let me also say thanks to Blanche, John and Anita, Sharon, Robert, Roger, Dick, Doreen, Gordon, Sister Yvette and Father Peter et al. for all

of their work which they put into making the Society work. God bless you all.

I am back in Edmonton now and it does feel as if I am back home. I could not have done this work without the unquestioning support of my parents, Nuala and Brian, who were always there for me and encouraged me when things were not easy. I must also thank my sister, Maeve, and brother-in-law, Derald, for all of the help they gave me over the years. I know I could be a real pain sometimes. I would also like to thank Zulma and Marcel for their wonderful daughter and the rest of the Cherlet clan for all of their prayers and support. I must also thank Dorothy and Andrei for their kind support over the years - it finally is done, yeah!! Thanks also to Terry, Chris, Rekha, Dawn and Malcolm, and Ian and Jill for maintaining our ties over the years. It's good to be back home to enjoy your company.

A thesis is not complete without a big thank you to my supervisors, Chris Purton and Ann Gower. Chris should be given a great deal of credit for the things which worked well in the thesis (I'll take the blame for the rest). He really is a very patient man and believes strongly in being unconventional - thank God! I can't thank you enough Kimosabe, I hope I haven't let you down. Ann has been kind enough to support me for all of these years and has been great bringing this thesis home down the final stretch (I hope you learned something about star formation along the way). I must also thank my committee, particularly Colin Scarfe, for reading earlier versions of this thesis and all of the editorial comments they made. I would also like to thank John Scalo and Lynne Hillenbrand who also provided editorial comments and insight into improving the thesis and keeping me on the right track.

Last, but not least, I must thank the Father, Son and Holy Spirit for giving me the strength and perseverance to complete this thesis.

Dedication

I have saved for my dedication an acknowledgement of that most special person in my life, my bestest buddy, my fianceé, my Cathy. Thank you so much for all of your help and support you have given me over the years. I look forward so much to the adventures we shall share throughout our lives together. God bless you, keep you safe, and protect you. All ways, your David.

Introduction

The Historical Development of Our Understanding of Star Formation

The first model of star formation can be attributed to Immanuel Kant and Pierre Simon Laplace who, in the eighteenth century, proposed the 'nebula theory' to account for the formation of the solar system. In their original model, they envisioned a large thin disk of gas, approximately the size and mass of the current solar system, undergoing contraction, from which the Sun formed at the center with the planets forming in rings of material which had broken away from the contracting disk. Problems with the distribution of angular momentum in this system, the inability to explain planetary orbits inclined to the plane, as well as the inability of the rings of the proposed size to avoid being disrupted by tidal forces proved insurmountable. Furthermore, the manner in which the disk first formed was not addressed. However, the work of Kant and Laplace has served to plant the seed for contemporary models of star formation and the related problem of planetary formation.

In the nineteenth century, the contemporary mathematical framework for tackling the problem of star formation was formulated by R. J. E. Clausius in his derivation of the virial theorem. A very interesting exposition of the historical development of this theorem is given by Collins (1978). A rigorous development of this formulation is not the focus of this thesis but the underlying principle is clear if one considers that the change in the dynamical state of a system is a balance between the forces which are trying to disperse the system and those trying to condense it. Clausius was able to show that the mathematical description of this balance is:

$$\frac{1}{2}\frac{d^2 I}{dt^2} = 2T + \Omega, \tag{I.1}$$

where I is the moment of inertia of the system, T the kinetic energy of the system and Ω the potential energy of the system. The simplest application of this formula to the problem of star formation was first carried out by Sir James Jeans who considered a cloud of gas which was stable (i.e., a system in which there is no change in its rotational inertia), in which the kinetic energy of the system would be due to its thermal motion and its potential energy would be determined by its self-gravity. For

such a system, Eq. I.1 reduces to:

$$0 = 2\left(\frac{1}{2}Mv^2\right) + -\alpha\frac{GM^2}{R}. \tag{I.2}$$

where M, the virial mass, is the total mass contained within radius R, v is the mean three-dimensional velocity of the particles due to their thermal motion, α is a factor included to generalize the equation to allow for different geometries and G is Newton's gravitational constant. The minimum mass which must be contained within radius R such that the force due to self-gravity of the system at least equals its tendency to disperse due to its thermal motion is given by Eq. I.2 and is known as its Jeans mass. A mass larger than this, for a given gas temperature and radius, will undergo collapse while for a smaller mass the system will disperse.

Of course it was realized that Eq. I.2 did not contain all of the possible contributing forces to the system. Over a period of time the influence of additional forces, e.g., magnetic fields and rotation (Chandrasekhar & Lebovitz 1962), turbulence (von Weizäcker 1951), and external pressure (Ebert 1955, Bonnor 1956), have been included. A more complete formulation of the problem, assuming a stable system, may now be given as:

$$P - \Omega = 2T + B + 2L, \tag{I.3}$$

where P represents the contribution to the energy of the system due to any external pressure, Ω represents the potential energy of the system as before, T represents the kinetic energy of the system which must now include the contributions due to thermal motion and turbulent motion, B is the total net magnetic energy of the system and L represents the energy due to rotation.

Contemporary Approaches to Understanding Star Formation

Various assumptions have to be made in approaching a theory of star formation for a given region. It is quite common for a particular model of the star forming process to rely upon a reduced form of Eq. I.3 in that only some of the (relevant) forces at play are considered. As an example, in the analysis of the star formation in Camelopardalis presented in this thesis, the role of external pressure is not considered even though many of the CO clouds found in the region do not appear to exceed their virial mass and should quickly dissipate without this additional force. However, one of the main points of interest in this thesis is the relation between

the molecular clouds and newly formed stars, not necessarily the longevity of the clouds (which would require details of the external pressure). The assumption that the external pressure is constant throughout the field is common to most studies of star forming regions and is adequate for the analysis conducted in this thesis.

Furthermore, understanding star formation is inherently difficult as it is difficult to define what constitutes a 'system' exactly in a particular situation. For example, an extreme case would be a starburst galaxy, in which case the whole galaxy, or at least a significant portion of it, constitutes the system undergoing the transformation from gas to stars. The complexity of this system changes as it evolves and the importance of the different forces may vary with time.

Contemporary models of star formation have approached the problem, for the most part, from two different points of view. One point of view considers star formation in terms of the structure of the molecular clouds from which the stars came (von Weizäcker 1951, Larson 1979, 1981, 1991, 1992), i.e., they are produced as a natural consequence of the structure seen in the interstellar medium (ISM). The other point of view considers star formation in terms of the details of the formation and evolution of individual stars (Myers & Benson 1983, Shu et al. 1987, Myers 1991). The two approaches are not mutually exclusive. On the contrary, one of the main thrusts of contemporary star formation theory is an attempt to synthesize the observations and theories developed from these two points of view.

On the Evolution of Molecular Clouds

Historically, there were two schools of thought on the organization of the ISM, which can be now be extended to molecular clouds. Von Weizäcker (1951) proposed a model of the ISM where in the structure of the clouds could be described by classical turbulence (Kolmogorov 1941), whereby differences in the velocity field served to organize material in a series of eddies with a transfer of energy, via viscous heating, from the largest scale to the smallest. At the smallest scale, heat is then dissipated via radiative cooling. If the smallest clouds can satisfy the Jeans criterion then the smallest clouds will collapse and form a star. On the other hand, Hoyle (1953) argued for a gravitationally-driven structure, i.e., turbulence in a gravitational field rather than a pressure field, where fragmentation at all levels of organization occurred as a natural result of the gas cooling. Again, the final unit in this fragmentation scenario was a Jeans mass cloud which produced a star. The difference between these two

propositions is subtle but very important, and one which will be addressed in some detail in this chapter. As Hoyle (1953) very succinctly summarized:

> "The rise of pressure [in a velocity field] due to compression in ordinary turbulence tends to disrupt the denser elements of material. It is for this reason that the density of a particular sample of material fluctuates in ordinary turbulence, sometimes being denser than the general average and sometimes less dense. The formation of a denser element in gravitational turbulence, on the other hand, only increases the ability of the element to hold itself together. Thus there is a rooted difference between the two cases: denser elements are evanescent in ordinary turbulence, denser elements tend to become permanent condensations in gravitational turbulence."

While the von Weizäcker and Hoyle models of molecular clouds are useful they cannot entirely represent the truth of the matter. Both of these models are essentially 'top-down' views of the organization of molecular clouds in the Galaxy and are very limited in their application. If either the von Weizäcker or Hoyle model were strictly correct then the star formation associated with these clouds, and all clouds in the Galaxy, should be rapid, with the molecular material being quickly converted into stars. This is not seen in the Galaxy today where the observed star formation rate, ~ 3 $M_\odot$ yr^{-1}, is conspicuously low and the lifetime of molecular clouds, $1-3\times10^7$ yr (Blitz & Shu 1980, Elmegreen 1985) is appreciable. This difficulty with time scales for both the von Weizäcker and Hoyle models was first noted by Oort (1954) and modelled by Field & Saslaw (1965). In the modification to the theory proposed by Oort (1954) it was proposed that the largest molecular clouds were continually being replaced by smaller ones which coalesced and which, in their turn, had been built up from even smaller clouds, and so on, down to the smallest cloud scale. It should be noted that application of Oort's (1954) 'bottom-up' model alone is also unsatisfactory as it does not allow for a realistic break up of the most massive clouds by stellar winds after the formation of a sufficiently massive star (Elmegreen 1987) [1] and/or supernovae (Tenorio-Tagle & Bodenheimer 1989). Nor does it ad-

[1] Elmegreen (1993) considers the formation of clouds via 'pressurized' events as being a separate process, a *discontinuous* rather than a *continuous* process, from the two described here. However, the objects he attributes to these events – shells, sheets, cometary globules and galactic chimneys – may be modelled just as well in

dress, in any detail, how such a star is formed from the most massive clouds (Field & Saslaw 1965), or allow for destructive collisions between clouds (Struck-Marcel & Scalo 1984).

Hence, any molecular clouds we observe, e.g., the Cam OB1 clouds or Perseus clouds, represent a snap-shot of the current state of affairs, which is a balance between the tendency for the clouds to break up into smaller clouds and the tendency for smaller clouds to conglomerate to form larger molecular complexes.

On the Formation of Individual Stars

The formation of an individual star is still a very poorly understood process but the standard model for this process at present (Shu et al. 1987) involves the inside-out collapse of a rotating isothermal molecular cloud core which has a $1/r^2$ density profile. Collapse of such a core leads to the formation of a proto-star and disk at the center of the core. Material from the infalling core continues to accrete onto the proto-star after first falling upon the much larger disk. Termination of the infall occurs when outflows from the proto-star, either from bipolar outflows or stellar winds, disperse the remaining core material.

In the model of Shu et al. (1987) magnetic fields serve as the main support mechanism regulating the size of the initial core and subsequent proto-star formed. Cores which are gravitationally unstable but supported by the local magnetic field (magnetically sub-critical cores), collapse slowly as the supporting magnetic field gradually escapes (ambipolar diffusion). Cores in which the magnetic field support exceeds the minimum to prevent gravitational collapse (magnetically super-critical cores), avoid collapse until the mass contained within the molecular core exceeds what can be supported, after which rapid collapse occurs. Given that the super-critical cores can be more massive than the sub-critical cores before the onset of collapse, it is believed that the super-critical cores produce massive stars.

While the model of Shu et al. is attractive in the sense that it provides a comprehensive framework in which to study the evolution of the proto-star and is observationally consistent with the density profiles seen in cloud cores, as least as measured by present techniques (Myers 1983), it is by no means universally accepted. Goodman et al. (1990) note there is no unequivocal evidence for an alignment of

---

terms of the two general processes operating in the evolution of the ISM so there is no additional insight to be gained from making this distinction.

cloud features with the ambient magnetic field. This argument was extended to cloud cores (Myers et al. 1991) and bipolar outflows (Heiles et al. 1993), where it was shown that neither the axis of rotation nor the direction of the outflows was correlated with the ambient magnetic field. Furthermore, this model of star formation leads to the formation of single stars (Bodenheimer *et al.* 1993) and cannot account for the high frequency ($\sim$ 50%) of multiple systems seen in very young star forming regions.

An alternative model by Adams & Fatuzzo (1996) proposes that the Shu et al. model be generalized to include other support mechanisms, e.g., turbulence and thermal pressure, in which case the rate of build up onto the proto-star from the surrounding core material is related to the rate of rotation of the core and the effective sound speed a_{eff}, i.e., the rate at which material can be transported to the proto-star from the surrounding molecular core. In his early work, Larson (1981) proposed that the proto-stellar core was built up entirely by accretion processes, in a manner somewhat reminiscent of the Oort model for cloud evolution, with the termination of infall again occurring when the radiative pressure and stellar winds prevented further accretion. In this model Larson argued that the initial proto-stellar mass should be a function of the core density and temperature ($\rho \geq 10^4$ cm^{-3}, T $\approx$ 10 K) which for typical cores should yield a proto-stellar mass $\sim$ 1 $M_\odot$. Finally, in a re-examination of the problem, Larson (1991, 1992) suggested an alternative solution in which turbulence was the dominant force for organizing the ISM and molecular cores represented the smallest organized unit of this structure.

None of these models address the problem of multiple-star formation directly. In the original work of Hoyle (1953) no rotation was assumed in the cloud fragmentation process but this model was extended by Zinnecker (1984) to the smallest fragment sizes, resulting in the formation of binary stars. In all the models of individual star formation discussed so far, it is assumed that any companion stars which form around the main proto-star form in the disk produced as a result of the collapse of a rotating core. Details of the mechanism for the formation of the disk, its size relative to the proto-star, the amount of the system's angular momentum it contains, are still very poorly understood (Bodenheimer et al. 1993). Furthermore, whether any successful models for the formation of multiple star systems can be extended to explain the formation of clusters or whether they form by some other means, e.g. fragmentation of the core before collapse, remains to be seen.

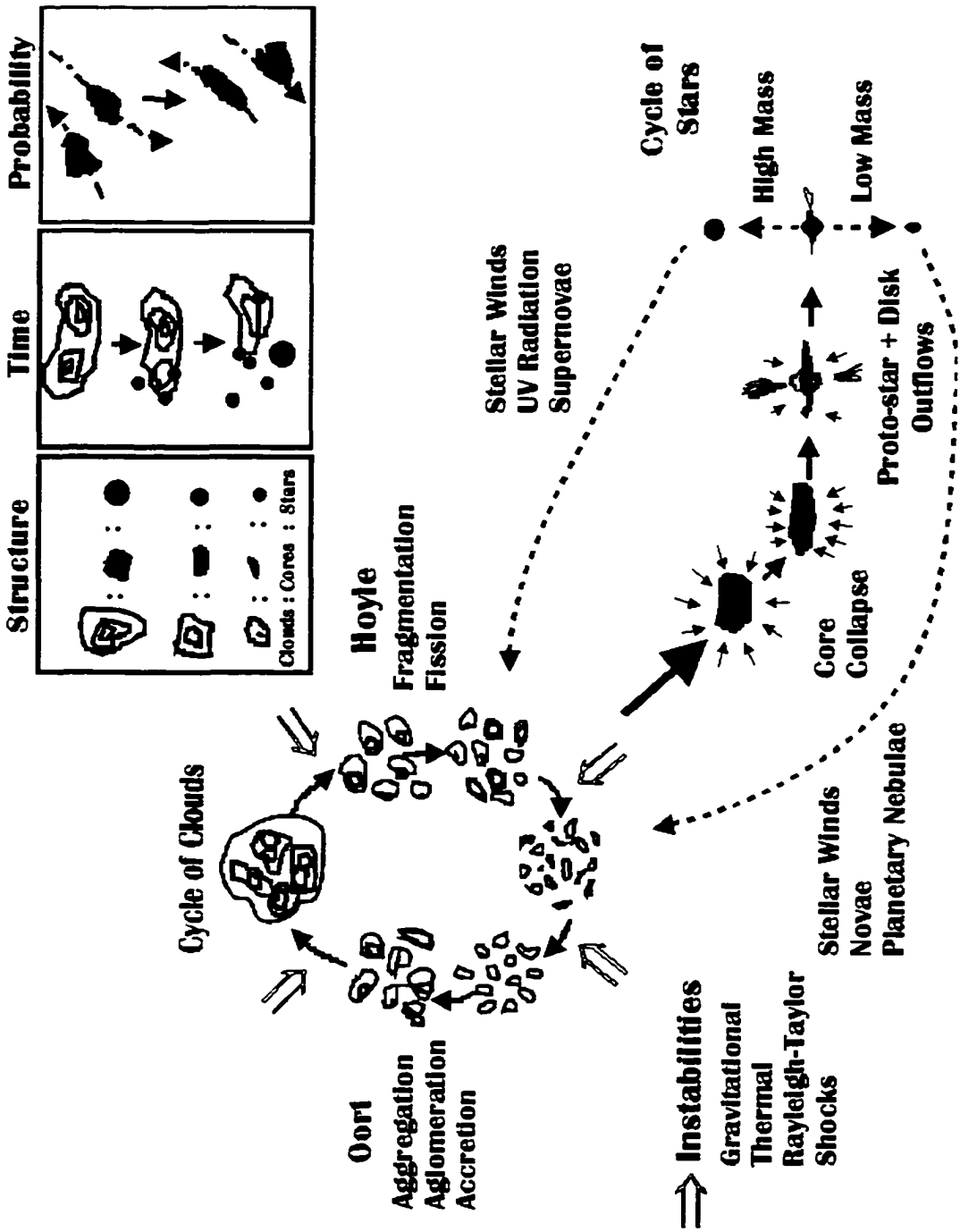

Figure I.1 A schematic diagram of the relationship between the ISM and stars. The cycle of clouds represents the possible states of the molecular clouds, while the cycle of stars illustrates the evolution of stars for different masses. The conversion of the ISM into stars is shown as a solid arrow, while the enrichment of the ISM by the stars via stellar winds and supernovae remnants are shown as broken arrows. The fundamental elements of the problem of star formation, *structural*, *temporal*, and *stochastic*, are highlighted in the insert.

Figure I.1 provides a pictorial summary of the current state of star formation theory. In this overview of the problem, the relationship between the ISM and the stars - the Galactic ecology – is represented by two cycles: the cycle of clouds and the cycle of stars. The cycle of clouds is not really a closed cycle because low mass stars, and to a lesser extent high mass stars, permanently remove gas from the ISM. However, this time scale, $\sim 10^8 - 10^9$ yr, is long in comparison with the length of a single star forming event, e.g., the time to form an association, $\sim 10^7$ yr (Hillenbrand et al. 1993).

Observational Constraints on the Formation of Stars

There are several observations which are useful in constraining any model for the conversion of the ISM into stars.

1. Larson (1981, 1982, 1991, 1992) noted that there was a relationship between the most massive star formed in a star forming region and the most massive molecular cloud associated with the star forming region, based upon a literature search of the data then available. This relationship is described by

$$M_* \propto M_{cloud}^n, \tag{I.4}$$

with $n = 0.43$. Larson argued that if the stars were forming in an hierarchical manner i.e., the most massive star formed from a given subsystem was related in a similar fashion to the mass in the subsystem, then the distribution of stars would follow a power-law distribution given by,

$$\frac{dN}{dlogM_*} \propto M_*^{-x}, \tag{I.5}$$

where $x = 1/n = 2.33$. Larson allows for both accretion, which was the premise of his early work (Larson 1981), and turbulent fragmentation, which is the premise of his more recent work (Larson 1992), to be the responsible agents.

2. Observations of many star forming systems, including both high-mass star and low-mass star forming regions, throughout the Galaxy show an initial mass function (IMF) [2] which is relatively constant with $x = 1.7 \pm 0.5$ (Scalo 1987).

3. Star formation is going on throughout the Galaxy in two modes: "loosely aggregated" star formation occurs in smaller and sparser clouds with predominately low-mass star formation scattered throughout the region, e.g., Taurus (Larson 1982, Evans 1991), whereas "tightly packed" star formation occurs in denser, isolated molecular clouds and results in the formation of more massive stars from the more massive cores, e.g., ρ Ophiuchi (Lada et al. 1993). However, neither mode is completely absent in a star forming region where the other mode is most evident, e.g., Orion (Evans 1991).

---

[2] There is some confusion in the literature about the calculation of the IMF in terms of mass bins or logarithm mass bins. Throughout this thesis the IMF is defined in terms of the change in the number of stars (and clouds) per mass bin, in which case $\frac{dN}{dM} \propto M^{-(1+x)}$.

4. Not all giant molecular clouds (GMC, $M \geq 10^5$ $M_\odot$) produce stars (Blitz 1993), and some are doing so at a very low rate, e.g., the GMC detected by Maddalena et al. (1986).
5. Star formation is not coeval but rather contemporaneous (Stahler 1985, Palla & Stahler 1990, 1991, Garmany 1994). There is also evidence for the formation of low-mass stars after large mass stars have appeared (Hillenbrand et al. 1993).
6. It is necessary but not sufficient that there be high-density cores present to ensure star formation; star formation is strongly favored in regions possessing a substantial total mass (Lada et al. 1993).
7. Cores appear to be elongated and dominated by rotational motion which does not appear to be well correlated with the large-scale structure of the molecular cloud (Myers et al. 1991). As stated in the previous section, there is no overwhelming evidence for the alignment of the cores with the ambient magnetic field (Heiles et al. 1993, Goodman et al. 1990), but this point is still contentious. Recent work by Vallée & Bastien (1996) suggests such an alignment may be in effect but there are a large number of possible magnetic field configurations proposed and the uncertainty in the measurements is large. Furthermore, the magnetic field which they have measured may not be the one deep inside the molecular cloud.
8. The largest cores appear to be embedded in the center of the most massive clouds with smaller cores distributed about them (Blitz 1993).
9. The star forming efficiency for a molecular complex as a whole is low, typically only a few percent, but is very high, greater than 50%, for the star forming molecular cores (Evans 1991).
10. At least half of the stars studied which can be associated with star forming regions are multiple star systems; of these 87% are binary systems (Bodenheimer et al. 1993).

The observational constraints listed above suggest that *the star forming process is regulated in three different ways; structurally (as suggested by points 1 through 3), temporally (points 4 and 5) and stochastically (points 6 through 10).* A simple overview of a typical star forming event may be as follows; molecular material forms, by whatever means, and arranges itself quickly into a hierarchical structure with stars being produced directly from the cores of these structures. Massive cores, formed at the center of large molecular clouds tend to form the most massive stars.

These cores interact via tidal or hydrodynamic mechanisms, and in a small number of encounters, one, some or all cores involved become unstable and collapse. Star formation is favoured in regions of high density gas as the total number of interactions increases and the cross-section for a star forming interaction increases (due to the decreased relative velocity of the interacting cores). Cores appear to be flattened and are probably disk-like which may be the result of rotation or ambipolar diffusion but their collapse, in general, appears to be unstable, in which case multiple star systems or possibly stellar clusters are formed.

Why Camelopardalis? What can it tell us about the Star Forming Process?

Camelopardalis OB1 (Cam OB1) is a very extensive OB association ($134° \leq l^{II} \leq 151°$, $-3° \leq b^{II} \leq +7°$) [3] lying at a distance of 975 pc (see Chapter 4, Humphreys 1978, Dame et al. 1987). Star formation in the vicinity in the recent past ($\sim 1 - 5 \times 10^7$ yr) can be traced out by the OB association itself as well as by large, extensive and old HII regions, e.g. S202 (Sharpless 1959) or supernova remnants (α Cam is a very well studied runaway star in the region believed to have originated in NGC1502 but the remnant of the companion star to α Cam is no longer visible, Blaauw 1964). More recent star formation in the region ($\sim 10^5 - 10^6$ yr) includes the very energetic outflow AFGL490 (Campbell et al. 1986, Mitchell *et al.* 1995), the newly detected outflow AFGL490-iki (Purton et al. 1995), the R-Association Cam R1 (Racine 1968), as well as infrared sources detected by the *IRAS* satellite (Beichman et al. 1988) which have the infrared colors of (ultra compact) UC HII and HII regions, masers, outflows, etc. (Walker & Cohen 1988). Hence, Cam OB1 appears to be an active star forming region producing intermediate mass stars (3 to 25 $M_\odot$, early A- to late O-type) albeit at a much less prodigious rate than some of the more energetic intermediate and massive star forming regions in the Galaxy, e.g. Orion and Monoceros (Larson 1982).

Cam OB1 is worthy of study for several reasons. Firstly, very little is known

[3] In regards to conventions; all Galactic coordinates refer to the new Galactic coordinates (l^{II}, b^{II}) and will be referred to as (l, b) throughout this thesis, the radial velocities measured in the Local Standard of Rest are based upon standard solar motion, and all equatorial coordinates are referred to the mean equinox and equator of B1950.0 unless otherwise specified.

about this region of the Galaxy. Examining the Palomar Observatory Sky Survey (POSS) prints shows that Cam OB1, in projection, lies near to the very energetic W3/4/5 star forming region and most studies carried out along this line-of-sight have concentrated on this dynamic region. Studying Cam OB1 is an excellent opportunity to investigate a relatively poorly known region of the Galaxy where the possibility of new discoveries, e.g., AFGL490-iki, is great. Secondly, Cam OB1, by virtue of being a somewhat quieter and gentler star forming region allows the study of the formation of an OB association in which the formation of very massive stars and their evolution, via stellar winds or supernova remnants, have not destroyed the primary mechanism responsible for producing the stars. Thirdly, as in studies of other star forming regions, Cam OB1 can be tested for consistency with the observable constraints outlined in the previous section. An exhaustive examination of star formation in the Cam OB1 region would require observations at many different wavelengths with different instruments and is beyond the scope of this thesis. However, what this thesis attempts to do is provide a framework for our understanding of star formation within the Cam OB1 region. This thesis also suggests further observations, which will support or reject the claimed method of star formation. Finally, it also comments on the applicability of the star forming mechanism(s) seen in Cam OB1 to elsewhere in the Galaxy.

Outline of the Thesis

Since the primary data for this thesis consist of a CO survey of the Cam OB1 region, the first three chapters will focus on this material. Chapters 4 through 7 identify the sites of star formation in the region and consider the star forming process in terms of the three elements proposed to characterize it, i.e., the structural relationship between the parent molecular clouds and newly formed stars, temporal evolution of the clouds, and the probability of the onset of star formation. Chapter 8 compares the structure of the clouds in Cam OB1 with the more distant Perseus region. The final chapter provides a summary of the current knowledge of star formation in Cam OB1 and makes some suggestions for further observations. The outline of the thesis, in detail, is as follows:

Chapter 1 discusses the physics of the radio emission by the CO molecule as well as essential definitions used throughout the remainder of the thesis. It also presents background material necessary to provide some insight into the underlying

assumptions and limitations of CO molecular observations.

Chapter 2 presents the CO data for the thesis. These data have been published (Digel et al. 1996) and form part of a larger survey of the second quadrant being undertaken at the Center for Astrophysics (CfA).

Chapter 3 deals with the improvement in quality in the present CO data over the previously available CO data for this region. The improvement in data quality is examined via Fourier transform techniques and structure tree statistics. Results of this analysis suggest there is no preferred scale size and there exists a hierarchical structure in at least one of the molecular clouds in the Cam OB1 region.

Chapter 4 examines the optically identified stars in the Cam OB1 region taken from the SIMBAD data base. A fit to the data shows that the distance to the association is 975 ± 90 pc and the association has been evolving contemporaneously for the last $1-50 \times 10^6$ yr. There is strong evidence for the presence of both pre-main sequence and evolved stars in the association.

Chapter 5 considers the most recent star formation in the region by analyzing the infrared sources selected from the *IRAS* data base (Beichman *et al.* 1988). The current star formation, traced out by these sources, is shown to coincide with the current site of interaction between two molecular complexes. A pointed survey, undertaken with the Dominion Radio Astrophysical Observatory 26m telescope, of methanol masers of the entire survey region failed to detect any new sources in the Cam OB1 region, but a new source associated with IRAS 02455+6034 was detected in the Perseus arm (near W5). Data for these observations have been published (Lyder & Galt 1997). High resolution observations of selected sites in the Cam OB1 region of CO emission, undertaken with the James Clerk Maxwell Telescope, revealed the presence of a second powerful outflow, AFGL490-iki. An announcement of this discovery has been made (Purton et al. 1995).

Chapter 6 deals with confirming the association between the stars assigned to Cam OB1 and CO emission features. This is accomplished from morphological arguments and physical arguments, i.e., the ionization of the Cam OB1 gas by the hot Cam OB1 stars and the warming of the dust associated with the Cam OB1 clouds by the Cam OB1 stars.

Chapter 7 analyzes the star forming history of the Cam OB1 region and argues that star formation in Cam OB1 has had three epochs of activity. The first occurred over a period of $1-50 \times 10^6$ yr ago and probably involved the collision of two molec-

ular complexes. A second epoch of star formation appears to have been triggered by shock compression of one of these complexes $3 - 1 \times 10^6$ yr ago. The most recent epoch of star formation is coincident with their current points of intersection. The IMF for the stars in Cam OB1 agrees with that seen elsewhere in the Galaxy. The cloud mass function for many of the CO complexes in the region, including the interacting complexes, shows a similar scaling law as the IMF. In all cases the star forming efficiency is low (less than a few percent).

Chapter 8 compares the molecular clouds in Cam OB1 with those in Perseus. It is shown that the clouds in Cam OB1 cannot be distinguished from those in Perseus on the basis of the degree of their turbulent support, but many of the clouds in Cam OB1 are not gravitationally bound. It is also argued that this last group of clouds are the youngest clouds in Cam OB1.

Chapter 9 is a summary of the analysis of the Cam OB1 region provided in the thesis and makes some suggestions for further studies.

Appendices of technical details deemed necessary to the thesis, but not to the main body of work, are also included. Appendix B contains data on Perseus stars not directly related to the thesis but discussed in the published survey (Digel et al. 1996), which referenced this work.

Chapter 1

General Overview of CO Observing

The basic physics of CO emission is reviewed; this includes the modelling of CO emission assuming statistical equilibrium and application of the equation of radiative transfer. The detection of CO emission by ground based telescopes is also discussed taking into account the attenuation of the CO signal by the atmosphere and the efficiency of the coupling of the telescope beam to the CO signal. Physical quantities of importance characterizing a CO 'cloud' are also defined, i.e., radius, linewidth, CO mass, virial mass and luminosity.

1.1 Introduction

Molecular hydrogen, H_2, is one of the major components of the interstellar medium (ISM). It is also the major constituent of molecular clouds, which are the sites of star formation. Unfortunately, direct detection of H_2 via vibrational or rotational (quadrupole) transitions is not easy due to their relative weakness or location in a spectral region of poor atmospheric transmission. With the first successful detection of ^{12}CO $J = 1 - 0$, $\nu = 115.2712$ GHz, λ =2.6 mm (Wilson et al. 1970), hereafter referred to as CO, there became available a useful probe of the molecular environment of star forming regions. In this chapter, the underlying basic physics of the CO molecular transition, and the limitations and assumptions made in observing it, will be discussed. Physical quantities of interest, e.g., the mass of a molecular cloud, based upon the observations will also be derived. This chapter will be limited to a highly idealized system in order to present the main concepts relevant to observing CO, while a discussion of the uncertainties in the quantities dependent upon the observing procedure, e.g., the acceptable noise level for a given spectrum, will be deferred until Chapter 2.

The layout of this chapter will be as follows: §1.2 presents the physical principles applied in observing the emission from a CO cloud assuming the CO line emission is purely the result of collision processes. This section also discusses the equation of

radiative transfer for the CO line emission when illuminated by a weak background source (2.7 K background radiation field), and the detection of the CO line by a ground based telescope. §1.3 discusses the measured physical quantities (§1.3.1), e.g., the linewidth of the CO line, as well as derived physical quantities (§1.3.2), e.g., the CO luminosity of a CO cloud. §1.4 summarizes the main assumptions and constraints made in CO observing.

1.2 Physical Principles

Molecular transitions are more easily modelled if it is assumed that the motion of the relatively light electrons can be completely decoupled from that of the much heavier parent nuclei (Born-Oppenheimer approximation). Under such conditions the total energy of a molecular system is given by (Lang 1980):

$$E_{tot} = E_{el}(r_e) + E_{vib} + E_{rot}, \tag{1.1}$$

where $E_{el}(r_e)$ represents the electronic binding energy at the equilibrium separation r_e, E_{vib} the vibrational energy and E_{rot} the rotational energy. Typical values for $E_{el}(r_e)$ are 5 — 10 eV at $r_e \sim 1$ Å. This contribution to the total energy does not play a role in the current observations and will not be considered further. For a simple diatomic molecule, $E_{vib} \approx \hbar\omega_{vib}(v + \frac{1}{2})$ with vibrational quantum numbers $v = 0, 1, 2, \ldots$. While these transitions can be observed and are useful they are not responsible for the line-emission considered here. The rotational energy of a simple diatomic molecule or linear polyatomic molecule assumed to rotate rigidly can be written as $E_{rot}^{(J)} = hBJ(J+1)$ where $J = 0, 1, 2, \ldots$ is the rotational quantum number, B is the rotational constant (in Hz) and h is Planck's constant. For a molecule like CO that possesses a permanent electric dipole moment, i.e., a separation of the centers of charge and mass, the molecule can undergo a strong electric dipole transition obeying the selection rule $J_{upper} - J_{lower} = \Delta J = +1$. Figure 1.1 is a simple schematic illustrating the lower transition states of CO.

Observationally, the problem is one of viewing a cloud of CO gas against the background radiation field and being interested in the contribution to the net radiation field, as viewed along a line-of-sight through the cloud, due only to the cloud. If the incident radiation impinging upon the far side of the cloud possesses a specific intensity defined as I_ν (this is the energy being emitted by a source per unit solid angle of the source which then falls onto some area of the cloud per unit bandwidth

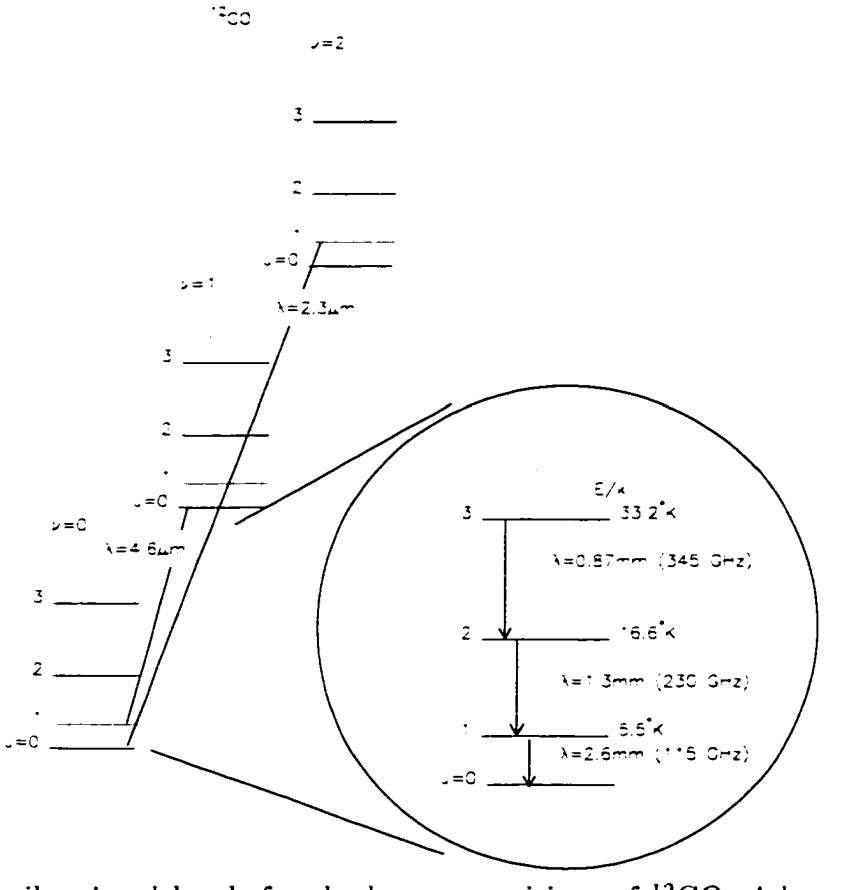

Figure 1.1 Ro-vibrational levels for the lower transitions of ^{12}CO. Adapted from Genzel (1992) and Scoville & Sanders (1987).

per sec, e.g., in cgs units this would be in ergs s^{-1} cm^{-2} sr^{-1} Hz^{-1}) then there should be some moderation of this radiation due to the addition of sources radiating within the cloud and some depletion due to some sources absorbing within the cloud. If this is the case, then an equation for the change in radiation intensity as it passes through the cloud (the transfer of radiation) is given by (Rybicki & Lightman 1979, Böhm-Vitense 1989):

$$\frac{dI_\nu}{ds} = j_\nu - \alpha_\nu I_\nu \tag{1.2}$$

where ds is the increment in distance along the line-of-sight through the cloud from the far side (say at some distance s_o as viewed by an observer) to the near side (say at some distance s as viewed by an observer). The first term on the right-hand side of Eq. 1.2 represents the added emission to the incident radiation and is defined as the emission coefficient (ergs s^{-1} cm^{-3} sr^{-1} Hz^{-1}) while the second term represents

the attenuation of the incident radiation (hence the negative sign) where α_ν is defined as the absorption coefficient (cm^{-1}). In some formulations of the problem, a term is included to account for photon scattering along the line-of-sight (Rybicki & Lightman 1979). However, it is assumed for the molecular clouds examined here that the optical depth is greater than one (emitted photons do not travel far before being re-absorbed) and that collisions dominate the equilibrium state of the cloud so that scattered photons, on average, do not contribute to the radiative transfer. This would not be the case for diffuse clouds where the contribution from scattered light could make a contribution to the radiation field.

It is sometimes simpler to think of the attenuation of the incident radiation in terms of the relative loss of intensity as it passes through the cloud rather than as a function of position in the cloud. This change of variables can be accomplished by defining the optical depth, $d\tau_\nu(s)$, as the total absorption per increment of length ds, i.e.,

$$d\tau_\nu(s) = \alpha_\nu ds. \tag{1.3}$$

and, hence, for the whole cloud

$$\tau_\nu = \tau_\nu(s) = \int_{s_o}^{s} \alpha_\nu(s')ds'. \tag{1.4}$$

It is now a simple matter to rewrite Eq. 1.2 in terms of the change in optical depth through the cloud, i.e., the change of the incident radiation intensity as function of optical depth, given by

$$\frac{dI_\nu}{d\tau_\nu} = S_\nu - I_\nu. \tag{1.5}$$

where S_ν is defined as the source function, the ratio of the emission coefficient to the absorption coefficient, i.e.,

$$S_\nu = \frac{j_\nu}{\alpha_\nu}. \tag{1.6}$$

Eq. 1.5 can now be solved making use of an integration factor ϵ^τ and integrating over the length of the cloud, from $\tau = 0$ to $\tau = \tau$, to obtain

$$I_\nu = I_\nu(0)e^{-\tau} + S_\nu(1 - e^{-\tau}). \tag{1.7}$$

Hence, the intensity of radiation emerging from the cloud is composed of the initial incident radiation attenuated by the cloud's total absorption plus the cloud's contribution to the radiation (assuming S_ν is spatially constant – a contribution from

scattering could be inserted at this point in which case S_ν is now the ratio of the emission coefficient to the sum of the absorption and scattering coefficients, but then Eq. 1.5 must be solved by more sophisticated analytical or numerical methods) over the length of the cloud. The solutions to this equation include the 'optically thin' case ($\tau < 1$) when Eq. 1.7 reduces to $I_\nu = I_\nu(0) + S_\nu\tau$, and the 'optically thick' case ($\tau > 1$) when the cloud's emission dominates the background emission giving $I_\nu = S_\nu$. Finally, the excess line intensity above the 2.7 K background continuum emission, ΔI_{line}, is given by

$$\Delta I_{line} = [I_\nu - I_\nu(0)] = [S_\nu - I_\nu(0)][1 - \epsilon^{-\tau}]. \tag{1.8}$$

The equation of radiative transfer describes only one aspect of the physics of CO emission. A complete solution to the problem also requires an understanding of the state of the gas in terms of the state of each molecule. Such knowledge cannot be obtained directly but may be inferred from a statistical approach. The simplest approach (Genzel 1991, 1992) considers a two level system to describe the CO rotational transition: a lower state l (no rotation) and an upper state u (rotating) with a change in energy between the two states given by $\Delta E = h\nu$ (photon at 115 GHz). If collisions are the sole agent for producing transitions between the two states ($u \rightarrow l, l \rightarrow u$) and there are n molecules (collision partners - these would be primarily H_2 molecules) per unit volume (cm^{-3}), then the transition rates per molecule per collision partner per sec are given by

$$C_{ul} = C_{u-l} = n\gamma_{ul} = n < \sigma_{ul}v >, \tag{1.9}$$

and

$$C_{lu} = C_{l-u} = C_{ul}(g_u/g_l)\epsilon^{-h\nu/kT_{kin}}. \tag{1.10}$$

σ_{ul} (cm^2) is the cross section for a collision $u \rightarrow l$ at velocity v ($cm\ s^{-1}$), γ_{ul} ($cm^3\ s^{-1}$) is the overall collision rate coefficient for $u \rightarrow l$, g_u and g_l are the statistical weights for the upper and lower states, respectively, given by $2J + 1$, and k is Boltzmann's constant. If the distribution of collision energies is given by a Maxwell-Boltzmann distribution at kinetic temperature, T_{kin}, then the average collision rate, $< \sigma_{ul}v >$, will be given by

$$\gamma_{ul} = < \sigma_{ul}v > = \frac{4}{\sqrt{\pi}}\left(\frac{\mu}{2kT_{kin}}\right)^{\frac{3}{2}} \int_o^\infty (\sigma_{ul}(v)v)v^2 e^{-\mu v^2/(2kT_{kin})}dv, \tag{1.11}$$

where μ is the reduced mass of the molecule and collision partner system. Typical values of γ_{ul} for CO with H_2 as its collision partner are 1.8×10^{-12} cm^3 s^{-1} and 3.7×10^{-12} cm^3 s^{-1} at 10 K and 100 K respectively (Spitzer 1978).

If the system is also allowed to be de-excited, i.e., to undergo $u \rightarrow l$ transitions by emitting a photon, then the relative populations in the u and l states for a system of n molecules may be found by the principle of detailed balance to be

$$n_l(\gamma_{lu}n) = n_u(\gamma_{ul}n + A_{ul}). \tag{1.12}$$

where A_{ul} is the Einstein coefficient for spontaneous emission. A_{ul} may be found from

$$A_{ul} = \frac{64\pi^4\nu^3}{3hc^3}|P_{ul}|^2. \tag{1.13}$$

where c is the speed of light, ν is the radio frequency at which the line is observed ($= 2B(J+1)$ where J is the lower state J) and P_{ul} is the dipole matrix element for the transition $u \rightarrow l$. In the case of a pure rotational transition for a linear molecule such as CO, $|P_{ul}|^2$ has been determined to be (Spitzer 1978)

$$|P_{ul}|^2 = M^2\frac{J+1}{2J+1}. \tag{1.14}$$

where M is the permanent dipole moment for the molecule which must be determined experimentally. For CO $M = 0.112$ Debye (1 Debye $= 10^{-18}$ e.s.u-cm). For the $J = 1 - 0$ transition of CO $B = 57.6$ GHz and hence, $A_{10} = 6 \times 10^{-8}$ s^{-1}.

Defining $n_{tot} = n_l + n_u$ and the critical density, $n_{cr} = A_{ul}/\gamma_{ul}$, it is now possible to re-write Eq. 1.12 in the form

$$\frac{n_u}{n_{tot}} = \frac{(g_u/g_l)e^{(-h\nu/kT_{kin})}}{1 + (g_u/g_l)e^{(-h\nu/kT_{kin})} + n_{cr}/n}. \tag{1.15}$$

The critical density is an important parameter as it defines the density at which the population becomes thermalized, i.e.,

$$(n_u/n_l)_{thermal} = (g_u/g_l)e^{(-h\nu/kT_{kin})}. \tag{1.16}$$

One of the problems in analyzing CO emission is that there is no consensus among radio astronomers on exactly when Eq. 1.16 is applicable. Values between 1 and 2 for the assumed ratio of n to n_{cr} are not uncommon in the literature. For this work it is assumed that $n = n_{cr}$.

A further modification which must be taken into account in determining the equilibrium state of the CO gas is the effect of line blocking. The above derivation for the distribution of molecules in each energy state assumes that a photon at a particular frequency (or velocity), once produced, will escape from the gas cloud without re-combining, i.e., the gas is optically thin to the emitted radiation. For emission regions which are optically thick, i.e., regions where the photon does not travel far before being absorbed, the Einstein coefficient is effectively reduced. If the optical depth, τ at a particular velocity can be determined then the reduction in the A_{ul} can be calculated. Assuming β represents the effective line blocking and $\beta \propto 1/\tau$ then $A_{ul} \rightarrow A_{ul}\beta(\tau)$ and Eq. 1.15 can be re-written such that

$$\frac{n_u}{n_{tot}} = \frac{(g_u/g_l)e^{(-h\nu/kT_{kin})}}{1 + (g_u/g_l)e^{(-h\nu/kT_{kin})} + n_{cr}\beta(\tau)/n}. \tag{1.17}$$

Measurements of τ for most giant molecular clouds in the Galaxy suggest that it is ≥ 10 (de Jong et al. 1980, Scoville & Sanders 1987) and with $n_{cr} \geq 3000$ cm^{-3} assuming no line blocking, then the effective density when the CO line is thermalized will be ≈ 300 cm^{-3}.

The observed radiation intensity from a transition which is in thermal equilibrium, such as CO observed in the radio region, can be expressed in terms of the excitation temperature, T_{ex}, or Rayleigh-Jeans radiation temperature at radio wavelengths, T_{RJ}, which will equal the kinetic temperature, T_{kin}, as well as the rotational temperature, T_{Rot}, i.e.,

$$S_\nu = \frac{2h\nu^3}{c^2}\,[exp\,(\frac{h\nu}{k\,T_{ex}}) - 1]^{-1} \approx \frac{2k\nu^2 T_{RJ}}{c^2} = \frac{2k\nu_{Rot}^2 T_{Rot}}{c^2}. \tag{1.18}$$

The background radiation will also follow a similar prescription with T_{back} in place of T_{ex}. Hence, the intensities (Eq. 1.8) may be written in terms of radiation temperatures,

$$T_{line} = (T_{Rot} - T_{back})\,[1 - exp\,(-\tau_\nu)]. \tag{1.19}$$

Finally, one last effect which must be taken into account is the fact that the clouds are not uniform but are usually very fragmented and hence they may or may not fill the beam of the telescope. In order to generalize Eq. 1.19 to take this into account, it must be modified so that

$$T_{Rot} = T_{Rot}\left(\frac{\Omega_{cloud}}{\Omega_{beam}}\right) + T_{back}\left(\frac{\Omega_{not\ cloud}}{\Omega_{beam}}\right), \tag{1.20}$$

where Ω_{cloud} represents the area of the CO cloud, $\Omega_{not\ cloud}$ represents the area within the beam but outside the cloud and Ω_{beam} represents the beam of the telescope. In principle, one can determine this modifying ratio, or filling factor, by observing with successively smaller beams with higher velocity resolution until T_{line} does not change. In practice, there are usually not enough data available to check this point and normally it is assumed that the filling factor is unity, as was assumed in the present survey (Digel et al. 1996).

So far the discussion has considered only the physics of CO emission at the source but this is not the entire picture. One complication is that the CO signal must also pass through the Earth's atmosphere where it is subject to attenuation that is highly weather dependent. It is also necessary to consider how efficiently the telescope detects the radiation in order to determine the true radiation temperature (T_{line}). What the telescope will measure is commonly referred to as the antenna temperature, T_A. If the effects of the atmosphere are first ignored, i.e., if the telescope were placed above the atmosphere, then the response of the telescope is given by:

$$T'_A(\theta_o, o_o) = \eta_R \frac{\int_{4\pi} T_R(\theta, o) P_n(\theta - \theta_o, o - o_o) d\Omega}{\int_{4\pi} P_n(\theta, o) d\Omega}. \qquad (1.21)$$

where η_R is the efficiency with which the source couples to the telescope, $T_R(\theta, o)$ represents the radiation temperature of the source and $P_n(\theta, o)$ represents the power pattern (sensitivity) of the telescope, both as a function of position in the sky in (θ, o) coordinates, and $d\Omega$ represents the solid angle of integration. Essentially, Eq. 1.21 is the convolution of the telescope beam with the source. If the telescope is well designed then most of the power is in the main beam and it is useful to define the forward looking beam efficiency, η_L, by:

$$\eta_L = \frac{\eta_R \int_{2\pi, Forward} P_n(\theta, o) d\Omega}{\int_{4\pi} P_n(\theta, \phi) d\Omega}. \qquad (1.22)$$

and what the telescope detects in the forward direction[1] is given by:

$$T_A^* = \frac{T'_A}{\eta_L}. \qquad (1.23)$$

[1] It was pointed out by the referee for the present survey (Digel et al. 1996) that the limits in the forward direction for the CfA survey was not 2π but rather down to the first nulls in the forward direction. Given that most of the sensitivity in the

If the effects of the atmosphere are then included it follows that T_A may be found from:

$$T_A = T'_A \epsilon^{-\tau} + \eta_L T_{Atm}(1 - \epsilon^{-\tau})$$
$$= \eta_L T^*_A \epsilon^{-\tau} + \eta_L T_{Atm}(1 - \epsilon^{-\tau}). \quad (1.24)$$

where τ is the optical depth of the atmosphere for the source elevation and T_{Atm} is the temperature of the atmosphere.

In principle, Eq. 1.24 could be solved directly for each observation but this is not the usual procedure at the CfA. What is done is known as the 'chopper wheel calibration', where T_A for a source is found relative to the temperature of a chopper wheel momentarily placed in front of the receiver. This procedure, in detail, is as follows:

1. Calculate the receiver temperature, T_{Rx}, and gain G using a hot (ambient temperature) and cold ($N_{2,liq}$) load. The voltages from the receiver for these two loads are given by:

$$V_{Cold} = G(T_{Cold} + T_{Rx}). \quad (1.25)$$

and

$$V_{Hot} = G(T_{Hot} + T_{Rx}). \quad (1.26)$$

Eq. 1.25 and 1.26 may be solved simultaneously to obtain T_{Rx} and G.

2. Determine the parameters η_L, T_{Atm} and τ by 'antenna tipping'. In this procedure, many observations of the sky at different elevations are taken in order to form a system of equations with each equation of the form:

$$V_{Sky} = G(\eta_L T_{Atm}(1 - \epsilon^{-\tau}) + (1 - \eta_L)T_{Amb} + T_{Rx}). \quad (1.27)$$

where T_{Amb} is the ambient temperature. The first term in Eq. 1.27 represents the contribution to the signal from the sky, the second term the contamination of the signal from ground radiation and the third term the noise contribution from the receiver. In solving Eq. 1.27 τ is assumed to be composed of two

---

forward direction was contained in the first nulls this discrepancy is not serious, however, for clarity the temperature scales in the Digel et al. (1996) were given as T^*_{mb} to indicate they were temperatures derived from the response of the main beam of the telescope.

components, τ_{O_2} and τ_{H_2O}. τ_{O_2} is due to oxygen in the upper atmosphere and is relatively constant ($\tau_{O_2} \approx 0.378$ at 115 GHz: Kutner 1978, Digel 1991) while τ_{H_2O} is due to water vapor in the lower atmosphere and is highly variable. This procedure is repeated every four to six hours, or more frequently when the weather is changing rapidly (Kutner 1978, Kutner & Ulich 1981), in order to update the solution for η_L, T_{Atm} and τ.

3. Determine T_A^* using the chopper wheel calibration. By looking at a second source, such as a chopper wheel at temperature T_L temporarily placed in front of the receiver, while pointing at the same position in the sky where V_{Sky} was obtained, the response of the system, V_L, is found to be:

$$V_L = G(T_L + T_{Rx}). \tag{1.28}$$

From Eq. 1.27 and 1.28, a calibration signal, ΔV_{Cal}, defined by:

$$\Delta V_{Cal} = V_L - V_{Sky}, \tag{1.29}$$

may be formed. If it is assumed that $T_L \sim T_{Amb} \sim T_{Atm}$ then it follows that Eq. 1.29 may be re-written as:

$$\Delta V_{Cal} \sim G\eta_L T_{Amb}\epsilon^{-\tau}. \tag{1.30}$$

Similarly, the voltage measured at the back end of the receiver when looking at a source is given by:

$$V_{source+sky} = G(\eta_L T_A^* \epsilon^{-\tau} + \eta_L T_{Atm}(1 - \epsilon^{-\tau}) + (1 - \eta_L)T_{Amb} + T_{Rx}). \tag{1.31}$$

and the difference between Eq. 1.31 and 1.27, ΔV_A, may be found to be:

$$V_{source+sky} - V_{Sky} = \Delta V_A \sim G\eta_L T_A^* \epsilon^{-\tau}. \tag{1.32}$$

Hence, for any source, T_A^* may be obtained from a comparison of Eq. 1.30 and Eq. 1.32, i.e.,

$$T_A^* = \frac{\Delta V_A}{\Delta V_{Cal}} T_{Amb}. \tag{1.33}$$

Eq. 1.33 is a first-order approximation of T_A^*. In general, the assumption that $T_L \sim T_{Amb} \sim T_{Atm}$ does not hold so that a correction factor, CF, of the form (SEST Handbook):

$$CF = 1 + \left(\frac{T_L - T_{Atm}}{T_L}\right)(e^{\tau} - 1) + \left(\frac{1}{\eta_L} - 1\right)\left(\frac{T_L - T_{Amb}}{T_L}\right)e^{\tau}. \tag{1.34}$$

must be applied to ΔV_{Cal}, i.e.,

$$\Delta V'_{Cal} = CF\Delta V_{Cal}, \tag{1.35}$$

and Eq. 1.34 becomes

$$T_A^* = \frac{\Delta V_A}{CF\Delta V_{Cal}} T_{Amb}. \tag{1.36}$$

The quantity T_A^* as derived from Eq. 1.36 is essentially what is measured at the backend of the receiver as the source temperature.

Finally, in order to recover the line temperature for the CO emission, as coupled to the main beam, a last correction for forward spillover and scattering efficiency of the support structure must be applied to give

$$T_{line}^* = \frac{T_A^*}{\eta_{fss}}. \tag{1.37}$$

where $\eta_{fss} = 0.82$ for the CfA antenna (Bronfman et al. 1988). In the literature T_{line}^* is often referred to as T_R^* and for consistency this practice will now be followed.

1.3 Physical Quantities of Interest

There are several physical quantities of which are of fundamental importance to the description of CO. Measurable quantities include the linewidth for the observed CO line, the boundary of the CO emission as defined by the half-maximum radius of the peak emission (the details of the selection method of this radius will be provided in Chapter 7) and the centroid of an emission feature weighted by temperature. From these measured quantities it is possible to derive the CO luminosity for a given emission feature (provided the distance is known), as well as the CO mass. It is also possible, assuming that the features are in virial equilibrium, to derive a virial mass. An estimate of the uncertainty in these parameters is provided in Appendix A.

1.3.1 Measured Physical Quantities

i. Linewidth Figure 1.2 shows a typical spectrum for an emission feature in the Cam OB1 region (velocity coverage of -5 to -22 km s^{-1}). This feature is defined by a rectangular box in (l, b, v) co-ordinates as a spatially and kinematically single feature. Given the identification of a CO feature, the linewidth is defined as the full width at half maximum ($FWHM$) for a Gaussian profile fitted to the average spectrum contained within the defining boundary. In practice, this was performed in a program, *cloud_find*, written by the author which called the in-house Interactive Data Language (IDL) library to make use of the resident line fitting routine *curvefit*. This program required an input function in the form of a Gaussian, i.e.,

$$\text{Mean } T_R^*(v) = \text{Offset} + \text{Maximum Mean } T_R^* \times exp\ -\left[\frac{(v - \text{Velocity of Peak})^2}{2\ \sigma^2}\right], \tag{1.38}$$

where $FWHM = 2.3556\ \sigma$ (Lang 1980), as well as its derivative (contrary to the IDL disclaimer) in order to fit the data properly.

However, the apparent $FWHM$ for a given spectrum requires one more correction before it can be used. All observations obtained with the CfA instrument involve the convolution of the instrument's spectral response (0.65 km s^{-1}) with the true velocity profile of the emission line. Hence, the true $FWHM$ for any emission feature will be given by the de-convolution of the apparent $FWHM$ with the correlator channel width or

$$FWHM(\text{true, km s}^{-1}) = (FWHM(\text{apparent, km s}^{-1})^2 - 0.65^2)^{1/2}. \tag{1.39}$$

In addition, the true $FWHM$ is derived from the one dimensional line-of-sight velocity, and hence is referred to as Δv_{1d}. In some instances, a three dimensional $FWHM$ is required in deriving a physical quantity of interest. In these cases, assuming random motions, then $\Delta\ v_{3d}$ is given by (Myers 1985)

$$\Delta v_{3d} = (\frac{3}{8\ ln2})^{1/2}\ \Delta v_{1d}. \tag{1.40}$$

For brevity, any future references to Δv_{1d} will simply be Δv.

ii. Radius The selection of a cloud radius is certainly more problematic. There are several methods which have been employed to define such a radius including the radius for a circular area equivalent to the area of the cloud defined at some arbitrary threshold average temperature or intensity (Dame 1983, Sanders et al. 1984,

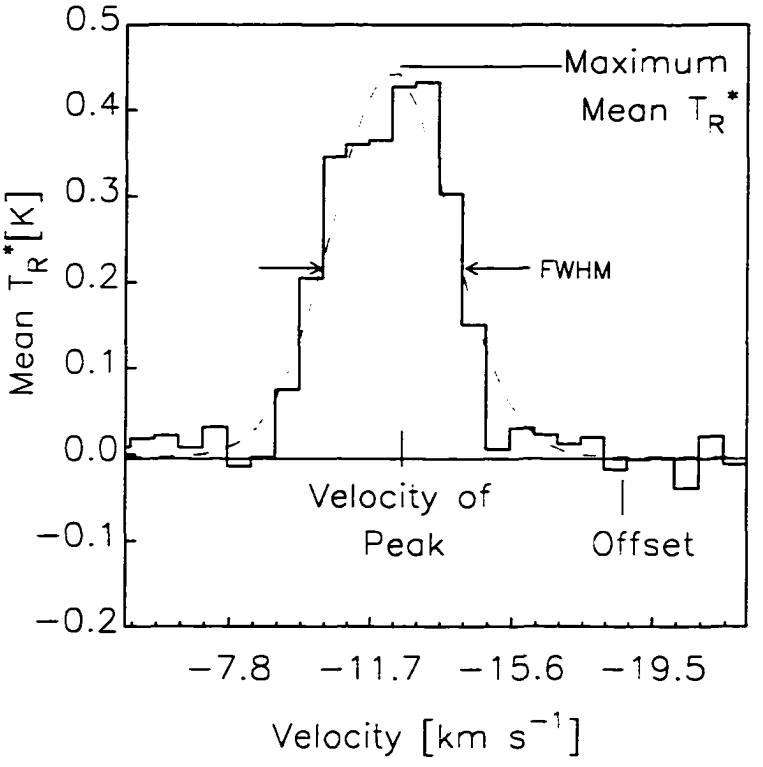

Figure 1.2 Sample spectrum for the Cam OB1 emission centered on $(l, b, v) = (141.9, +6.5, -12.0)$. Each channel represents the mean emission fitted over a rectangle selected to encompass only the emission feature of interest. The histogram is the actual data while the dashed line represents the fitted solution characterized by: the peak mean emission (0.45 K), the $FWHM$ (2.7 km s^{-1}), the position of the peak value (-12.3 km s^{-1}) and baseline offset (-0.0 K).

Maddalena et al. 1986, Peters & Bash 1987, Digel 1991, Dobashi et al. 1992). In some cases, the radius is related in some geometric fashion to the observed emission feature, e.g., as a weighted mean of the spatial dispersion (Solomon et al. 1987), while in others the cloud radius is derived from the number of detections on the survey grid spacing (Tereby et al. 1986, Chair et al. 1994) or by the chord cut along a particular axis of the survey (Sanders et al. 1985) or by the longest axis seen (Larson 1981).

In this thesis the definition of a cloud radius is essentially geometric but now it is assumed that the observed cloud radius is that derived from an equivalent circular area as traced out by the half-maximum intensity contour for a selected emission feature identified in an integrated map over a given velocity range (Digel

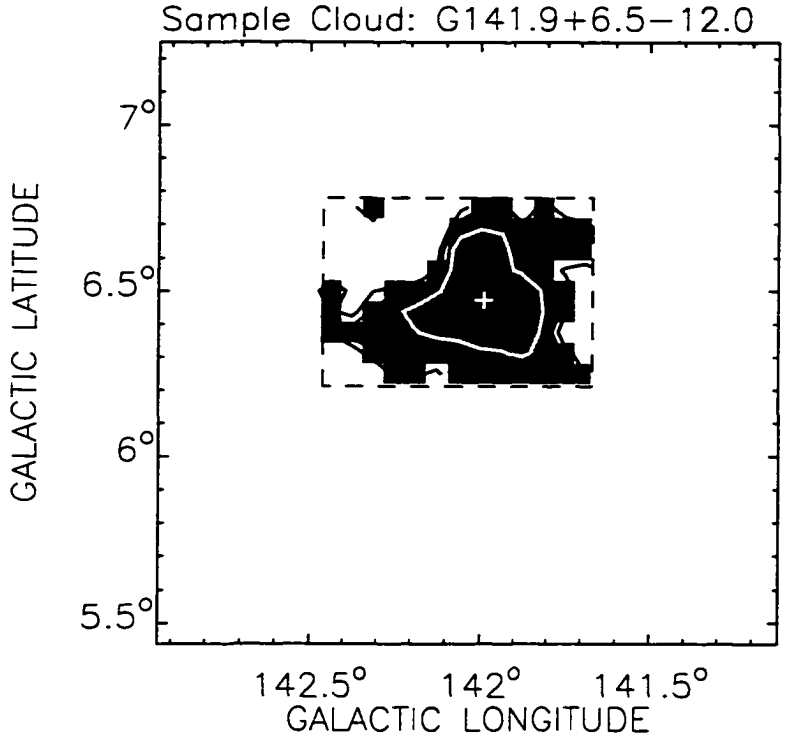

Figure 1.3 Sample map for the Cam OB1 emission centered on $(l, b, v) = (141.9, +6.5, -12.0)$, bounded as indicated by the broken line and integrated from −5 to −22 km s^{-1}. Each dark contour represents a 3σ level (1.17 K km s^{-1}). The projected centroid of emission is shown by the white cross and the half-maximum contour level (3.48 K km s^{-1}) by the white contour.

et al. 1996), i.e.,

$$r_{\rm Observed} = \left(\frac{\rm Area_{Half-maximum\ intensity}}{\pi} \right)^{1/2}. \qquad (1.41)$$

The advantages of this procedure over previous methods are the ease with which the radius can be defined, and its relative independence of the sensitivity of the survey. Again, as in the case of the linewidth, a correction for the finite beam width must also be taken into account. The data presented in this thesis and presented as a part of a recent survey (Digel et al. 1996) have been smoothed to a resolution of 10′. Hence, a true half-maximum radius taking into account the convolution with the 10′ beam is given by

$$r_{\rm True} = \left(r^2_{\rm Observed} - 5^2 \right)^{1/2}. \qquad (1.42)$$

where the observed radius is measured in minutes of arc. Figure 1.3 is a sample map for the cloud used for constructing the spectrum shown in Figure 1.2.

iii. Centroid of Emission It is important to determine the centroids as they may be used to indicate whether there are any interesting trends in the motion of clouds seen in the field. e.g., discontinuities in the velocity field indicative of a shear or possible cloud-cloud collision. The definition used for the centroid of a cloud is the emission weighted center of the cloud in (l, b, v) space, i.e.,

$$\bar{l} = \frac{\sum_{i=1}^{pixels\ in\ cloud} T_{Ri}^{*}\ l_i}{\sum_{i=1}^{pixels\ in\ cloud} T_{Ri}^{*}}. \tag{1.43}$$

$$\bar{b} = \frac{\sum_{j=1}^{pixels\ in\ cloud} T_{Rj}^{*}\ b_j}{\sum_{j=1}^{pixels\ in\ cloud} T_{Rj}^{*}}. \tag{1.44}$$

and

$$\bar{v} = \frac{\sum_{k=1}^{pixels\ in\ cloud} T_{Rk}^{*}\ v_k}{\sum_{k=1}^{pixels\ in\ cloud} T_{Rk}^{*}}, \tag{1.45}$$

where the limits are determined for each cloud as previously discussed (§1.3.1.*i*). The centroid for a cloud is calculated in the program *cloud_find* and the designation of the cloud is made based upon the centroid (l, b, v) values (to the first decimal place). e.g., G141.9+6.5–12.1 refers to the cloud centered on (141.934, 6.473, -12.10).

1.3.2 Derived Physical Quantities

i. Luminosity The luminosity of a molecular cloud (K km s^{-1} pc^2) is the integrated CO line intensity over the total area of the cloud. This is given by

$$L_{CO} = D^2 \int_{Solid\ angle\ of\ cloud} \int_{velocity\ range} T_R^{*}\ dv\ d\Omega. \tag{1.46}$$

where D is the distance to the cloud in pc, T_R^{*} is the radiation temperature, dv is the increment in velocity in km s^{-1} and $d\Omega$ is the increment in angular area in radians. This equation may then be written in terms of the maximum line temperature seen in the cloud, $T_R^{*}(max)$, the area under the Gaussian curve fitted to the velocity

distribution and the $FWHM$ of the velocity profile fitted by a Gaussian profile, Δv, (Dame 1983), i.e.,

$$L_{CO} = D^2 \, 2 \sqrt{\frac{\pi}{ln2}} \; T_R^*(max) \; \Delta v \int_{Solid\ angle\ of\ cloud} d\Omega. \qquad (1.47)$$

In the course of writing this thesis it was noted that there was a slight discrepancy between the method of calculating L_{CO}, method 1, used by the author and that of Digel et al. (1996), method 2. In method 1, the author fitted a Gaussian profile to the average value of all of the pixels contained within the cloud boundary at each velocity and multiplied by the total area contained within the cloud boundary. In method 2, a Gaussian profile was fitted to the sum of all pixel values within the cloud boundary which was then multiplied by the area of one pixel (method 2) . The ratio between the two solutions should, in principle, be unity, but it was determined by a least-squares fit to the data that

$$L_{CO}(\text{method 1}) = L_{CO}(\text{method 2})/1.07, \qquad (1.48)$$

i.e., method 1 underestimated L_{CO} by $\sim 7\%$ relative to method 2. It is not clear what is the source of this discrepancy but all of the L_{CO}s quoted throughout this thesis have been scaled to be in agreement with method 2.[footnote] One possible explanation is that $\sqrt{\frac{\pi}{2ln2}}$ was used in Eq. 1.47 rather than the proper coefficient - L. B. Knee, private correspondence.

ii. Mass There are two methods of mass determination used throughout the thesis. The first, M_{CO}, is the 'CO mass' of the molecular cloud derived from the CO luminosity (Eq. 1.40). The second, M_{vir}, is the virial mass of the molecular cloud as determined from the virial theorem.

a. CO Mass It is well established that CO is a good tracer of the molecular mass of a cloud (Combes 1991, and references therein). The fundamental quantity of interest is the constant of proportionality, X, between the integrated line-of-sight CO intensity, $W(CO)$, and the H_2 column density, $N(H_2)$. This constant, defined by

$$X = \frac{N(H_2)}{W(CO)}, \qquad (1.49)$$

where

$$W(CO) = \int T_R^*(max) \; dv, \qquad (1.50)$$

can be determined in several different ways. The first direct determination of X made was based upon ultraviolet absorption by H_2 of nearby background stars (Savage et al. 1977). Since this technique could only be applied to nearby stars and to diffuse clouds, more indirect methods were then employed. These included photometric extinction measurements (Bohlin et al. 1978, Elias 1978) and star count measurements (Dickman 1988). In both of these methods there is an assumption that the gas-to-dust ratio is constant, which does not necessarily hold true. Furthermore, in the case of photometric extinction surveys, information is only gained for a small area, while in the case of star count measurements, a tremendous effort is required in treating a large area, which may also suffer from calibration and inherent statistical uncertainties (Dickman 1988).

More recently, there have been high-energy γ-ray observations of the Milky Way which examined the γ-ray intensity and its correlation to $N(H_2)$ and $W(CO)$, and, consequently X (Lebrun et al. 1983, Bloemen et al. 1984, Bloemen et al. 1986, Strong et al. 1988). This technique, which assumes that cosmic rays strike hydrogen nuclei in the ISM producing π mesons which in turn decay into γ-rays on a one-to-one basis, i.e., one γ-ray per nucleus, is still not established. There has been some debate as to whether the γ-rays fully penetrate the cores of molecular clouds to yield a true count of the hydrogen nuclei (Bloemen 1989) as well as the calibration of the relationship taking into account the variation of metallicity and/or temperature of the CO clouds with galactocentric radius (Digel et al. 1990, Digel et al. 1996). The calculation of CO masses determined in this thesis will assume that the best estimate of X is given by Strong et al. (1988) with a correction due to the fact that the CO data used in the comparison, which had been gathered at the CfA, assumed an incorrect intensity scale by a factor of 1.2. Hence, for this thesis it will be assumed that

$$X = 1.9 \times 10^{20} \quad (\text{molecules cm}^{-2}[\text{K km s}^{-1}]^{-1}). \tag{1.51}$$

Finally, it follows from Eq. 1.47, 1.49 and 1.50 that the CO mass (M_{CO}) for a molecular cloud is given by (Digel 1991, Digel et al. 1996)

$$M_{CO} = 4.2 \left(\frac{X}{1.9}\right) L_{CO}, \quad [M_\odot] \tag{1.52}$$

where X is in units of 10^{20} cm^{-2} [K km s^{-1}]$^{-1}$. This includes multiplication of the column density, $N(H_2)$, by a factor of 1.36 to account for helium and heavier elements (Allen 1973).

b. Virial Mass The virial mass, M_{vir}, of a molecular cloud of radius r and $FWHM$ velocity dispersion Δv is defined as the mass of an equivalent uniformly dense, non-rotating, spherical cloud which possesses the same velocity dispersion and size and is in gravitational virial equilibrium. With the additional constraints that there are no magnetic fields present nor ambient medium producing an external pressure, then Eq. 1.4 may be written as (Dame 1983)

$$M_{vir}\ \Delta v_{3d}^2 - \frac{3GM_{vir}^2}{5r} = 0.0\ . \tag{1.53}$$

Combining Eq. 1.40 and 1.53 it follows that for such a cloud

$$M_{vir} = \left(\frac{5}{8\ G\ ln2}\right)\ r\ \Delta v^2. \tag{1.54}$$

Finally, M_{vir} must be multiplied by $(4/3)^{1/2}$ to take into account that the r measured is the half-maximum r (Digel et al. 1996). Hence,

$$M_{vir} = 242.5\ r\ \Delta v^2, \tag{1.55}$$

where M_{vir} is in solar masses, r is measured in pc and Δv in km s^{-1}.

1.4 Summary of Assumptions and Constraints

The main points raised in this chapter with regard to CO observing are:

1. The CO molecule is assumed to be associated with molecular hydrogen gas where the local density exceeds the critical density to ensure thermal equilibrium.
2. The CO gas is assumed to be optically thick.
3. The filling factor for the CO clouds is assumed to be unity.
4. The observed line radiation, T_R^*, is the difference between the line radiation produced by the CO molecule and the background radiation after correction for spillover and scattering as detected in the main beam of the telescope.
5. The line profiles for a CO emission feature are assumed to be well modelled by a single Gaussian profile.
6. The radius of a CO cloud is derived from the area of the cloud contained within the half-maximum contour level.
7. A value of $X = 1.9 \times 10^{20}$ (molecules cm^{-2}[K km s^{-1}]$^{-1}$) is used throughout this thesis.
8. It is assumed that the clouds are spherical and non-rotating with no additional support from magnetic fields or external pressure in the determination of their virial mass.

Chapter 2

The Present Survey

Recent data (Digel et al. 1996) taken with the CfA 1.2 m telescope of ^{12}CO (J=1-0) are presented. The author was responsible for mapping a significant portion ($\sim$ 40 deg^2) of this survey ($\sim$ 100 deg^2). Maps made from this survey present the CO emission taken from different perspectives; l vs. v, b vs. v and l vs. b for different regions defined in the survey — Local, Cam OB1, Interarm, Perseus and Outer Galaxy. Each region is discussed in some detail emphasizing the main CO structures seen.

2.1 Introduction

Observations of the molecular gas associated with the extensive OB association Cam OB1 (Humphreys 1978) were carried out as part of a more extensive survey of the second quadrant of the Galaxy which included the W3/4/5 complexes (Digel et al. 1996, hereafter Di96). The second quadrant is excellent for studying the CO emission as it lies in a direction that is subject neither to velocity ambiguities (i.e., near and far side distances) nor velocity crowding associated with most previous surveys which sampled the inner Galaxy (see Combes 1991 for a good summary of those surveys). In this chapter, the details of the Center for Astrophysics [1] (CfA) survey will be presented, with an emphasis on the Cam OB1 CO emission.

This chapter is broken into four sections: §2.2 deals with the CfA telescope describing the various components of the telescope in a fairly brief manner. More details on the telescope can be found elsewhere (Dame 1983, Digel 1991, Leung & Thaddeus 1991). §2.3 summarizes the details of the observing run: dates, procedure, calibration, etc. In §2.4, maps of the survey in various useful projections, *l vs. v*, *b vs. v* and *l vs. b*, are presented. A complete set of maps is available upon request from the author, while the data are also included in the complete survey of the

[1] Harvard-Smithsonian Center for Astrophysics, MS 72, 60 Garden Street, Cambridge, MA 02138.

Second Quadrant to be released by the CfA. Finally, in §2.5 a brief summary of the main points raised in this chapter regarding the CO emission is provided.

2.2 The CfA Telescope

The CfA 'mini-telescope' is a 1.2 m millimeter-wave radio telescope located on the roof of Building D at the Harvard College Observatory, Cambridge, Mass. The telescope was originally located at Columbia University in New York City but was moved to Harvard in 1986. First light for the telescope at its current location was in January of 1988. A typical observing season for the telescope in its present location is from October to May. The telescope is easy to use and is well supported by the excellent staff at the CfA; in particular Tom Dame (software development), Sam Palmer (hardware) and Seth Digel (daily operations), were instrumental in making the author's stay pleasant and productive. A summary of the main components of the telescope: the antenna and mount, receiver, spectrometer and computer control/data retrieval system is provided below.

Figure 2.1 is a simple schematic diagram highlighting the main components of the antenna and mount. Figure 2.2 shows the author next to the telescope during his stay at the CfA. The telescope possesses a 1.2 m parabolic primary and 17.8 cm hyperbolic secondary operating in a Cassegrain configuration providing an effective f/D of 2.8. The primary is a monolithic aluminum casting providing a f/D of 0.375 which has been milled to high precision (better than $\lambda/65$ at 115 GHz) and is quite stiff (Digel 1991). In 1988 the primary beam was mapped and shown to possess a main beam FWHM of 8'.7. This pattern had not been re-checked up to the observing season when the present survey was completed but repeatability of the observations for standard calibration sources suggested no major degradation. The telescope antenna, receiver, and mount are contained in a 5.2 m Ash dome with a 191 cm entrance slit covered by a Goretex screen to protect the instrument from the elements and maintain a relatively constant temperature within the dome (Palmer 1993).

A simple schematic of the receiver is shown in Figure 2.3. A brief summary for the system is as follows:

1. A scalar feed couples the microwave signal (ν_{CO}) to the mixer.
2. A Gunn oscillator provides a local oscillator (LO) frequency $\sim$ 1.4 GHz below the frequency of interest, ν_{CO}, i.e., $\sim$ 115 GHz. The LO is frequency controlled in a phase locked loop circuit by comparing the difference between the output

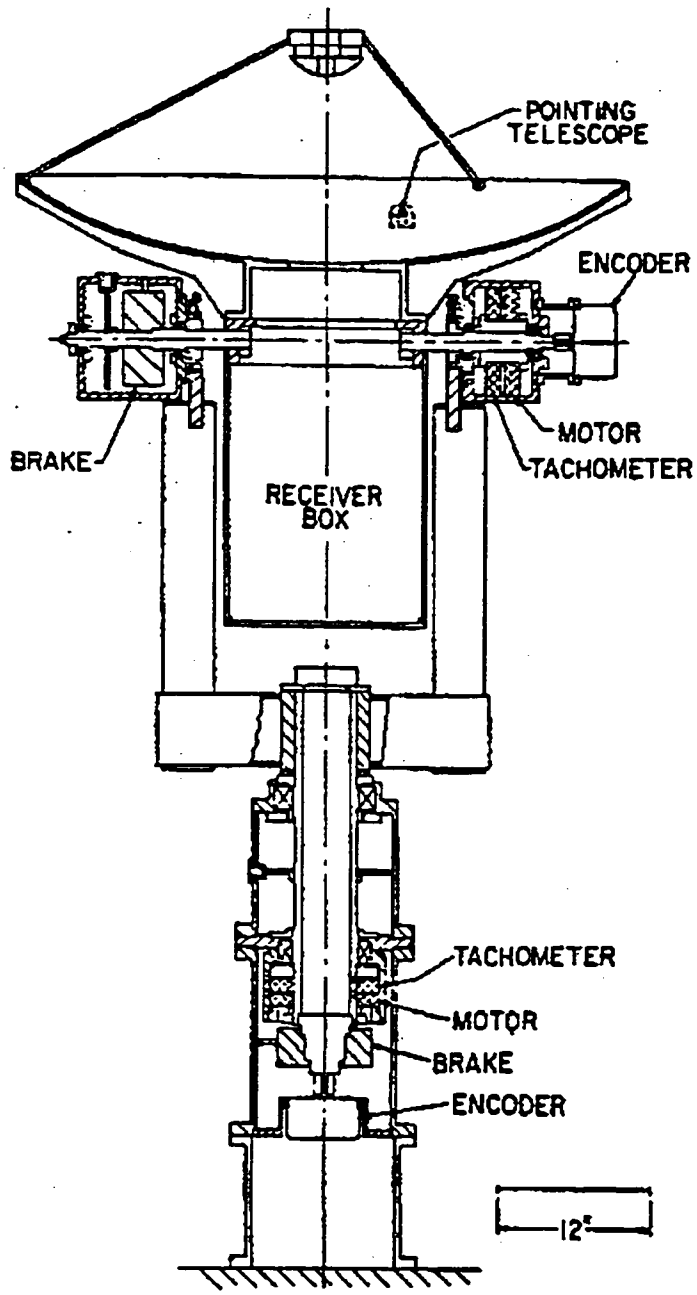

Figure 2.1 Schematic diagram of CfA 1.2 m telescope showing 1.2 m primary, secondary, mount and drive apparatus (Dame 1983). The receiver box is detailed in Figure 2.3.

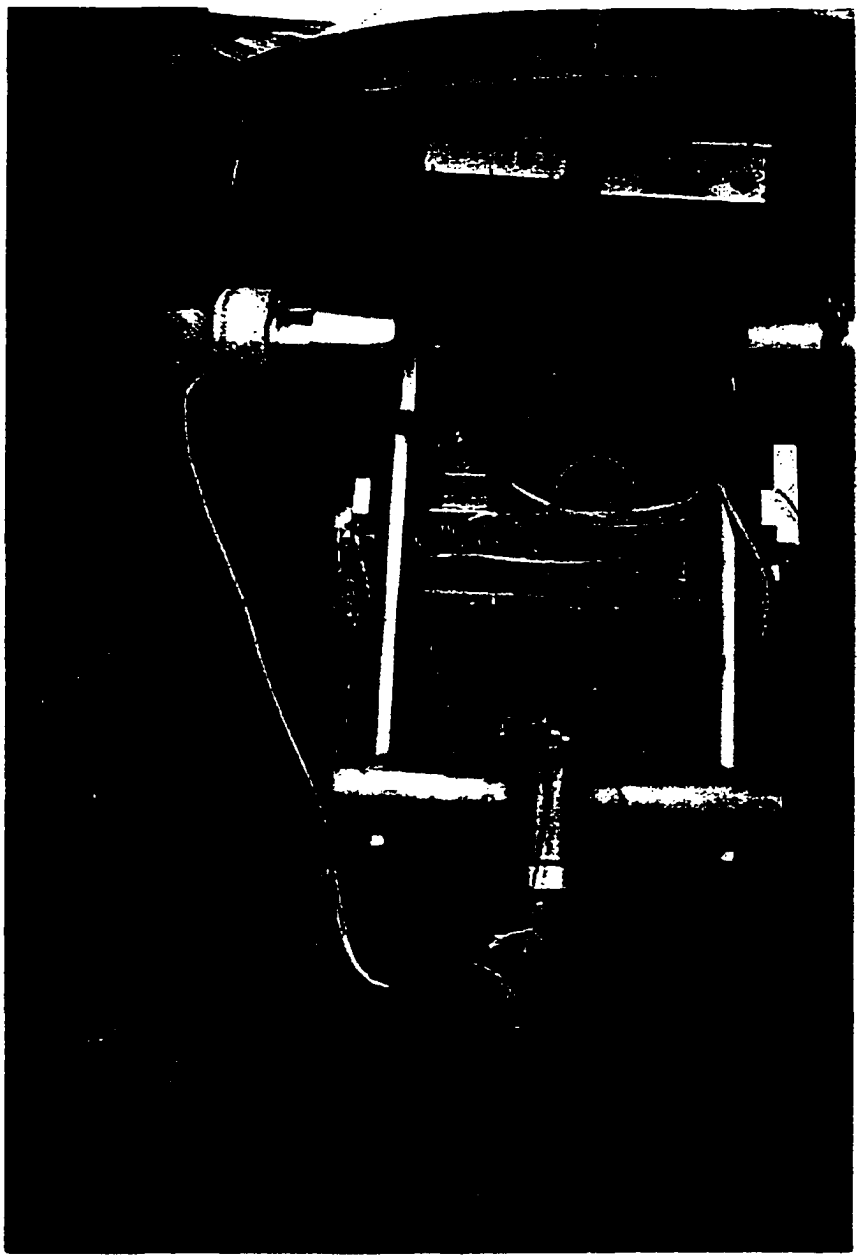

Figure 2.2 Author standing next to the CfA 1.2 m telescope. The bottom of the main dish, the receiver, mount and drive assembly are clearly visible. The author is standing on a hydraulic hoist used to lift the He_{liq} and $N_{2,liq}$ to the receiver dewar. (Photo by S. Digel)

of the Gunn oscillator and a reference frequency.

3. A superconducting-insulating-superconducting (SIS) junction serves as a mixer for the two signals (ν_{LO} and ν_{CO}) operating as a heterodyne receiver. Many harmonics of the input signals and their products are produced in the mixer but only one is passed out through a low pass filter as IF (intermediate frequency). The IF is produced at the beat frequency of ν_{CO} - ν_{LO}.
4. The IF is amplified by a 27 dB amplifier.
5. The IF is mixed a second time with a second LO ($\nu_{2nd\ LO} \sim 1.24$ GHz) down to a frequency of $\sim$ 150 MHz and again amplified before passing to the spectrometer.

Steps 1 - 4 occur within the receiver front-end which is contained in a He_{liq} cooled dewar operating at $\sim$ 4 K. This dewar is surrounded by an outer jacket dewar which is cooled by $N_{2,liq}$.

The spectrometer consists of two filter banks, each containing 256 channels, which can be selected in software. The high-resolution spectrometer, which was used for this survey, sampled only the central 64 MHz of the 150 MHz second intermediate frequency signal. This central portion was divided into 16 bands of 4 MHz bandwidth which were in turn further divided into 16 contiguous channels of 0.25 MHz by two-pole Butterworth filters. Each spectrometer channel had a velocity resolution of 0.65 km s^{-1} for a total coverage of 166 km s^{-1} at the CO signal frequency. The low-resolution spectrometer operated in an analogous manner but with bands 8 MHz wide and channels 0.5 MHz wide. The low-resolution spectrometer was used only for double-checking baselines and off positions.

Computer control of the telescope was maintained by control system software on an Apple Macintosh IIfx. This system was essentially the same as the operating system used during the earlier Dame (1983) survey but has been continuously updated to incorporate more safety features, e.g., a He_{liq} dewar temperature monitor. As each spectrum was gathered it could be manipulated immediately, e.g., baseline fitting of various orders, or simply examined to make sure it looked reasonable. At the end of the shift or after several shifts the data were passed to an HP Apollo workstation where they could be viewed as a data cube or written to a FITS (Flexible Image Transport System) tape.

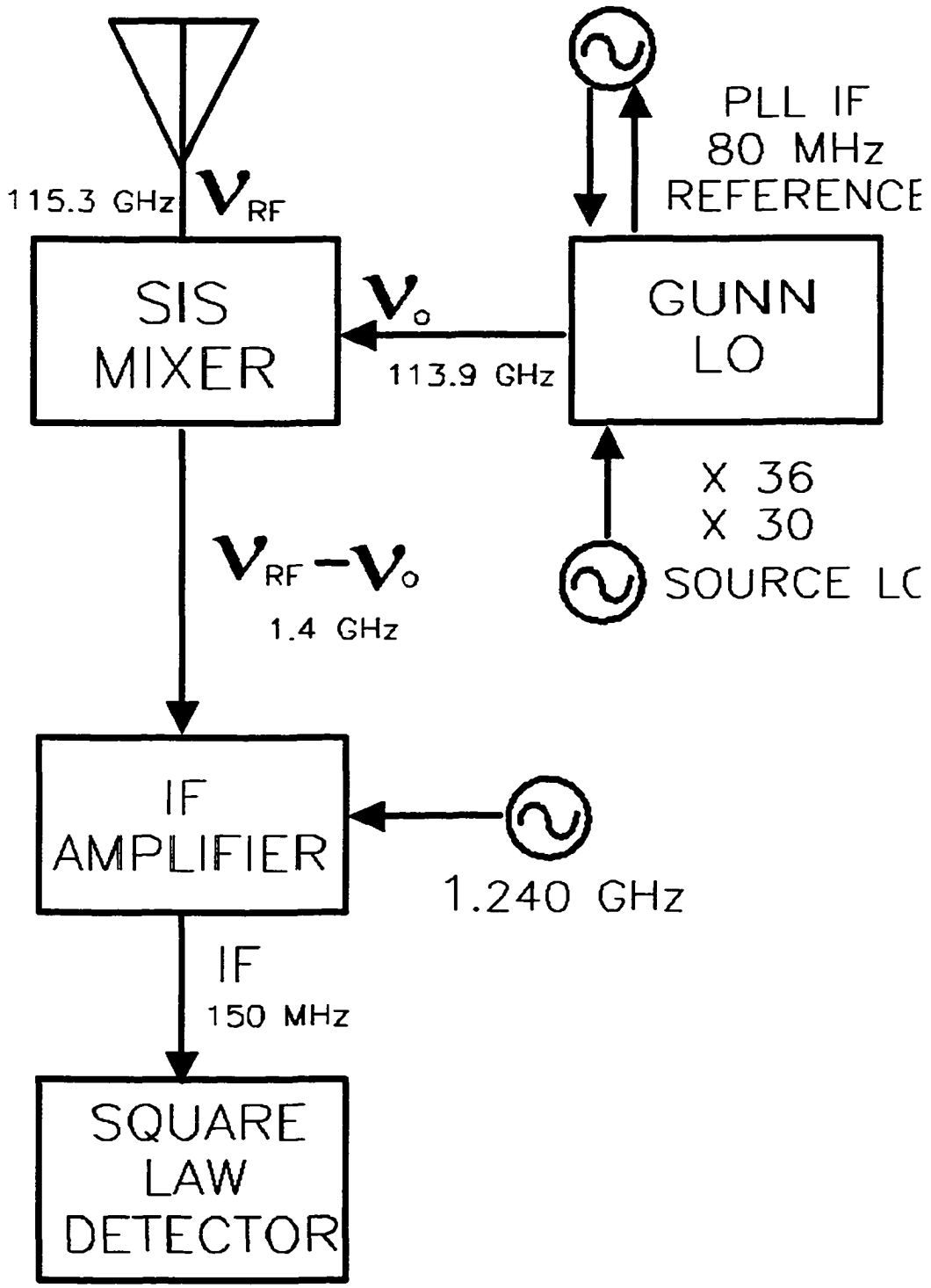

Figure 2.3 Schematic diagram of the receiver for the CfA 1.2 m telescope.

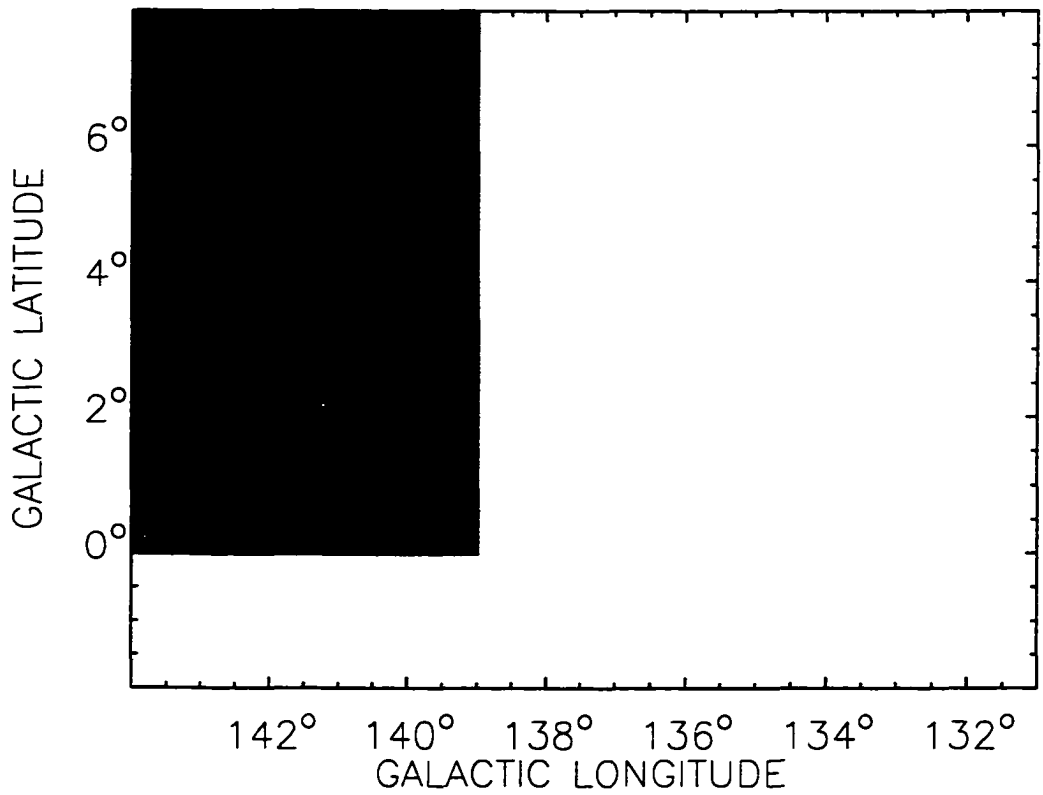

Figure 2.4 Survey boundaries showing the boundaries for the present survey (Di96). Data gathered are shown by the shaded regions. The author was solely responsible for the darkly shaded area and assisted with the lightly shaded area.

2.3 The Observations

Observations included in the present survey were carried out during the 1992-1993 observing season, i.e., from October 1992 to April 1993. The survey covered $\sim$ 100 deg^2 (from $l = 131°$ to $l = 144°, b = -2°$ to $b = +4°$ and from $l = 139°$ to $l = 144°, b = +4°$ to $b = +8°$) and comprised a total of 25,248 spectra. The author was solely responsible for collecting the data from $l = 139°$ to $l = 144°, b = +0°$ to $b = +8°$ ($\sim$ 10768 spectra, including bad scans) shown in Figure 2.4. The author also assisted, to a much lesser degree, in observing the remainder of the survey. A summary of the observing run for the author is provided below:

November: 6 shifts.

December: 15 shifts.

January: 5 shifts.

Total: 26 shifts. $\rightarrow$ 414 spectra/shift.

2.3.1 Observing Procedure

The observing procedure at the CfA may be loosely broken down into two components: occasional observations required for pointing calibration and daily observations for data gathering.

i. Occasional Observations These observations check the pointing of the telescope, prior to the start of the observing season, by observations with a small optical telescope, aligned with the main axis of the telescope (Dame 1983), of 50 or so stars located at various positions throughout the sky. The results of this check indicated the telescope achieved a blind pointing accuracy of better than 1′ (Puche 1993). Periodic observations of the radio continuum emission from the limb of the Sun were also performed on a weekly basis in order to double-check the stability of the pointing.

Observations were also made at the beginning of the season in order to select suitable off positions, i.e., positions free from CO emission to be used in solving Eq. 1.9. Candidate positions were selected by first examining an *Infrared Astronomical Satellite*, *IRAS* (Beichman et al. 1988) 60 μm map for regions apparently devoid of emission and hence, warm dust and gas. These candidate positions were checked for CO emission by frequency switching for a period of a few minutes. Promising off positions were checked by frequency switching down to a level of 0.07 K (rms) per channel. Table 2.1 lists the off positions used for the present survey.

Table 2.1: Off Positions

l [deg.]	b [deg.]	l [deg.]	b [deg.]
131.0	-3.0	137.0	-3.0
132.0	-3.0	137.5	3.0
134.0	-5.0	138.0	-3.0
134.5	2.5	139.0	-5.0
135.0	-5.0	142.0	6.0
135.0	3.0	143.0	6.0
136.0	-5.0	144.0	-3.0
136.5	3.0	145.0	2.0

ii. Daily Observations Observations for all shifts followed a standard procedure to a large extent. These were:

a. Cryogenics and Dome Maintenance At the beginning of each shift, and during the shift, as required, the He_{liq} and $N_{2,liq}$ dewars would have to be filled to ensure that an operating temperature of $\sim$ 4 K was maintained in the He_{liq} dewar. The He_{liq} level in the receiver dewar was checked by means of a flutter tube after each fill. $N_{2,liq}$ was kept in an outer jacket dewar and was simply topped up until overflowing.

It was also necessary to monitor weather conditions throughout the shift to make sure the equipment in the dome did not become too cold or that tracking by the telescope wasn't affected by gusty wind conditions. A dome temperature maintained near 10°C was ideal for the proper running of the electronics housed in the dome. Even though the entrance slit was covered with Goretex on cold evenings when the dome temperature dropped appreciably, heaters were used to maintain the ideal dome temperature. For those evenings when the telescope was tracking poorly due to gusty wind conditions closing the upper and/or lower shutter usually alleviated the problem.

b. Calibration Calibration of the telescope for CO observations followed a standard chopper wheel calibration (see Chapter 1) which comprised of essentially three steps:

1. The determination of the receiver temperature, T_{Rx}, and system gain, G, using a hot and cold load. Normally, the receiver temperature would be between 60 K and 70 K if properly tuned. If the receiver temperature was too high then the coupling between the Gunn oscillator and receiver had to be reduced.
2. Determination of the system parameters η_L, T_{Atm} and τ by 'antenna tipping'. This is calculated at the beginning of an observing shift and then every 4 - 6 hours thereafter unless the weather is changing rapidly.
3. The chopper wheel calibration. This comparison of the on- and off-source power (voltages) with a chopper wheel of known temperature provides a natural scale for the conversion between voltage and temperature for the receiver.

As a last check, to make sure the telescope was properly calibrated, observations were made of a standard source, e.g., W3(OH) or NGC7538. A plot of temperatures previously observed for this source, a Gaussian distribution of observed integrated line intensities, provided an estimate of the acceptable deviation in this quantity.

c. Data Collection An observation consisted of sampling an 'off' position, an 'on'

position, and then a second off position. Spectra were then obtained by subtracting a reference spectrum, obtained from a weighted average of the two off positions' spectra, from the on position spectrum (Eq. 1.15). The average of two off positions for each on position, one above and one below the on position in elevation, were taken as the reference spectrum as it should be representative of a reference spectrum which would be obtained at the on position. In the case where there were no known off positions available, either above or below the source, such that the source position could be bracketed by two off positions, then the two closest off positions, regardless of relative position, were used to compose the reference spectrum. Finally, to correct for any variation in the sensitivity of the spectrometer, a linear baseline was fit through the final source spectrum after reference subtraction.

The total time required for an observation follows from the standard measure of the sensitivity of a system given by Kraus (1986)

$$\Delta T_R^* \propto \frac{T_{sys}}{(\Delta\nu\ t)^{1/2}}. \tag{2.1}$$

where T_{sys} is the total system temperature, $\Delta\nu$ is the bandwidth per channel (250 KHz) and t is the total integration time on the source. With the additional constraint that the time observing the off positions equals that for the on position it follows that the total time per observation is $2t$. For sources at the upper transit a total observing time of typically $\approx$ 10 seconds was adequate to achieve a $\Delta T_R^* = 0.29$ K. For a source at the lowest practicable elevation the total time was $\approx$ 300 seconds per observation.

Finally, in order to increase the sensitivity of the survey without a great loss in resolution, the original data (which had a resolution of 8.7) were convolved with a beam of 4.9, resulting in a final data cube which possessed a resolution of 10′ and a sensitivity of $\sim$ 0.14 K per channel. Table 2.2 summarizes the relevant parameters for the survey.

Table 2.2: Summary of Survey Parameters

Observing Mode	Position Switching
Spatial Coverage	$131° \leq l \leq 139°$: $-2° \leq b \leq +4°$
	$139° \leq l \leq 144°$: $-2° \leq b \leq +8°$
Beamwidth Original/Smoothed (FWHM)	8.7/10.0
Sampling Interval	$\Delta l, \Delta b$: 3.75
Total Number of Spectra	25,248
Velocity Coverage (LSR)[a]	-133 to +33 km s^{-1}
Sensitivity per Channel Original/Smoothed	$T_R^* = 0.29$ K/0.14 K

a) Based upon standard solar motion.

2.4 The Data

As mentioned in §2.3 the author was responsible for mapping ~ 40 deg^2 of the survey which entailed taking more than 10,000 spectra. Some of these (277) were bad for several reasons including: poorly fit baselines, offsets, missing data or very noisy data. Figure 2.5 illustrates an example of each of these problems as well as a good spectrum for comparison.

The main regions detected in the survey are summarized in Figure 2.6. These are the 'Local' emission, defined over the velocity range +10 to -5 km s^{-1}, the 'Cam OB1' emission, defined from -5 to -22 km s^{-1}, the 'Interarm' region, defined from -22 to -30 km s^{-1}, and the 'Perseus' emission, defined over the velocity range -30 to -70 km s^{-1}. Other representations which are useful include a plot of Galactic longitude vs. radial velocity (LSR), *l vs. v* (Figure 2.7), Galactic latitude vs. radial velocity (LSR), *b vs. v* (Figure 2.8) and Galactic longitude vs. Galactic latitude, *l vs. b*, for the various identified regions (Figures 2.9 through 2.14).

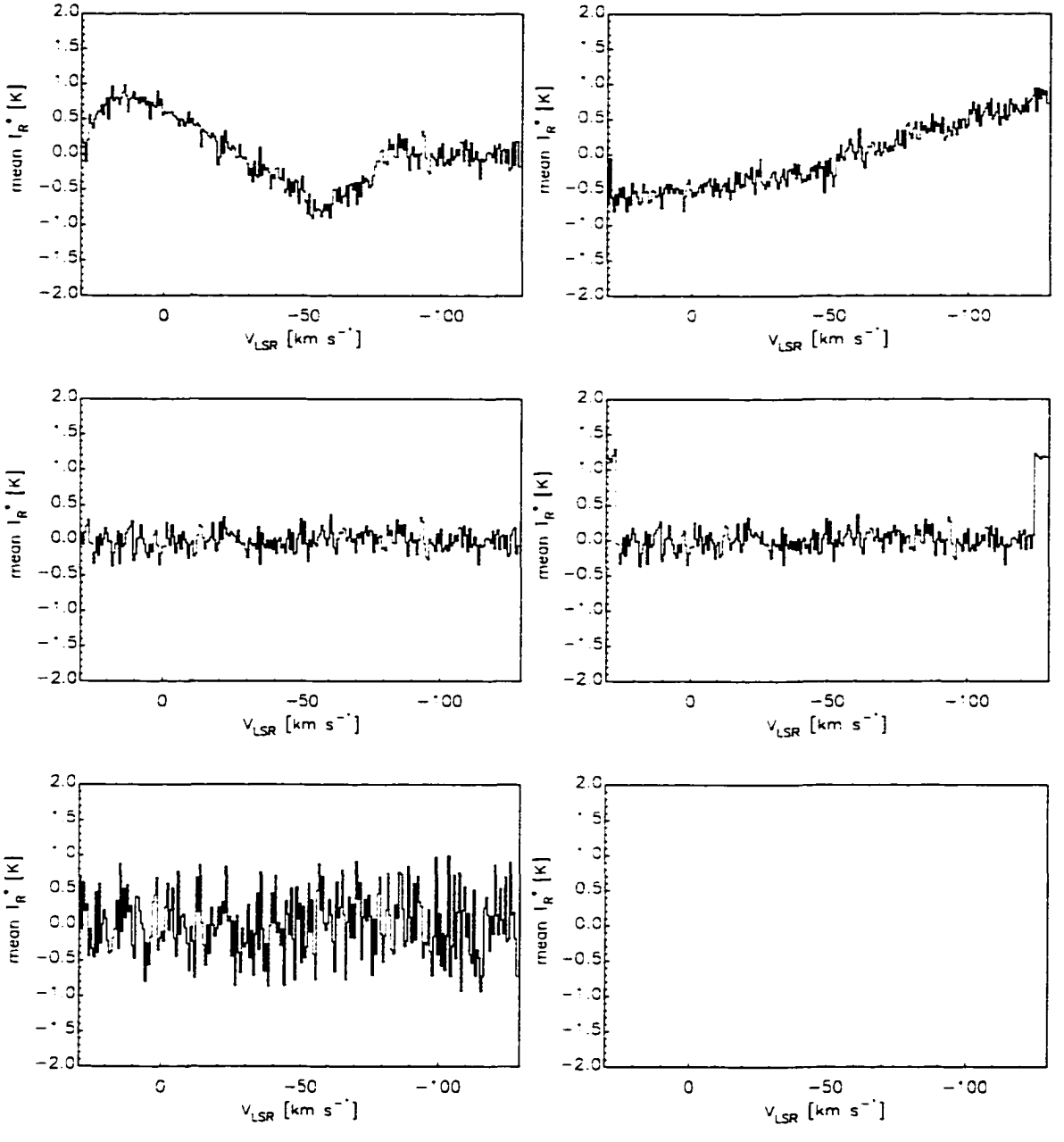

Figure 2.5 'Bad' spectra detected throughout the observing run. Starting at the upper left corner and moving clockwise these are: a bad baseline (S-shaped greater than the acceptable noise, 0.29 K, per channel), a bad baseline (linear fit but tilted), improper offset between the 250 kHz and 500 kHz filterbanks, missing data, and noisy data (usually due to a short integration). The last spectrum, center left, is an acceptable one.

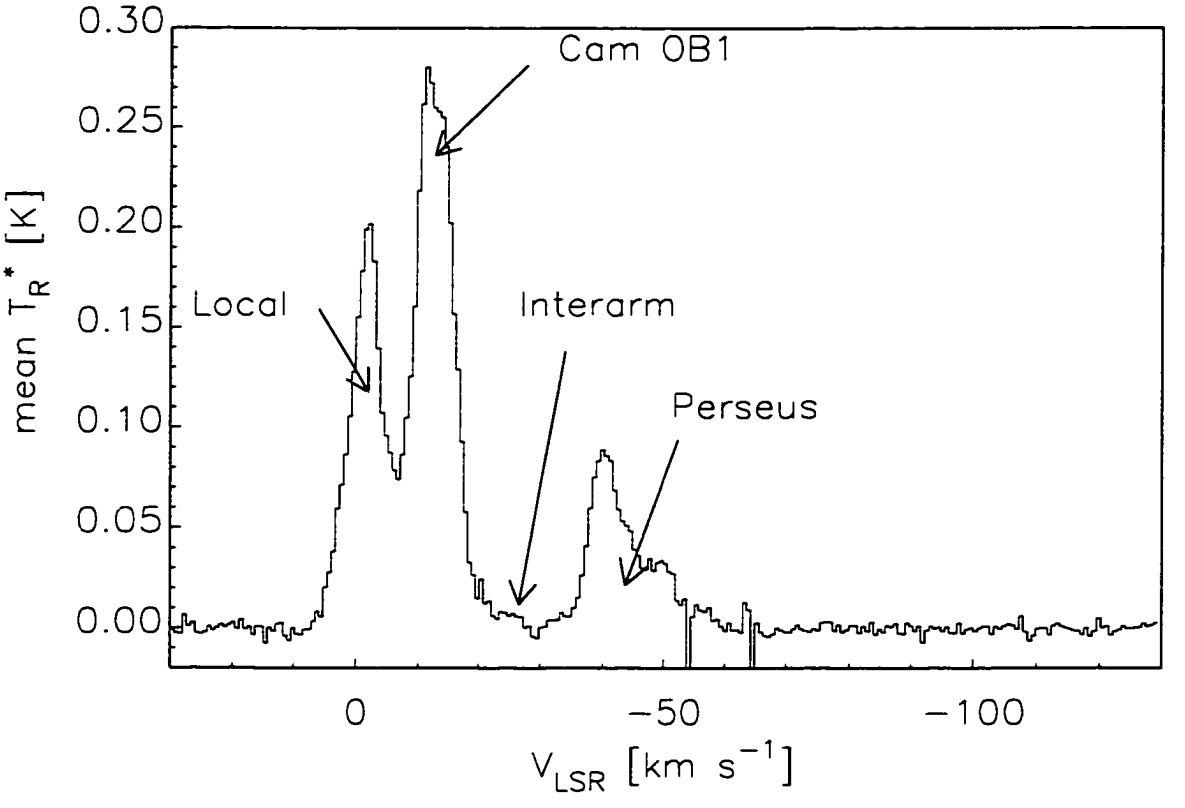

Figure 2.6 Average CO spectrum (corrected for atmospheric attenuation and coupled to the main beam, Eq. 1.37) for the surveyed region. Several emission features are clearly visible and are labelled appropriately:

Local Emission: +10 to -5 km s^{-1}.

Cam OB1 Emission: -5 to -22 km s^{-1}.

Interarm Region: -22 to -30 km s^{-1}.

Perseus Emission: -30 to -70 km s^{-1}.

Outer Galaxy: -70 to -130 km s^{-1}. (Not labelled in Figure 2.6)

The overall linear baseline fitting is excellent, suggesting a good selection of off positions, i.e., free from CO emission and close to the on position. Two bad spectrometer channels are visible at $\sim$ -55 and -65 km s^{-1}.

2.4.1 b vs. v

Figure 2.7 illustrates the CO emission obtained by integrating over the longitude range of the survey ($l = 131°$ to $144°$). As in the case of Figure 2.6 there are several distinct regions of emission. The Local emission ($v = +10$ to -5 km s^{-1}) is very well defined over most b with some blending with the Cam OB1 emission ($v = -5$ to -22 km s^{-1}) near $b = +4°$ and $b = -1°$. In the case of the $b = -1°$ region the blending may be confined to a single identifiable feature near $v = -7$ km s^{-1}. It is also apparent from this figure that not all of the Local emission in this direction has been detected, i.e., it extends to greater latitudes. In the case of the Cam OB1 emission, the emission decreases substantially at the edge of the field, near $b = +6°$, but it cannot be ruled out that there is more emission at higher latitudes. In the case of the Perseus emission ($v = -30$ to -70 km s^{-1}) this is not the case. The Perseus emission ends quite abruptly near $b = +2.5°$ which for an assumed distance of 2500 pc (Chapter 4) corresponds to $z \sim 100$ pc.

In Figure 2.7 it is also clear that the arm-interarm contrast is very strong with only a few small clouds present in the Interarm region ($v = -22$ to -30 km s^{-1}). The majority of these features are near $b = -2°$ which are also coincident with some peculiar velocity features in Perseus. If these features were really associated with the Perseus emission they would be suggestive of a shell-like structure. However, examination of other views, e.g., Figure 2.8, shows the features in the Interarm and Perseus regions are at two different longitudes and are not associated.

There also appears to be some emission near -55 km s^{-1} (from $b = +2°$ to $+4°$) and -65 km s^{-1} (in the Perseus region). However, from Figure 2.6 it is clear that there are some bad spectrometer channels at these velocities which suggests that these features may not be real. Other features at more negative velocities defining the Outer Galaxy, i.e., $v = -70$ to -130 km s^{-1}, have been detected (Di96) using a moment analysis scheme, which are not apparent in this representation. In Di96, a moment analysis was used to emphasize the faint features but this technique does not follow Gaussian statistics and it is difficult to estimate the uncertainty for any detected feature. Hence, the more classical method of detecting features seen in integrated maps is preferred by the author.

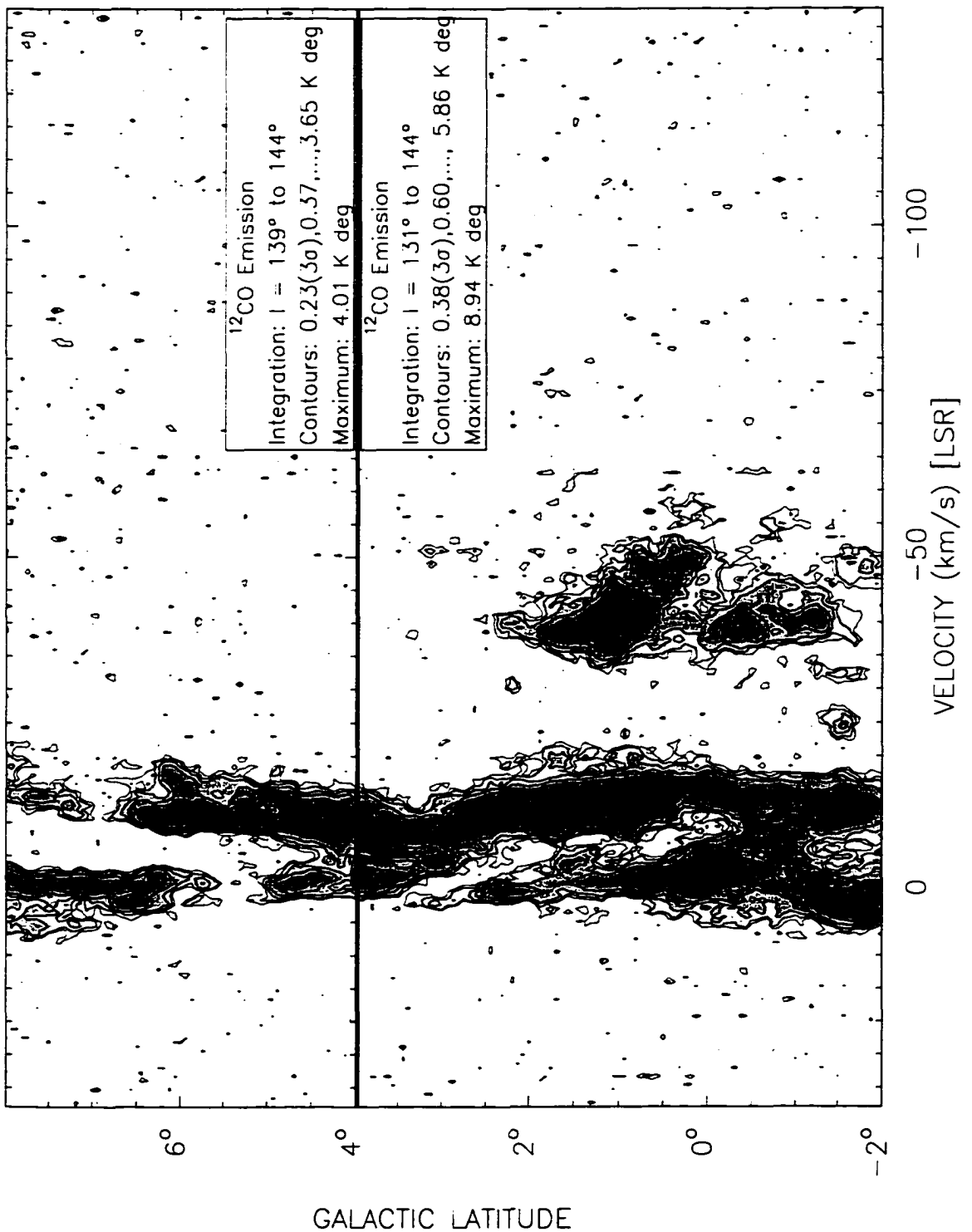

Figure 2.7 b *vs.* v for survey. A contouring scheme has been selected to show a minimum 3σ level over the entire range of the survey. Contours increase by a factor of 1.58 to yield 5 contours per decade.

2.4.2 l vs. v

Figure 2.8 provides a view of the CO emission in the l *vs.* v plane of the Galaxy. As in the case of the b *vs.* v plot (Figure 2.7) the various identified regions are clearly delineated. Blending does occur between the Local and Cam OB1 emission over the longitude range $l = 131°$ to $l = 136°$, with a prominent spur of Local emission near $l = 132°$ which extends into the velocity range defining the Cam OB1 emission. This feature corresponds to the $b = -1°$ feature seen in Figure 2.7. It also appears that the Local emission is slightly broader in this longitude range which may be due to projection effects, i.e., the superposition of features at slightly different velocities, e.g., the $b = +4°$ emission as seen in Figure 2.7, when viewed from the l *vs.* v perspective.

The brightest feature seen in the field lies in the Cam OB1 emission near $l = 142°$ and is coincident with one of the most energetic molecular outflows in the Galaxy, AFGL490 (Snell et al. 1984, Campbell et al. 1986). One striking feature of the CO emission associated with this outflow, from this perspective, is its cavity-like appearance with a large scalloped feature opening towards more negative velocities. In this case this feature is the superposition of CO at different latitudes and velocities (Chapter 6).

In the Interarm region there are two main emission features: two clouds near $l = 144°$ and a relatively isolated feature near $l = 135°$. There also appears to be some very weak and broken emission from $l = 132°$ to $l = 135°$ with $v \approx -25$ km s^{-1}. These fragmentary emission features may be associated with the Cam OB1 emission.

The Perseus emission (arm) is very well defined and dominated by the W3 molecular complex centered on $l = 133.5°$. At slightly higher longitudes are W4 ($l = 135°$) and W5 (from $l = 136.5°$ to $l = 139°$). W5 also appears to have a shell-like feature centered on $l = 139°$ with the front of the shell at $v = -30$ km s^{-1} and the back of the shell at $v = -50$ km s^{-1}. Most of the CO emission is contained in these three complexes with the exception of one feature at $l = 141°$. At higher longitudes the emission is much more fragmentary.

There are no obvious features in the Outer Galaxy, i.e., in the velocity range -70 km s^{-1} to -130 km s^{-1}.

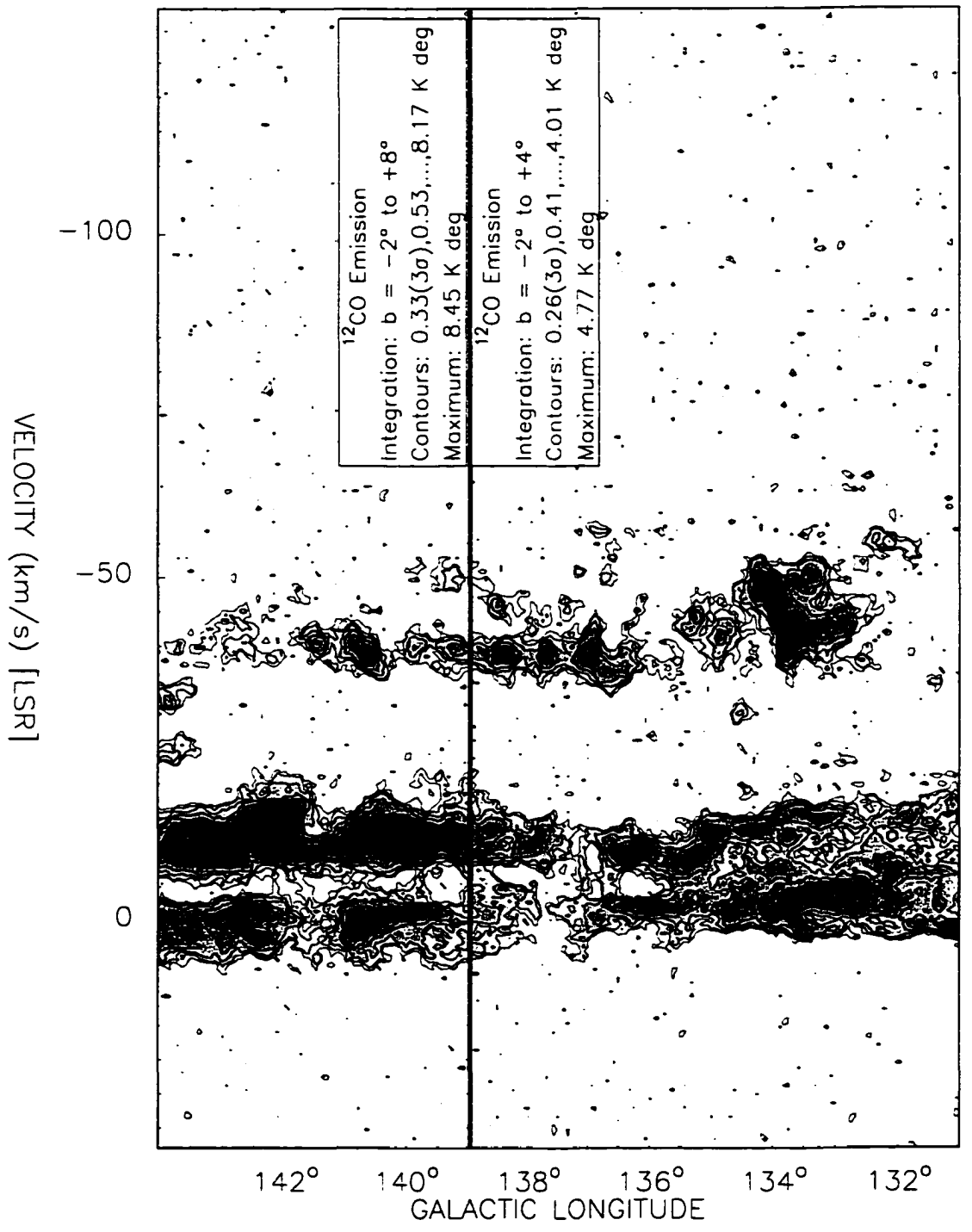

Figure 2.8 *l vs. v* for survey. A contouring scheme has been selected to show a minimum 3σ level over the entire range of the survey. Contours increase by factors of 1.58 to yield 5 contours per decade.

2.4.3 l vs. b : Local Emission (+10 to −5 km s^{-1})

The general impression of the Local emission (Figure 2.9) is that it is very fragmented and complicated, with a large portion of it lying along the Galactic equator. There are emission features seen at higher latitude which may make a significant contribution to the total amount of molecular gas seen in this part of the Galaxy, but it is not possible to assess this contribution, given the survey boundaries.

Prominent throughout this region is a long filamentary feature stretching from $l = 144°$ and $b = -2°$ to $l = 131°$ and $b = 0°$ which shows localized peak emission at $l = 142.°7$, $b = -1.°6$ (there is some weak nebulosity on the POSS plates at this location), $l = 140.°8$, $b = -1.°2$ and $l = 135.°0$, $b = -0.°2$. This last feature is in a complicated region but appears to be related to LDN 1363, 1370 and 1365, and LBN 656 and 657 (Lynds 1962). Other noticeable features in this velocity range include smaller filamentary features which possess brightened cores at $l = 142.°6$, $b = +0.°8$, $l = 142.°7$, $b = +4.°7$, $l = 143.°9$, $b = +6.°7$, $l = 140.°4$, $b = +7.°8$, $l = 132.°8$, $b = +3.°8$, and $l = 131.°2$, $b = +2.°0$ (possibly associated with LBN 341).

Figure 2.10 is a velocity moment map of the Local emission, i.e., the velocity moment calculated for each pixel in the integrated map which has been weighted by the sum of the radiation temperature along the line-of-sight over the Local emission velocity range. This is given by:

$$\bar{v}_{each\ pixel} = \frac{\sum_{velocity\ channels\ for\ each\ pixel} T_R^{\blacksquare}\ v}{\sum_{velocity\ channels\ for\ each\ pixel} T_R^{\blacksquare}}. \qquad (2.2)$$

where the summation over each pixel is carried out over the velocity range in question (in this case from +10 to −5 km s^{-1}). A minimum cutoff of 5 σ(= 0.70 K) has been used in selecting pixels in constructing the map, to ensure that only true emission features add to the map. A lower cutoff does provide the same information but the background becomes heavily mottled by noise which makes interpretation of the velocity features difficult. In Figure 2.10, it can be seen that for the most part the Local emission does lie near 0 km s^{-1}, with some major features between $l = 131°$ and $l = 136°$ closer to −5 km s^{-1}. There are no clear gradients or distinguishing features in the velocity field of the map.

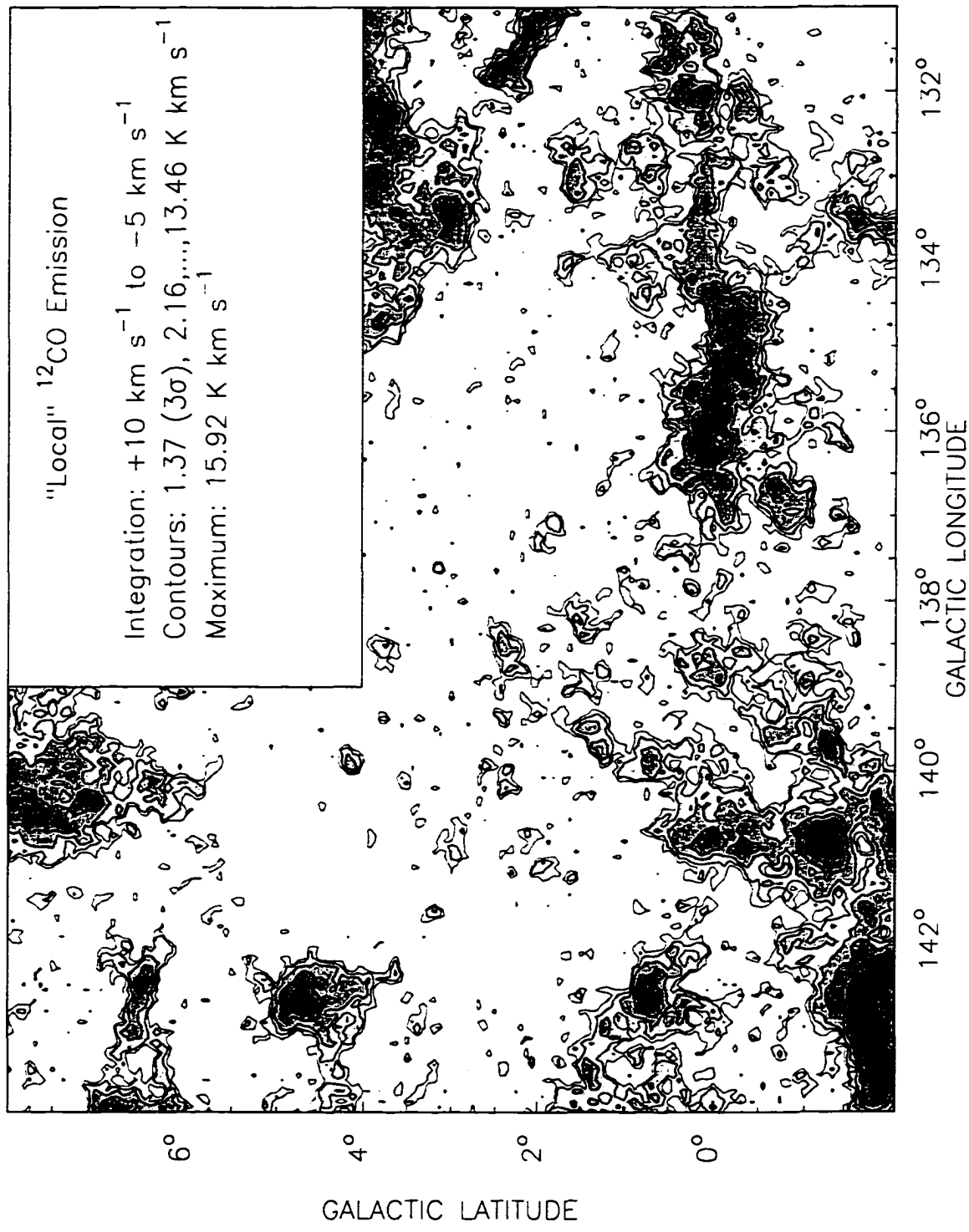

Figure 2.9 *l vs. b* for Local emission. A contouring scheme has been selected to show a minimum 3σ level over the indicated velocity range. Contours increase by factors of 1.58 to yield 5 contours per decade.

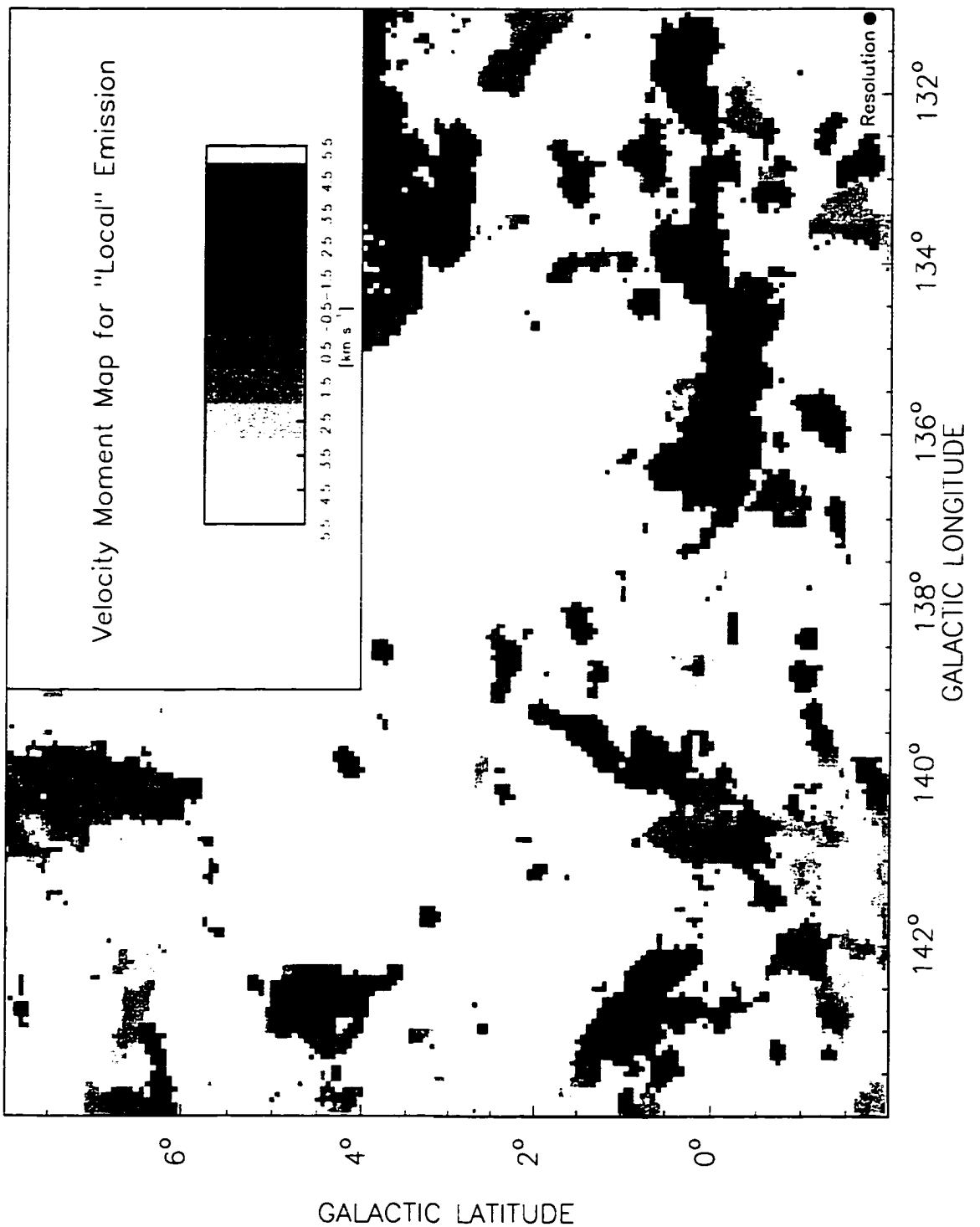

Figure 2.10 Temperature weighted moment map of the Local emission. A minimum cutoff of 5 $\sigma(= 0.70$ K) has been set for selecting real features from the noise. The gray scale indicates the emission-weighted central velocity of the molecular features.

2.4.4 *l vs. b*: Cam OB1 Emission (−5 to −22 km s^{-1})

Molecular emission associated with Cam OB1 (Figure 2.11) is also very fragmented and complex. Overall, the emission is divided into two main features: one running along the galactic plane from $l = 131°$ to $l = 136°$ and a second from $l = 139°, b = +6°$ down to $l = 144°, b = -2°$. Note that there is a turn southwards in the direction of the lower emission feature from $l = 136°$ to $l = 138°$. This may also possibly be seen in the more northerly emission but the boundaries of the survey prevent confirming this observation. Furthermore, there is a suggestion of this turnover in the Local emission (Figure 2.9) and in the Perseus emission (Figure 2.14). In the case of the Perseus arm this is usually attributed to a warp in the galactic plane (see Burton (1992), Chapter 7, for a discussion of this point). Usually the warp is not shown to extend into the molecular emission in the solar neighborhood but the present observations suggest otherwise.

Cam OB1 emission is dominated by the very bright complex at $l = 142.^{\circ}0$, $b = +1.^{\circ}8$ which is also associated with the very energetic molecular outflow AFGL490 (Campbell *et al.* 1986). From the POSS plates it would appear that this feature is also associated with LBN 681, 682 and 684 (Lynds 1962). An unidentified dark nebula visible on the POSS plates may also associated with this complex. Lying above this feature there is a long arc-like emission feature which stretches from $l = 140.^{\circ}5$, $b = +2.^{\circ}6$ to $l = 143°$, $b = +8°$. The most southerly emission of this feature appears to be related to LBN 676 and LDN 1377. Other emission features of importance in this region include a long filament which stretches from $l = 140.^{\circ}8$ to $l = 137.^{\circ}9$ along $b = +2.^{\circ}4$. This is a complicated structure which appears to be associated with LDN 1378 - 1386. At longitudes below $l = 138°$ the emission is generally weaker than at higher longitudes. The dominant feature is a long arc-like filamentary structure running from $l = 136.^{\circ}4$, $b = -2.^{\circ}0$ to $l = 132°$, $b = 0.^{\circ}0$. On the POSS plates this feature may be associated with the weak nebula LBN 665 and an unidentified bright nebula near $l = 133.^{\circ}0$, $b = 0.^{\circ}0$. More details on the molecular clouds and the associated population I objects are provided in Chapters 4 - 6.

Figure 2.12 displays a velocity moment map of the Cam OB1 emission. There appear to be two distinct velocity components, i.e., well fit by Gaussian velocity profiles, one approximately at -9 km s^{-1}, and the other approximately at -14 km s^{-1}. These two components appear to meet in three places; firstly, along a distinct ridge of CO emission running along $b = +2°$ from $l = 138°$ to $l = 143°$ (which shows

a marked discontinuity of $\sim$ 4 km s^{-1} in the velocity structure of the emission), secondly near $l = 134°, b = 0°$, and thirdly, near $l = 140°, b = +6°$. In the first two cases, the velocity contrast between the two components is quite dramatic, while in the third case the contrast is smaller and is developed over a much larger area. It is not possible on the basis of Figures 2.11 and 2.12 alone to determine whether the two (velocity) components of CO emission are physically interacting, or overlap due to a line-of-sight coincidence. In Chapters 6 and 7, it will be shown that only in the case of the emission along $b = +2°$ from $l = 138°$ to $l = 143°$ are the two components of molecular gas interacting.

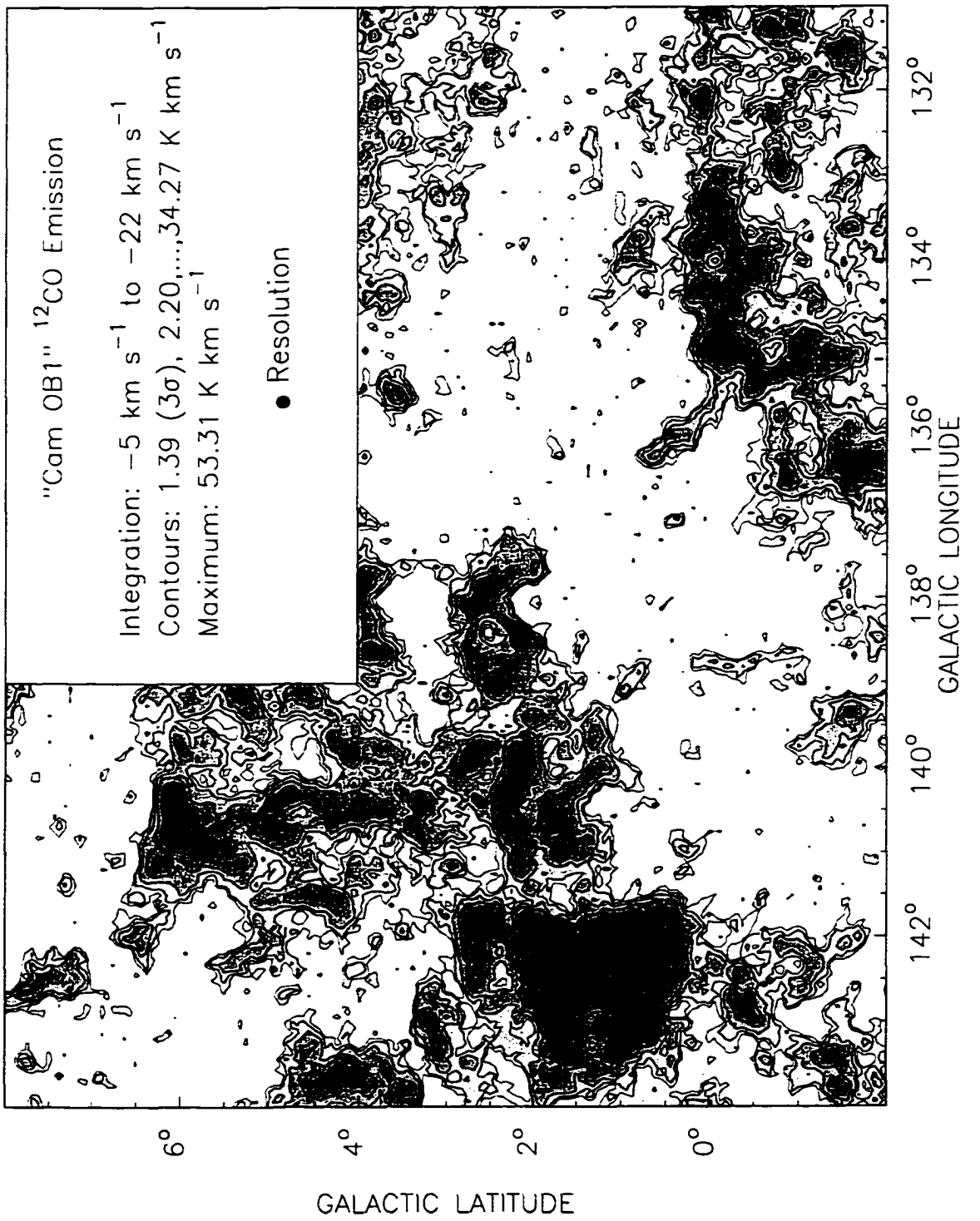

Figure 2.11 *l vs. b* for Cam OB1 emission. A contouring scheme has been selected to show a 3σ level over the indicated velocity range. Contours increase by factors of 1.58 to yield 5 contours per decade.

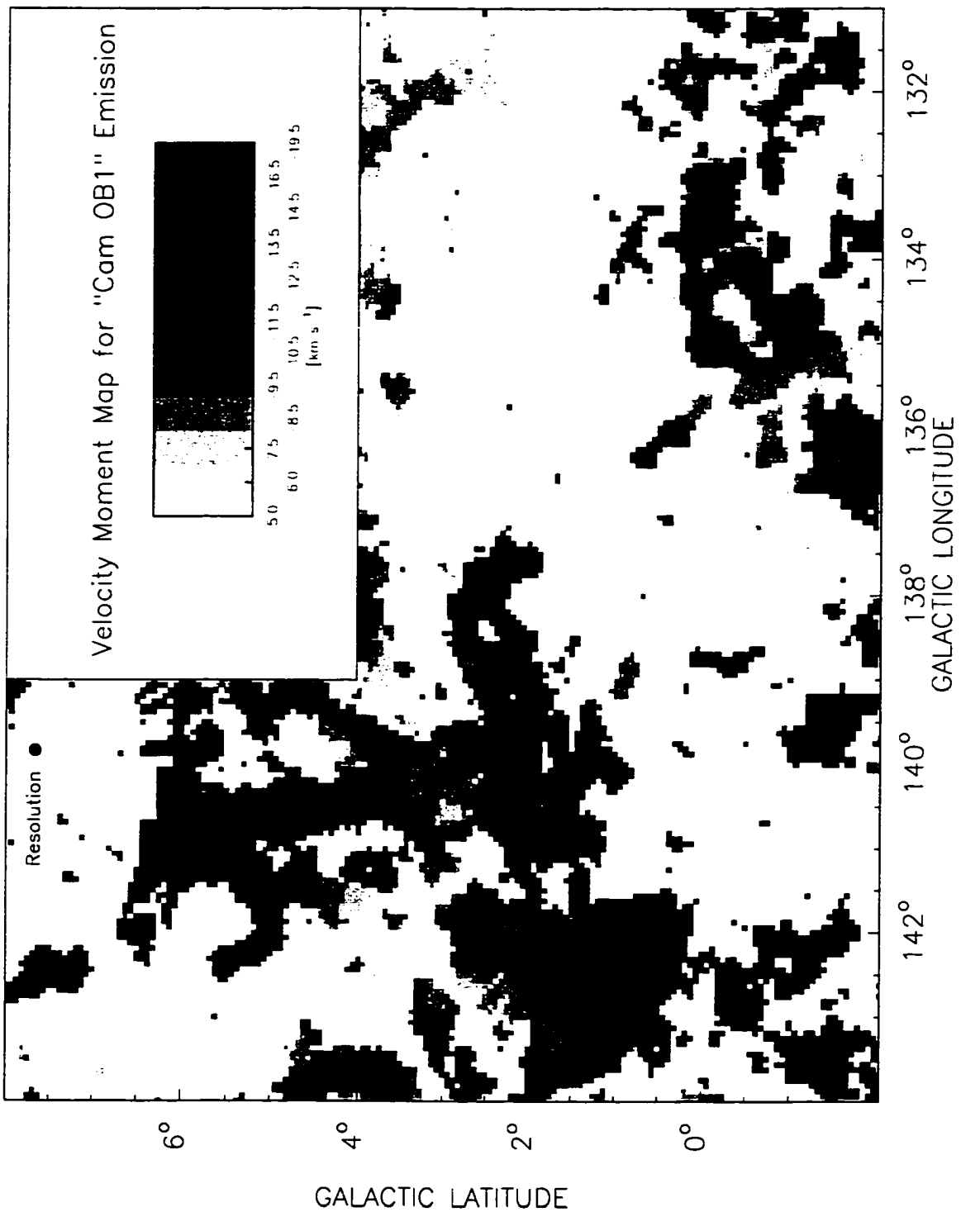

Figure 2.12 Temperature weighted moment map of the Cam OB1 emission. A minimum cutoff of 5 $\sigma(= 0.70$ K) has been set for selecting real features from the noise. The gray scale indicates the emission-weighted velocity of the molecular features.

2.4.5 *l vs. b*: Interarm Emission (−22 to −30 km s^{-1})

The Interarm emission shown in Figure 2.13 is very sparse and lies in two well-defined regions. The main feature, near $l = 144°, b = -1.5°$, is seen in Figure 2.8 to be composed of two components. One component lies at the edge of the Cam OB1 emission, i.e., at -22 km s^{-1}, while the second lies at the edge of the Perseus emission, i.e., at -30 km s^{-1}. It is tempting to assign the more negative feature to Perseus on the basis of morphology but its velocity suggests it is an Interarm object. Some means, other than kinematic information, is required to settle this matter.

The second main feature in the field comprises a cluster of three small features centered on $l = 134°, b = +1°$. The brightest of the three, near $l = 134.5°, b = +2°$ lies at slightly more positive velocities and at higher latitudes than the W3/W4 region in Perseus. This feature is seen in Figures 2.7 and 2.8. The other two features in this group are more problematic. It is not easy to determine where these features lie in either Figures 2.7 or 2.8. In both of these figures it is possible to identify Perseus emission which may extend into the Interarm region and account for these last two features.

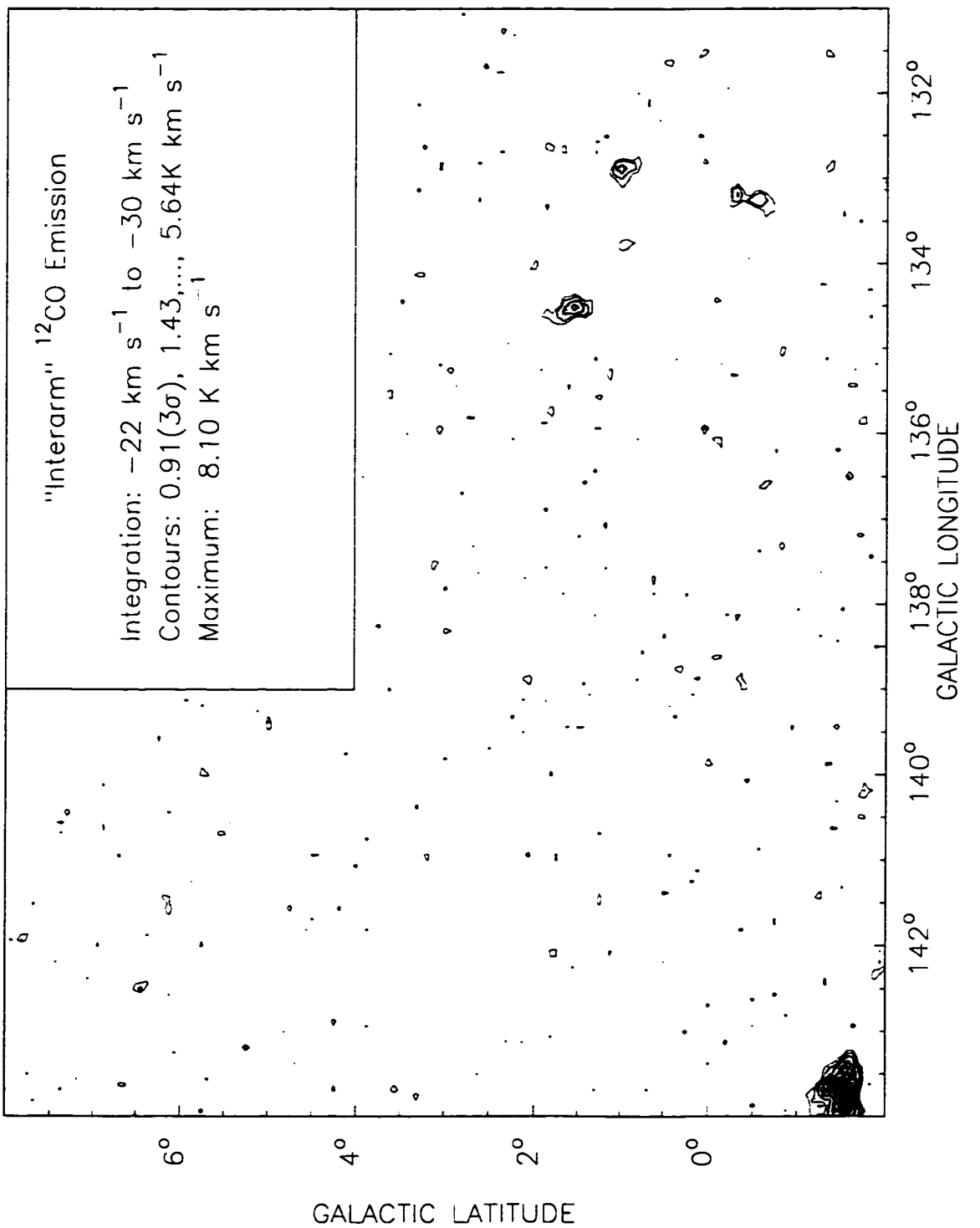

Figure 2.13 *l vs. b* for Interarm region. A contouring scheme has been selected to show a 3σ level over the indicated velocity range. Contours increase by factors of 1.58 to yield 5 contours per decade.

2.4.6 l *vs.* b: Perseus Emission (−30 to −70 km s^{-1})

Perseus emission (Figure 2.14) is quite complicated with features that are fragmentary, shell-like and filamentary. However, there are four main bright features. The first is the W3 (IC1795) region which is centered on $l = 134°.b = +1°$ (Lada et al. 1978, Braunsfurth 1983) and is the brightest and most massive region seen in the survey. On the POSS plates W3 stands out as a very bright emission feature and is associated with many LDN and LBN. The second is the W4 (IC 1805) region which lies next to W3 and comprises a thin band of molecular clouds with constant longitude at $l = 135°$. The third is the W5 (IC 1848) region which is a long filamentary feature stretching from $l = 136°$ to $l = 139°$ approximately along $b = +2°$. Below this main feature there is a thin ridge of emission which is also part of W5 (Braunsfurth 1983) which, together with the main upper ridge, form a shell-like structure. Both the upper and the lower ridge of W5 are seen on the POSS plates as extinction features. Finally, there is a long filamentary feature extending from $l = 140°.b = +1°$ to $l = 142°.b = -1°$. This feature may be associated with LBN140.77−1.42 (Green 1989) and a 'spur' evident in the Perseus HI emission (Braunsfurth & Reif 1984). It is very striking how quickly and clearly the molecular emission seen along this ridge changes direction, turning southward away from the W3/4/5 complex.

There also appears to be a considerable number of smaller clouds which follow the general pattern established by the main features, mentioned above, but with a much larger dispersion in l and b. Chapter 8 will deal in some detail with the Perseus emission in a comparative study of the cloud structure in Perseus and the Cam OB1 region.

In Figure 2.15 velocity moment maps for the Perseus emission are presented. There are two prominent features. Firstly, there is a large velocity gradient seen in the W3 complex which has been detected before (Lada et al. 1978) and discussed in some detail (Elmegreen & Wang 1988). Secondly, a feature which has not been previously discussed, to the author's knowledge, is the appearance of two distinct velocity components at approximately -35 km s^{-1} and -55 km s^{-1} which are seen over the entire field. The more negative component of the emission appears to lie above and below the more positive emission, except in the case of the W3 complex where they seem to meet.

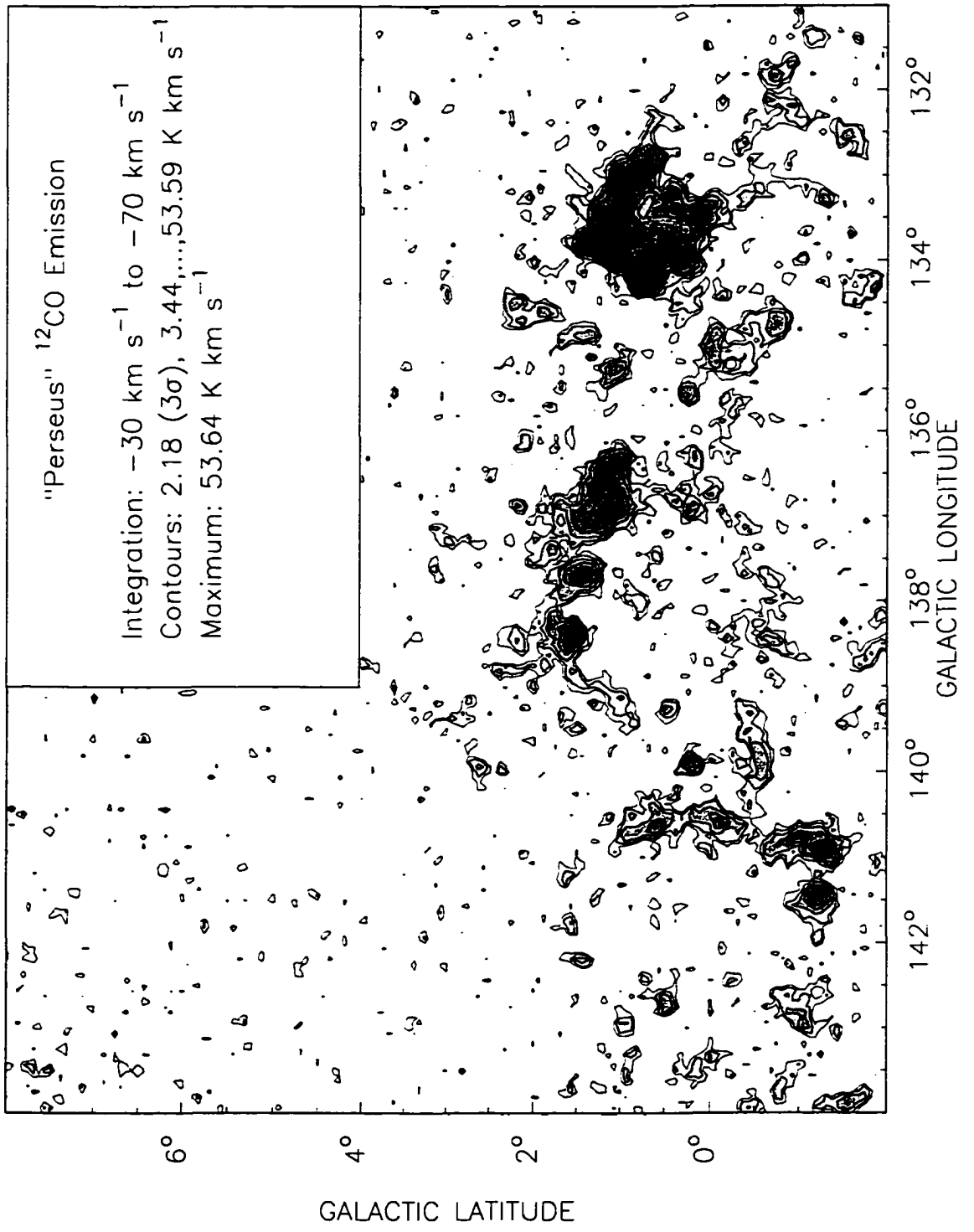

Figure 2.14 *l vs. b* for Perseus emission. A contouring scheme has been selected to show a 3σ level over the indicated velocity range. Contours increase by factors of 1.58 to yield 5 contours per decade.

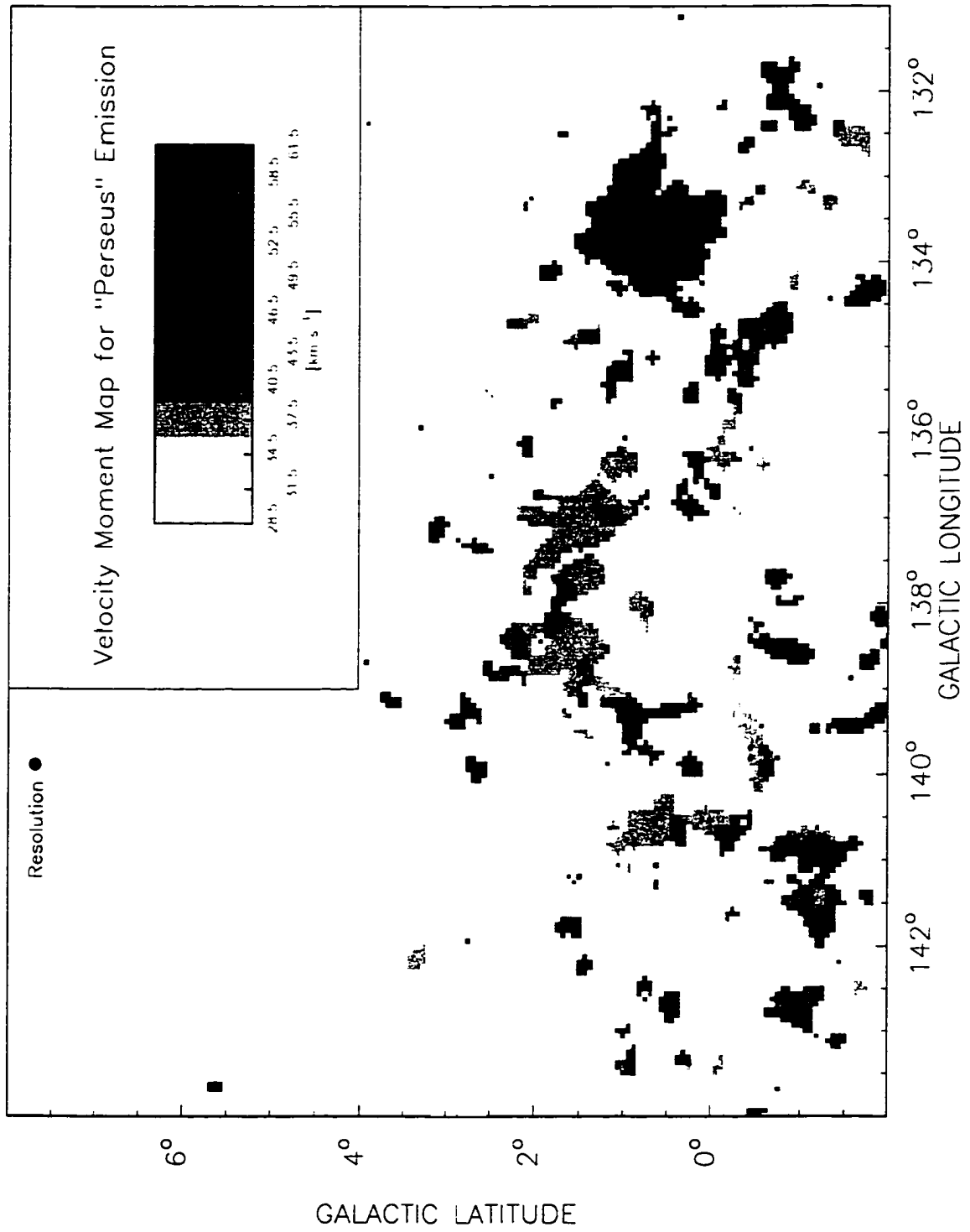

Figure 2.15 Temperature weighted moment map of the Perseus emission. A minimum cutoff of 5 $\sigma = 0.70$ K has been set for selecting real features from the noise. The gray scale indicates the velocity coverage of the molecular features.

2.4.7 *l vs. b*: Outer Galaxy (−70 to −130 km s^{-1})

There are two features readily apparent in the Outer Galaxy from a *l vs. b* perspective (Figure 2.16). These were detected in Di96 as well as some smaller, fainter ones ranging in velocity from -60 km s^{-1} to -104 km s^{-1}. There is the suggestion of a third feature near $l = 135°, b = +3°$ which Di96 also detected but this feature is not easily distinguishable from noise. It should be noted that in Di96 a moment analysis was employed which only adds emission above some arbitrary threshold to an integrated map. This technique is more sensitive to faint structure and is very useful for searching for candidate objects but it is difficult to assign uncertainties to such features. By further subdividing a region in velocity to encompass only one particular candidate object it is possible to make use of the more classical integration method to determine exactly how well the candidate object really stands out above the noise.

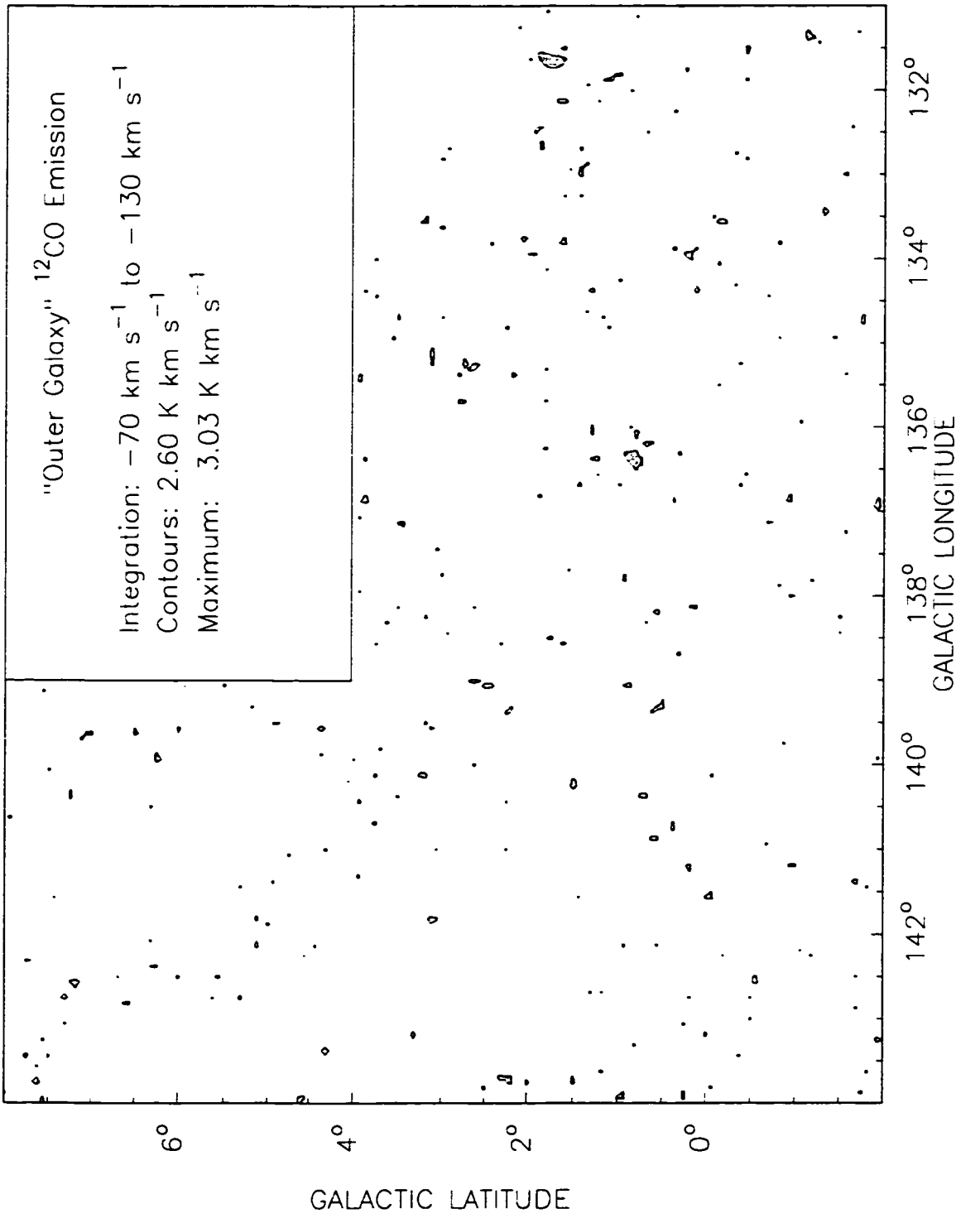

Figure 2.16 *l vs. b* for Outer Galaxy. A contouring scheme has been selected to show a 3σ level over the indicated velocity range. Contours increase by factors of 1.58 to yield 5 contours per decade.

2.5 Conclusions

New data from a recent survey (Di96) are presented. The main points of this survey *noted in this chapter* are:

1. The survey was fully sampled and taken with sufficient sensitivity to provide a useful database for continuing studies.
2. Maps were presented from various perspectives illustrating the richness in structure seen in the CO emission.
3. Several distinct regions - Local, Cam OB1, Interarm, Perseus and Outer Galaxy - were clearly identified as separate kinematic (velocity) entities.
4. In the case of Cam OB1 emission there appear to be two distinct velocity components, with mean velocities of ~ -9 and ~ -13 km s^{-1}. It is not possible on the basis of this data set alone to determine whether the two velocity components in Cam OB1 are interacting or are line-of-sight coincidences.
5. There appears to be a warp in the CO emission clearly seen in the Perseus region and possibly seen in the Cam OB1 region.
6. The CO emission in the Perseus region also shows two distinct velocity components which appear to be spatially separate except in the W3 region.

Chapter 3

Why the New Survey?

A fully sampled, sensitive survey of the CO molecular gas in the Cam OB1 region recently taken with the CfA 1.2m telescope (Digel et al. 1996) reveals a rich structure compared to the original CfA survey (Dame et al. 1987). A Fourier analysis of this structure suggests that it follows a similar distribution of power with scale length to that seen in HI in the region. A structure tree analysis of a sample cloud in the region suggests it is similar to the Taurus star forming region and hierarchical in nature.

3.1 Introduction

Dame et al. (1987, hereafter referred to as Da87 or the original survey) published a composite survey of the galactic plane of the Milky Way (all l, $|b| \leq 3°$) taken from 5 major surveys and studies of 11 individual regions. The intent of the original survey was to provide some insight into the large scale structure of the Milky Way, e.g., location of spiral arms and scale height of CO gas. In this regard the original survey must be considered a success as it has proven to be a standard reference in many studies of Galactic structure (Burton 1992).

However, there are several observational limitations to the original survey. For the most part, the data were gathered using the 'superbeam' technique (Dame & Thaddeus 1985) in which spectra were obtained on a square grid of points about one beamwidth (8.7) apart, followed by the summation of all spectra within 30′, i.e., the final pixels were 30′ square. This led to a final resolution somewhat greater than 30′ with a 3σ brightness temperature sensitivity of 0.1–0.35 K in the original survey temperature scale (the range in sensitivity is indicative of the composite nature of the original survey). All further references to temperatures from the original survey will be divided by 0.82 to bring them onto the same temperature scale as the present survey of Digel et al. 1996 (hereafter Di96 or the present survey). Examination of

emission-free channels in the original survey over the area considered in the present survey led to an estimation of a 1σ rms noise of 0.26 K.

By comparison, the present survey was fully sampled and has a sensitivity of 0.14 K after being smoothed from 8.'7 to 10' (T_R^* is the radiation temperature or the observed antenna temperature after correction for atmospheric attenuation, spillover and beam coupling). Both surveys were observed with a velocity resolution of 0.65 km s^{-1}. Hence, it is expected that the present survey should have both higher spatial resolution and greater sensitivity than the original survey, and therefore should reveal more detail of the CO emission.

Previous studies of the structure of the ISM in the Cam OB1 region have only considered the atomic component of the ISM, i.e., HI, in an attempt to discern whether there are any preferred scale lengths over which the HI is organized (Green 1993, hereafter Gr93). The lack of any such preference suggests that the mechanism regulating the structure of the atomic component of the ISM, e.g., turbulence (Scalo 1987), is operative and equally effective over all scale lengths. It is also important to know whether the CO emission in the region also follows the same scaling law, or if not, at what scale lengths the CO emission is clumped. A comprehensive model of the structure of the ISM and its implications for the Galactic ecology requires a good measurement of both of these components of the ISM. A related question is whether the structure of the CO emission, or more generally the ISM, is self-similar or hierarchical: i.e., whether the number of cloud fragments is identical at all scale lengths or the contrast in intensity between levels of fragmentation is constant (Scalo 1988). Self-similarity in a turbulent ISM has been claimed before (Larson 1981) but never considered in the case of the Cam OB1 region.

In this chapter some of the questions regarding the structure of the CO emission in Cam OB1 will be addressed in a comparative study between the present and original surveys. Details of the relationship of the CO to individual star forming regions, e.g., star forming efficiencies, CO cloud mass function, etc., as well as a discussion of possible star forming mechanisms will be presented elsewhere (Chapters 7 and 8). The analysis of the structure of the CO emission will be both qualitative (§3.2.1) and quantitative, using a two dimensional Fast Fourier Transform (FFT) (§3.2.2.1) and structure tree statistics (§3.2.2.2). A discussion of the analysis will be presented in §3.3, and a summary will be presented in §3.4.

3.2 Comparison of Original and Present Surveys

3.2.1 Qualitative Comparison

Integrated CO emission and velocity moment (Eq. 2.2) maps from the two surveys are shown in Figures 3.1 and 3.2, respectively. From an examination of these two data sets the following observations can be made:

i. Morphology In Figure 3.1 several features stand out:

1. The present survey clearly contains more diffuse emission and small emission features. A comparison of the average intensities for the velocity-integrated maps taken in Figure 3.1 (2.10 K km s^{-1} in the original survey versus 2.24 K km s^{-1} in the present survey) suggests that ~ 93 % of the emission detected in the present survey had been detected in the previous work.
2. Small emission features detected in the present survey are scattered throughout the field but in many cases were not detected in the original survey, e.g., the emission near $l = 134°, b = +1°$. In some cases the emission feature was detected, but was completely misrepresented and out of position, e.g., in the original survey the emission near $l = 137°.5, b = +0°.5$ has no clear analog in the present survey, but may be a combination of two or three features or possibly due to noisy spectra.
3. In both surveys the emission is divided into two main 'streams'. In the present survey these streams are running parallel to each other and appear to follow the warp in the plane of the Milky Way seen in this direction (see Weaver & Williams 1973, Kerr et al. 1986). The northern stream extends from $\sim l = 144°, b = 0°$ to $l = 138°, b = +4°$ and the southern stream from $l = 138°, b = -2°$ to $l = 131°, b = 0°$. There does appear to be a turn over in the direction of the southern stream near $l = 135°, b = 0°$. There are no data in the present survey to determine whether this also holds for the northern stream. In the case of the original survey it is not easy to see the warp in the more northerly stream as the components are very block-like in appearance and could equally well be modelled as running parallel to one another at constant Galactic latitudes.
4. Brighter, core-like features are shown in more detail in the present survey, e.g., the feature near $l = 142°, b = +1°$ appears as a roughly circular feature in the original survey, while in the present survey it is composed of at least three different emission peaks.

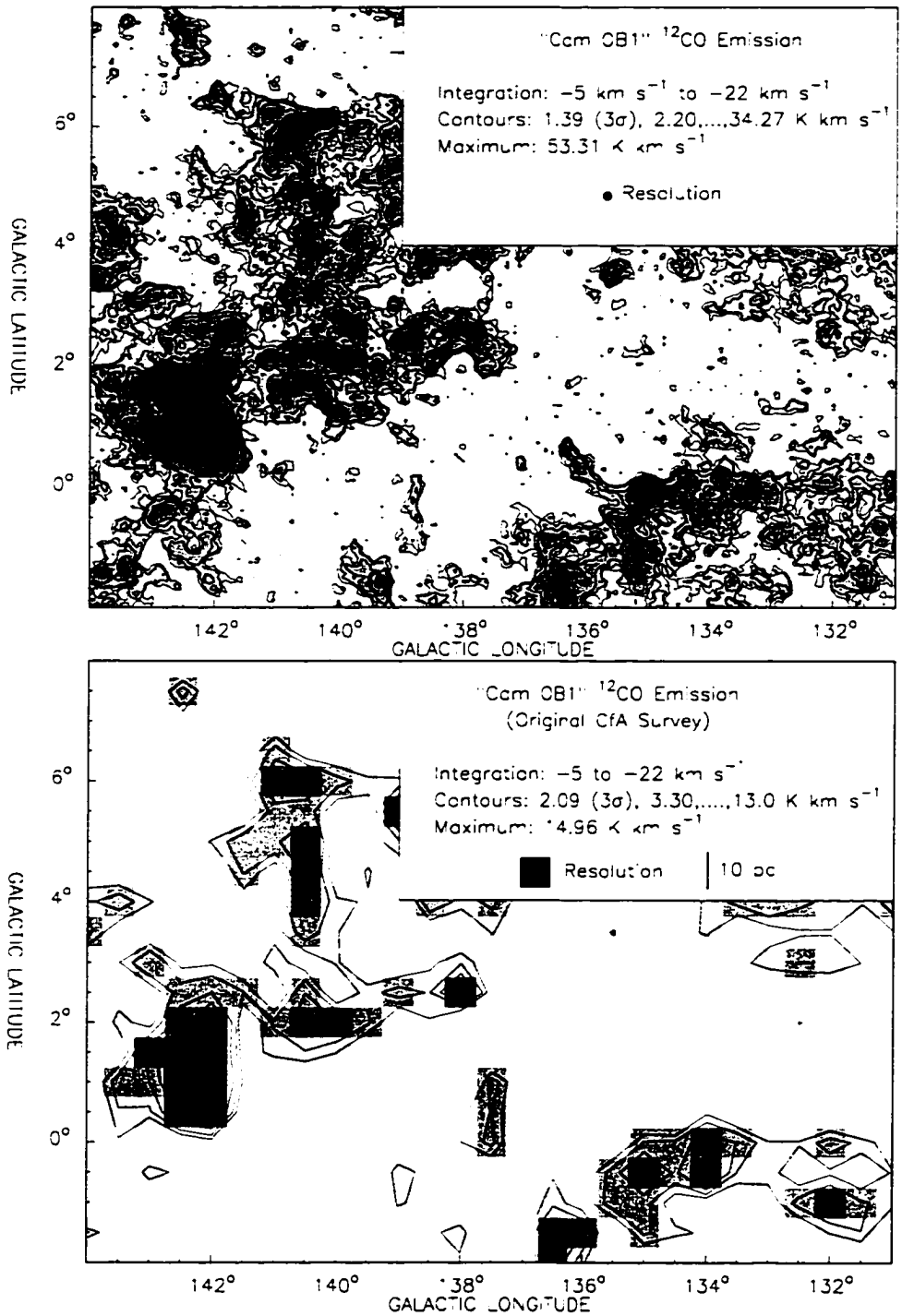

Figure 3.1 Integrated CO emission in Cam OB1 — present survey (Di96), upper, and original survey (Da87), lower. Differences in the peak temperature values can be attributed to different observing methods (sampling and gridding strategies) and temperature scales (calibration).

ii. Velocity Structure In the case of the velocity structure in Cam OB1 as determined from the two surveys (Figure 3.2) it follows that:

1. In the present survey, at least at higher longitudes ($l \geq 137°$), the velocity structure is well represented by two main features, centered on $v = -9$ km s^{-1} and $v = -13$ km s^{-1}, which appear to be superimposed upon one another. In the original survey this structure is not clear as the emission appears to be very heavily blended. Only in the case of the emission near $l = 134°, b = 0°$ are the velocity features very similar in appearance between the two surveys.
2. There appear to be several cases of single pixels at more negative velocities in the original survey, e.g., near $l = 135°, b = +1°$, which have no analog in the present survey. In some cases, the broader beam of the original survey has blended in nearby emission which can be seen in the field of the present survey, as in the case mentioned in point 1 above. In other cases, the beam has probably blended emission from nearby regions, which are just out of the field of view, or possibly from regions which are at slightly more positive or negative velocities, e.g., the feature near $l = 134°, b = +3°$.

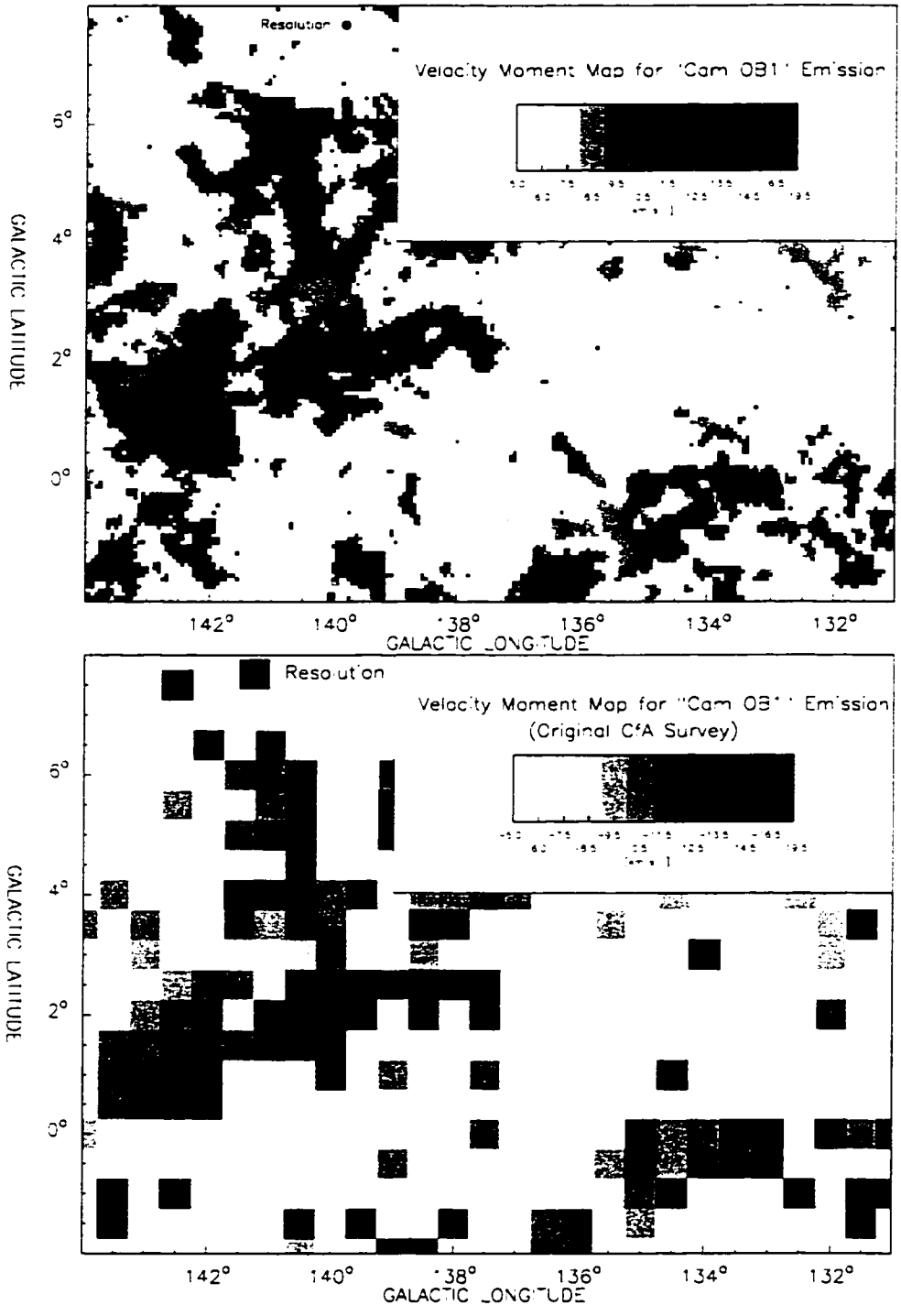

Figure 3.2 Comparison of velocity moment maps for the Cam OB1 region between the original survey (Da87, lower) and present survey (Di96, upper) using a similar shading scheme. There are similarities in the makeup of the two maps, but in general the contrast between regions of differing velocity in the original survey is less pronounced and more difficult to interpret.

3.2.2 Quantitative Analyses

3.2.2.1 A FFT Analysis of the CO Emission Structure

A quantitative measure of the structural information contained in the present survey (Di96) and the original survey (Da87) was made from a Fourier analysis of the two. In this analysis, it is assumed that any source in the sky consists of an ensemble of point sources with coordinates (x, y) of different brightnesses which may be equally well represented by an intensity distribution which is constituted by the superposition of sine waves at different wavelengths and amplitudes. In the two dimensional case, this intensity distribution may be written as (Leinert 1994):

$$I(x, y) = \int_{-\infty}^{+\infty}\int \tilde{I}(u, v)\epsilon^{+2\pi i(ux+vy)}dudv. \tag{3.1}$$

where u and v are the spatial frequencies in the x and y direction, respectively, which measure the number of wavelengths fitting into a unit length or unit angle. In astronomical applications the spatial frequency is taken as [arcsec^{-1}] or [(image size)$^{-1}$]. $\tilde{I}(u, v)$, the composite of sine wave amplitudes at different wavelengths, i.e., the Fourier transform of $I(x, y)$, may then be obtained from:

$$\tilde{I}(u, v) = \int_{-\infty}^{+\infty}\int I(x, y)\epsilon^{-2\pi i(ux+vy)}dxdy. \tag{3.2}$$

It is also possible, as was used in the analysis presented below, to write the Fourier transform of $I(x, y)$ in terms of a modulus $|\tilde{I}(u, v)|$ and phase o, i.e.,

$$\tilde{I}(u, v) = |\tilde{I}(u, v)|\epsilon^{io(u,v)}. \tag{3.3}$$

Fourier transforms of the two data sets were obtained using a standard Fast Fourier Transform (FFT) algorithm (Press et al. 1989). Since the data for the two surveys being compared cover identical areas any unwanted effects due to the shape or extent of the boundaries should be similar in the two resultant transforms. The amplitude components of the FFTs of the two data sets are given in Figures 3.3, 3.4 and 3.5. The input map for both surveys had to be padded to a $2^n \times 2^m$ grid (l and b) in order to use the FFT algorithm and was set at 1024 × 1024. The border area, and also any non-data pixels in the input were set to zero before performing

the FFT. The relationship between the grid spacing in the output map of the FFT and the input image or sky plane, is given by:

$$\Delta u = \frac{1}{N\ \Delta l}. \tag{3.4}$$

where Δu is the FFT grid spacing in a particular direction, i.e., the spatial frequency or sampling rate in the output FFT map in meters (or wavelengths if it is recalled that 1 $\lambda = 2.6 \times 10^{-3}$ m), N is the dimension (1024 for both directions) of the FFT, and Δl is the grid spacing in the sky ($\Delta l = sin(\Delta\theta)$ where $\Delta\theta$ = angular spacing between grid points in the sky plane; for small $\Delta\theta$, $sin(\Delta\theta) \approx \Delta\theta$).

i. Present Survey Figure 3.3 shows the amplitude of the two dimensional FFT for the present survey (upper plot), which has a pixel size of 3.'75 and resolution of 10'. The FFT image was obtained from an input map consisting of average radiation temperatures. The lower plot shows the log of the square of the average radiation temperature (the power at a particular scale length, Gr93) as a function of the log of the radius from the central pixel of the azimuthally averaged bins in the FFT image used to calculate the average radiation temperature. Figure 3.4 shows the FFT for the present survey but only considers the smaller scale lengths (or conversely, the larger scale structure in the sky).

In Figures 3.3 and 3.4 there are four distinct FFT features:

1. The very broadest FFT structure, seen only in Figure 3.3, extends out to a scale length of $\sim$ 1 m (roughly the antenna diameter) and is associated with the smallest resolved features ($\sim$ 10') in the sky. This structure is symmetric about the origin with no apparent preference in orientation, but it is quite weak.
2. Two finger-like structures, seen over the smaller scale lengths ($\sim$ 0.2 m) shown in Figure 3.3, run parallel to one another out at a position angle of $\sim -20°$ as measured clock-wise from the top of the figure. In Figure 3.4, this structure is more pronounced but appears more plateau-like with the central portion of the 'plateau' fairly well filled in out to a scale length of $\sim$ 0.1 m ($\sim$ 1.'8). The orientation and shape of this FFT structure strongly suggest that it represents the two streams of CO emission seen in the image plane, i.e., the plateau is elongated for the correct scale length to span the length of the two streams and it is at an angle of 90° to the CO image in the image plane, as expected for a FFT.
3. A bright 'S' shaped feature at the center of the FFT plane which is associated

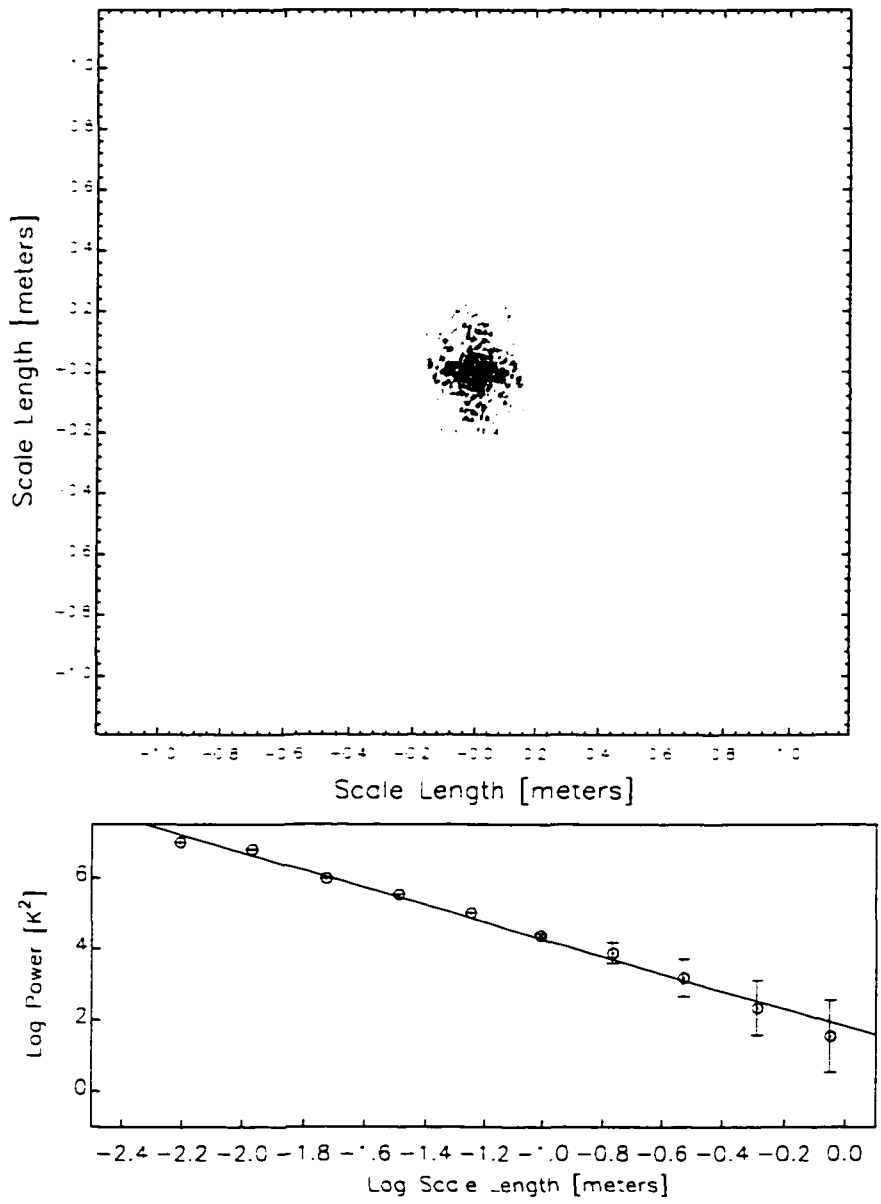

Figure 3.3 Two dimensional FFT of present survey (Di96). Top view shows the FFT (amplitude) of the square of the average radiation temperature, $\bar{T}_R^*$, over the velocity range, $v = -5.5$ to -22 km s^{-1}. Shading levels are at 140, 11344, 31511, 87532 and 504184 K^2 with shading weights selected to enhance the central features. The bottom view is an azimuthally averaged representation of the log of the square of the amplitude of the same data as a function of the log of the distance from the central pixel. The line fitted to the data represents an unweighted least-squares fit while the error bars represent a 1σ deviation in the azimuthally averaged data.

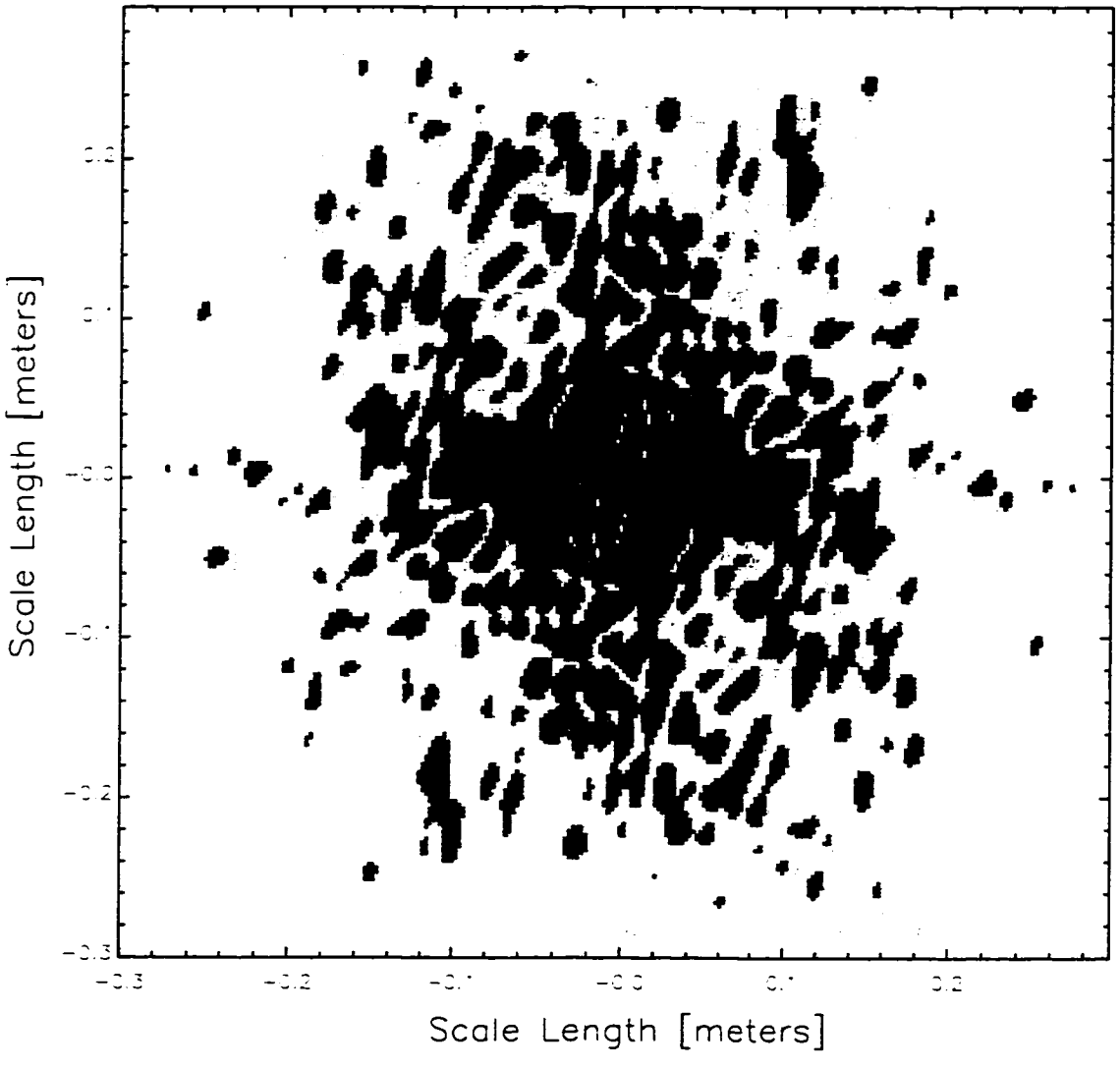

Figure 3.4 Close up of two dimensional FFT of present survey (Di96) shown in Figure 3.3. Shading levels are at 35. 87..... 20522 K^2 with the shading weights chosen to emphasize the 'plateau'-like structure seen running almost vertically through the image over the scale length -0.2 m to 0.2 m.

with the broadest scale structure in the sky. The alignment of the arms of this feature is at a position angle of 15° (clock-wise from the top) and extends out to ~ 0.025 m (7'.25 in the sky). Note that the position angle of the arms of this structure differs from that of the plateau by $\sim 35°$ as it is not obvious from the CO map that the best representation of the data at the largest scale sampled is not dominated by the plateau described in point 2 above.

4. The vertical and horizontal stripes through the center of the FFT shown in Figure 3.3, which run along 0 scale length in both coordinates, are due to edge effects. The asymmetry in the weighting of these stripes can be attributed to the asymmetry of the field, i.e., the absence of data in the upper right hand corner of the field.

Azimuthally averaged data in the lower diagram of Figure 3.3 provide additional information on clustering at particular length scales in the map but at the cost of losing any information on orientation angles. The quantity plotted in that diagram is the log of the square of the amplitude of the FFT as a function of the radii of the azimuthally averaged annuli. Fitting an unweighted least-squares fit to this data leads to the solution:

$$\log(\text{Power } [\text{K}^2]) = (1.73 \pm 0.10) + (-2.52 \pm 0.08) \log(\text{Scale Length [m]}). \quad (3.5)$$

where the uncertainty in the slope and intercept are 1σ values. The uncertainty in each point in the azimuthally averaged FFT is a 1σ variation in the mean binned value, i.e., the log of ($n^{1/2} \times 0.14$ K) where n is the number of pixels in each bin.

In order to examine the strength of the claim of a 'plateau' shape in the FFT plane highlighted in Figure 3.4, it is useful to plot solutions from strips or wedges of data taken along the plateau and perpendicular to it. Taking strips ~ 100 pixels wide in these two directions leads to:

$$\log(\text{Power } [\text{K}^2]) = (1.88 \pm 0.03) + (-2.42 \pm 0.02) \log(\text{Scale Length [m]}). \quad (3.6)$$

along the plateau, and

$$\log(\text{Power } [\text{K}^2]) = (1.74 \pm 0.06) + (-2.51 \pm 0.05) \log(\text{Scale Length [m]}). \quad (3.7)$$

perpendicular to the plateau. There is only weak evidence that there is a difference in the slope of the overall fit to the data, Eq. 3.5, and the data fitted along the plateau (the difference is just within the 1σ limit). Reducing the width of the

test strip along the plateau increases the difference in slopes for the FFTs between the plateau-aligned and plateau-perpendicular solutions but with a commensurate increase in the uncertainty of the fit to the slope of the plateau-aligned solution. A comparison of the slope for the data taken along the perpendicular strip is in very good agreement with the overall fit and well within the limits to the fit along the plateau. Hence, there is no difference in the slope of the fit for the azimuthally binned data along the plateau or perpendicular to it.

In the case of the y-intercept for the solutions fitted to along the plateau, perpendicular to it and the overall fit there is a significant difference between the fit along the plane and the overall fit. A similar difference exists between the fit along the plateau and perpendicular to it but the uncertainty is too large in the case of the perpendicular-fit y-intercept to determine whether this difference is significant.

What does it mean? The similarity of the solutions for all of the cases considered suggest that the distribution of material, i.e., the number of features at any size scale, is the same regardless of direction in the sky. The difference in the offsets or y-intercepts for the solution along the plateau and perpendicular to it suggest there is simply more material, at all scale lengths, along the plateau.

ii. Original Survey Figure 3.5 shows the two dimensional FFT for the original survey (Da87). In order to simplify the comparison of the original survey with the present survey, the original survey has first been re-gridded, using an in-house software package *mapconvrt* (this makes use of a cubic spline routine to interpolate the data onto the new grid), so that it lies on the same grid as the present survey, i.e., 3.75 pixels. A comparison of the modified original survey image with the original did not reveal any major discrepancies between the two. This was confirmed from a visual inspection of FFT images made from the original and modified original maps which were in agreement over the scale lengths for which they could be compared, i.e., the inner 0.2 m of Figure 3.5. A summary of some of the key features seen in the original survey is as follows:

1. In contrast to the FFT of the present survey there is no discernable asymmetry over the intermediate or large scale lengths, i.e., there is no comparable 'plateau' feature detected in the FFT of the original survey. Indeed, the high degree of symmetry at these scale lengths suggests that there is no preferred position angle or size for CO emission over these scale lengths. This may be attributed to the coarse binning of the original survey where information over these scale lengths

has been seriously diminished.

2. There is an 'S' shaped feature seen at the center of Figure 3.5 which is not as well defined as for the present survey. The orientation angle and extent of the feature are similar to the present survey and have probably been produced by the same emission feature in the image plane. This suggests that on the largest scale the distribution of CO is similar in both surveys, as modelled by an FFT.
3. Like the present survey, edge effects and the asymmetry of the field produce the vertical and horizontal stripes seen at the very longest scale lengths.

It is very instructive to now consider the azimuthally binned FFT for the original survey (lower diagram in Figure 3.5). In this case, the least-square fit to the log of the square of the power (the broken line in Figure 3.5) is given by:

$$\log(\text{Power } [\text{K}^2]) = (2.83 \pm 0.24) + (-1.71 \pm 0.14) \log(\text{Scale Length [m]}). \quad (3.8)$$

It is clear, from the comparison of the solution obtained from the present survey (Eq. 3.5, solid line in Figure 3.5), that information on the structure of CO emission is missed at the largest scale lengths, i.e., the smallest angular structure in the sky, as indicated by the sharp drop off of the FFT in the azimuthally binned FFT for the original survey, compared to the new. The drop off occurs at a log scale length of ~ -0.82 (1°.22 on the sky), and represents the effective limit of the original survey if a circular beam is assumed (a square beam would yield a limit of 1°). More surprisingly, there is a considerable amount of information regarding the largest structure in the sky, i.e., at the smallest scale lengths, which is missed in the original survey when compared to the present survey. The difference in the slopes and the intercepts of the present and original survey exceeds the uncertainties in both of these quantities which suggests that the solution obtained from the present survey represents a real improvement in the description of the structure of CO emission in Cam OB1.

In summary, the present survey shows a marked improvement over the original survey in the information it provides through FFT analysis leading to a better measure of CO structure at all scale lengths.

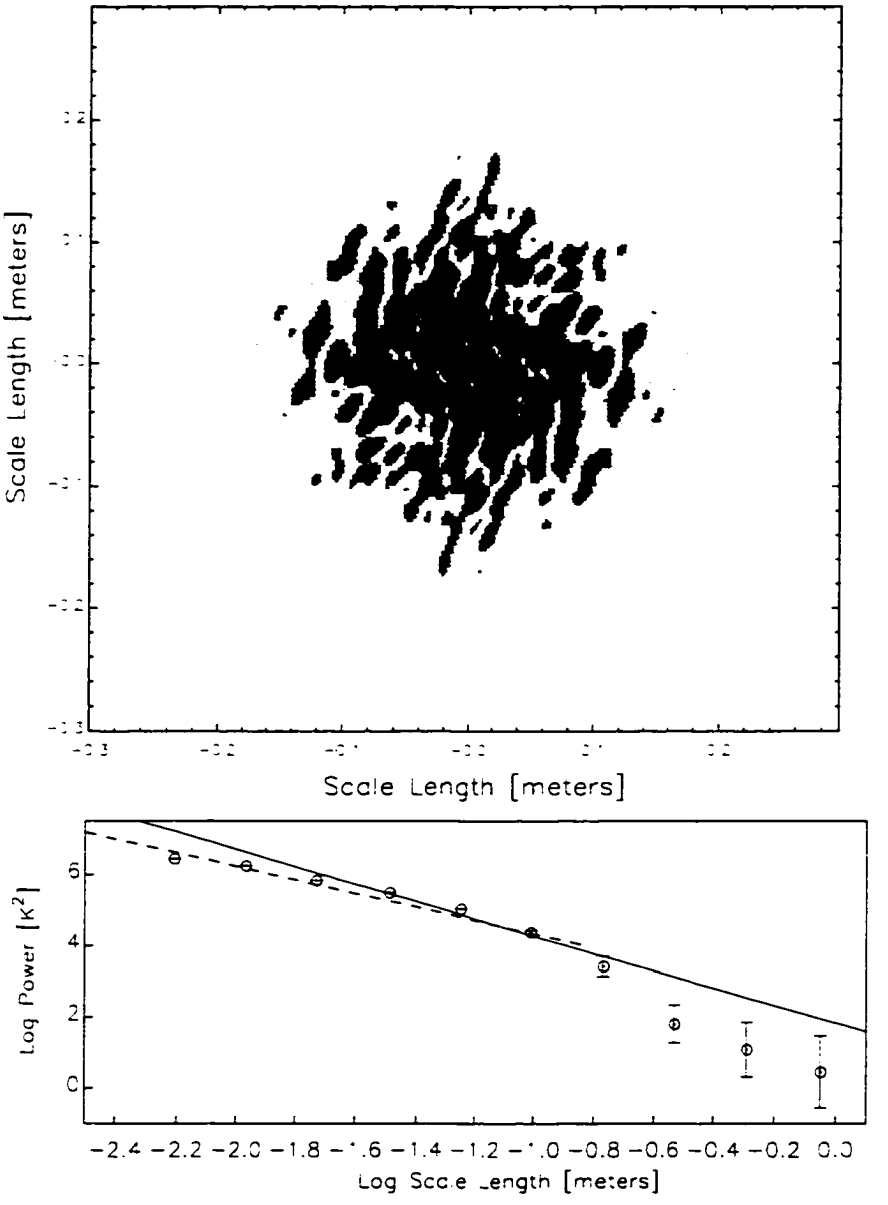

Figure 3.5 Two dimensional FFT of original survey (Da87). Note that the scale is the same as for Figure 3.4 as the original survey only samples the largest scale structure accessible by the present survey. Top view shows the FFT (amplitude) of the average radiation temperature, $\bar{T}_R$, over the velocity range, $v = -5.5$ to -22 km s^{-1}. Shading levels are the same as for Figure 3.3. The bottom view is an azimuthally averaged representation of the log of the square of the amplitude of the original survey as a function of the log of the radius. The broken line represents an unweighted least-squares fit to the original data (Eq. 3.8) while the error bars represent a 1σ deviation in the average. The solid line represents the similar fit to the present survey (Eq. 3.5), which is the solid line shown in Figure 3.4.

3.2.2.2 Structure Tree Statistics

Structure tree statistics are a useful tool for detecting structure in a two dimensional image of a three dimensional object. A typical astronomical application is to consider the image of a CO 'cloud' as viewed from its integrated CO emission. A two dimensional image of such an object will appear to be an 'island' with many emission peaks. However, it may also be the case that the island really is composed of many separate features which are not physically related to each other, but are the result of a chance alignment along the line-of-sight. By looking at the parentage of the peaks, i.e., considering an emission peak to be the progeny of a broader emission feature (parent) if it is contained within the boundary of the parent, it is possible to distinguish between such scenarios as a random distribution of clouds or a perfectly geometrical hierarchy of clouds (Scalo 1985, 1988; Houlahan & Scalo 1990, 1992). This type of investigation is extremely important in so far as some models of star formation are based upon the fragmentation of molecular clouds in which the smallest fragments, stellar-mass cores — the precursors to stars — are produced in a single stage (Shu et al. 1987, Solomon et al. 1987, Mouschovias 1991) as opposed to multi-staged fragmentation models (Nakano 1976, 1977, Carlberg & Pudritz 1990, Henriksen 1991). The former case would be identified with strongly random structure trees while the latter with hierarchical structure trees.

This section will not exhaustively examine all of the clouds detected in the present survey (Di96) but will consider one feature, centered on $l = 142.^{\circ}5, b = +0.^{\circ}5$, to serve as an example of the structure in CO clouds in Cam OB1 not detected in the original survey (Da87). Figure 3.6 shows the CO emission and the corresponding structure trees for the original and present surveys.

An algorithm for constructing the structure tree is detailed in Houlahan & Scalo (1992). The structure trees presented here are derived using a simplified version of that algorithm. A summary of the procedure employed is as follows:

1. Select a minimum contour level to establish a root. In both cases of the present and original survey this was set at their respective 3σ levels.
2. Increase the contour level and determine whether any progeny clouds exist at the new contour level. A progeny is first identified as a 'cloud' if it is at least two beam widths across in any direction. The only exception to this are the small isolated features detected in the original survey at the root level which were retained for illustration but not used further in the analysis.

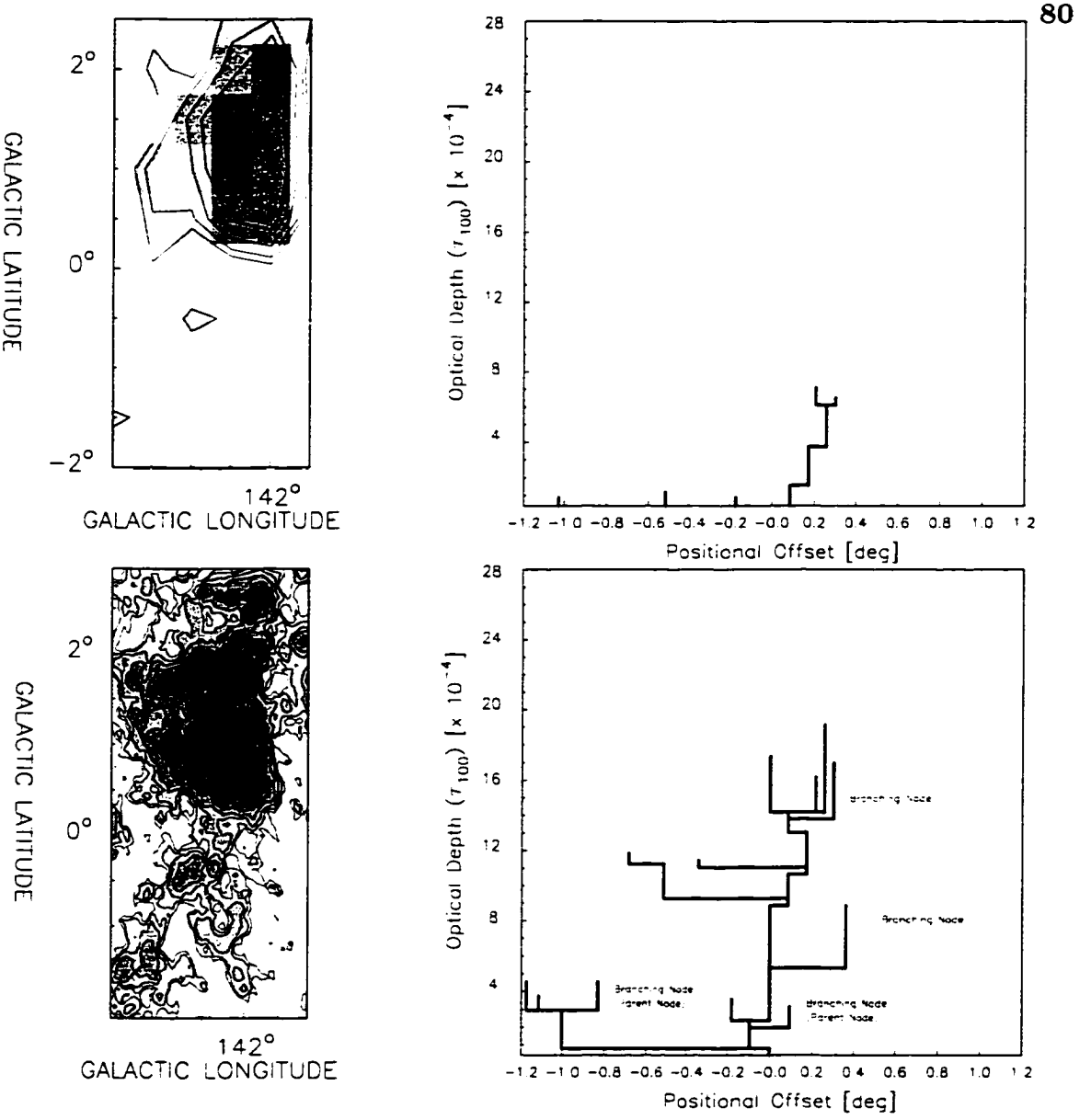

Figure 3.6 View of sample cloud and structure tree from original survey (top) and present work (bottom). Contouring is as for Figure 3.1, i.e., a minimum contour of 3σ with an increase by a factor of 1.58 for each step thereafter. An equivalent 100μm optical depth has been derived for the CO emission assuming it is optically thin, has a standard dust-to-gas ratio (100), and the dust follows a λ^{-1} emissivity law. With $N(H_2) = 1.25 \times 10^{21} A_v[cm^{-2}]$ (Scheffler & Elsässer (1987), $A_v = 2000\tau_{100\mu m}$ (Houlahan & Scalo 1992) and $N(H_2) = 1.9 \times 10^{20} W(CO)$ (Strong et al. 1988) it follows that $\tau_{100\mu m} = 7.4 \times 10^{-5} W(CO)$. In both structure trees the positional offset is taken in the Galactic latitude direction from the centroid of the lowest intensity contour level.

3. Increment the contour level until the whole tree has been traversed. For this analysis 100 levels were selected between the minimum 3σ level and the maximum detected signal. The top of a branch (a single cloud) is pruned when it falls below the detection criterion set in Step 2. This will clip the tips of the trees but does not alter the conclusions derived below. (As a check of this point, an examination of each branch tip was performed and it was found that in all cases the emission fell to zero within three contour levels of the claimed tree tip, i.e., the emission fell to zero within a very small change in tree height.)
4. Construct the tree, identify the main components and calculate the relevant statistics.

There are several definitions required to perform the analysis of a structure tree and its statistics. These include (Houlahan & Scalo 1992):

Root This is the lowest intensity level in the structure which serves to define the largest extent of the cloud as a simply closed contour.

Path A line connecting tip to root through all intermediate clouds as determined by the lineage.

Node This is the position in the tree of an intermediate cloud in terms of its mean intensity and centroid. The cloud's intensity has been converted into an optical depth in Figure 3.6 in order to allow a direct comparison of the structure tree from Houlahan & Scalo (1992).

Branching Node A node at which two or more paths merge. This corresponds to a parent cloud with at least two children.

Segment A sequence of branching nodes with similar weight, i.e., size and center of mass above the root.

Parent Node The lowest branching node in a segment. If there are similar segments in a tree then the lowest branching nodes in other segments are referred to as uncles.

The analysis of the structure tree statistics, presented in this thesis, will be limited to a comparison of idealized models of perfectly geometric hierarchies. In this case, there are four parameters which are necessary to characterize the structure — η, D, L and θ (Scalo 1985, 1990). η is the number of progeny per generation above the root (for a self-similar hierarchy this number is constant), D measures the intensity contrast between levels, L is the number of levels in the image and θ measures the spatial distribution of children around their common parent. L is set as the number of planes making up the image as seen along the line-of-sight in Monte

Carlo simulated data or the number of different emission regions that can be isolated kinematically along the line-of-sight of the present survey. These parameters are not measured directly, with the exception of L, but can be obtained from measurements of properties of the tree. In terms of these properties, these parameters are given by:

$$\eta = \frac{N - 1}{B}. \tag{3.9}$$

where N is the total number of nodes in the system and B is the number of branching areas (a branching node with the branches at slightly different heights, or optical depths, but still believed to have a common node).

$$\theta = \frac{\text{mean displacement of the children in a segment}}{\text{mean displacement of the parents in a segment}}. \tag{3.10}$$

where the position of the feature in question is measured from the position of the root and

$$D = \frac{(1 + C)}{\theta}. \tag{3.11}$$

C is the change in path length in going from one tree level to the next. In practice, C is determined from:

$$C = \frac{\text{mean height of the tips of the children above parent node}}{\text{mean height of the tips of the parent (and uncles) above root}}. \tag{3.12}$$

From Figure 3.6 the difficulty in deriving any meaningful structure statistics for the CO cloud based upon the original survey is obvious, since the tree is composed of only one segment and only one node at the tree tip. Only one segment was detected due to the lower sensitivity, i.e., the second segment at the root of the tree was not detected, while the poorer resolution only allowed detection of the brighter features separated by $\sim 1°$ (one beam width). Furthermore, the tip of the tree appears to occur at a lower optical depth due to the gross averaging that occurs when binning the observations in the original survey. From the original survey it is only possible to derive a value for η ($= 0$), L($= 3$) and D (~ 5). θ is not defined for this structure as there is only one parent in the tree.

In the case of the present survey, the structure tree is more informative. With the resolution and sensitivity of the present survey it is possible to see a definite pattern to the structure tree emerge. The main difficulty in interpreting the tree lies in the treatment of the central branching region of the larger segment (indicated by the broken line in Figure 3.6). The nodes in this region do appear at appreciably

different heights above the root, but the height of the tips all fall within a very narrow range, certainly comparable in extent to the range seen elsewhere in the tree. Hence, in characterizing this branching region it has been assumed that it is indeed a branching node with three children. With this assumption, it follows that the structure tree for the present CO data is characterized by the following parameters: $\eta = 2.3, \theta = 0.33$, and D = 11.8. L is set at 3 as there appear to be three main CO features making up this cloud complex (Chapter 7). If the assumption regarding the central branching region does not hold, then B, the number of branching areas, will increase for the same number of branching nodes and thus, reduce the value of η.

Houlahan & Scalo (1990, 1992) also showed that clouds which have a self-similar hierarchical structure will have a frequency distribution for their cloud sizes and a density-size relationship related to their hierarchical structure. For a self-similar hierarchy, the frequency distribution of clouds as a function of radius, r, is given by:

$$f(r) \propto r^{\alpha}. \tag{3.13}$$

where α may be obtained from

$$\theta = \eta^{1/(1+\alpha)}. \tag{3.14}$$

and η is the number of fragments per level of hierarchy and θ is the relative size of fragments at successive levels. The density-size scaling law for a self-similar hierarchy is given by:

$$\rho \propto r^{p}. \tag{3.15}$$

where p may be obtained from

$$D = \eta^{p/(1+\alpha)}. \tag{3.16}$$

where D is the volume density contrast, i.e., the contrast in the density of successive levels in the hierarchy. Hence, for the molecular cloud considered here it follows from from Eq. 3.14 and 3.16, that it has a size distribution with $\alpha \sim -1.8$, and density-size scaling law with $p \sim -2.2$. It is interesting to note that the value of p derived here, which is based upon a relatively large cloud structure, i.e., $\sim 3 - 20$ pc, is similar to that detected in high-resolution studies of molecular cores (Myers 1983), which lends support to the claim that this structure holds over a large range of scale

sizes and is common. High-resolution studies of the entire cloud system are required to confirm this.

From Figure 3.6 it is quite clear that the structure tree statistics derived from the original survey cannot be used for this type of analysis. However, the richness of structure seen in the structure tree revealed in the present survey suggests that the CfA 1.2 m telescope is very useful for gathering data suitable for this type of analysis, even given its moderate resolution, provided the data are fully sampled with good sensitivity.

3.3 Discussion

In §3.2.2.1 and §3.2.2.2 two quantitative methods, FFTs and structure tree statistics, were used to measure the improvement in image quality of the present survey over the original survey. It is now worthwhile to extend this analysis and compare the results gleaned from the present survey by comparing these results to other surveys conducted on the surveyed region and elsewhere in the Galaxy. To this end, the first comparison will be with the HI (Gr93), in order to consider whether the power-law describing the distribution of power with scale length derived for CO from the present survey is similar to that for HI. A second comparison will be of the structure tree statistics derived from *IRAS* (Beichman et al. 1988) 60μm and 100μm emission for the Taurus star forming region (Houlahan & Scalo 1992), in order to provide some frame of reference for the results obtained for the Cam OB1 region.

The analysis of HI in Cam OB1 (Gr93) was performed on data obtained with an interferometer. As such, the structural information contained within the data had to be carefully treated in order to account for the correlation between signal strength and noise, as well as a difference in the sensitivity of the correlators making up the spectrometer. After these corrections had been applied, Gr93 found that the exponent, m, of the power-law distribution of power of HI, $P_{\rm H_I}$, as a function of scale length, r, normalized to the power at a scale length of 100λ, i.e.,

$$P_{\rm H_I} = P_{100\lambda}\left(\frac{r}{100\lambda}\right)^m \qquad (3.17)$$

is given by $m = -2.57 \pm 0.18$ over the velocity range -5.7 to -10.7 kms^{-1}, $m = -2.18 \pm 0.11$ over the velocity range -10.7 to -15.7 kms^{-1} and $m = -2.33 \pm 0.13$ over the velocity range -15.7 to -20.7 kms^{-1}. From these values it is reasonable to

assume that $m = -2.36 \pm 0.16$ is representative of the exponent, m, for the power-law distribution of HI as a function of scale size over the velocity range defining the Cam OB1 CO emission. This value of m is in agreement with the value of the exponent of the power-law fit to the CO emission derived from the present survey, i.e., -2.52 ± 0.08 (Eq. 3.5), and may suggest that the force(s) responsible for organizing the HI is also operative and equally effective in organizing the CO, at least down to the resolution of the present survey (at a distance of 975 pc for Cam OB1 this corresponds to a scale $\sim$ 3 pc). Scalo (1987) has suggested that turbulence could be the primary support mechanism in molecular clouds which follow a Kolmogorov prescription (Larson 1981). If this is the case, the distribution of power with scale-length should be described by a power-law with an index $\sim -8/3$ (Leinert 1994). This is in good agreement with observations for both HI and CO.

A second quantity of interest suggested by Gr93 is the total power seen at some particular physical length. In the case of the HI survey a length of 100 pc was chosen as a standard length, as the power over this length could be determined over a large range of distances; from Figure 4 of Gr93 it is possible to derive a mean power at a scale length of 100 pc for HI of $820 \pm 300 \mathrm{Jy}^2$ over the range of velocities quoted above. Conversion of this quantity to the same units as the CO power may be obtained from (DRAO in-house memorandum, 1996),

$$\text{Flux Density[mJy per beam]} \times \frac{0.385\ \mathrm{E}}{1.13\ \nu^2\ \mathrm{R}^2} = \text{Flux Density[K]}. \qquad (3.18)$$

where E is the ratio of minor to major axis of the DRAO Super Synthesis Telescope (SST) beam, ν is the observing frequency in GHz and R is the minor axis, in arcmin, of the SST beam. For Gr93 the data were smoothed to $2' \times 2'$ at an observing frequency of 1.42 GHz. The power in the HI emission, seen at 100 pc scale lengths, in Cam OB1 region is $(1.46 \pm 0.53) \times 10^6\ \mathrm{K}^2$. From Eq. 3.5, the power in the CO emission at a scale length of 100 pc (R, the radius of the corresponding scale length in the Fourier plane is 0.062 m) is $(6.03 \pm 0.20) \times 10^4\ \mathrm{K}^2$. Thus, the ratio of the power in HI to CO at a scale length of 100 pc is $\sim$ 25. It is difficult to interpret what exactly this ratio means, or indeed what the 'power' is for either component of the ISM, as the FFT image of the data is not a simple composite of sky brightness or intensity. However, this ratio, and the value for the power in each component, may prove useful in constraining any models or simulations of the ISM in the Cam OB1 region.

There is additional information on the structure of the CO emission in the Cam OB1 region to be gained from the structure tree statistics. The analysis of the structure tree statistics for the Taurus star forming complex based upon the *IRAS* 60μm and 100μm emission (Houlahan & Scalo 1992) serves as a good example of another well-studied star forming region in the Galaxy. From their analysis of $\tau_{100\mu m}$ versus positional offset from the root, Houlahan & Scalo (1992) determined that the Taurus star forming complex has a structure tree best characterized by $\eta = 9.8, \theta = 0.16$, L = 2 and D = 9.6. The nature of these clouds was determined by comparing them to Monte Carlo simulations of: a) ideal clouds, i.e., uniformly dense cores with r^{-2} variation in their envelopes, which were constrained to be hierarchical in their physical makeup and spatial position (hierarchical models), b) the same models but randomly distributed in space (random models), or c) a mixture of the two (mixed). The solution for the Taurus region turned out to be best represented by a mixed-model, but one dominated by hierarchical structure. One complication in the analysis of structure in the Taurus region was the difficulty in separating foreground from background material solely from integrated dust emission maps. In principle, applying the structure tree analysis to CO emission has the advantage over a dust emission study for the same region, as the additional CO velocity information may be used to eliminate foreground and background contamination.

A comparison of the structure tree for the sample Cam OB1 cloud (η = 2.3, $\theta = 0.33$, L = 3 and D = 11.8) to that of Taurus suggests that the Cam OB1 cloud is sparser than Taurus (smaller η), possesses better defined branches (larger θ), with more levels (larger L) but with approximately the same density contrast per level (D). In order to check whether the sample Cam OB1 cloud is better modelled as being hierarchical or random or mixed, Houlahan & Scalo (1992) suggest that a branching factor, E_o, which is equivalent to η as it is calculated in Eq. 3.9, is a useful diagnostic, i.e., a value for E_o of less than 5 is a good indicator of hierarchical structure. The solution provided by the CO data taken in the present survey does suggest such a structure, but it must be kept in mind that it was only derived from a coarse structure tree for one cloud. However, on the other hand the CO data do have the advantage over a dust emission study of being less susceptible to contamination by foreground and background material. In Figure 3.6, the range of optical depth is similar to that covered by Houlahan & Scalo (1992) for Taurus ($\tau_{100\mu m} : 1 \times 10^{-5} - 4.4 \times 10^{-3}$), while the velocity maps for the region (Chapter 2)

show that the CO emission is well contained within the Cam OB1 velocity range. This is only assumed in the case of the Taurus emission. With these considerations in mind, it would appear that some of the Cam OB1 CO emission, like the Taurus region, has a strong hierarchical component to its structure. Higher resolution CO data and additional Monte Carlo simulations are required to refine this solution.

3.4 Conclusions

The following conclusions can be drawn from this comparison of the present (Di96) and original (Da87) surveys of the Cam OB1 region:

1. The improvement in data quality expected from the present survey is clearly seen in both the integrated map of the emission and the velocity moment maps (Figures 3.1 and 3.2).
2. An FFT analysis of the region from the two surveys suggests there is considerable additional structure seen in the new survey. The distribution of power as a function of scale length for the present survey is given by:

$$\log\,(\text{Power}\,[\text{K}^2]) = (1.73 \pm 0.10) + (-2.52 \pm 0.08)\,\log\,(\text{Radius}\,[\text{m}]).$$

3. A comparison of the CO structure to the structure seen in HI suggests that both the CO and HI have the same structural scaling law. This suggests that the force(s), e.g., turbulence, operative in organizing the HI may be equally operative and efficient for organizing the CO.
4. A comparison of the structure trees taken from a sample cloud in the Cam OB1 region suggests that it can be modelled as possessing a hierarchical structure similar to that found for the Taurus star forming complex. No comment on this sample cloud is possible from the original survey.
5. The structure tree statistics for the sample cloud have a solution $\eta = 2.3$, $\theta = 0.33$, L = 3 and D = 11.8.
6. An analysis of the cloud density profile shows $\rho \propto r^{-2.2}$ which is similar to molecular cores seen elsewhere in the Galaxy (Myers 1983). This is consistent with the model of molecular clouds in which they are turbulent and have a self-similar hierarchical structure.

Chapter 4

Population I Objects

An investigation of the optically identified Population I objects within the boundaries of the present survey (Digel et al. 1996) is carried out. From the analysis of these objects it is determined that the distance to: 1) the Local emission is 250 ± 50 pc, 2) the Perseus emission is 2500 ± 200 pc, and 3) the Cam OB1 emission is 975 ± 90 pc. An HR diagram for the Cam OB1 stars reveals that star formation has occurred in the region for $\sim 1 - 50 \times 10^6$ yr. At present, the most active site of star formation is Cam R1, which shows an asymmetry in the distribution of optically-identified Population I objects: the majority of the pre-main sequence stars lie in the northern half of the association while the main sequence and evolved stars lie in the southern half.

4.1 Introduction

Population I objects were first identified as a stellar population closely associated with spiral arms by Baade (1944a, 1944b) in his examination of nearby galaxies. A complete discourse on these objects is beyond the scope of this thesis (Mihalas & Binney 1981 provide an overview), but for practical purposes Population I objects will be divided into two categories, Population I objects and extreme Population I objects (hereafter referred to as PIo and ePIo, respectively). PIo will include OB associations, R associations, galactic clusters, OB field stars, Be stars, classical cepheids and Herbig Ae/Be (HAe/Be) stars. ePIo will be designated as 'non-stellar' objects which are associated with star forming regions, i.e., they trace out the current epoch of star formation. These include pre-main sequence stars, i.e., T-Tauri and HAe/Be stars identified by their infrared emission, masers, molecular outflows, as well as reflection nebulae and emission nebulae (HII regions).

It is important in the analysis of any star forming region that both PIo and ePIo be considered for two reasons. Firstly, if the PIo contain a relatively young population of stars (say $1 - 10 \times 10^6$ yr) which can still be associated with their

parent cloud on the basis of the interaction between the stars and parent cloud (via dissociation fronts, ionization fronts or reflection nebulae), positional coincidence and similar space velocities, then the fundamental problem of assigning a distance to the parent cloud and any ePIo embedded in the cloud may be confidently addressed. If the PIo form a cluster or association, as is the case for the Cam OB1 stars, then it is best to fit a standard main sequence to these objects (Blaauw 1963, Mermilliod 1981, Garmany & Stencel 1992, hereafter GS92), thereby reducing the effect of uncertainties of an individual measurement, to obtain the distance to the PIo (and associated parent cloud). Secondly, the association of the PIo with the parent cloud, and the presence of ePIo in that cloud provide an opportunity to study the long term evolution of a star forming region, including the interplay of possibly distinct generations of stars (Chapters 6 and 7).

If it is not possible to obtain a distance to a parent cloud and its associated ePIo from associated PIo, then it is necessary to determine this distance by one of two means. If sufficient data exist, then it is possible to consider departures from a statistical model of stellar densities and obscuration, to infer the location of excess obscuration along the line-of-sight, e.g., the extinction survey in the region by Heeschen (1951). This method is best suited to the determination of the distance to the Local emission in the present survey (Digel et al. 1996, hereafter Di96). For more distant emission, where there are no known PIo present, the distance to the emission must be determined from a standard kinematic model of the Galaxy (Brand & Blitz 1993). The Local emission (-5.5 km s^{-1} $\leq v_{LSR} \leq +10$ km s^{-1}) and Cam OB1 emission (-22 km s^{-1} $\leq v_{LSR} \leq -5.5$ km s^{-1}) are well situated in the second quadrant of the Galaxy for this type of analysis, which avoids the distance-velocity ambiguities inherent to studies of the first and fourth quadrants. However, the Perseus arm (-70 km s^{-1} $\leq v_{LSR} \leq -30$ km s^{-1}), which lies beyond Cam OB1, is known to show departures from the circular motion (streaming motions) assumed in standard kinematic models (Roberts 1972).

This chapter will consider only the PIo: ePIo will be considered in Chapter 5. The breakdown of this chapter is as follows: §4.2 will deal with the selection of PIo in the field and the distances to the different regions of the Galaxy seen along the line-of-sight, i.e., Local emission will be discussed in §4.2.1, Perseus emission in §4.2.2 and finally, Cam OB1 emission in §4.2.3. In §4.3.1 an observer's HR diagram for the Cam OB1 stars, including Cepheids and classical Be stars, will be constructed.

In §4.3.2 the observer's HR diagram will be transformed into a theoretician's HR diagram in order to derive time scales for the evolution of these stars. In §4.4 the findings from this chapter will be summarized.

4.2 Population I Objects

Selection of PIo has made extensive use of the SIMBAD database (hereafter simply SIMBAD) [1] as the principal source of stellar data. Figure 4.1 shows all of the stellar objects (2260) detected within the boundaries of the present survey (Di96) at the time of writing. Previous experience working with SIMBAD shows that while it is not complete, typically $\sim$ 80% of the stellar objects studied and available in the literature are included in it. From a comparison of Figure 4.1 and Table 4.1, which contains information on known open clusters and R-associations included in the surveyed region, it follows that the most prominent open clusters have been identified, and only the smallest and least studied ones were omitted.

4.2.1 The Distance to the Local Emission

The determination of the distance to the Local CO emission made use of the star-count analysis of Heeschen (1951) which extended to stars down to 15^{th} magnitude. In his work, Heeschen examined selected areas in the Perseus region of the Galaxy, including the region considered in the present survey, and deduced, "...The obscuration is ascribed to two clouds: one cloud is at a distance of 200-300 parsecs and the other at the distance of 800 parsecs from the sun. The nearer cloud accounts for most of the patchiness of the region, while the cloud at 800 parsecs is nearly uniform in density." Figure 4.2 is an integrated map of the Local CO emission in which several regions, identified in the original work of Heeschen, have been indicated using his original designation.

From Figure 4.2 and Table 4.2 it is evident that the Local emission lies at a distance of 300 pc for the emission at lower galactic latitudes, and at 200 pc for emission at higher latitudes. For this thesis it will be assumed that

[1] SIMBAD is operated at CDS, Observatoire de Strasbourg 11, rue de l'Universite, 67000 STRASBOURG, France. The Canadian link to the CDS is provided by the Canadian Astronomical Data Centre (CADC) located at the Dominion Astrophysical Observatory, Herzberg Institute of Astrophysics, National Research Council of Canada, 5071 West Saanich Rd., R.R. 5, Victoria, British Columbia, Canada.

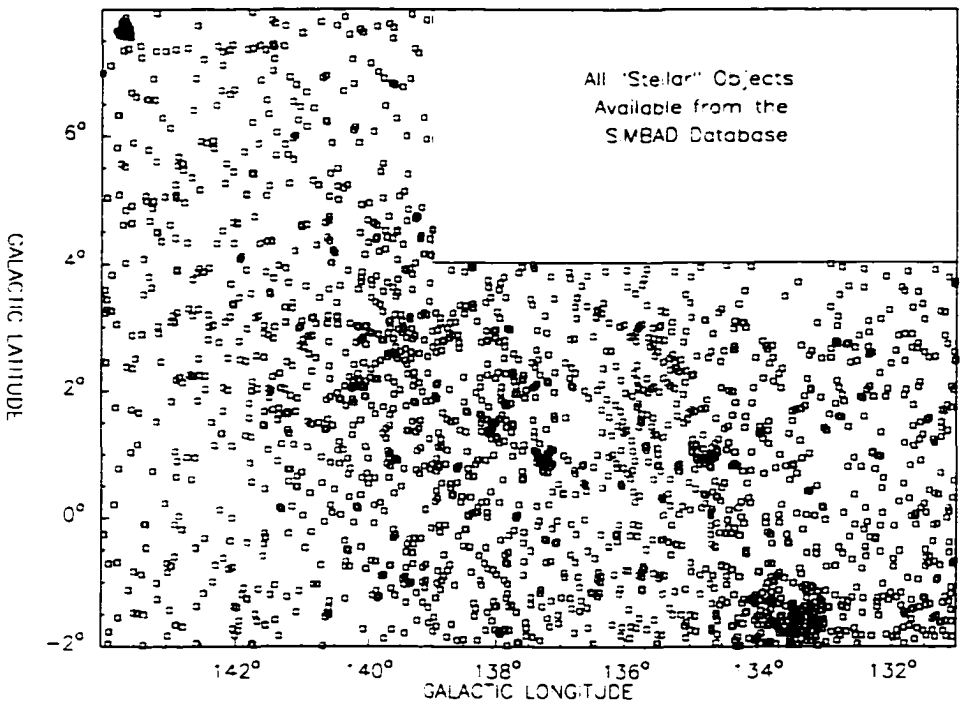

Figure 4.1 All stellar objects in SIMBAD contained within the survey boundaries (Di96). Some obvious clusterings of objects have been identified in the *Sky Catalogue 2000.0* (Hirshfeld & Sinnott 1985) and are tabulated below (with the exception of Cam R1 which is taken from Herbst 1975). D refers to the apparent cluster diameter. No. to the number of cluster members and R. the quoted distance to the cluster. 'Not easily identified' means the cluster is located in a busy field. 'easily identified' means the contrast between the cluster and surrounding field is great. 'not included' indicates there is no obvious cluster of objects at the indicated position (a sparse cluster).

Table 4.1: Open Clusters and R-Associations in Field

Name	l [°]	b [°]	D [']	No.	R [kpc]	Appearance
NGC 743	131.21	-1.60	5	12	N/A	Not easily identified
Stock 6	132.88	+2.79	20	20	N/A	Not easily identified
Stock 2	133.44	-1.89	60	50	0.32	Easily identified
IC 1805	134.73	+0.92	22	40	2.10	Easily identified
Cz 13	135.66	+2.31	6	10	N/A	Easily identified
NGC 1027	135.78	+1.49	20	40	1.00	Easily identified
Cz 8	135.80	-1.58	7	10	2.40	Not included
Berk 65	135.83	+0.27	5	20	3.30	Not included
King 4	136.02	-1.20	3	20	2.20	Not included
IC 1848	137.19	+0.92	12	10	2.20	Easily identified
Cr 33	138.10	+1.35	40	25	N/A	Easily identified
Cr 34	138.26	+1.46	25	N/A	N/A	Easily identified
Stock 23	140.11	+2.08	15	25	N/A	Easily identified
Cam R1	142.00	+2.00	N/A	5	0.87	Easily identified
King 6	143.36	-0.08	7	35	N/A	Not included
NGC 1502	143.66	+7.65	8	45	0.95	Easily identified
Tombaugh 5	143.94	+3.57	17	60	1.80	Easily identified

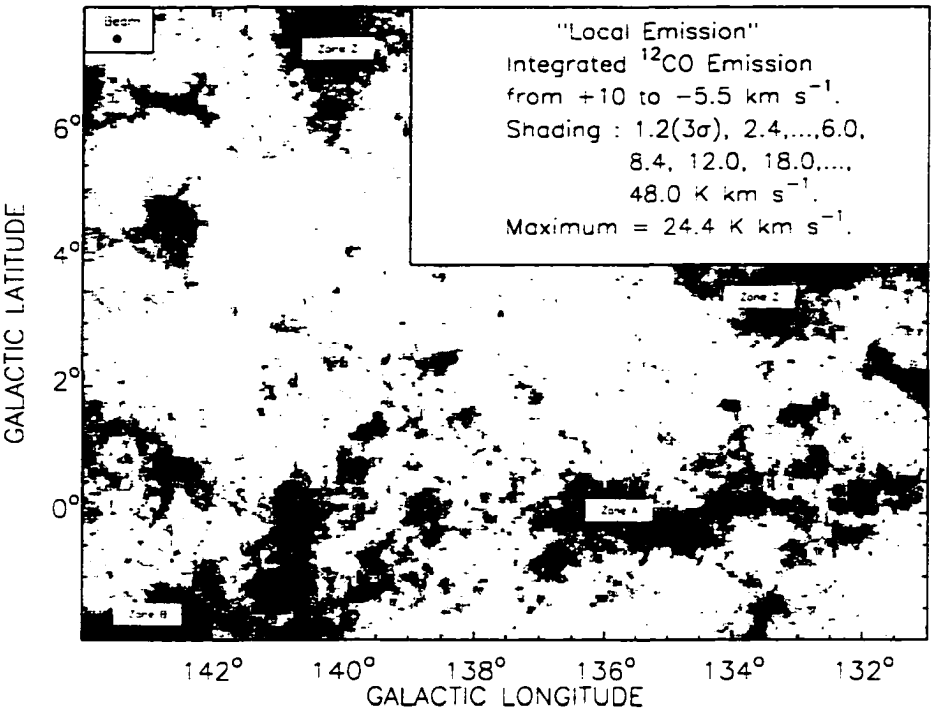

Figure 4.2 Overlay of Heeschen's (1951) areas of obscuration onto the Local emission. The data describing the obscuration due to the Local emission in each region are given below according his original scheme. Positions in (l^{II}, b^{II}) are included in parentheses. Details of the obscuration due to the Cam OB1 emission (assigned a constant distance of 800 parsecs by Heeschen) will be dealt with in §4.2.3.

Table 4.2: Obscuration in Surveyed Region (after Heeschen 1951)

Region	Obscuration [Mags]		
	At 200 pc	At 300 pc	At 800 pc
Zone B,+2.°5 (143°, −1.°5)	.....	1.6	0.9 .....
Zone A, 0.°0 (138°, 0.°0)	.....	1.5	1.1 .....
Zone Z,+2.°5 (133°, +3.°5)	1.0		1.4 .....
Zone Z,+5.°0 (140°, +7.°0)	1.0		1.3 .....

the Local emission lies at a distance of 250 ± 50 parsecs at all latitudes considered in the present survey.

4.2.2 The Distance to the Perseus Emission

The Perseus emission, in the direction covered by the present survey, is dominated by the giant molecular complexes associated with the giant HII regions W3, W4 and W5. GS92 conducted an extensive literature search of OB associations in the northern Milky Way in order to ascertain the extent of intrinsic scatter in the O-star calibration: this study included two rich associations, Cas OB6 and Per OB1, in the Perseus region covered in the present survey. Cam OB1 was considered briefly in the study of GS92, but the paucity of O-stars in its membership precluded it from being useful in the calibration of the O-star classification scheme. Figure 4.3 is an overlay of the stars identified as belonging to Cas OB6 and Per OB1 (GS92, Humphreys 1978), contained within the present survey boundaries, over the CO emission from the present survey. A table of the stellar data for these associations is included in Appendix B.

The technique employed by GS92 to determine the distance to the Perseus stars, and by association, the Perseus CO emission, was to: a) compare the main sequence B stars in the associations Per OB1 and Cas OB6 with a standard model of main sequence stars (Blaauw 1963, Mermilliod 1981), and then, b) transform the observed HR diagram to a theoretical one (Flower 1977) in order to determine the state of evolution of the cluster (Maeder & Meynet 1988). The published (GS92) distances for these associations are 2.3 kpc for Per OB1 and 2.4 kpc for Cas OB6. Given that the stars in Cas OB6 clearly lie in front of the associated molecular gas, and assuming the gas is of comparable depth to the width of the largest complexes, $\sim 100-200$ pc, then a resonable mean distance for the Perseus CO emission is ~ 2500 pc. Examining the fit of the standard main sequence to the data for Per OB1 and Cas OB6 (Figure 1 in GS92) it appears that an uncertainty of $\sim 0\overset{m}{.}2$ in the fit is not unreasonable, which translates into $\sim \pm 200$ pc in the distance determination. Hence, a good estimate of the distance to the Perseus CO emission is 2500 ± 200 pc.

Additional information which may be gleaned from the GS92 survey includes statistics on physical parameters of the two associations which can aid in discriminating between the Perseus arm stars and foreground, Cam OB1 stars. The two parameters which are of relevance to this work are the distance derived from the

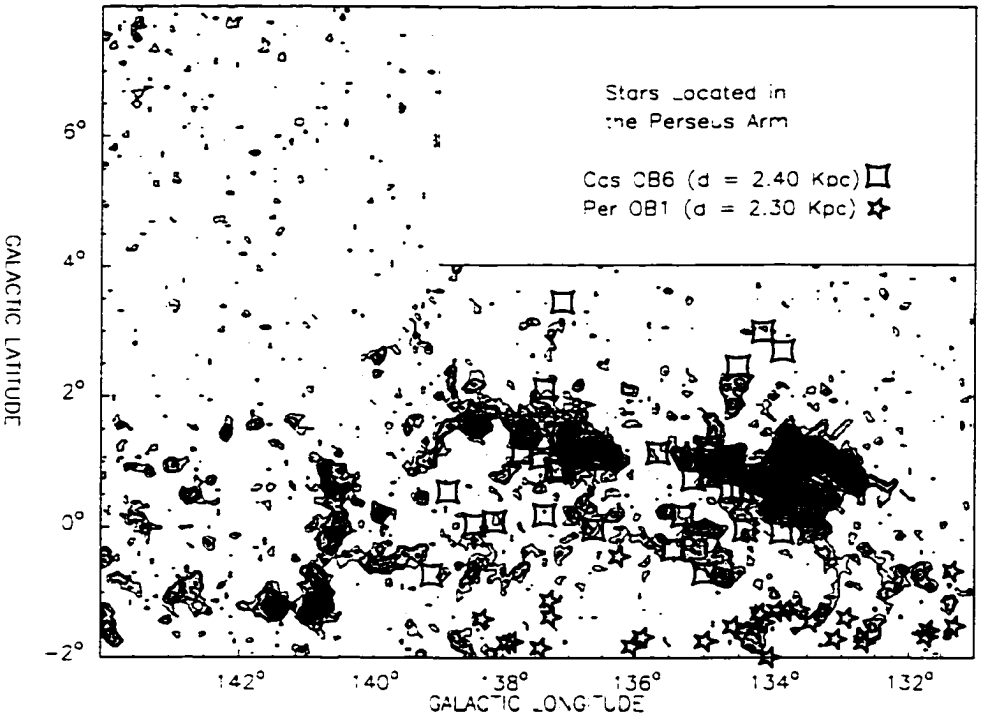

Figure 4.3 Location of stars in Cas OB6 and Per OB1, as listed by GS92, in the Perseus arm ($-30 \geq v_{LSR}/kms^{-1} \geq -70$). The distance to the associations (and associated molecular gas) has been determined by cluster main sequence fitting to the B stars in the associations. The spatial positions for the stars have been taken from Humphreys (1978).

distance modulus relationship and the measured stellar radial velocity.

The distance modulus relationship is given by

$$m_V - M_V = 2.5\ log\ (d) - 5 + A_V, \tag{4.1}$$

where m_V and M_V are the apparent and absolute V magnitudes of the star, respectively, d is the distance in pc, and A_V is the extinction of the star light in the V band due to intervening material (primarily dust); formally, A_V is given by

$$A_v = R\ [(B-V)_{\text{Observed}} - (B-V)_o]. \tag{4.2}$$

where $(B-V)_{\text{Observed}}$ and $(B-V)_o$ refer to the observed and intrinsic color, respectively, for the star. In Appendix B, the distance to the Perseus stars using Eq. 4.1 is given as Dist 1 and has been derived using the intrinsic colors and absolute magnitude-color relationship due to Schmidt-Kaler (1982) as found in Lang (1992),

with $R = 3.1$ (Fitzpatrick & Garmany 1990). These relationships are for stars which are very young, i.e., they have just arrived on the zero-age main sequence (ZAMS). GS92 chose the intrinsic colors as listed in FitzGerald (1970) and absolute magnitude-color relationship given by Blaauw (1963) and Mermilliod (1981), with $R = 3.0$. The very close agreement between the values of Dist 1, on average (see Appendix B), and the claimed distances for the associations suggests that: a) Dist 1 is a reasonable first guess for the distance to the stars in the associations, and b) the stars in the associations are relatively young.

From an inspection of the distribution of the radial velocities for Per OB1 and Cas OB6 (see Appendix B - there are very few B main sequence stars in GS92 from which to derive any meaningful statistics), the dispersion in the mean radial velocity appears to be quite large in the case of Cas OB6 (somewhere between 11 and 14 km s^{-1}), but much less for Per OB1 (less than 2 km s^{-1}). The best estimate for the mean velocity of both associations, derived from all of the stellar radial velocities, suggests that Perseus stars should, on average, have a velocity of ~ -43 km s^{-1}.

As a final note regarding radial velocities for the Perseus stars, it has already been pointed out that the Perseus arm is known to be undergoing a streaming motion (Roberts 1972) which will lead to a peculiar distance/radial velocity relationship, i.e., rotation curve, for the molecular gas. The most recent estimate of this relationship was carried out by Brand & Blitz (1993) who considered HII regions throughout the Galaxy. They obtained the following value for Oort's constant A:

$$A = \frac{v_{LSR}}{d\ sin(2l)cos^2(b)} = 12.6 \text{ km s}^{-1} \text{ kpc}^{-1}. \qquad (4.3)$$

where d is measured in kpc, and l and b are the Galactic longitude and latitude, respectively. Using this average value for A, the molecular gas in Perseus (with a $v_{LSR} = -43$km s^{-1} at $l = 138°, b = +2°$) would be placed at a distance of ~ 3.4 kpc. This is significantly further away than the distance derived assuming the gas is associated with Per OB1 and Cas OB6.

4.2.3 The Distance to the Cam OB1 Emission

Determination of the distance to the Cam OB1 molecular emission follows the same algorithm as that for the Perseus emission as outlined in GS92, i.e., by main sequence fitting to B stars associated with it. An overview of the main sequence fitting method to obtain the distance to the Cam OB1 stars is as follows:

1. Select all B main sequence stars in SIMBAD which have good UBV measurements and fall within the survey boundaries (40 in total).
2. Eliminate those stars from Step 1 which are listed as being in Perseus in GS92 (18 stars).
3. Eliminate those stars from Step 1 known to be in the Perseus arm from SIMBAD (3 stars, from Haug 1970).
4. Tabulate the data for those stars which survive Steps 2 and 3 (19 stars, Table 4.3) and plot an observational HR diagram (Figure 4.4) of them.
5. Determine the best fit to an empirical main sequence. An initial guess of M_V for the candidate stars is made from Eq. 4.1 assuming some initial distance (DIST 1 was useful here and suggested that 1000 pc was a good initial guess). An observed main sequence will lie below this empirical main sequence if the initial guess for the distance is too high and above it if too low. From the offset between the estimated solution and the empirical solution, determine the correction necessary to the distance to bring the estimated solution into agreement with the empirical fit and update the value of the distance. In the fitting procedure, give the most weight to those stars already listed in SIMBAD as being members of Cam OB1 and the least to those which are known to be variable. Include emission line stars in this procedure as their relatively narrow emission lines should not have adversely affected the broad-band UBV photometry (Jaschek & Jaschek 1987).
6. Estimate the uncertainty in the main sequence fit from the range with which it is possible to slide the empirical main sequence above and below the best fitting solution and still obtain a reasonably good fit to the data.

Details of how the stars are placed on the observer's HR diagram are the same as followed in GS92. These are:

1. Determine the reddening free parameter (the abscissa), Johnson's Q (Johnson 1958, Sharpless 1962), which is a measure of the star's color after taking into account the effects of differential reddening. The Q value, for B-type main

sequence stars is defined as:

$$Q = (U - B)_{\text{Observed}} - \frac{E_u}{E_y} (B - V)_{\text{Observed}}. \tag{4.4}$$

where (for main sequence stars up to spectral type A0)

$$\frac{E_u}{E_y} = 0.72 + 0.05\ E_y. \tag{4.5}$$

and

$$E_y = (B - V)_{\text{Observed}} - (B - V)_o. \tag{4.6}$$

In keeping with GS92, the $(B - V)_o$ value is taken from the interpolated values of FitzGerald (1970). For main sequence stars of spectral type B0 to B8, inclusive, the intrinsic color is given as:

$$(B - V)_o = -0.318 + 0.017\ x. \tag{4.7a}$$

where x is the numerical increment for the spectral type, i.e. B0 = 1, B0.5 = 2, etc. For main sequence stars from B8 to A4, inclusive, the intrinsic color is given by:

$$(B - V)_o = -0.138 + 0.032\ y. \tag{4.7b}$$

where y is now incremented such that B8 = 1, B9 = 2, etc. Note: For B8 stars the mean of the two solutions from Eq. 4.7a and 4.7b was used.

2. The ordinate for the observer's HR diagram is the stellar absolute magnitude, M_V. The empirical main sequence, given by Blaauw (1963) for stars earlier than B1.5 and by Mermilliod (1981) for stars later than B1.5, can be placed on this immediately.

From the fit of the Cam OB1 B main sequence stars to the empirical main sequence (Figure 4.4), it is a reasonable estimate that the distance to the association is 975 pc. The uncertainty in the fit, as fitted by hand, is $\sim \pm 0\overset{m}{.}2$ which translates into an uncertainty of ± 90 pc. This uncertainty is representative of the uncertainty in the fit to the main sequence for the association. The uncertainty for an individual stellar measurement can be considerably more than this; any given UBV measurement has a typical uncertainty of $\pm 0\overset{m}{.}01 - 0\overset{m}{.}02$ (Ochsenbein 1974) while the uncertainty in $(B-V)$ due to the uncertainty in spectral type (one sub-division) is $\pm 0\overset{m}{.}02$ and for the uncertainty in luminosity class (say between class V and III)

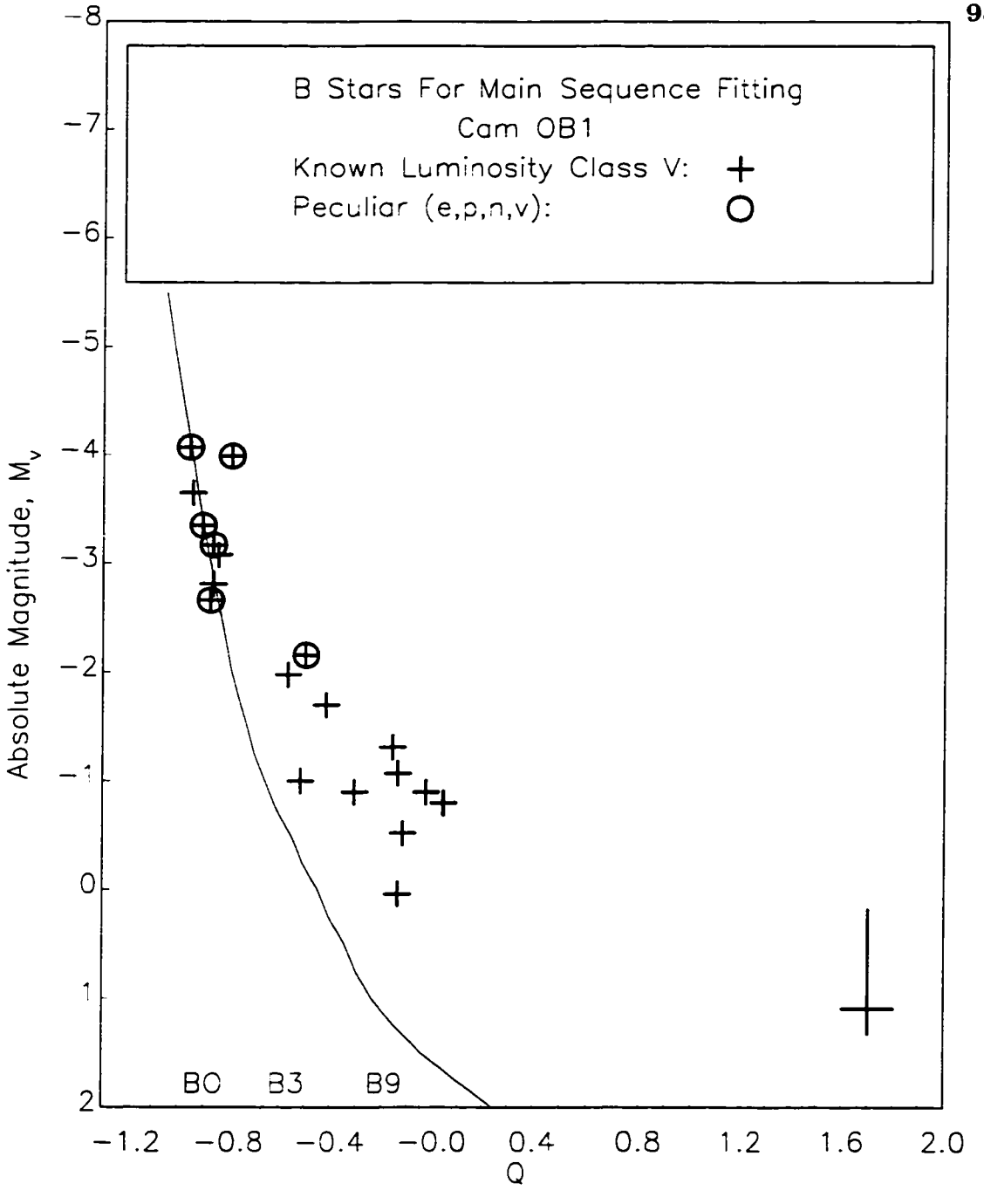

Figure 4.4 Overlay of B main sequence stars - normal B stars indicated by crosses and peculiar B stars by crosses overlaid with a circle - against empirical main sequence - solid line (Blaauw 1963, Mermilliod 1981). There is excellent agreement between the two for an assumed distance of 975 pc. The large cross indicates the maximum possible uncertainty of an individual measurement due to incorrect labelling, etc., but the reasonably good fit to the the data argues against such large uncertainties for any of the data included in this study.

Table 4.3: Data for B Stars, Main Sequence Fitting

No.	Name[a]	l^b [deg.]	b^b [deg.]	MK Des.[c]	U[d] [mag]	B[d] [mag]	V[d] [mag]	$v_{r,LSR}^e$ [km s^{-1}]	Dist [f] [kpc]	$(U-B)_o^g$ [mag]	$(B-V)_o^g$ [mag]	Q^h [mag]	M_V^i [mag]
1	BD+61 382	131.90	+0.26	B1:V:	11.39	11.53	10.70		1.26	0.95	0.27	0.88	2.66
2	BD+60 503	134.92	+0.46	B1.5V	10.31	10.61	9.95		0.97	0.88	0.25	0.87	2.81
3	LS I +59 136	135.20	0.42	B0.5V	11.66	11.60	10.52		0.96	1.02	0.29	0.95	3.65
4	BD+58 488	135.70	0.78	B0.5V	10.27	10.53	9.85		1.24	1.02	0.29	0.85	3.08
5	HD 17114	137.26	0.32	B1Vvar	9.21	9.66	9.16	+51.0	0.99	0.95	0.27	0.87	3.17
6	HD 237015	137.38	+0.97	B6V	9.45	9.68	9.44	15.0 D	0.67	0.50	0.15	0.42	1.70
7	BD+61 506	137.47	+2.45	B9V	10.36	10.35	10.18	+0.0	0.70	0.18	0.07	0.12	0.52
8	BD+61 529	138.48	+3.34	B3V	9.53	9.85	9.54	17.0	0.81	0.67	0.20	0.57	1.98
9	BD+61 534	138.87	+3.15	B8V	9.59	9.63	9.47	3.0	0.60	0.35	0.11	0.16	1.31
10	BSD 9-1102	139.13	+2.80	B9.5V	12.13	11.92	11.48		0.82	0.10	0.04	0.14	0.04
11	BD+61 549	139.33	+3.84	B5V	10.12	10.12	9.94	26.0	1.03	0.56	0.16	0.14	1.07
12	BD+60 648	139.59	+2.69	B5V	10.00	10.35	10.13		1.06	0.56	0.16	0.52	1.00
13	HD 21806	139.76	+6.48	B1Vn...	7.51	8.06	7.75	22.0 D	0.68	0.95	0.27	0.80	3.99
14	BS D9-1315	139.97	+3.47	B9V	10.33	10.15	9.96	6.0	0.61	0.18	0.07	0.04	0.80
15	HD 237091	140.06	+1.92	B1:V:mpe	8.93	9.34	8.70	+7.6 E	0.66	0.95	0.27	0.96	4.07
16	HD 20761	140.12	+3.78	B9V	9.97	9.89	9.74	+19.0	0.59	0.18	0.07	0.03	0.90
17	BD+59 624	140.21	+2.07	B5V	10.76	10.82	10.51		1.11	0.56	0.16	0.31	0.90
18	HD 237134	140.91	+2.86	B5Ve	9.65	9.84	9.46		0.62	0.56	0.16	0.50	2.16
19	HD 237121	141.21	+1.39	B0.5Vs	8.88	9.40	8.93	12.0 C	1.10	1.02	0.29	0.91	3.35

a. Catalog designation of star as given by, in order of preference, its HR, BD, LS I, BSD or UBV entry.

b. Galactic co-ordinates (l^{II}, b^{II}) of star.

c. MK classification of star as listed in GS92.

d. UBV photometric indices.

e. Radial velocity of star corrected to Local Standard of Rest assuming standard solar motion. The letter index, when listed in SIMBAD, gives the quality of the spectra: A - excellent to E - poor.

f. Distance from $m_v - M_v = 5\,log(d) - 5 + A_v$, assuming the intrinsic colors and abolute magnitude-color relationship of Schmidt-Kaler (1982) as given in Lang (1992), and R = 3.1 (Fitzpatrick & Garmany 1990).

g. Intrinsic colors interpolated from FitzGerald (1970).

h. Q parameter as derived from Eq. 4.4.

i. Absolute magnitude of star from Eq. 4.1, given distance from main sequence fitting.

is $\pm 0^{m}.02$ (FitzGerald 1970). These uncertainties would be the extreme case if the data were of very poor quality. The reasonably good agreement between the empirical main sequence and the main sequence B stars for Cam OB1 shown in Figure 4.4 argues against such an event. However, for completeness, the uncertainty in Q, assuming the maximum predicted uncertainty from Eq. 4.4 ($\pm 0^{m}.11$), and the uncertainty in M_V, assuming it is only affected by evolutionary effects (brightening by $\sim 0^{m}.50$, Maeder & Meynet 1988) or misidentification ($\sim -1^{m}.00$ for class V stars misidentified as class III, Lang 1992), is also shown in Figure 4.4 by the cross in the lower right hand corner. From Figure 4.4 it is reasonable to conclude that the distance to the Cam OB1 stars is 975 ± 90 pc.

4.3.1 The Observer's HR Diagram for Cam OB1

Constructing the observer's HR diagram for the Cam OB1 stars employs basically the same method as used in the distance determination in the previous section. There is only one slight modification: now the definition of Q must be generalized to include stars other than main sequence stars. The steps for completing the observational HR diagram are:

1. Select all stars in SIMBAD which have good UBV measurements and fall within the survey boundaries (214 in total).
2. Reject those stars already identified as being Perseus stars in GS92 (68 stars in GS92 in total), or identified as Perseus stars in SIMBAD (27 stars, these are included in Appendix B).

Using the above algorithm there were 119 stars which survived the selection process, including the 19 B main sequence stars identified in the previous section, which are probably part of the Cam OB1 association. Completing the placement of these candidate stars on the observer's HR diagram required the following steps:

1. Stars without a luminosity class identification are assumed to be class V (the most probable assignment).
2. In the case of non-main sequence stars, use the more general definition of the Q parameter given by:

$$Q = (U-B)_{\text{Observed}} - \frac{(U-B)_{\text{Observed}} - (U-B)_o}{(B-V)_{\text{Observed}} - (B-V)_o} \times (B-V)_{\text{Observed}}. \quad (4.8)$$

For these stars, the intrinsic colors were taken from Fitzpatrick & Garmany (1990) for luminosity classes Ia, Iab (by interpolation) and Ib and spectral type

earlier than G0, as well as the luminosity class II stars earlier than spectral type A0. For luminosity class II stars of spectral type A0 and later, and for luminosity classes III and IV, the intrinsic colors were taken from FitzGerald (1970). Determination of the $(U-B)_o$ color for many of these classes of stars was determined from a hand-fit spline through the values of FitzGerald (1970).

After the first pass through the data it was found that 17 stars lay well below the main sequence for Cam OB1. It was assumed these stars are not members of Cam OB1, and they have been removed from the data set for any further analysis (they are included in Appendix B). Table 4.4 presents a summary of the stellar data for those stars which have been selected as members of Cam OB1. Figure 4.5 is the observer's HR diagram for this data.

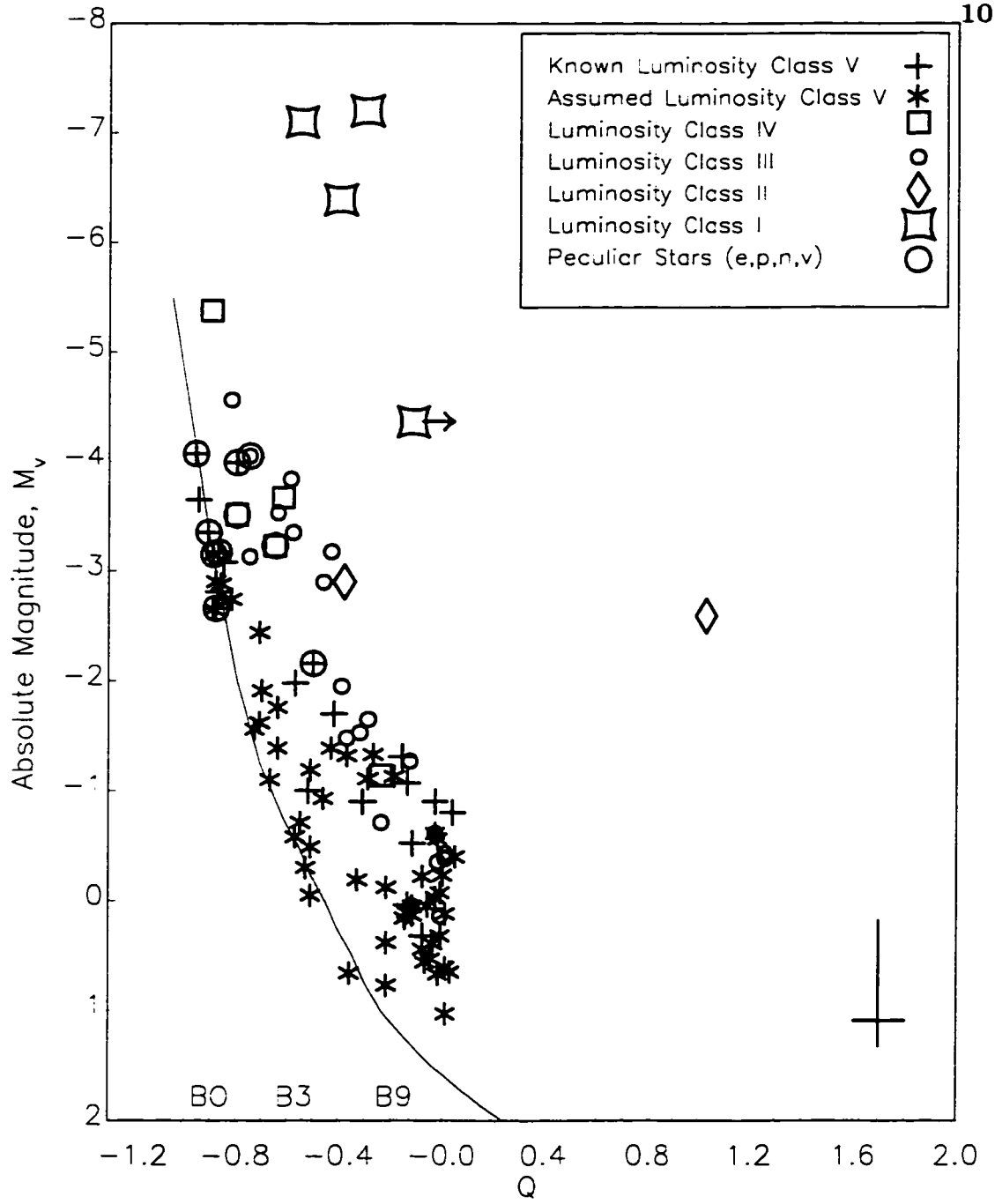

Figure 4.5 Observer's HR diagram of Cam OB1. There is clear evidence for evolution along the entire length of the main sequence sampled. The main sequence turnoff occurs at approximately B0. One star (HD 13686) is a K3Ib star with Q value too blue for its spectral type (as indicated by the arrow). This is probably due to the fact the $(U - B)_o$ color changes very rapidly at this spectral type for Ib supergiants (FitzGerald 1970) and a small error in the U or B photometry could easily produce a large shift in Q. The excellent agreement with the empirical main sequence over the entire range of Q sampled also strongly supports the distance determination of 975 pc. As for Figure 4.4, the maximum possible uncertainty for an individual stellar measurement is indicated by cross in the lower right hand corner.

Table 4.4: Data for Cam OB1 Population I Objects

No.	Name[a]	l^b [deg.]	b^b [deg.]	MK Des.[c]	U^d [mag]	B^d [mag]	V^d [mag]	$v^i_{r:n}$ [km s^{-1}]	Dist [pc]	l^j [kpc]	$(U-B)^g_o$ [mag]	$(B-V)^g_o$ [mag]	Q^h [mag]	M^i_V [mag]	log T^j_{eff}	M^k_{bol} [mag]	t_m/t^l_{pm} [10^6 yr]	Comments
1	BD+61 382	131.90	+0.26	B1:V:	11.39	11.53	10.70		1.26	0.95	0.27	0.88	2.66	4.48		5.70	8 /	
2	HD 13686	132.28	+1.91	K3Ib	10.96	8.88	7.01	+3.0 D	1.02	1.54	1.41	0.12?	4.36	3.61		5.03	29 /	
3	BD+60 503	134.92	+0.46	B1.5V	10.31	10.61	9.95		0.97	0.88	0.25	0.87	2.81	4.47		5.79	8 /	
4	HD 15000	134.99	1.50	F5II	7.85	7.82	7.42	12.7 C	0.76	0.08	0.38	1.03	2.59	3.82		2.52	100/	
5	LS I +59 136	135.20	0.42	B0.5V	11.66	11.60	10.52		0.96	1.02	0.29	0.95	3.65	4.53		6.98	3 /	
6	BD+58 488	135.70	0.78	B0.5V	10.27	10.53	9.85		1.24	1.02	0.29	0.85	3.08	4.45		5.95	8 /	
7	HD 17114	137.26	0.32	B1Vvar	9.21	9.66	9.16	+51.0	0.99	0.95	0.27	0.87	3.17	4.47		6.15	7 /	Variable
8	HD 237015	137.38	+0.97	B6V	9.45	9.68	9.44	15.0 D	0.67	0.50	0.15	0.42	1.70	4.14		2.78	98 /	
9	BD+61 506	137.47	+2.45	B9V	10.36	10.35	10.18	+0.0	0.70	0.18	0.07	0.12	0.52	3.92		0.54	/1	
10	BSD 9-1528	137.84	+2.99	B6	11.37	11.44	10.96		0.96	0.15	0.14	0.46	0.93	4.17		2.18	100/1	
11	BSD 9-1541	138.04	+2.95	A0	11.82	11.53	11.12		0.67	0.04	0.02	0.03	0.03	3.85		0.02	/1	
12	BSD 9-1606	138.17	+3.40	B5	11.30	11.28	10.74		0.89	0.56	0.16	0.43	1.39	4.15		2.53	100/1	
13	BSD 9-1637	138.38	+3.37	B8	11.41	11.39	11.09		1.03	0.19	0.11	0.22	0.12	3.99		0.34	300/2	
14	BD+61 533	138.38	+3.95	B8	8.93	9.25	9.18		0.59	0.37	0.11	0.37	1.32	4.10		2.17	170/1	
15	BD+61 529	138.48	+3.34	B3V	9.53	9.85	9.54	17.0	0.81	0.67	0.20	0.57	1.98	4.25		3.70	75 /	
16	BD+61 530	138.64	+3.09	B9	10.76	11.06	10.77		0.77	0.18	0.07	0.53	0.30	4.22		1.84	87 /3	
17	BD+61 534	138.87	+3.15	B8V	9.59	9.63	9.47	3.0	0.60	0.35	0.11	0.16	1.31	3.95		0.25	500/2	
18	BD+60 635	138.91	+2.96	B7III	9.66	9.73	9.50	36.0	0.96	0.45	0.12	0.32	1.53	4.08		2.13	174/1	
19	BSD 9-1042	139.07	+2.28	A0III	11.52	11.29	10.90		0.83	0.04	0.03	0.02	0.35	3.99		0.57	400/2	
20	BSD 9- 448	139.10	+1.84	B8	12.44	12.12	11.40		0.65	0.17	0.11	0.29	1.11	4.04		1.61	/1	
21	BSD 9-1102	139.13	+2.80	B9.5V	12.13	11.92	11.48		0.82	0.10	0.04	0.14	0.04	3.93		0.00	500/2	
22	BD+60 645	139.14	+3.23	B8III	9.86	9.88	9.57		0.78	0.38	0.10	0.29	1.65	4.08		2.25	174/1	
23	BD+60 646	139.19	+3.19	B6III	9.88	10.05	9.77		1.14	0.47	0.14	0.37	1.48	4.13		2.58	99 /	
24	BD+61 557	139.20	+4.40	B8	9.21	9.40	9.29		0.59	0.27	0.11	0.27	1.33	4.03		1.69	200/1	
25	BSD 9-1134	139.28	+2.87	B9III	11.30	11.19	10.96		1.33	0.20	0.08	0.12	0.05	4.02		0.25	450/3	
26	BSD 9-1814	139.28	+4.02	B9	11.01	10.80	10.51		0.69	0.18	0.07	0.02	0.56	3.85		0.56	/1	
27	BSD 9-1137	139.32	+2.82	A0	12.77	12.47	12.09		1.10	0.04	0.02	0.01	1.03	3.83		1.03	/3	
28	BD+61 549	139.33	+3.84	B5V	10.12	10.12	9.94	26.0	1.03	0.56	0.16	0.14	1.07	3.93		1.11	/1	
29	BD+59 604	139.40	+2.27	B9III	10.40	10.24	9.92	+10.0	0.72	0.20	0.08	0.13	1.27	4.01		1.55	200/1	
30	BSD 9- 453	139.41	+1.38	B9	12.57	12.23	11.74		0.91	0.18	0.07	0.06	0.05	3.88		0.05	/1	

Table 4.4 cont.: Data for Cam OB1 Population I Objects

No.	Name[a]	l^b [deg.]	b^b [deg.]	MK Des.[c]	U^d [mag]	B^d [mag]	V^d [mag]	$v^e_{r,sp}$ [km s^{-1}]	Dist [f] [kpc]	$(U-B)^g_o$ [mag]	$(B-V)^g_o$ [mag]	Q^h [mag]	M^i_V [mag]	log T^j_{eff}	M^k_{bol} [mag]	t_m/t^l_{pm} [10^6 yr]	Comments
31	BSD 9-1155	139.42+2.84		A2III	11.34	11.08	10.77		0.86	0.07	0.09	0.01	0.14	3.99	0.09	400/2	
32	HD 19968	139.46+2.97		B5III	7.25	7.64	7.55	7.0 C	0.76	0.51	0.16	0.43	3.17	4.16	-4.37	47 /	
33	BD+61 554	139.46+3.92		B8	9.65	9.73	9.59	3.0	0.65	0.18	0.11	0.19	1.13	3.97	1.25	/1	
34	BSD 9-1856	139.48+4.31		B5	13.02	12.91	12.19		1.34	0.56	0.16	0.51	0.49	4.21	1.99	50 /3	
35	BSD 9-1174	139.49+2.92		B9	11.82	11.57	11.26		0.94	0.18	0.07	0.01	0.12	3.83	0.12	/1	
36	BD+60 655	139.51+3.20		B8IV	10.49	10.26	9.98	29.0	0.78	0.41	0.10	0.24	1.14	4.01	1.39	250/1	
37	BD+59 603	139.52+2.02		A0III	10.72	10.66	10.36		0.74	0.04	0.03	0.03	0.61	3.99	0.83	500/2	
38	BD+61 552	139.56+3.55		B6	10.46	10.68	10.32		0.85	0.15	0.15	0.51	1.19	4.21	2.65	30 /2	
39	BSD 9-1161	139.58+2.57		B2	11.02	11.17	10.34		0.78	0.81	0.23	0.88	2.90	4.48	5.95	8 /	
40	BD+60 648	139.59+2.69		B5V	10.00	10.35	10.13		1.06	0.56	0.16	0.52	1.00	4.21	2.48	100/	S202
41	BSD 9- 535	139.61+2.14		A0V	11.53	11.39	11.10		0.79	0.04	0.02	0.08	0.32	3.89	0.32	/1	
42	BSD 9-1829	139.63+3.63		B9	11.50	11.43	11.23		1.09	0.18	0.07	0.08	0.44	3.89	0.44	/1	
43	BD+61 566	139.64+4.40		B5	9.75	10.14	9.75		0.70	0.56	0.16	0.70	1.91	4.34	4.13	16 /	
44	BSD 9-1842	139.72+3.71		A0	11.70	11.47	11.16		0.79	0.04	0.02	0.01	0.32	3.84	0.32	/1	
45	BSD 9-1891	139.72+4.42		A0	12.32	12.01	11.65		0.92	0.04	0.02	0.03	0.65	3.81	0.65	/1	
46	HD 19441	139.73+1.26		B3III	7.90	8.24	7.87	30.0 C	0.66	0.72	0.20	0.59	3.84	4.30	5.68	25 /	S202
47	UBV 3031	139.73+1.41		B9	12.84	12.42	11.82		0.80	0.18	0.07	0.08	0.22	3.89	0.22	/1	
48	BSD 9-1904	139.75+4.52		B9	11.07	10.93	10.73		0.86	0.18	0.07	0.01	0.07	3.84	0.07	/1	
49	HD 21806	139.76+6.48		B1Vn...	7.51	8.06	7.75	22.0 D	0.68	0.95	0.27	0.80	3.99	4.42	6.69	8 /	
50	BSD 9-1840	139.78+3.57		B9	11.29	11.01	10.71		0.74	0.18	0.07	0.05	0.40	3.80	0.40	/1	
51	BD+59 613	139.90+2.19		A1III	11.05	10.83	10.52		0.76	0.01	0.00	0.01	0.39	3.99	0.61	500/2	
52	BSD 9-1262	139.96+2.91		A0	12.01	11.76	11.45		0.92	0.04	0.02	0.01	0.61	3.83	0.61	/1	
53	BSD 9-1315	139.97+3.47		B9V	10.33	10.15	9.96	6.0	0.61	0.18	0.07	0.04	0.80	3.80	0.80	/1	
54	BSD 9-1289	140.04+3.02		B7	11.63	11.81	11.38		1.11	0.13	0.13	0.53	0.30	4.22	1.85	50 /3	
55	HD 237090	140.05+1.91		B0.5IV:nnvar	9.15	9.55	9.01	6.0	1.39	1.02	0.29	0.80	3.51	4.42	7.16	12 /	S202, Variable
56	HD 237091	140.06+1.92		B1:V:nnpe	8.93	9.34	8.70	+7.6 E	0.66	0.95	0.27	0.96	4.07	4.5	7.47	4 /	S202, Be star
57	BSD 9- 645	140.08+2.44		A0	12.62	12.33	11.87		0.88	0.04	0.02	0.07	0.56	3.88	0.56	700/2	
58	BSD 9-1279	140.09+2.84		A0	12.48	12.16	11.70		0.82	0.04	0.02	0.04	0.39	3.86	0.39	/1	
59	HD 20798	140.11+3.87		B2III-IV	8.06	8.63	8.37	2.0 C	1.39	0.92	0.24	0.75	3.13	4.40	5.60	25 /	Cam R1, DG13
60	HD 19820	140.12+1.54		O9IV	7.10	7.62	7.11	4.2 A	0.90	1.13	0.31	0.90	5.38	4.49	8.50	7 /	S202,Algol type

Table 4.4 cont.: Data for Cam OB1 Population I Objects

No.	Name[a]	l^b [deg.]	b^b [deg.]	MK Des.[c]	U^d [mag]	B^d [mag]	V^d [mag]	$v^e_{r,\odot}$ [km s^{-1}]	Dist [f] [kpc]	$(U-B)^g_o$ [mag]	$(B-V)^g_o$ [mag]	Q^h [mag]	M^i_V [mag]	log T^j_{eff}	M^k_{bol} [mag]	t_m/t^l_{pm} [10^6 yr]	Comments
61	HD 20761	140.12+3.78		B9V	9.97	9.89	9.74	+19.0	0.59	0.18	0.07	0.03	0.90	3.85	0.90	/1	
62	HD 20134	140.16+2.16		B2.5IV-V	7.01	7.53	7.39	12.5 C	0.64	0.77	0.22	0.62	3.67	4.29	5.59	25 /	S202, Be star
63	BSD 9-1309	140.17+3.02		A0	12.00	11.79	11.35		0.72	0.04	0.02	0.14	0.11	3.93	0.07	500/2	
64	BSD 9-1286	140.19+2.76		B9	12.59	12.11	11.49		0.67	0.18	0.07	0.03	0.61	3.85	0.61	/1	
65	BD+59 624	140.21+2.07		B5V	10.76	10.82	10.51		1.11	0.56	0.16	0.31	0.90	4.06	1.40	150/2	
66	BSD 9- 600	140.22+1.82		A0	13.31	12.84	12.13		0.70	0.04	0.02	0.12	0.05	3.92	0.02	/1	
67	BSD 9- 614	140.24+1.87		A0	13.19	13.11	12.36		0.73	0.04	0.02	0.15	0.16	3.94	0.16	500/3	
68	BSD 9- 638	140.25+2.04		A0III	11.49	11.18	10.81		0.82	0.04	0.03	0.01	0.38	3.99	0.60	500/2	
69	BSD 9-1320	140.28+3.06		A0	13.88	13.61	12.86		0.92	0.04	0.02	0.36	0.66	4.10	0.39	200/3	
70	BSD 9- 660	140.29+2.22		A1III	11.43	11.11	10.72		0.74	0.01	0.00	0.01	0.43	3.99	0.66	500/2	
71	BD+58 574	140.32+0.94		B1	10.36	10.71	10.08	9.0 E	1.26	0.95	0.27	0.89	2.65	4.48	5.85	8 /	S202
72	BSD 9- 692	140.35+2.60		B9	11.50	11.41	11.14		0.94	0.18	0.07	0.12	0.13	3.92	0.09	700/2	
73	BSD 9-1377	140.44+3.66		B9	12.05	11.71	11.28		0.80	0.18	0.07	0.00	0.23	3.83	0.23	/1	
74	BSD 9-1366	140.49+3.39		A0	12.83	12.48	12.01		0.93	0.04	0.02	0.02	0.67	3.85	0.67	/1	
75	HD 20295	140.58+1.91		B5III	8.22	8.61	8.35	32.0 D	0.86	0.51	0.16	0.46	2.90	4.19	4.20	47 /	
76	HD 20508	140.60+2.39		B1.5IVvar	8.05	8.47	8.23	28.0 C	0.88	0.88	0.25	0.65	3.23	4.31	5.23	28 /	S202, Variable
77	BSD 9-1336	140.61+2.77		A0	13.04	12.76	12.15		0.81	0.04	0.02	0.22	0.38	3.99	0.15	500/3	
78	BSD 9- 156	140.75+1.50		B6	11.34	11.55	11.00		0.88	0.50	0.15	0.67	1.10	4.32	3.15	22 /	
79	HD 20898	140.80+3.06		B2IIIvar	7.97	8.40	7.97	2.0 D	0.91	0.92	0.24	0.75	4.05	4.37	6.27	17 /	S202, Variable
80	LS I +58 119	140.86+1.48		B5	10.72	11.02	10.50		0.82	0.56	0.16	0.73	1.56	4.37	3.98	15 /	S202
81	BSD 9- 780	140.86+2.87		A0	12.62	12.49	12.04		0.97	0.04	0.02	0.22	0.77	3.99	0.55	500/3	
82	BSD 9-1390	140.86+3.15		A0	13.26	12.83	12.24		0.87	0.04	0.02	0.05	0.53	3.87	0.53	/1	
83	HD 237134	140.91+2.86		B5Ve	9.65	9.84	9.46		0.62	0.56	0.16	0.50	2.16	4.20	3.58	60 /	Be star
84	BSD 9- 786	140.97+2.69		B8	11.73	11.93	11.54		0.86	0.47	0.11	0.51	0.06	4.21	1.41	3 /3	
85	BSD 9- 796	141.04+2.71		B6	11.46	11.66	11.21		1.12	0.50	0.14	0.57	0.58	4.25	2.28	50 /1	
86	HD 20547	141.09+1.68		B3III	8.07	8.55	8.18	15.0 D	0.76	0.72	0.20	0.64	3.53	4.30	5.33	25 /	S202, Binary
87	HD 237121	141.21+1.39		B0.5Vs	8.88	9.40	8.93	12.0 C	1.10	1.02	0.29	0.91	3.35	4.50	6.50	8 /	S202
88	BSD 9- 800	141.23+2.46		B8	11.88	11.86	11.43		0.77	0.28	0.11	0.33	0.19	4.07	0.86	100/2	
89	BSD 9- 778	141.31+2.05		B6	10.90	11.16	10.80		1.06	0.50	0.15	0.55	0.71	4.24	2.31	30 /1	
90	HD 20959	141.44+2.23		B3III	7.88	8.28	8.02	18.0 C	0.82	0.72	0.20	0.58	3.35	4.26	5.90	17 /	S202

Table 4.4 cont.: Data for Cam OB1 Population I Objects

No.	Name[a]	l^b [deg.]	b^b [deg.]	MK Des.[c]	U^d [mag]	B^d [mag]	V^d [mag]	$v_{r\pm n}^e$ [km s^{-1}]	Dist [f] [kpc]	$(U-B)_o^g$ [mag]	$(B-V)_o^g$ [mag]	Q^h [mag]	M_V^i [mag]	log T_{eff}^j	M_{bol}^k [mag]	t_m/t_{pm}^l [10^6 yr]	Comments
91	HD 21291	141.50	+2.23	B9Ia	4.39	4.62	4.21	6.8 B	1.02	0.57	0.03	0.55	7.10	4.01	7.48	9 /	S202,Cam R1
92	BD+61 623	141.50	+5.22	B2e	9.02	9.51	9.03		0.71	0.81	0.24	0.89	3.15	4.48	6.20	5 /	Be star
93	HD 20041	141.57	-0.41	A0Ia	6.60	6.52	5.79	11.9 B	1.37	0.39	0.01	0.40	6.39	3.99	6.71	15 /	DG12,Cam R1
94	BD+58 611	142.12	+2.52	B8II	12.04	11.51	10.49		1.06	0.46	0.09	0.38	2.90	4.06	3.50	80 /	S202
95	HD 21389	142.19	+2.06	A0Iab:	4.99	5.10	4.54	6.0 A	0.63	0.31	0.02	0.30	7.20	3.99	7.52	11 /	DG17,Cam R1
96	HD 25090	143.19	+7.34	B0.5III	7.09	7.64	7.31	3.0 C	1.08	1.05	0.29	0.82	4.56	4.43	7.36	22 /	
97	NGC 1502 49	143.61	+7.65	B3	10.99	11.22	10.72		1.06	0.67	0.20	0.64	1.39	4.30	3.39	22 /	NGC1502
98	UBV M 30866	143.64	+7.63	B3	10.69	10.99	10.49		0.96	0.67	0.20	0.71	1.62	4.35	3.86	22 /	NGC1502
99	UBV M 30864	143.66	+7.62	B1	9.85	10.23	9.66	51.0 D	1.13	0.95	0.27	0.86	2.88	4.46	5.78	8 /	NGC1502
100	BD+62 655	143.68	+7.76	B2	9.63	9.99	9.56		0.97	-0.81	0.23	0.71	2.44	4.35	4.74	15 /	NGC1502
101	BD+61 678	143.70	+7.69	B2	9.47	9.89	9.41	23.0 C	0.84	-0.81	0.24	0.82	2.74	4.43	5.54	8 /	Binary
102	AG+62 344	143.71	+7.62	B3	11.23	11.34	10.72		0.90	-0.67	-0.20	0.64	1.76	4.30	3.76	22 /	NGC1502

a. Catalog designation of star as given by, in order of preference, its HR, BD, LS I, BSD or UBV entry.

b. Galactic co-ordinates (l^{II},b^{II}) of star.

c. MK classification of star as listed in GS92.

d. UBV photometric indices.

e. Radial velocity of star corrected to Local Standard of Rest assuming standard solar motion. The letter index, when listed in SIMBAD, gives the quality of the spectra: A - excellent to E - poor.

f. Distance from $m_v - M_v = 5\ log(d) - 5 + A_v$, assuming the intrinsic clolors and abolute magnitude-color relationship of Schmidt-Kaler (1982) as given in Lang (1992), and R = 3.1 (Fitzpatrick & Garmany 1990).

g. Intrinsic colors interpolated from FitzGerald (1970).

h. Q parameter as derived from Eq. 4.4.

i. Absolute magnitude of star from Eq. 4.1, given distance from main sequence fitting.

j. T_{eff} calculated from (B - V) (Flower 1977), after conversion from Q (Johnson 1958).

k. M_{bol} obtained from M_V after application of bolometric correction, BC (Flower 1977).

l. Ages for main sequence stars, t_m, from the models of Maeder & Meynet (1988), and for pre-main sequence stars, t_pm, from Palla & Stahler (1993). Stars which have an ambiguous age determination have an entry for both t_m and t_pm.

4.3.2 The Theoretician's HR Diagram for Cam OB1

In order to estimate the state of evolution of the Cam OB1 association it is necessary to first transform the Observer's HR diagram found in §4.3.1 into a Theoretician's HR diagram, i.e., $(Q, M_V) \rightarrow (T_{\rm eff}, M_{\rm Bol})$. Once transformed into this form it is possible to estimate the ages of the stars by comparing them to standard evolutionary tracks. For main sequence stars and evolved stars the standard models of Maeder & Meynet (1988) were used, and for the pre-main sequence stars, of intermediate mass (2 $M_\odot$ - 8 $M_\odot$), the models of Palla & Stahler (1993) were used. The evolutionary tracks for lower mass stars will not be considered as there are none in the sample.

The algorithm for converting from the observer's HR diagram to the theoretician's diagram is as follows:

1. For class V through class III stars convert Q to a $(B-V)$ value using the relationship $Q = (B-V)/0.332$; for class II and class I stars this relationship does not appear to hold (Johnson 1958). In the latter case, the intrinsic $(B-V)$ colors for a given spectral type have been derived by interpolating in the tables of FitzGerald (1970).
2. Convert the de-reddened $(B-V)$ for all stars, found in step 1, to an effective temperature by means of interpolated values fit to the tables of Flower (1977).
3. Convert M_V to $M_{\rm Bol}$ using the bolometric corrections, BC ($M_{\rm Bol} = M_V + BC$), again by means of interpolated values from the tables of Flower (1977).

Figure 4.6 is a plot of this transformation and the plotted data are included in Table 4.4 (the third- and second-last columns). Analyzing Figure 4.6, in terms of stellar masses, suggests the following conclusions:

1. Stars more massive than 6 $M_\odot$
   a. The upper main sequence is very well defined with a turnoff that coincides with spectral type B0 which suggests an age somewhat less than 10^7 yr. This is in agreement with Mermilliod (1981) who derived a similar result for NGC 1502, a member cluster of Cam OB1.
   b. The position of the supergiants in the HR diagram indicates that additional star formation must have been going on in the region for at least $1 - 2 \times 10^7$ yr. Furthermore, the presence of many evolved main sequence stars and post main sequence stars in the 6 - 9 $M_\odot$ range indicate that star formation in the region can be pushed back to $\sim 5 \times 10^7$ yr. Chapter 6 deals with evidence

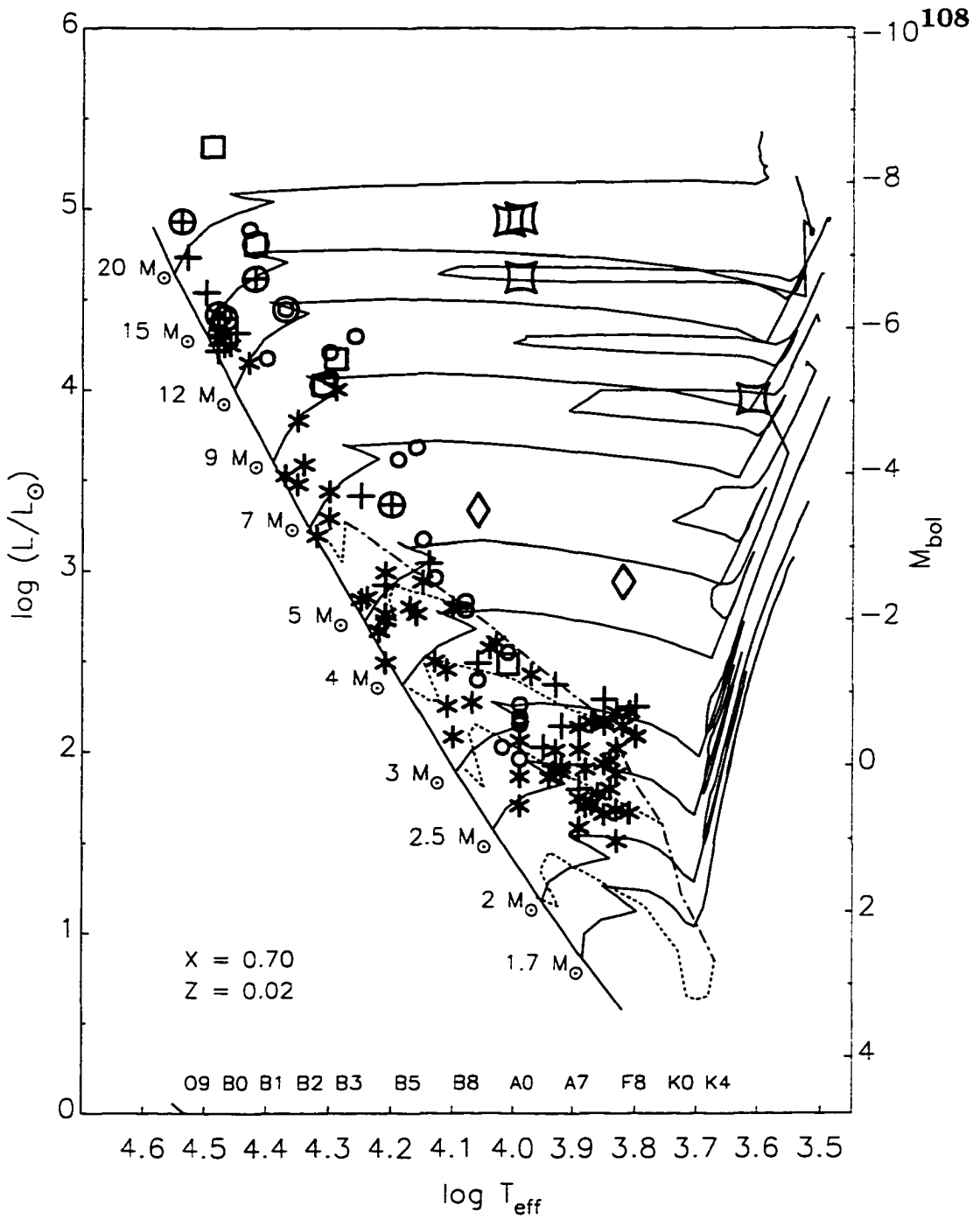

Figure 4.6 Theoretician's HR diagram of Cam OB1. The main sequence and evolved stellar tracks (solid lines) are from Maeder & Meynet (1988) while the pre-main sequence tracks (dashed lines), which represent the path of stars once they emerge from their natal cocoon and have ceased to accrete material (dash-dot line), are taken from Palla & Stahler (1993). The symbols are the same as for Figures 4.5.

supporting the physical connection between these more evolved stars with the Cam OB1 emission.

c. There does appear to be a gap in the population of main sequence stars between 9 and 12 $M_\odot$, but given the incompleteness of the survey it cannot be ruled out that these stars exist, but have been missed. It is also possible that misidentification of some stars could contribute to the presence of such a gap, e.g., HD 20798 is assumed to be a class III star to simplify its placement on the HR diagram (just below the 12 $M_\odot$ main sequence evolutionary track), while in fact it is classified as a class III-IV star. The change in BC for the very early stars differs dramatically between luminosity classes (a full magnitude for a B3 star between luminosity class III and class V - Flower 1977) and contributes to some of the scatter in Figure 4.6.

d. It should also be noted that there are no known Cepheid variables (late F- to early G-type supergiants) in the Cam OB1 region considered in the present survey nor were any identified in this work.

2. Stars between 6 $M_\odot$ and 2 $M_\odot$

a. There are 6 stars which lie to the right of the main sequence but are classified as main sequence stars. These stars fit extremely well onto the pre-main sequence evolutionary tracks of Palla & Stahler (1993). The placement of these stars in the theoretician's HR diagram cannot be explained as due to errors in either co-ordinate (the error in $\log T_{\rm eff} \sim \pm 0.05$ while the error in $M_{\rm Bol} \sim 0\overset{\rm m}{.}2 - 1\overset{\rm m}{.}0$) or the conversion to the theoretical plane or other effects such as rapid rotation (Finkenzeller & Mundt 1984) or duplicity (De Geus 1990), both of which will tend to brighten the star. Hence, these stars are almost certainly pre-main sequence stars.

b. There is a second population of stars in the theoretician's HR diagram in this mass range which have poorly determined or ambiguous ages and fit equally well onto both the pre-main sequence and main sequence evolutionary tracks. Within this group there is a group of class III stars clustered about $T_{\rm eff} = 4.0$ and fainter than $M_{\rm Bol} \sim -1^{\rm m}$. This collection of stars is present in the observer's HR diagram (Figure 4.5), but does not stand out as such a distinct feature as it does in the theoretician's diagram. Herbig (1985) has noted the presence of class III stars in the vicinity of the Trapezium Cluster (see also Finkenzeller & Mundt 1984 and Berrilli et al. 1992) which he

argues are pre-main sequence stars, rather than evolved stars, on the basis of their overabundance of Li I (6707 Å). However, it is not expected that this element will survive for an appreciable length of time (less than 10^5 yr) in the atmospheres of stars more massive than ~ 2.5 $M_\odot$ (Hillenbrand, private communication). It may be that the transformation from the observer's HR diagram to the theoretician's HR diagram has produced the clustering of these objects but they still are almost certainly pre-main sequence stars.

It is useful to plot the spatial distribution of all stars in the Cam OB1 region in order to discern any patterns in their distribution as well as to provide some clue as to the nature of the stars below 6 $M_\odot$ which have poorly determined or ambiguous ages. Figure 4.7 (upper diagram) shows a plot of the position of the stars in Cam OB1 as a function of their ages, while Figure 4.8 is a plot of the Cam OB1 stars by luminosity class. From the spatial distribution of stars shown in Figure 4.7 it would appear that, for the most part, there are stars of all age groups scattered throughout the region. The two obvious concentrations of stars in the region are NGC 1502 (upper left hand corner) and Cam R1 (boxed region). NGC 1502 has been previously discussed (Mermilliod 1981) but Cam R1 has not been discussed in any great detail.

A histogram of the age distribution of stars in Cam R1 is also provided in Figure 4.7 (lower diagram). From this distribution it would appear that the oldest stars (age IV stars) are scattered uniformly throughout Cam R1. It is also apparent that there is a concentration of younger main sequence and evolved stars (ages I - III stars) in Cam R1 S. It is interesting that the ratio of ages I, II and III stars is the same in Cam R1 S and Cam R1 N, but the total number of stars in Cam R1 S (15) and Cam R1 N (4) is prohibitively small and does not allow a statistical analysis to test this observation. If this ratio does indeed hold then it suggests that both populations come from the same parent population, but there are simply not as many stars in Cam R1 N, and that most, but not all, of the star forming activity in the Cam R1 region within the last $\sim 1 - 30 \times 10^6$ yr ago, occurred in Cam R1 S.

There is also a very interesting correlation of stars with poorly determined ages in the Cam R1 region with the other stellar populations. In Cam R1 S, the total number of such stars (14) equals the combined number of pre-main sequence stars (6) and class III stars (7) - the two dominant populations of stars with known ages. In Cam R1 N, there is a large increase in the number of stars with poorly determined

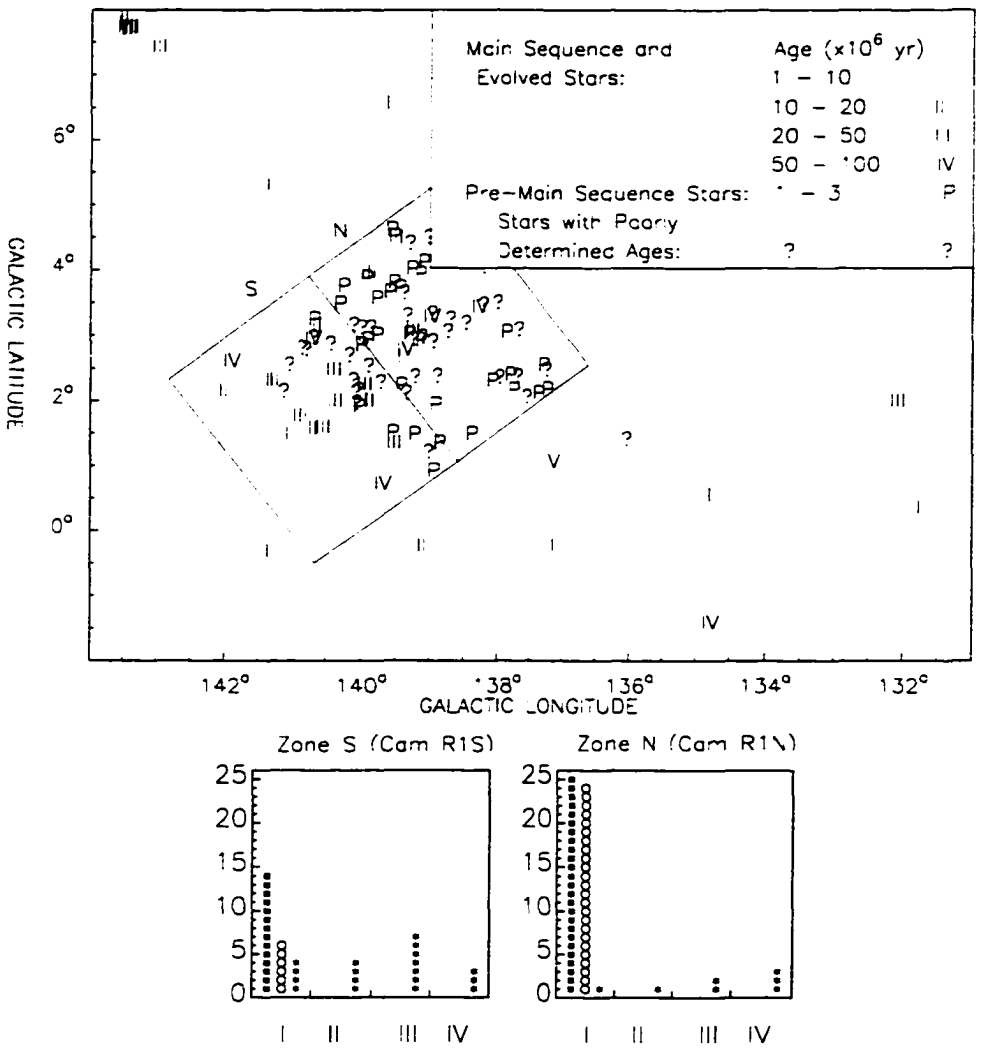

Figure 4.7 The upper diagram is the spatial distribution of stars in the Cam OB1 region by ages. The defining boundaries for Cam R1 N and Cam R1 S are illustrated in this diagram. In the lower diagram the number distribution of stars in the Cam R1 region, i.e., in the region highlighted by the rectangular grid in the upper diagram, is plotted. The symbols used in the lower diagram are:

asterisk: main sequence or evolved stars

open circle: pre-main sequence stars

solid squares: stars with poorly determined ages.

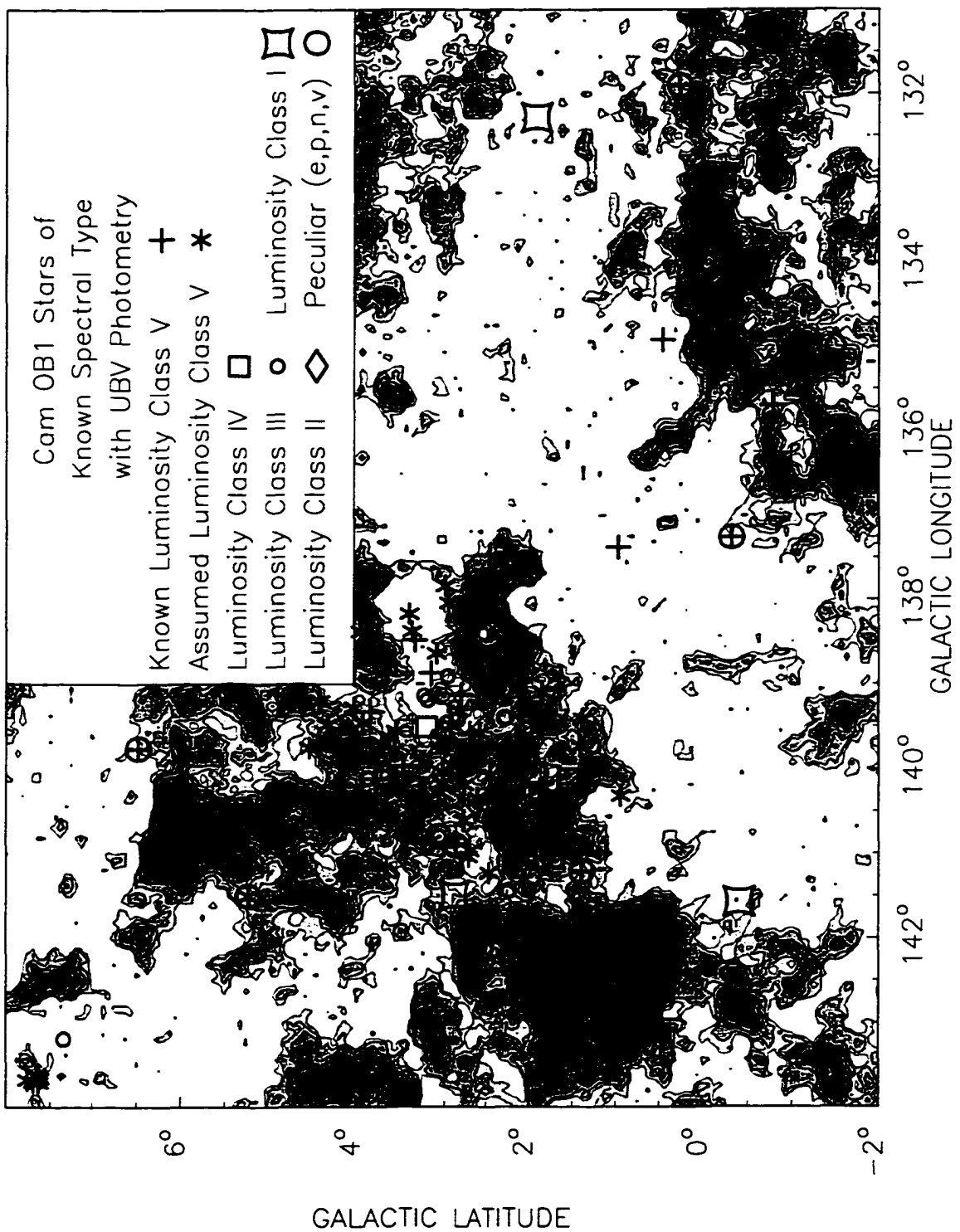

Figure 4.8 Overlay of Cam OB1 stars on Cam OB1 CO emission. A contouring scheme has been selected to show a minimum 3σ level over the indicated velocity range. Contours increase by factors of 1.58 to yield 5 contours per decade.

ages (25), but this is very well matched by the increase in pre-main sequence stars (24), while the number of age class III stars decreases (2). On the basis of the population distribution, and with no additional information, it would appear that, in Cam R1 S, the stars with poorly determined ages probably are an equal mix of pre-main sequence stars and evolved stars, while in Cam R1 N, the stars with poorly determined ages are probably pre-main sequence stars.

The question remains, "are the old stars (say 30 - 100 $\times 10^6$ yr) in the mass range 2 - 6 $M_\odot$ identified as lying in the Cam R1 region really part of Cam OB1?" The original spectral survey of the region (Schwassmann & van Rhijn 1947), as well as the follow up work by Jonas (1971), where many of the class III stars were given their luminosity classification, was complete for stars as faint as $m_v \sim 12^m$ within the boundaries considered here. If this is the case, then the enhancement in late B- and early A-type stars seen in the Cam R1 region is in fact a real enhancement over the normal space distribution for these stars in this region. There may very well have been some dispersion of these stars into the surrounding space, which we see in the presence of age class IV stars, but for the most part the stars are well contained within the Cam R1 boundaries. Whatever the star forming process, it seems to be gentle enough and sufficiently long lived to have produced stars within a relatively small space over several 10^7 yr.

4.4 Conclusions

Summarizing the results of this chapter we have the following:

1. In agreement with Heeschen (1951), the Local CO emission identified in the present survey (Di96) is at a distance of 250±50 pc.
2. In the case of the Perseus CO emission, the work of GS92 places the two associated stellar groups Cas OB6 and Per OB1 at a distance of 2.40 kpc and 2.30 kpc, respectively. Since these two groups lie in front of the Perseus CO emission, a representative distance for this emission is 2500±200 pc. This differs significantly from the kinematic distance (~ 3.5 kpc) derived from Brand & Blitz (1993).
3. It is possible to construct a main sequence of B-type stars in the Cam OB1 region in an observer's HR diagram. From the fit of this main sequence to standard empirical models it follows that the distance to the Cam OB1 stars, and by association the Cam OB1 CO emission, is 975±90 pc.

4. It is possible to extend the observer's HR diagram to include the more evolved stars, hotter and cooler stars on the main sequence and pre-main sequence stars down to an $M_V \sim +1^m$.
5. It is also possible to construct a well defined theoretician's HR diagram for the Cam OB1 stars which suggests that star formation has been going on in the region for $\sim 50 - 1 \times 10^6$ yr, as judged from the main sequence stars and evolved stars in the mass range 6 - 25 $M_\odot$.
6. There is a well defined population of pre-main sequence stars with ages $\sim 3 - 1 \times 10^6$ yr concentrated in the Cam R1 region. In particular, these stars are concentrated in the northern half of this complex (Cam R1 N).
7. The more evolved stars in the Cam R1 region are concentrated in the southern half of this complex (Cam R1 S).
8. There exists a population of stars which have poorly defined ages whose spatial location suggests they are primarily pre-main sequence stars in the northern half of the Cam R1 region (Cam R1 N) and equally mixed pre-main sequence and main sequence stars in the southern half of the Cam R1 region (Cam R1 S).
9. Whatever the star forming mechanism at play in Cam OB1 it appears to be a relatively gentle and long-lived process and has produced a concentration of stars in the Cam R1 region.

Chapter 5

Extreme Population I Objects

An analysis of sources in the IRAS point source catalog, coincident with the Cam OB1 region, is presented. A number (16) of these sources can be characterized as candidate extreme Population I objects on the basis of their infrared colors. Additional observations looking for methanol masers and molecular outflows are also presented. No masers were discovered in the Cam OB1 region, but a new one, associated with IRAS 02455+6034, was discovered in the background Perseus arm. A new molecular outflow, AFGL490-iki, which is associated with IRAS 03234+5843, was detected in the Cam OB1 region.

5.1 Introduction

In Chapter 4, a theoretician's HR diagram was constructed for the Cam OB1 stars in order to provide some insight into their evolutionary state. In this chapter the objects in Cam OB1 associated with star forming regions will be identified on the basis of their infrared emission, in order to trace out the most recent epoch of star formation. These extreme Population I objects (ePIo) include: HAe/Be stars, methanol (CH_3OH) masers, molecular outflows, reflection nebulae and HII regions. Together with Chapter 4, it should then be possible to compile a record of the star formation that has occurred in the Cam OB1 region from a few $\times 10^7$ yr ago to the present time. The *IRAS* point source catalog (Beichman et al. 1988), served as the principal data set for all of the analysis in this chapter. Additional observations of methanol masers and molecular outflows, carried out by the author, were motivated to a large degree by this analysis. Confirmation of the association between the ePIo and PIo (Population I objects) in the Cam OB1 region, as selected in Chapter 4 and 5, will be made in Chapter 6.

ePIo are a very diverse group of objects, driven by different physical processes. HAe/Be stars included in this list, i.e., identified by their infrared emission, represent intermediate-mass stars which still have residual dust from their natal cocoon

surrounding them in the form of shells or disks (Hillenbrand et al. 1993). For stars less massive than 6 $M_\odot$ there is a 'birthline' where these stars cease to accrete material and become optically visible (Palla & Stahler 1993), while still undergoing further contraction until they arrive on the main sequence. These optically visible HAe/Be stars have been identified and discussed in Chapter 4.

Methanol masers were first detected in studies towards the galactic center (Ball et al. 1970) and the Orion star forming region (Barrett et al. 1971). While it is poorly understood, it is believed that the pumping mechanism for the methanol maser considered here (the $5_1 - 6_0 A^+$ transition at 6.6 GHz) is due to the amplification of the infrared continuum emission coming from an UC (ultracompact) HII region (Menten 1991), i.e., from the HII region generated by a massive star during the earliest stage of its evolution ($t < 10^4$ yr, Wood & Churchwell 1989). Observations of candidate objects selected on the basis of their infrared colors (Lyder & Galt 1997) did not reveal any methanol masers in the Cam OB1 region, within the boundaries of the present CO survey (Digel et al. 1996, hereafter Di96). This would suggest that there are no massive stars (say $M \geq 20 M_\odot$), at least at this early stage of evolution, in the Cam OB1 region considered in the present survey. However, these observations did lead to the discovery of a new methanol maser associated with the infrared source IRAS 02455+6034 located in the Perseus region.

Molecular outflows are believed to be associated with the very earliest evolutionary period of a proto-star while it is still accreting material (Fukui et al. 1993). Indeed, it has been argued that these outflows are ultimately powered by the potential energy released by the accretion process (Strom et al. 1988), and serve as the only means to remove sufficient angular momentum to allow the growth of the stellar core (Hartmann & MacGregor 1982). The lifetime of an outflow is typically $\sim 5 \times 10^4$ yr (Fukui 1989), in agreement with the accretion time scales. Hence, an outflow is the surest signature of the very earliest stages of star formation. As it turns out, there are at least two outflows in the Cam OB1 region covered by the present survey (Di96) — the well known and very energetic outflow AFGL 490 (Snell et al. 1984, Kawabe et al. 1984, Campbell et al. 1986, Hasegawa 1986, Mitchell et al. 1992, Mitchell et al. 1995) and its newly discovered companion outflow AFGL 490-iki (Purton et al. 1995).

Finally, reflection nebulae and HII regions represent the interaction of the interstellar medium (ISM) with stars; reflection nebulae are produced by the scattered

starlight from neighboring dust, while HII regions are produced by emission from gas which has been ionized by hot stars. The time scales for these objects are more difficult to estimate. Reflection nebulae can be produced either by relatively old stars which are recent interlopers into the region, e.g., the Pleiades, or by relatively young stars which are known to be part of a star forming region, e.g., Orion. Well developed HII regions can be identified at optical wavelengths by their characteristic H_α emission, and they may be relatively old, i.e., as old as the lifetime of the main sequence star(s) energizing them (Chapter 6 identifies these sources in detail). UC HII regions are associated with the very earliest evolution of massive stars and are very short lived (see the discussion on outflows above).

The outline of this chapter is slightly different from the others in this thesis, as it includes additional observations of methanol masers and molecular outflows, which are of interest in their own right. Hence, the sections dealing with these objects are presented in the form of mini-papers within the chapter. §5.2.1 will describe the selection of infrared objects in the Cam OB1 region, while in §5.2.2 the infrared sources which have been selected will be characterized, i.e., whether they are UC HII regions, or HAe/Be stars, etc. §5.3 will present an investigation of the ePIo in Cam OB1 on the basis of their optical and radio emissions. In §5.4 the results of a survey for 6.6 GHz methanol masers, undertaken in the Fall of 1994 with the 26m dish at the Dominion Radio Astrophysical Observatory (DRAO), will be presented. In §5.5 high resolution (20″) observations of ^{12}CO (J=2-1) of selected regions within Cam OB1, gathered in January 1995 with the James Clerk Maxwell Telescope (JCMT), will be presented. These high resolution observations led to the discovery of the molecular outflow AFGL490-iki (Purton et al. 1995). §5.6 will provide a summary of the study of ePIo, identified by their *IRAS* colors, in the Cam OB1 region.

5.2 Infrared Objects in Cam OB1

5.2.1 Selection of Candidate Infrared Objects in Cam OB1

The principal source of information in this chapter is a catalog of data taken with the *Infrared Astronomical Satellite (IRAS)*, which orbited the Earth during 1983 and mapped 96% of the sky at 12, 25, 60 and 100 μm. Reliable detections of 245,889 point sources and extended structures smaller than 8′ were obtained in at least one of the bands. The sensitivity of the survey for point sources, away from spatially confused regions of the sky, was $\sim$ 0.5 Jy at 12, 25 and 60 μm and $\sim$ 1.5

Jy at 100 μm. The angular resolution of the instrument varied between $\sim 2'$ at 12 μm to $6'$ at 100 μm while the positional accuracy was typically better than $20''$. The bandwidths (FWHM) for the four bands, from 12 to 100 μm respectively, were 7.0, 11.2, 32.5 and 31.5 μm (Beichman et al. 1988). All of the infrared sources (1639) listed in SIMBAD within the boundaries of the present survey are shown in Figure 5.1, which includes a few sources which have been detected only at 2 μm from ground based observations.

The strategy for selecting those objects associated with the Cam OB1 emission is slightly different from that employed for the PIo, in the sense that it is assumed that the ePIo of interest are indeed very young objects and must be very closely coincident with the molecular gas from which they formed. Furthermore, the association of the ePIo with the molecular gas must be unique and real, i.e., they should be associated only with the Cam OB1 molecular gas, they must represent a real enhancement over the background source count, and it must be possible to characterize the sources in terms of their infrared colors.

The selection of candidate ePIo in the Cam OB1 region required two passes through the data. The first pass, the initial selection of infrared sources, may be summarized as follows:

1. A 'control region' in the present survey, judged to be free of ongoing star forming activity on the basis of its random coverage, was selected. The chosen region is bounded by $144° \geq l \geq 139°$, $+8° \geq b \geq +4°$ (see Figure 5.1).
2. The control region, selected in Step 1, was then divided into cells of reasonably large size, in order to obtain meaningful statistics on the variation of source counts in a cell. A cell size of $0.^{\circ}5 \times 0.^{\circ}5$ was judged to be adequate, resulting in 80 cells in the control region. Assuming that the statistics for the number of sources per cell followed a Poisson distribution, the background source level away from any star forming regions was found to be 1.96 sources cell^{-1} with a 1σ deviation of 1.40 sources cell^{-1}. The 'background' sources included a mix of true background sources, e.g., background galaxies, as well as sources which may be in the foreground or in Cam OB1 but are unrelated to star forming regions, e.g., carbon stars or planetary nebulae.
3. A density map covering the entire survey, but with pixels of $0.^{\circ}5 \times 0.^{\circ}5$, was then generated by placing the sources in Figure 5.1 into the appropriate cell. An enhancement was defined on this grid as such, if the total number of sources in

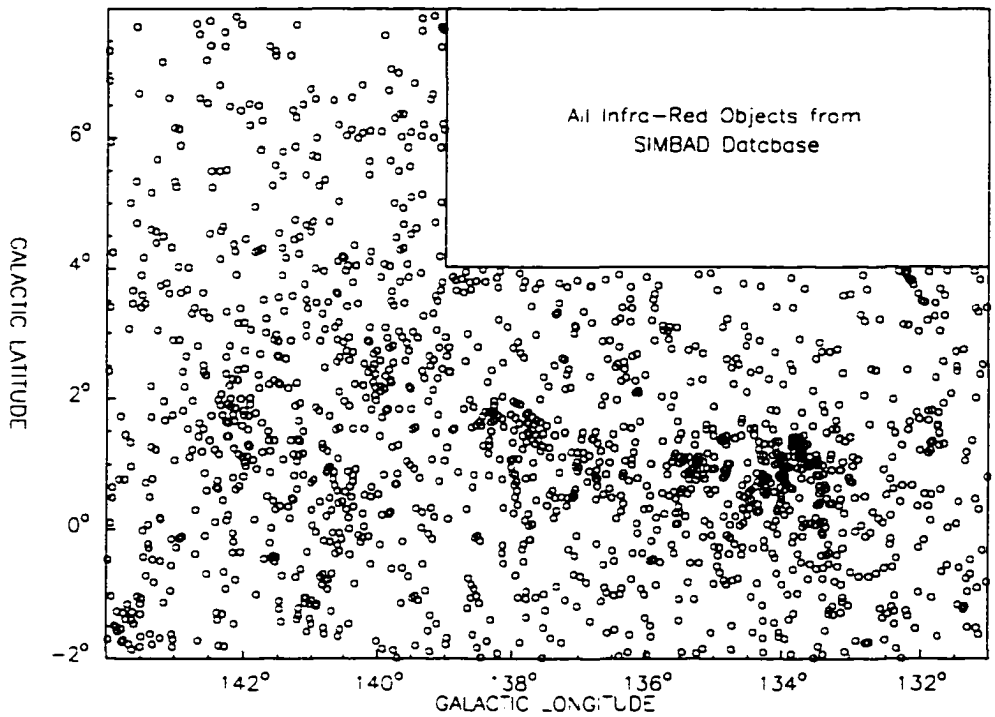

Figure 5.1 Location of all infrared objects (1639) within the present survey boundaries (Di96) as selected from the SIMBAD. Some clustering is obvious in the field but a mathematical treatment is required to separate true enhancements from the background (see text).

the cell lay at least 3σ above the mean, i.e., 6.16 sources cell^{-1}. This intermediate step is not shown.

4. The density map generated in Step 3 was then regridded onto a grid similar to the present survey, i.e., $0.^{\circ}0625 \times 0.^{\circ}0625$ pixels, using the DRAO inhouse routine *mapconvrt* (cubic spline) and the enhanced regions were then compared with the three distinct zones of CO emission, i.e., Local, Cam OB1 and Perseus. Figure 5.2 shows these comparisons.
5. Candidate ePIo were then selected if it was determined they lay within an enhanced region with respect to the background source counts, i.e., within the first contour level in Figure 5.2. In Figure 5.2, the number of sources (132) included in the enhanced region (total area ~ 3.3 deg^2) suggests an average density of $\sim$ 40 infrared sources deg^{-2}, an enhancement by a factor of five over the control region.

In Figure 5.2 there are several obvious clusters of infrared sources which can be as-

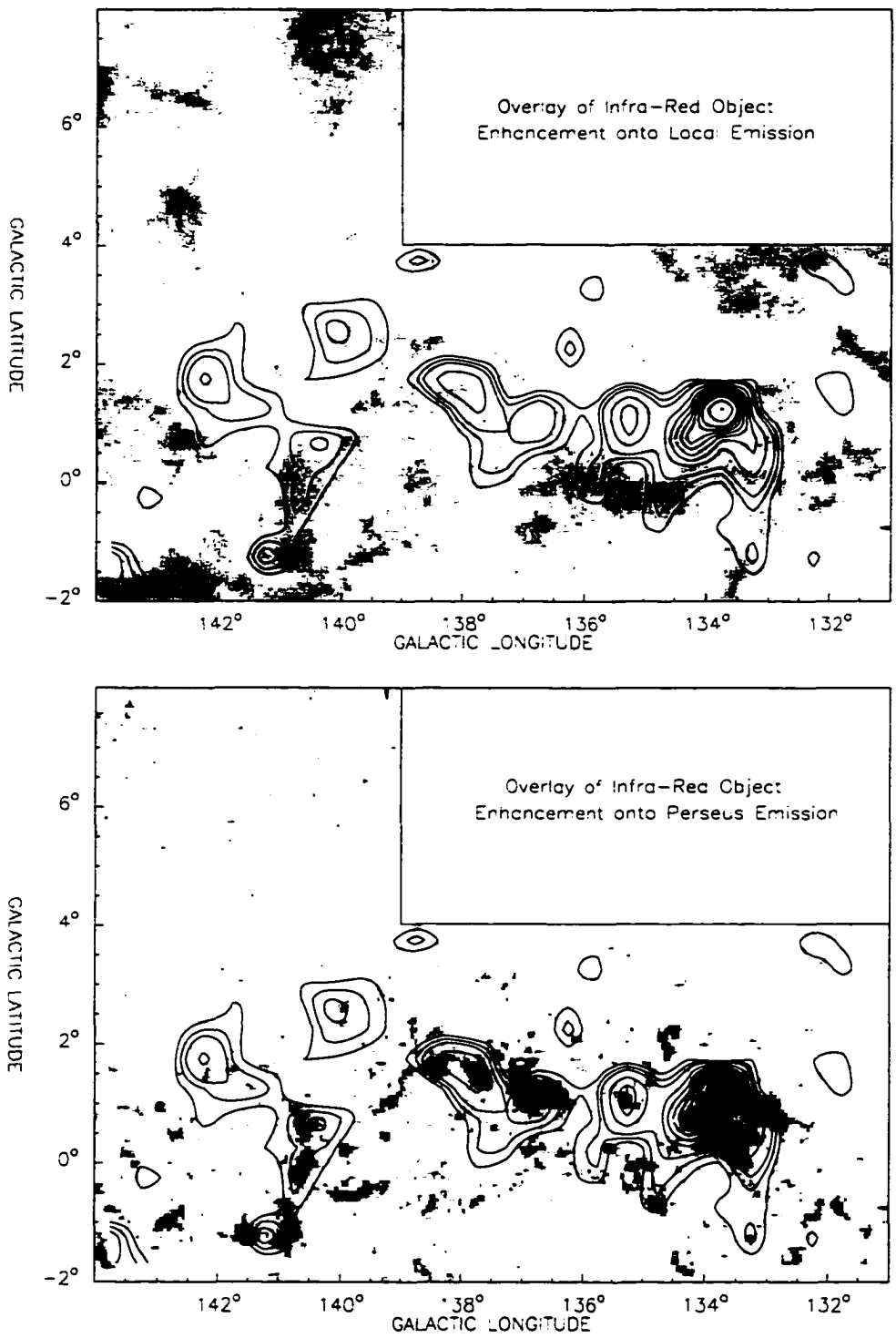

Figure 5.2 Overlay of enhanced density of infrared features onto CO emission. The infrared source density contours are 6.16 (3 σ), 8.16, 10.16, 15.00, 20.00.....

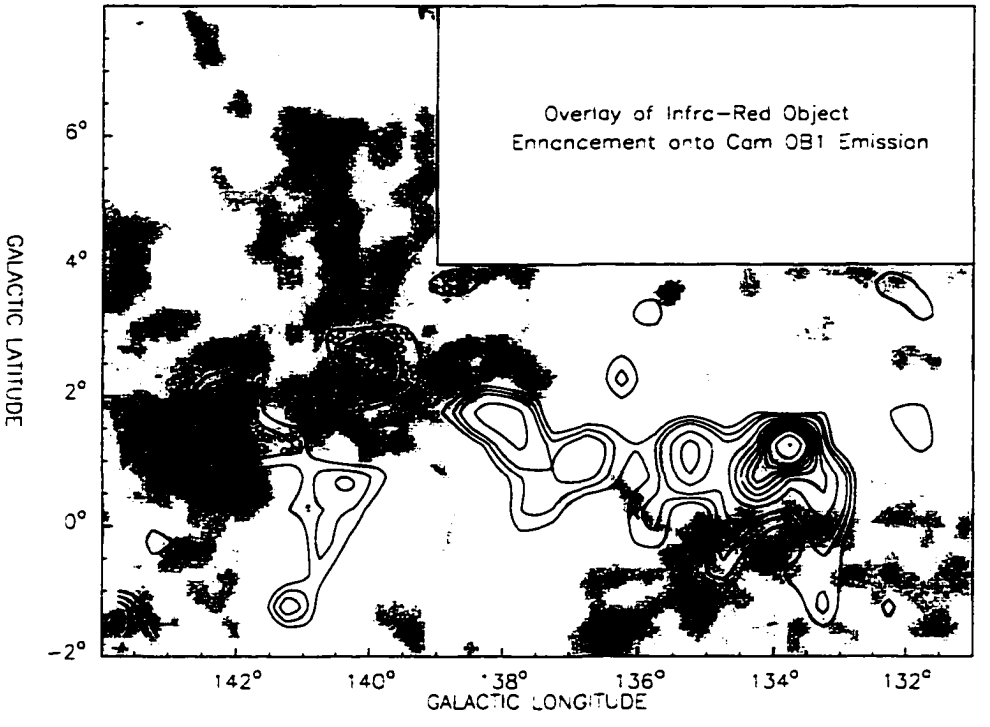

Figure 5.2 cont. 50.00, 70.00, 90.00 sources cell^{-1} (where a cell is defined as a 0°.5 × 0°.5 region). The *IRAS* sources in the Cam OB1 region, within the enhanced infrared source regions, are also shown (open circles) for illustration.

The CO emission is shaded at a minimum (3σ) level appropriate for each region and increased by a factor of 1.58 thereafter. The apparent cutoff in the density contours at lower Galactic b and higher Galactic l is an artifact of the plotting program.

sociated with CO emission. The dominant infrared clustering in the survey field takes the form of an enhanced band of sources which are very well correlated with the Perseus CO emission between $l = 133°$ and $l = 139°$ and from $b = -2°$ to $b = +3°$. The strongest enhancement in the number of sources seen in the dataset ($l = 133°.5, b = +1°$) is associated with the W3 region. Two small enhancements near $l = 134°.75, b = -0°.5$ and $l = 135°.75, b = +0°.25$ can be associated with features in Perseus or the Local emission. However, given the star forming activity along this line-of-sight (Garmany & Stencel 1992), these sources are probably associated with the Perseus emission. The same argument can be applied to the enhancement centered on $l = 140°.5, b = 0°.0$, which closely follows the turnover in the Perseus CO emission near $l = 138°.5, b = +1°.5$.

There are three infrared features which stand out as probably being associated

with the Cam OB1 CO emission. These features, in order of decreasing size, are centered on $l = 142°.0, b = +2°.0$, $l = 140°.0, b = +2°.5$ and $l = 138°.5, b = +3°.5$. The largest is coincident with the active star forming region Cam R1 (Chapter 4). It should be noted there are some Perseus CO emission features which could be associated with these enhancements, but the morphology (large width) of these enhancements and a better positional coincidence with Cam OB1 CO emission suggest that the majority of the infrared sources comprising these enhancements are associated with the nearby Cam OB1 emission (and in particular with the feature defined as Complex F in Chapter 7 for the first infrared enhancement, and Complex B for the second and third infrared enhancements). There may be some contamination of these three enhancements by Perseus infrared sources, whose contribution is difficult to estimate, but this will be minimized in a second pass through the data.

Other features which require some comment include two strong infrared source enhancements near $l = 141°.0, b = 0°.0$ and $l = 143°.5, b = -2°.0$, which are probably Perseus sources as they are located near strong Perseus CO emission. Finally, there is an enhancement near $l = 132°.5, b = +3°.5$ which is well correlated with Local and Cam OB1 emission. There do not appear to be any young stars or clusters in this region (Chapter 4) indicating whether this feature may be associated with a star forming region in Cam OB1 or the Local emission. Given the lack of corroborating evidence that these objects are associated with the Cam OB1 emission they will not be included in any further analysis.

The second pass of the selection process was to select from the list of infrared sources identified as probably associated with the Cam OB1 emission a subset of the best quality possible, in which the sources can be well modelled from their infrared emission, and in which any possible contamination from background sources is minimized. There are three steps to this process:

1. An initial trial selection process was chosen which required that all infrared sources in the Cam OB1 enhanced regions have at least a moderate quality flux measurement in two adjacent *IRAS* wavelength bands (63 sources in total). Figure 5.3 (lower two diagrams) shows two color-color planes ([60 - 25] vs. [25 - 12] and [100 - 60] vs. [60 - 25]) for those sources which could be placed on at least one or both of these diagrams. *IRAS* colors are defined in this thesis to be non-color corrected quantities, i.e., the flux density calculated at the nominal center of each bandpass has assumed a source flux density $S_\lambda \propto \lambda$, and are given

by:

$$[25-12] = log(\frac{F_{25}}{F_{12}}), \tag{5.1}$$

$$[60-25] = log(\frac{F_{60}}{F_{25}}). \tag{5.2}$$

and

$$[100-60] = log(\frac{F_{100}}{F_{60}}). \tag{5.3}$$

For comparison, the control region infrared point sources subject to a similar constraint are also shown in Figure 5.3 (upper two diagrams).

In Figure 5.3 it would appear that, on the whole, the sources selected in the enhanced infrared density regions in Cam OB1 do differ in their location in both color-color plots from those of the control region. In the case of the [12–25–60] plane, the control region stars are clustered around a value of $[25-12] \sim -0.3$, $[60-25] \sim -0.2$, which are suggestive of stellar photospheres (Walker et al. 1989, hereafter W89). There do appear to be a few control region sources which are redder, i.e., [60 - 25] > 0.5, in the [12–25–60] plane but the uncertainties in their fluxes militate against drawing any firm conclusions as to their nature. It also appears that the candidate Cam OB1 sources are redder, as a group, in the [25–60–100] plane than the control region sources. In many cases the Cam OB1 sources have uncertainties which suggest that they may indeed be redder than shown, which would increase the difference between the two data sets.

2. Even given the strong evidence for the difference between the control region and Cam OB1 infrared sources using the two flux criteria illustrated in Figure 5.3, there are still too many degrees of freedom in the placement of the Cam OB1 sources in both color-color planes. To reduce this uncertainty, the final list of infrared sources will be further restricted to sources (26) which have at least three moderate-quality *IRAS* flux measurements. The remaining sources (37), possibly associated with the Cam OB1 emission, are certainly intriguing, but they require further observations in the infrared in order to ascertain their nature.
3. The final step in the selection of Cam OB1 infrared sources is to reconsider the chance that some of the selected sources may not actually be associated with the Cam OB1 emission. In Figure 5.2 it appears that the only other potential contaminating sources are those which are associated with the Perseus emission. As has been previously argued in the section discussing Figure 5.2, the width

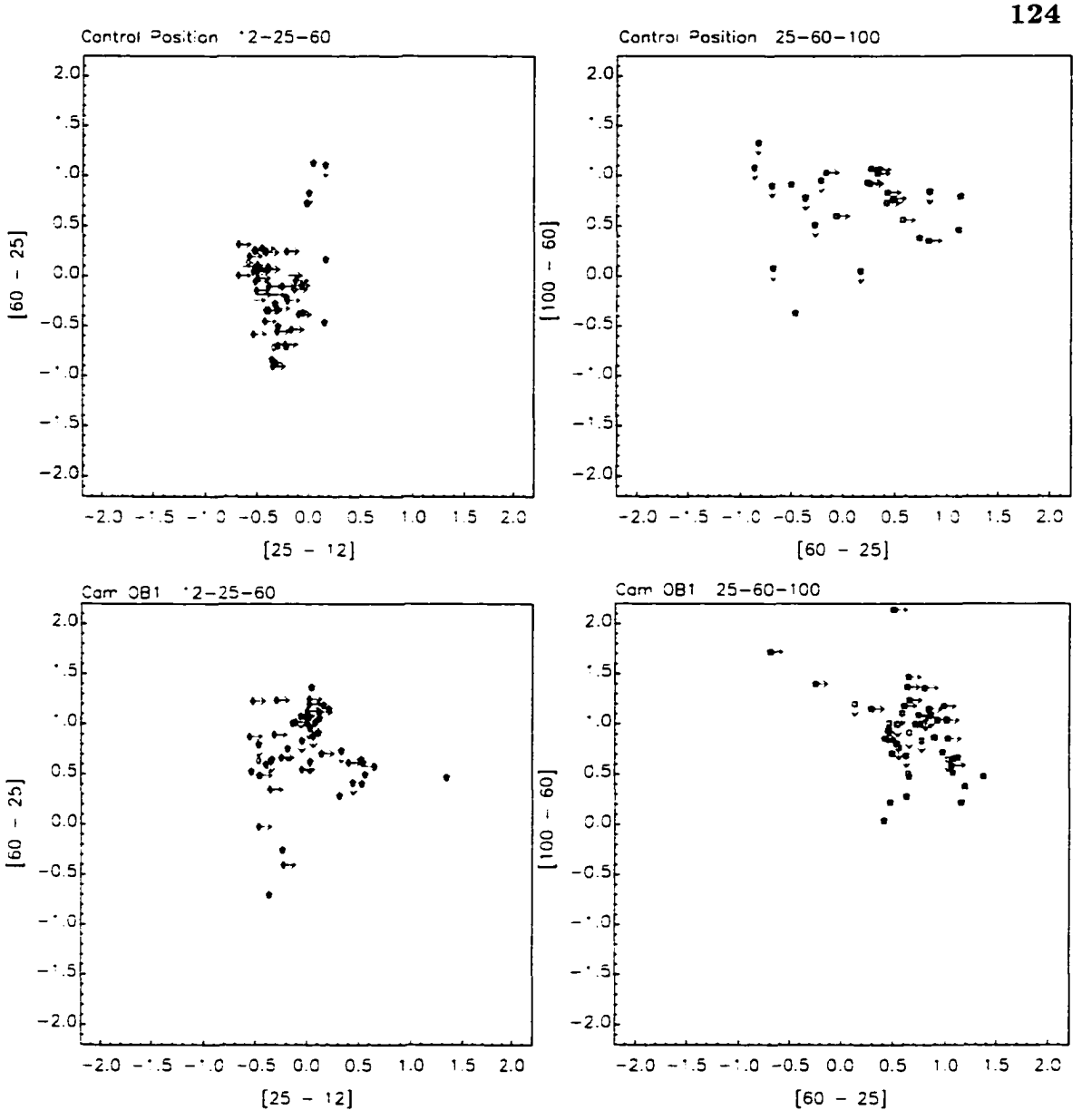

Figure 5.3 Color-color plots for infrared sources which have at least two adjacent wavelength *IRAS* fluxes of moderate quality. Sources in the control region are shown in the upper two diagrams, while those in the enhanced regions associated with Cam OB1 (see Panel 3 of Figure 5.2), are shown in the lower two. An open diamond indicates a source capable of being reliably positioned in the [12–25–60] plane and an open square indicates a source which may be positioned reliably only in the [25–60–100] plane. Five-point stars indicate sources capable of being positioned in both plots. An arrow attached to a symbol indicates the direction the source moves in the plot due to the quoted uncertainty or limits in the fluxes.

of the infrared enhancement regions assigned to the Cam OB1 region is much larger than that typical of the Perseus infrared source regions, suggesting that most of the infrared sources associated with the Cam OB1 region are correctly placed. In order to eliminate any Perseus sources, candidate Cam OB1 sources were not considered for further study if they had already been assigned to the Perseus region in the literature (Wouterloot & Brand 1989, McCutcheon et al. 1991, Wouterloot et al. 1993), or if they were also coincident with a 3σ level of Perseus CO emission as shown in Figure 5.2. This step eliminated 9 sources from the initial list of 63, or 7 sources from the final list of 26, leaving 19 candidate sources considered to be probably associated with Cam OB1.

5.2.2 The Nature of the Infrared Objects in Cam OB1

The availability of infrared data on star forming regions from *IRAS* led to the rapid growth of the characterization and understanding of these objects. Typical examples of the work on ePIos, based to a large extent on *IRAS* data, include HII regions (Chan & Fich 1995), UC HII regions (Wood & Churchwell 1989), T-Tauri stars (Rucinski 1985, Beichman et al. 1986, Wilking et al. 1992, Prusti 1992), HAe/Be stars (Weintraub 1990, Berrilli et al. 1992), outflows (Hasegawa 1986), reflection nebulae (Castelaz et al. 1987) as well as more general surveys of star forming regions including *IRAS* data (Strom et al. 1989, Carpenter et al. 1993, Lada et al. 1993, Odenwald & Schwartz 1993). In all of these cases the analysis had to contend with the confusion and sensitivity limits inherent to *IRAS*. Improvement to this situation can be made with specially enhanced versions of the *IRAS* data, e.g., HIRES (Laughlin 1991), or from using data gathered in pointed observations from newer spacecraft, e.g., ISO. Nevertheless, the observations presented in the second version of the *IRAS* point source catalog (Beichman et al. 1988) still represent the largest database from which to draw infrared data on star forming regions.

At the present time the most complete analysis of *IRAS* point sources, on the basis of their colors, is due to W89. In their analysis they constructed a set of 'Occupation Zones' (OZs) for sources which possessed at least a good quality flux measurement at 12, 25 and 60 μm, and whose identity was already known. Table 5.1 summarizes these results using the *IRAS* colors as defined in Eq. 5.1 - 5.3.

The conversion between the colors in W89 and the present work is given by:

$$[25-12] = \frac{[12]-[25]-1.56}{2.5}, \tag{5.4}$$

Table 5.1: Occupation Zones for IRAS Point Sources
(adapted from Walker *et al.* 1989)

Source	[25 - 12] Mean± 1σ(no)	[60 - 25] Mean± 1σ(no)	[100 - 60] Mean± 1σ(no)	Designation
Bright stars	$-0.59 \pm 0.05(1022)$	$-0.92 \pm 0.08(3142)$	$-0.42 \pm 0.11(509)$	a
O-rich stars	$-0.30 \pm 0.14(2679)$	$-0.92 \pm 0.08(3142)$	$-0.42 \pm 0.11(509)$	b
Optical C-rich	$-0.52 \pm 0.05(308)$	$-0.70 \pm 0.09(270)$	$-0.28 \pm 0.16(79)$	c
LRS C-rich	$-0.30 \pm 0.13(282)$	$-0.81 \pm 0.07(306)$	$-0.52 \pm 0.08(52)$	d
HII	$0.87 \pm 0.13(42)$	$0.84 \pm 0.18(60)$	$0.24 \pm 0.17(49)$	e
Blue ref. neb.	$0.11 \pm 0.13(31)$	$0.80 \pm 0.32(22)$	$0.43 \pm 0.18(6)$	f
Red ref. neb	$0.61 \pm 0.19(35)$	$0.61 \pm 0.33(27)$	$0.18 \pm 0.15(17)$	g
Blue PN	$0.15 \pm 0.20(41)$	$-0.18 \pm 0.31(41)$	$0.02 \pm 0.40(17)$	h
Red PN	$0.85 \pm 0.30(159)$	$-0.02 \pm 0.36(170)$	$-0.34 \pm 0.12(102)$	i
Blue galaxies	$0.18 \pm 0.11(179)$	$0.80 \pm 0.06(179)$	$0.28 \pm 0.12(343)$	j
Red galaxies	$0.48 \pm 0.10(95)$	$0.68 \pm 0.05(95)$	$0.28 \pm 0.12(343)$	k
Seyferts	0.48 ± 0.14	0.42 ± 0.13	0.20 ± 0.24	l
Quasars	$0.31 \pm 0.18(49)$	$0.15 \pm 0.20(56)$	$0.18 \pm 0.16(37)$	m
T Tauri	$0.14 \pm 0.11(43)$	$0.02 \pm 0.22(46)$	$0.16 \pm 0.24(16)$	n
LRS=3 stars	$0.20 \pm 0.10(127)$	$-0.66 \pm 0.15(140)$	$-0.54 \pm 0.09(21)$	o
LRS=6 stars	$-0.09 \pm 0.11(49)$	$-0.92 \pm 0.06(40)$	$-0.35 \pm 0.40(14)$	p
HHES	$0.57 \pm 0.29(26)$	$0.34 \pm 0.34(29)$	$0.25 \pm 0.31(28)$	q
Bipolar neb.	$0.23 \pm 0.33(20)$	$-0.01 \pm 0.48(21)$	$0.39 \pm 0.31(19)$	r

$$[60 - 25] = \frac{[25] - [60] - 2.26}{2.5}. \tag{5.5}$$

and

$$[100 - 60] = \frac{[60] - [100] - 1.11}{2.5}. \tag{5.6}$$

The bracketed quantities on the right hand side of Eq. 5.4 - 5.6 are the quantities originally presented in W89 (their Table I). In Table 5.1 the occupation zones are defined by the mean and standard deviation of the sample, whose size is given in parentheses. The designation for the zones are as follows: a) optically identified bright stars, b) optically identified oxygen-rich stars, c) optically identified carbon-rich stars, d) carbon-rich stars identified from the Low Resolution Spectra (LRS) Atlas (1986), e) HII regions, f) blue and g) red reflection nebulae as determined from their fit in the [12–25–60] plane and their [25 - 12] color, h) blue and i) red planetary nebulae determined from their fit in the [12–25–60] plane, j) blue and k) red galaxies, again determined from their fit in the [12–25–60] plane, l) seyferts, m) quasars, n) T Tauri stars, o) stars with LRS=3, i.e., evolved stars with silicate

absorption at 10 μm. p) stars with LRS=6, i.e., evolved stars with silicate emission and a red continuum. q) stars believed to be exciting Herbig-Haro objects and r) bipolar nebulae. The last two designations. q) and r), are assigned by the author based upon the work of W89.

In order to make the OZs as complete as possible, at least in regards to ePIo, the OZs defined by W89 were supplemented with the following additional zones:

HII regions were selected from *IRAS* using the filter devised by Hughes & MacLeod (1989). These are given by:

$$[25 - 12] \geq 0.40, \tag{5.7}$$

$$[60 - 25] \geq 0.25, \tag{5.8}$$

with the additional constraints that $F_{100} \geq 80$ Jy and the qualities of the 25 and 60 μm fluxes are at least moderate. Using this filter, Hughes & MacLeod (1989) determined that they would select a HII region with a contamination rate of 11% (this includes a 5% contamination rate by other ePIo, e.g., reflection nebulae, and a contamination of 6% by obviously non-ePIo, e.g., galaxies and PN). It should also be noted that this filter does agree with the HII region OZ in W89, but it is a more general characterization of the position of HII regions in both of the *IRAS* color-color planes.

UC HII regions were investigated extensively by Wood & Churchwell (1989) who determined that these objects could be identified using the following filter:

$$[25 - 12] \geq 0.57, \tag{5.9}$$

$$[60 - 12] \geq 1.30. \tag{5.10}$$

with no restriction on the 12 μm data but at least a good quality flux index at 25 and 60 μm. Using this filter, Wood & Churchwell (1989) determined that they were contaminated by non-ePIo, i.e., galaxies and optically visible stars, 8% of the time. This category of ePIo was not considered by W89, but it is important as it marks the very earliest stage of massive star formation, and thus should be included.

Finally, an OZ for HAe/Be stars has been included which is based upon the most probable identification of these objects as such, from Berrilli et al. (1992). This filter is defined as:

$$[25 - 12] = 0.27 \pm 0.37 \quad \text{(26 sources)}, \tag{5.11}$$

$$[60 - 25] = 0.25 \pm 0.65 \quad \text{(26 sources)}, \tag{5.12}$$

$$[100 - 60] = 0.31 \pm 0.27 \quad \text{(14 sources)}. \tag{5.13}$$

where the dispersion is the measure of the range seen in a rather uniform distribution of colors about the quoted mean value. Berrilli et al. (1992) checked whether the large range found in Eq. 5.11 - 5.13 could be attributed to confusion by comparing them to similar colors derived from Kuiper Airborne Observatory (KAO) 50 μm observations in conjunction with ground-based N band (10 μm) and Q band (20 μm) photometry, both of which had higher resolution. The scatter persisted, which suggests that the large range seen in the *IRAS* colors for HAe/Be stars is real. Figure 5.4 illustrates the placement of the OZs as defined in Table 5.1 and Eq. 5.4 - 5.13 in the two color-color planes ([12–25–60] and [25–60–100]) derived from the *IRAS* data.

Figure 5.5 shows the graphical placement of the 19 candidate ePIo in Cam OB1 in the [12–25–60] plane, while Figure 5.6 presents the same sources in the [25–60–100] plane. It is quite apparent from Figures 5.5 and 5.6 that it is not a simple matter to characterize most of the infrared sources in either color-color plane. Given the spatial confusion which can exist at the 100 μm band due to its relatively broad beam (6′), the greatest weight should be given to the position of the sources in the [12–25–60] plane.

In the [12–25–60] plane, shown in Figure 5.5, there are 3 objects which have been identified as having colors suggestive of a stellar photosphere (the open stars in Figure 5.5 and 5.6). Two of these sources are well separated from the remaining 17 sources in both colors, while the third, IRAS 03208+5812, can only be placed in this group if the uncertainty in its [60 - 25] color is large. These 3 objects are also very similar in their position in the [12–25–60] plane to the control region sources, which are probably dominated by unevolved stars. Hence, these objects are probably unevolved stars. It is not possible on the basis of *IRAS* data alone to decide whether these sources really are associated with the Cam OB1 emission, however, given that there is no further information in the literature suggesting that they are nearby, bright stars, it will be assumed that they are associated with the Cam OB1 region.

The remaining sources occupy positions in the [12–25–60] plane, and in many cases in the [25–60–100] plane, suggestive of ePIo. In the [12–25–60] plane, there appear to be two groups of sources. A group centered on [25 - 12] = 0.5, [60 - 25] = 0.4, contains four sources, IRAS 03236+5836, IRAS 03111+5938, IRAS

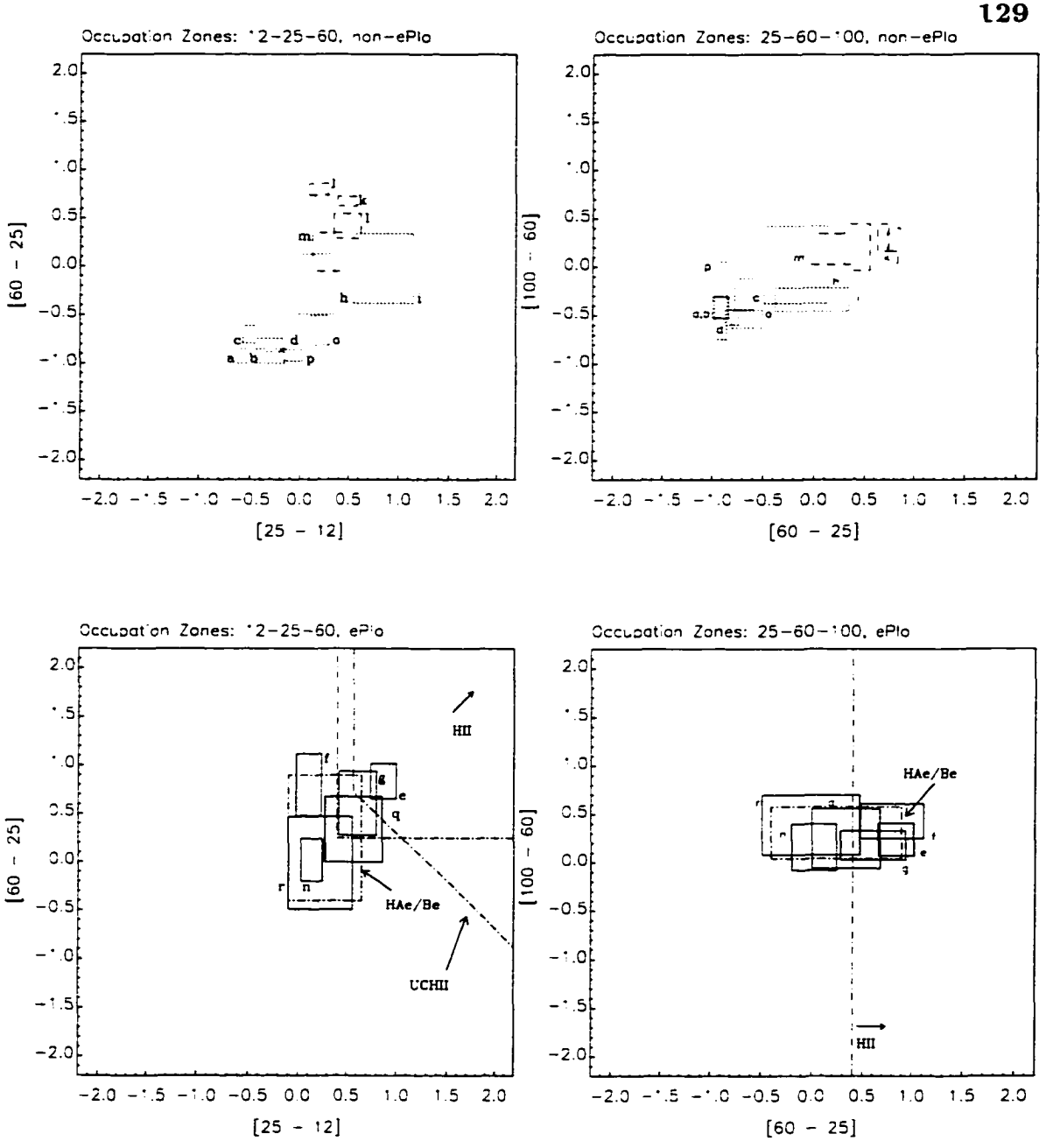

Figure 5.4 Occupation zones (OZs) for non-ePlo (top) and ePlo (bottom), as defined in Table 5.1 and Eq. 5.4 - 5.13. OZs for the non-ePlo include galactic objects not associated with star forming regions (dot-line boxes): a - bright stars, b - O-rich stars, c - optical C-rich stars, LRS C-rich stars, h - blue PN, i - red PN, o - LRS = 3 stars, p - LRS = 6 stars, and and extra-galactic objects (dash-line boxes): j - blue galaxies, k - red galaxies, l - seyferts, m - quasars. ePlo associated with star forming regions (solid-line boxes) include: e - HII regions, f - blue ref. neb., g - red ref. neb., n - T-Tauri stars, q - Herbig-Haro emission line stars, r - bipolar neb. Additional OZs for HII regions, UC HII regions and HAe/Be stars as defined in the text (dash-dot-line).

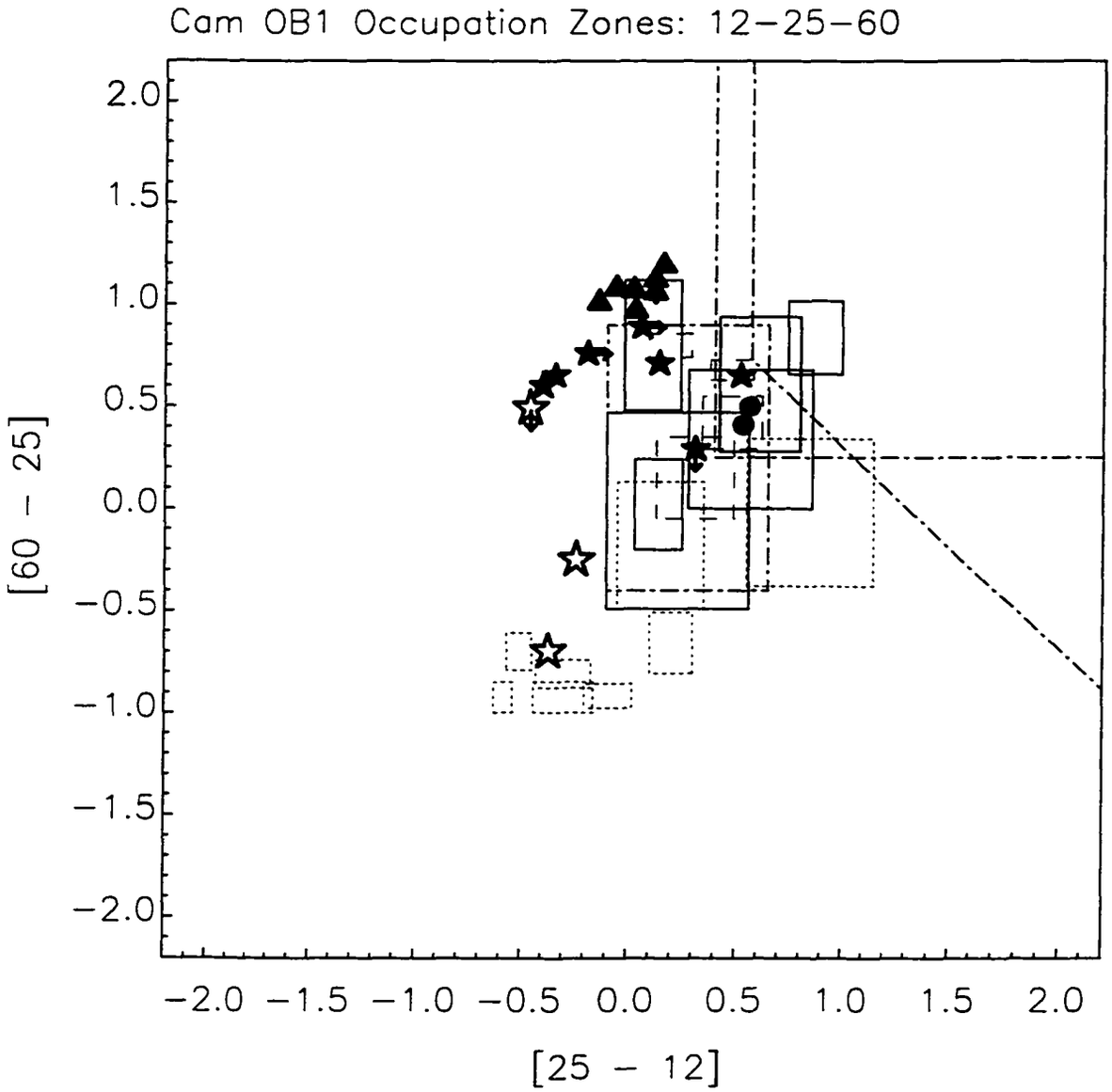

Figure 5.5 Positions of the 19 candidate ePIo in Cam OB1 in the [12–25–60] plane, with the occupation zones (OZs) as shown in Figure 5.4 superimposed. Solid-line and dash-dot-line boxes indicate OZs for ePIo associated with star formation. Dash-line and dot-line boxes indicate either OZs characteristic of extra-galactic objects or OZs for galactic objects not associated with star forming regions. Symbols for the objects are as follows: open stars - stars; filled stars - HAe/Be; filled triangles - blue reflection nebulae (BRN); filled circles - outflows. Errors in the colors due to upper limits in the fluxes are indicated by the arrows.

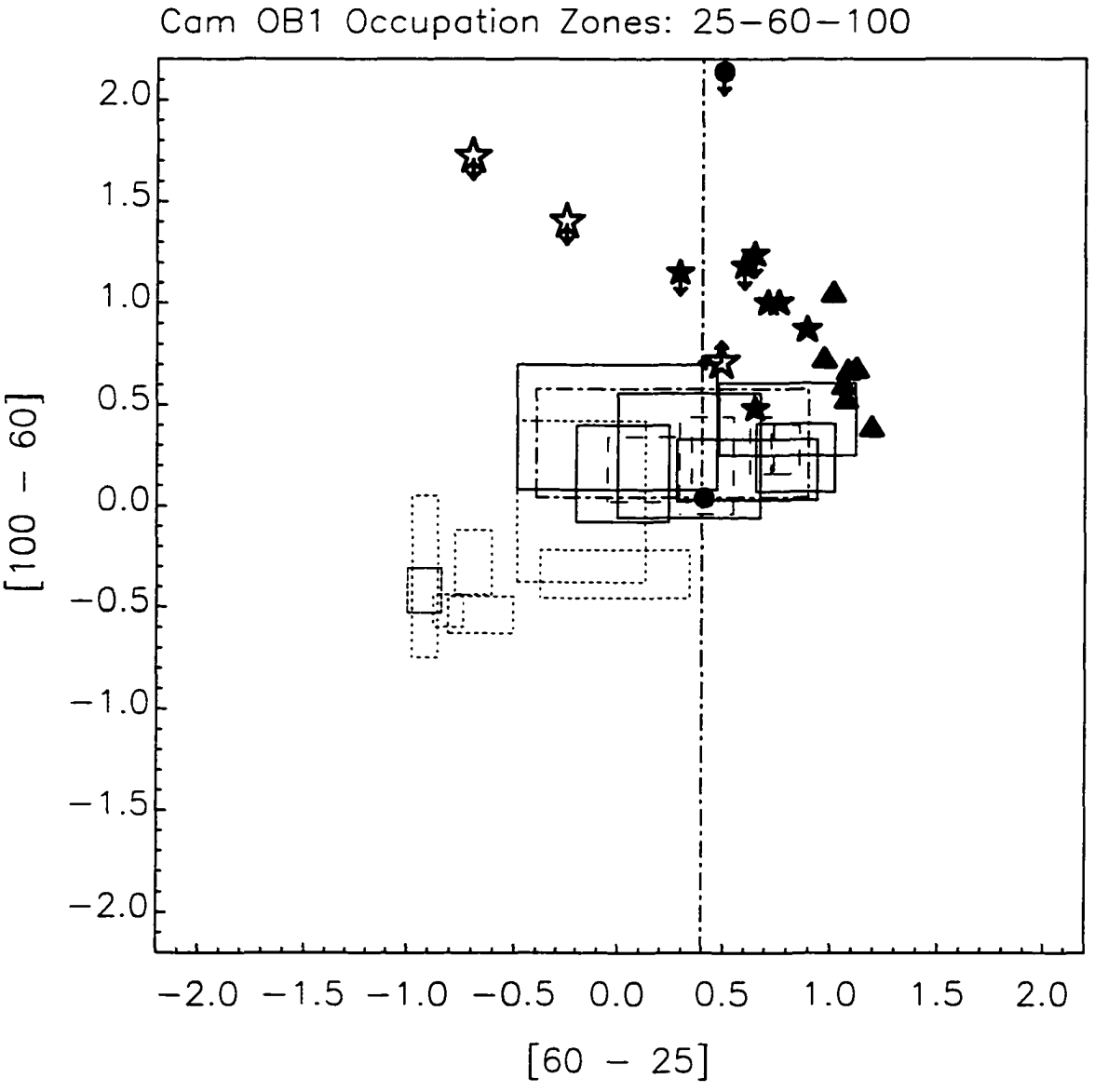

Figure 5.6 Occupation zones (OZs) in [25–60–100] plane for Cam OB1. Boxes and symbols are the same as for Figures 5.4 and 5.5.

03234+5843, IRAS 03243+5829, which include the two known outflows. The other group of sources, centered on [25 - 12] = 0.0, [60 - 25] = +0.75, coincides with the OZs for HAe/Be stars and blue reflection nebulae (BRN).

Table 5.2 provides the results of the tentative assignment of the sources to OZs as well as some other basic physical parameters. Assignment of a source as either an HAe/Be star or a BRN is somewhat arbitrary. This is not surprising as one of the original criteria used to classify HAe/Be stars as such is that they must be associated with reflection nebulosity (Herbig 1960). In fact, given that Cam OB1 is an active star forming region, it is possible that all the BRN are associated with young, hot luminous stars in Cam OB1. As a result of a search through the optically identified stars known to be in the Cam OB1 region (Chapter 4), there is a reasonably strong positional coincidence between 5 of the HAe/Be and BRN sources and these stars: IRAS 03111+6041 with BD+60 648 (B5V), IRAS 03116+5951 with HD237091 (B1V), IRAS 03111+5938 with HD 19820 (O9IV), IRAS 03164+5839 and IRAS 03167+5840 with HD 237121 (B0.5V).

There may be some additional information on the probability of the association of the optically identified stars with *IRAS* sources tentatively identified as HAe/Be stars or BRN on the basis of their *IRAS* luminosities. These luminosities (Table 5.2), which are derived from Carpenter et al. (1995), are given by

$$L_{IR} = 0.304(\frac{D}{kpc})^2 \sum_i [\frac{BW(\lambda_i)}{10^{12} Hz}](\frac{S_{\nu_i}}{Jy}), \tag{5.14}$$

where D is the distance to the source (0.975 kpc, Chapter 4), and $BW(\lambda_i)$ and S_{ν_i} are the bandwidth and flux density, respectively, of the λ_i *IRAS* band. The infrared luminosity for each source has a lower bound estimate, $L_{IR,L}$, given by summing up the contribution from the 12, 25 and 60 μm bands alone, and an upper bound, $L_{IR,U}$ (to within a factor of 2 - Carpenter et al. 1995), obtained by also adding the contribution from the 100 μm emission when this is of at least moderate quality. When the 100 μm emission is of at least moderate quality then the accepted luminosity, $L_{IR,Acc}$, is the same as the upper bound luminosity, $L_{IR,U}$. When the 100 μm flux density is an upper bound (poor quality index), $L_{IR,Acc}$ is taken to be the mean of the upper and lower bound luminosities. A comparison of the infrared luminosities listed in Table 5.2 for the ePIo identified as HAe/Be stars or BRN and the bolometric luminosities of the proposed associated stars shows that the infrared luminosities are significantly less (at most, only a few percent of the bolometric

Table 5.2: IRAS Data for Cam OB1 Extreme Population I Objects

Name	l [deg]	b [deg]	12μm[a] [Jy]	25μm[a] [Jy]	60μm[a] [Jy]	100μm[a] [Jy]	[25 − 12][b]	[60 − 25][b]	[100 − 60][b]	OZ[c]	$L^{d}_{IR,L}$ [$L_{\odot}$]	$L^{d}_{IR,U}$ [$L_{\odot}$]	$L^{d}_{IR,Acc}$ $L_{\odot}$]	M^{e}_{IR} [$M_{\odot}$]	Identity:Associated Star
IRAS 03118+6144	139.07	+3.67	5.91	2.54	0.51	26.65L	0.37	0.70	1.72	d	95	168	132	3.9	c-rich star
IRAS 03111+6041	139.54	+2.73	0.61	0.81	9.22	35.77L	0.12	1.06	0.59	f	39	137	88	3.5	BRN:BD+60 648
IRAS 03119+6025	139.77	+2.55	0.25L	0.22:	2.66	12.03	0.06	1.08	0.66	f	8	45	45	2.9	BRN
IRAS 03119+6017	139.84	+2.44	0.46	0.67	10.36	24.65	0.16	1.19	0.38	f	39	107	107	3.7	BRN
IRAS 03116+5951	140.04	+2.05	0.39	0.54	2.77L	27.90	0.14	0.71	1.00	f,HAe/Be	17	94	94	3.5	HAe/Be:HD 237091
IRAS 03111+5938	140.10	+1.83	0.38	1.27	5.73	17.17	0.52	0.65	0.48	f,HAe/Be	30	77	77	3.3	HAe/Be:HD 19820
IRAS 03139+6005	140.15	+2.40	0.30	0.40	5.26L	24.83	0.12	1.12	0.67	f	21	90	90	3.5	BRN
IRAS 03182+6017	140.51	+2.86	0.28L	0.18:	1.03:	10.24	0.19	0.76	1.00	f,HAe/Be	8	36	36	2.7	HAe/Be
IRAS 03164+5839	141.19	+1.36	0.87	0.35:	1.39:	21.24L	0.40	0.60	1.18	f,HAe/Be	17	76	47	2.9	HAe/Be:HD 237121
IRAS 03167+5840	141.22	+1.38	0.75	0.34	1.51:	26.32L	0.34	0.65	1.24	f,HAe/Be	16	89	53	3.0	HAe/Be:HD 237121
IRAS 03189+5828	141.56	+1.37	0.25L	0.26	3.08	10.09	0.02	1.07	0.52	f	13	66	66	3.2	BRN
IRAS 03234+5843	141.91	+1.91	0.50	1.81	5.66	784.90L	0.56	0.50	2.14	g,l,q,r,HII,HAe/Be	36	2200	1100	7.0	AFGL490-iki,outflow
IRAS 03208+5812	141.92	+1.28	1.83	0.63	1.96L	10.00	-0.46	0.49	0.71	?	33	61	61	3.1	star?,confused
IRAS 03236+5836	142.00	+1.82	82.39	278.40	716.70	784.90	0.53	0.41	0.04	g,l,q,r,HII,HAe/Be	5100	7300	7300	12	AFGL490,outflow
IRAS 03227+5824	142.02	+1.59	0.26L	0.30	2.31:	17.15	0.06	0.89	0.87	f,HAe/Be	12	59	59	3.1	HAe/Be
IRAS 03203+5740	142.15	+0.80	3.63	2.09	1.17	29.40L	-0.24	0.25	1.40	?	65	146	106	3.7	star?
IRAS 03267+5855	142.16	+2.30	0.52	0.38	3.92:	42.57L	0.14	1.01	1.04	?	20	137	79	3.4	BRN
IRAS 03243+5821	142.22	+1.65	0.69	1.42	2.74	38.82L	0.31	0.29	1.15	r,q,HAe/Be	27	134	81	3.4	HAe/Be
IRAS 03261+5829	142.34	+1.90	1.07	1.14	10.76	56.17	0.03	0.97	0.72	f	51	206	206	4.4	BRN

a) *IRAS* (Beichman *et al.* 1988) fluxes at 12, 25, 60 and 100 μm. A : following a flux value indicates a good quality flux measurement while a L represents an upper limit.
b) Colors from IRAS fluxes: $[25 - 12] = \log(F_{25}/F_{12})$, $[60 - 25] = \log(F_{60}/F_{25})$ and $[100 - 60] = \log(F_{100}/F_{60})$.
c) Occupation Zones as judged by Walker *et al.* (1989). See Table 5.1 for details. In summary the OZs are: a - bright stars, b - O-rich stars, c - optical stars, d - LRS C-rich stars, e - HII regions, f - blue reflection nebulae (BRN), g - red reflection nebulae, h - blue planetary nebulae, i - red planetary nebulae, j - blue galaxies, k - red galaxies, l - seyferts, m - quasars, o - T Tauri stars, o - LRS=3 stars, p - LRS=6 stars, q (author's designation) - Herbig Haro emission line stars, r (author's designation) - bipolar nebulae. Additional occupation zones are given for HII regions (Hughes & MacLeod 1989), UCHII regions (Wood & Churchwell 1989) and HAe/Be stars (Berrilli *et al.* 1992).
d) Luminosity of sources from IRAS emission. $L_{IR,L}$ has been calculated from the 12, 25 and 60 μm bands (Carpenter *et al.* 1995), $L_{IR,U}$ has been calculated in a similar manner from all four bands, $L_{IR,Acc}$ represents the accepted value of infrared luminosity in this paper. In the case of good 100 μm fluxes $L_{IR,U}$ and $L_{IR,Acc}$ are equivalent, while $L_{IR,Acc}$ is the mean of $L_{IR,U}$ and $L_{IR,L}$ when the 100 μm flux is an upper bound.
e) Mass of stars assuming the accepted infrared luminosity, $L_{IR,Acc}$, is equivalent to the bolometric luminosity and $L_{\odot} = M^{3.5}_{\odot}$ (Casoli *et al.* 1986).

luminosities). It has been observed with other BRN that a significant amount of stellar radiation, 10 - 50%, is reprocessed and emitted in the infrared (Sellgren 1984). This is not the case here, which suggests that either, a) the stars are quite far away from the BRN and may not be associated with the infrared sources or b) the identification is incorrect, or c) the radiation is being emitted outside of the *IRAS* bands. Sellgren's model suggests a peak in the emission near 3.3 - 3.4 μm due to small ($\sim$ 10 Å) particles. Additional infrared observations, particularly in the 1 - 10 μm range, are required to explore this possibility further.

While the *IRAS* data provide only limited information on the presence and nature of ePIo it can be concluded that:

1. There is an excess of infrared sources which can be associated with the Cam OB1 CO emission. This excess is concentrated in three specific areas centered on $l = 142.^{\circ}0, b = +2.^{\circ}0$, $l = 142.^{\circ}0, b = +2.^{\circ}5$ and $l = 138.^{\circ}5, b = +3.^{\circ}5$.
2. The [12–25–60] and [25–60–100] color-color planes constructed for sources with at least 3 moderate flux density measurements in these regions suggest that the majority of these sources are ePIo.
3. The ePIo associated with the Cam OB1 emission appear to lie in two groups in the [12–25–60] plane: the first group of 4 sources includes the two known outflows in the region while the second group possibly consists of HAe/Be stars or BRN. Higher resolution observations, particularly in the infrared, are required to model the interaction of the illuminating star(s) with attendant dust.

5.3 ePIo Identified by their Optical or Radio Emission

In the previous section ePIo have been identified on the basis of their infrared emission. However, many ePIo, especially HII and BRN, are extended objects which can be identified by their optical or radio emission. These objects have traditionally served not only as indicators of recent star formation but also as tracers of the spiral structure in the Galaxy. In particular, the seminal work of Georgelin & Georgelin (1976) has served as a standard reference for the construction of rotation curves of the Galaxy, which has only recently been superseded by the work of Blitz et al. (1982) and Brand & Blitz (1993). The region of the Galaxy studied in the present survey (Di96) is rich in HII regions identified in optical surveys (Shajn & Gaze 1951, Gaze & Shajn 1953, 1954, 1955, Sharpless 1959, Dubout-Crillon 1976, Parker et al. 1979), and radio recombination surveys (Reifenstein *et al.* 1970, Lockman 1989).

BRN have also been extensively studied in the region presently under investigation, primarily from the Palomar Observatory Sky Survey (POSS) plates (van den Bergh 1966, Racine 1968, Herbst 1975, van den Bergh & Herbst 1975).

Optical surveys of HII regions range in design from those with low spectral selectivity, $\Delta\lambda \sim 100-200$Å, with moderate sensitivity, ~ 50 cm^{-6} pc, e.g., Shajn & Gaze 1951, Gaze & Shajn (1953, 1954, 1955), Sharpless (1959), to those with higher selectivity, $\Delta\lambda \sim 10 - 50$Å, and higher sensitivity, ~ 30 cm^{-6} pc, e.g., Dubout-Crillon (1976), and Parker *et al.* (1979). Variation in the optical survey parameters can be attributed to the questions addressed in each survey. Surveys which serve to make the initial identification of HII regions (Shajn & Gaze 1951, Gaze & Shajn 1953, 1954, 1955, Sharpless 1959) made use of low selectivity to allow a large throughput of photons at or near H_α, while surveys considering the contribution from particular emission lines (Dubout-Crillon 1976, Parker *et al.* 1979) isolated those lines with very narrow filters.

Determination of the velocity of the H_α emission has been carried out primarily via Fabry-Perot interferometry (Georgelin & Georgelin 1976, Fich et al. 1990). Unfortunately, the H_α emission profile can be very broad, which makes it difficult to determine its central velocity. In some cases (Reifenstein et al. 1970, Lockman 1989), radio recombination lines have been used to determine the velocity of the H_α emission, with the proviso that the peak of the radio recombination line may not coincide exactly with the peak of the H_α emission (Fich et al. 1990). It is also possible to make use of H_2O or OH (or both) maser emission associated with young, massive stars (Genzel & Downes 1979, Cesaroni et al. 1988, Felli et al. 1992) to infer the velocity of the H_α emission. However, the H_2O/OH masers may also have a velocity component due to bulk motion, i.e., an outflow, which reduces the reliability of this measurement. The measurement given the most weight in this study for the velocity of the HII regions is the velocity of associated CO emission (Blitz et al. 1982, Wouterloot & Brand 1989, Fich et al. 1990). CO profiles are narrower, and hence give a more accurate measurement of the central velocity than H_α emission profiles, while still being coincident with one another, i.e., typically $v_{CO} - v_{H_\alpha} = 0.5 \pm 0.5$km s^{-1} (Fich et al. 1990). In the case of multiple CO emission features seen along the line-of-sight, the CO feature with the brightest temperature, after scaling for beam dilution, is the CO feature which is assumed to be associated with the HII region. Table 5.3 summarizes the data available for the optically identified

HII regions (4) with well-determined distances.

In many cases, the cataloged optical HII regions have only been imaged, and no cross-identification has been attempted with the optical HII regions of known distance. A comparison of the two sets of data suggests that in many cases the 'imaged only' optical HII regions are coincident with many of the better studied HII regions. Differences in the image shape and size can be attributed to differences in sensitivity between the surveys, as well as the detail with which each survey described a particular HII region. In the cases where there is some ambiguity regarding which CO feature is associated with an HII region, it is necessary to consider the quality of the image. If the HII region is faint it is assumed to be associated with the more distant CO feature, with the dust associated with the foreground CO obscuring the H_α emission. A brighter HII region is assumed to be closer and free from obscuration. This assignment is consistent with their appearance on the POSS plates. Hence, a particular optical HII region which has only been imaged can almost always be assigned a distance based upon a positional coincidence with an HII region of known distance or a CO feature of known distance. Table 5.4 summarizes the data available for the two optically identified HII regions without well determined distances.

Optically identified BRN have been extensively studied, to a large extent from the POSS plates (van den Bergh 1966, Racine 1968, Herbst 1975), in order to trace out the spiral structure of the Milky Way through the illumination of the associated dust by hot luminous stars. Table 5.5 presents the summary of these data for Cam OB1, taken primarily from van den Bergh (1966). van den Bergh (1966) has claimed that there is a relationship between the size of a reflection nebula and the B magnitude of the illuminating star ($B = 11.0 - 5 \log R(B)$, where R(B) is the angular radius of the nebula in arcmin as measured on the blue POSS plate). In two cases shown in Table 5.5 (HD 20041 and HD 20798) this holds true. However, in the case of the other two stars (HD 21291 and HD 21389), the illuminating star is fainter than expected. This may be an indication that there are more stars contributing to vB14 and vB15. Another point of interest is that there is a spatial coincidence between the optical HII region BFS29 and the optically identified BRN vB15. Both these objects are coincident with the A0Ia star, HD 21389.

Figure 5.7 shows a map of the ePIo selected on the basis of their *IRAS* colors or radio/optical identification against the associated Cam OB1 CO emission. It is very apparent from this figure that the ePIo, by and large, are clustered in two groups

Table 5.3: Optically Identified HII Regions in Cam OB1 (with Reliable Distances)

Object Name[a]	Alternate Designation[a]	l^b [deg.]	b^b [deg.]	v^c_{LSR} [km s^{-1}]	R[da] [kpc]	D[c] [arcmin]	Ref.[f]	Comments
BFS24		134.34	3.56	9.7	(0.77)	20	BFS	CO line emission.
S202		140.59	1.92			170	Sh	H_α image.
		140.60	1.90			170	DC	H_α image.
		140.59	1.92	11.5	(0.93)	170	BFS	CO line emission.
		140.57	1.94	2.6			FTD	H_α Fabry-Perot.
		140.59	1.92	11.5	0.98	170		This paper.
	BFS28	141.73	2.76	10.2	(0.83)	20	BFS	CO line emission. Part of S202.
		141.73	2.76	10.2	0.98	20		This paper.
	BFS29,DG17	142.18	2.06	10.9	(0.89)	30	BFS	CO line emission. Part of S202.
		142.18	2.06	10.9	0.98	30		This paper.

Table 5.4: Optically Identified HII Regions in Cam OB1 (without Reliable Distances)

Object Name[a]	Possible Associated[a] HII Regions	l^b [deg.]	b^b [deg.]	v^c_{LSR} [km s^{-1}]	R[d] [kpc]	D[c] [arcmin]	Ref.[f]	Comments
SG3.017	S202	139.62	2.70		0.98	20	SG3	H_α image.
SG3.018	S202	140.30	2.40		0.98	30	SG3	H_α image.

a) Object name or alternative found in SIMBAD.
b) Galactic coordinates (l^{II}, b^{II}).
c) Radial velocity of object corrected to the Local Standard of Rest based upon standard solar motion.
d) For Cam OB1 the distance (no parentheses) has been obtained from main sequence fitting of associated stars (Chapter 4). Distance obtained from a Brand rotation curve (Brand & Blitz 1993) are also given, i.e., from $R = v_{LSR}/A\ sin(2l)cos^2(b)$, where $A = 12.6$ km s^{-1}.
e) Angular diameter of object.
f) BFS:Blitz *et al.* (1982), DC:Dubout-Crillion (1976), FTD:Fich *et al.* (1990), Sh:Sharpless (1959), and SG3: Dixon & Sonneborn (1980).

Table 5.5: Properties of Optically Identified BRN

Name[a]	l [deg]	b [deg]	Neb. Type[b]	R(B)[c] [arcmin]	R(R)[c] [arcmin]	Associated Star[d]	Sp Type[d]	B[d] [mag]
vB10	141.6	-0.04	I	8.0	5.4	HD 20041	A0Ia	6.52
vB11	140.1	+3.9	II	3.1	2.3	HD 20798	B2III-IV	8.63
vB14	141.5	+2.9	II	23	23	HD 21291	B9Ia	4.62
vB15	142.2	+2.1	II	27	17	HD 21389	A0Ia	5.10

a) Number in catalog of van den Bergh (1966).

b) Nebular type - I: illuminating star is embedded in the associated nebula. II - illuminating star is outside the associated nebula.

c) Angular radius on blue POSS plate - R(B). and red POSS plate - R(R).

d) Stellar data for illuminating star.

centered on l = 142°. b = +2° (CO Complex F in Chapter 7) and l = 140°. b = +2°.5 (CO Complex B in Chapter 7). The former appears to be the more active of the two regions as it contains the only known outflows, AFGL490 and AFGL490-iki, while the latter is composed of lower luminosity HAe/Be or BRN. S202 clearly dominates the field and is coincident with many of the other ePIo. Only one source, IRAS 03118+6144, from the third density enhancement of infrared sources near $l = 139°.b = +3°.5$ survived the stringent selection process and it is a star.

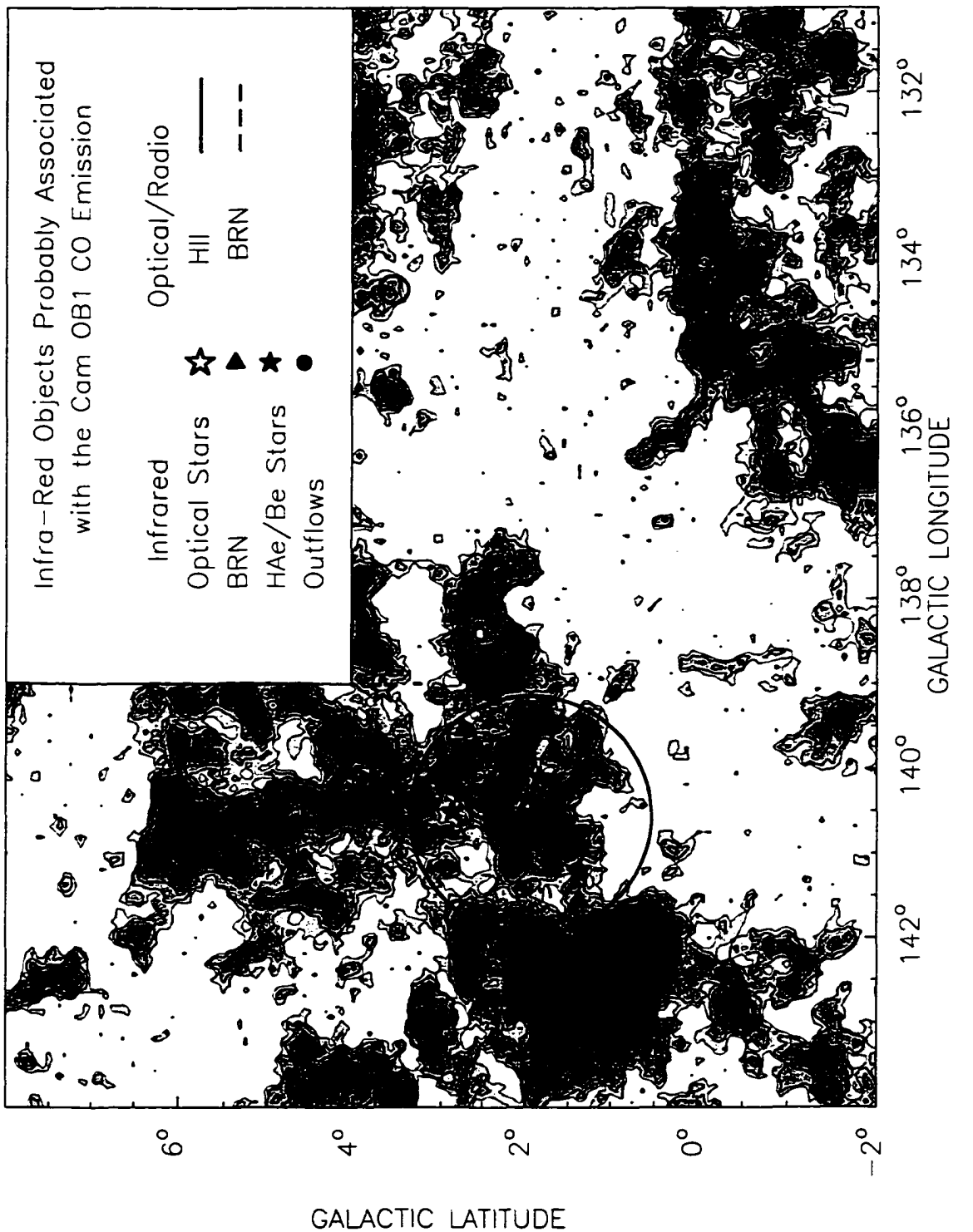

Figure 5.7 Location of infrared objects (19) coincident with the Cam OB1 CO emission and optically identified HII regions (4), radio identified HII regions (2), and optically identified BRN (4).

5.4 Methanol Masers

5.4.1 Introduction

Methanol masers occur during the early stages of evolution of massive stars when the stars are still embedded in their parental cocoon. In some cases these masers are positionally offset from UC HII regions, as measured by the position of their infrared emission and OH masers, and are believed to be associated with molecular outflows (Class I, Menten 1991). In other cases, such as the methanol masers considered throughout the remainder of this thesis ($5_1 - 6_0$ A^+, $\nu = 6.668518$ GHz), they are coincident with and pumped by the infrared emission from UC HII regions (Class II, ibid). The mechanism for producing these maser emissions is still very poorly understood. Ellingsen et al. (1996) have argued, on the basis of the positional coincidence of the peak radio continuum emission with the maser source, that one can make a distinction between a maser produced in a disk (maser coincident with the peak radio emission) and in an outflow (maser radially distributed along the axis of the outflow). However, of the two examples studied in detail by Ellingsen et al. (1996), only one could be modelled unambiguously as being associated with a disk, while the other could possibly be due to a disk or outflow or both. In either case it was not clear where the infrared source pumping the maser was located or how it was produced. This is indicative of our ignorance of how these masers are formed and further investigation is obviously warranted.

Given the great distance to regions of massive-star formation in the Galaxy (Orion is the closest at $\sim$ 400 pc) it follows that one needs high-resolution observations to understand the physics of these masers. A preliminary survey of candidate regions was undertaken with the DRAO 25.6m telescope [1] during the fall of 1994 to identify masers which may be associated with massive star formation in the outer Galaxy. The limits of the survey were set by the boundaries of the present CO survey (discussed in Chapter 2) while candidate sources were selected on the basis of their infrared colors and flux densities. One new maser, associated with IRAS 02455+6034, was detected.

[1] The DRAO 25.6m telescope is operated by the National Research Council of Canada as a national facility.

Table 5.6

Summary of Methanol Survey Parameters

with DRAO 25.6m Telescope

Observing Dates	Sept. - Dec. 1994
Observing Mode	Frequency Switching
	+0.50 MHz, $v_{LSR} \geq -30$ km s^{-1}
	-0.50 MHz, $v_{LSR} \leq -30$ km s^{-1}
Polarizations	Left and Right Circular
Bandwidth	0.50 MHz
Frequency Resolution	2.0 kHz
Velocity Resolution	0.09 km s^{-1}
Beamwidth (FWHM)	7'.4
T_{sys}	84 K

5.4.2 Observations

The 25.6m telescope at DRAO is suitable for preliminary surveys of methanol masers at 6.6 GHz provided one is cautious about its substantial error beam and large sidelobes. It has a moderately large collecting area, low noise receiver and a suitable spectrometer and large blocks of observing time for observations at 6.6 GHz can be obtained. Table 5.6 summarizes the relevant data for the methanol observations. Sources studied are listed in Table 5.7.

Source selection was made on the basis of infrared colors taken from *IRAS*. 'Class A' sources are designated as those sources which have colors and satisfy the minimum flux density requirements to be classified as both UC HII regions (Wood & Churchwell 1989) and HII regions (Hughes & MacLeod 1989). Twelve 'Class B' sources met the color criteria for both UC HII regions and HII regions but failed the minimum flux density requirements. Six 'Class C' sources met only the HII regions' infrared color and flux density requirements. Figure 5.8 shows the positions of the candidate *IRAS* sources searched in this survey superimposed on the present survey (Di96). In most cases CO emission could be associated with the *IRAS* sources,

Table 5.7
Positions Searched for the $5_1 - 6_0$ A^+ Methanol Maser

Name	l [deg]	b [deg]	v^b_{LSR} [km s^{-1}]	Range v^b_{LSR} [km s^{-1}]	Flux[c] Peak [Jy]	Flux[c] rms [Jy]	Comments[d]
Class A[a]							
IRAS 02230+6202	133.79	+1.42	−40			2.91	W3N.Contaminated by W3(OH)
IRAS 02232+6138	133.95	+1.06	−44.3	−42,−46.5	3880	9.01	W3(OH), H_2O maser
IRAS 02395+6244	135.28	+2.80	−71			3.09	AFGL 5077, H_2O maser
IRAS 02383+6241	135.81	+2.69	−71			3.72	
IRAS 02461+6147	136.39	+2.27	−43			2.16	AFGL 5085, H_2O maser
IRAS 02455+6034	136.84	+1.14	−45.4	−41,−46	35.0	0.73[e]	New maser
IRAS 02575+6017	138.30	+1.56	−38			2.21	OCL 369, H_2O maser
IRAS 02593+6016	138.50	+1.64	−39			2.22	S201
IRAS 03035+5819	139.91	+0.20	−40			2.43	BFS 26, H_2O maser
IRAS 03235+5808	142.25	+1.43	−47			2.25	AFGL 5095
Class B[a]							
IRAS 02171+6058	133.49	+0.18	−40			2.21	
IRAS 02244+6035	134.46	+0.13	−14			2.10	Contaminated by W3(OH)
IRAS 02333+5930	135.90	−0.46	−30			2.22	H_2O maser
IRAS 02437+6145	136.14	+2.12	−49			2.20	
IRAS 02407+6029	136.35	+0.82	−60			2.20	
IRAS 02541+6208	137.07	+3.00	−52			2.27	H_2O maser
IRAS 02503+6025	137.44	+1.26	−40			2.29	
IRAS 02589+6130	137.87	+2.70	−11			2.23	
IRAS 02598+6008	138.62	+1.56	−40			2.13	
IRAS 03101+5821	140.64	+0.67	−36			2.22	H_2O maser
IRAS 03211+6018	140.80	+3.06	−10			2.28	HD 12750 (B8)
IRAS 03306+5825	142.87	+2.18	−8			1.55	HD 24109 (B8)
Class C[a]							
IRAS 02245+6115	134.24	+0.75	−40			2.10	Contaminated by W3(OH)
IRAS 02421+6233	135.63	+2.76	−72			2.22	
IRAS 02531+6032	137.69	+1.52	−40			1.37	
IRAS 03064+5638	141.08	−1.06	−40			2.25	AFGL 5090
IRAS 03236+5836	142.00	+1.82	−14			1.77	AFGL 490, H_2O maser
IRAS 03211+5446	143.83	−1.56	−32			1.94	AFGL 5094

a) Class A refers to sources which meet all conditions to be UCHII regions (Wood & Churchwell 1989): [25 − 12] ≥ 0.57, [60 − 12] ≥ 1.30 with at least a good quality flux density measurement at 25μm and 60 μm, and HII regions (Hughes & MacLeod 1989): [25 −12] ≥ 0.40, [60 −25] ≥ 0.25 with F_{100} ≥ 80 Jy and at least a moderate flux density measurement at 25μm and 60μm. Class B sources meet the color criteria as above but not the flux density requirements. Class C sources satisfy only the conditions to be a HII region (Hughes & MacLeod 1989).
b) Central velocity of observation or, when a maser was detected, the velocity of peak maser emission and range in velocity over which it was detected.
c) Peak and 3 σ rms flux density of maser line.
d) H_2O masing from the indicated sources has been detected by Brand *et al.* (1994) or Comoretto *et al.* (1990). No H_2O masing from sources indicates the sources have been examined for H_2O masing but none has been detected.
e) These observations were obtained with frequency switching by 0.25 MHz in order to increase the signal-to-noise ratio.

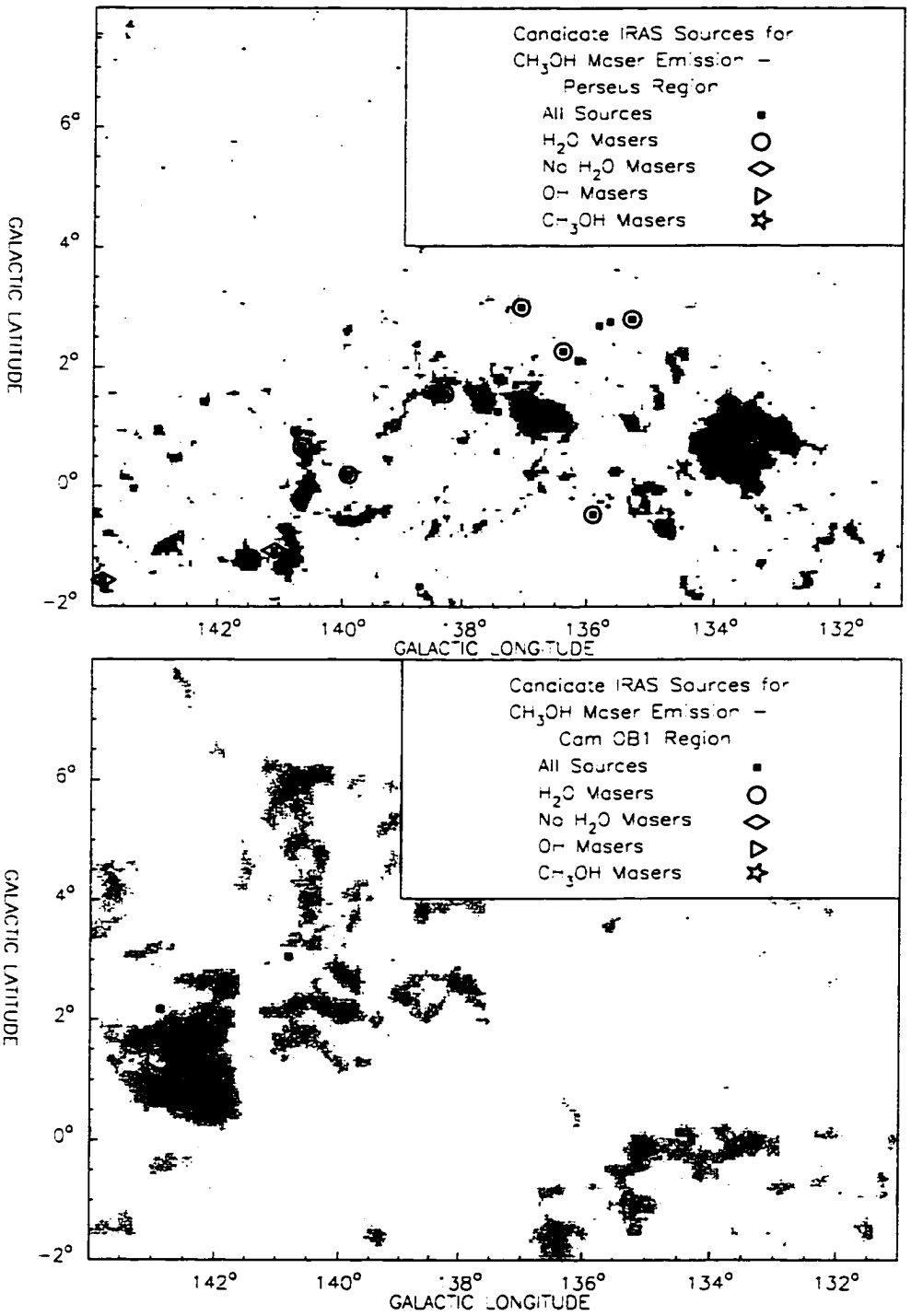

Figure 5.8 Overlay of *IRAS* sources examined for methanol emission over the integrated CO emission in the Perseus ($-70 \leq v_{LSR}/kms^{-1} \leq -30$) and Cam OB1 ($-22 \leq v_{LSR}/kms^{-1} \leq -5.5$) regions. The CO contours for both regions start at the 3 σ level, i.e., 1.37 K km s^{-1} for Cam OB1 and 2.18 K km s^{-1} for Perseus, and increase by a factor 1.58 thereafter.

which would support their selection as candidate star forming regions.

The observing frequency was switched every 8 seconds between the predicted frequency of the line and an offset reference frequency one bandwidth (0.5 MHz) away (+0.5 MHz for sources associated with Cam OB1 emission i.e., $-22 \leq v_{LSR}/\mathrm{km\ s^{-1}} \leq -5.5$, and -0.5 MHz for sources associated with Perseus emission, $-70 \leq v_{LSR}/\mathrm{km\ s^{-1}} \leq -30$). Records were averaged over sufficient time to ensure detection of moderately weak masers (typically 24 hr). Column 7 of Table 5.7 shows the rms noise level ($3\ \sigma$) for each observation. In a few cases the signal was identified as originating in W3(OH) and detected by the telescope's sidelobes. Such 'sources' were dropped from further investigation.

For the newly detected maser, a source associated with IRAS 02455+6034, further observations were made. In this case, four brief preliminary observations, one beamwidth away in each cardinal direction from the *IRAS* position, were first taken. From these, a more accurate position for the maser source was deduced: RA(2000) = $2^h49^m09^s.4$, DEC(2000) = 60°50′30″ or, in galactic coordinates $l = 136°.786$, $b = 1°.177$. This source was then re-observed for several days at the updated position with the frequency switched by only one half (+0.25 MHz) in order to increase the signal-to-noise ratio by folding the switched signal. The resultant spectrum is shown in Figure 5.9.

5.4.3 Discussion

The new maser (Figure 5.9) is clearly double-peaked and is reminiscent of what is seen in OH/IR stars. There is no simple classification for the spectra from methanol masers as they show considerable range in intensity and multiplicity of components (van der Walt et al. 1995). It is not possible from the present observations to determine whether there are two physically distinct masers along the line-of-sight or one maser emanating from two locations in the same region. Menten (1991) proposed that the $5_1 - 6_0A^+$ maser is due to the pumping by the infrared flux near 50 μm. This is consistent with the observed methanol flux density (35 Jy) and 60 μm flux density (168 Jy) for IRAS 02455+6034 if the efficiency of the pump is $\sim$ 20%. This efficiency is in good agreement with the masers found by Menten (1991), which ranged in efficiency from 5% (NGC 7538) to 42% (W3(OH)) for the five sources with measured *IRAS* flux densities. The peak flux density also falls within the range of observed flux densities found by Menten (1991). More extensive

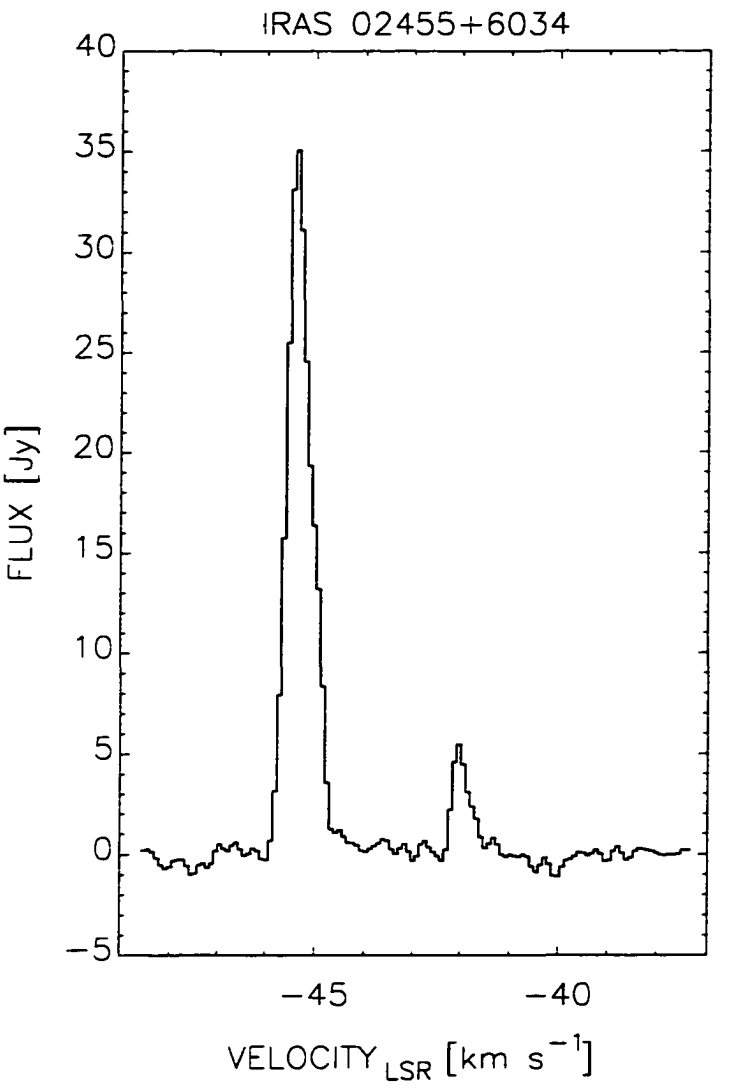

Figure 5.9 Spectrum for new methanol maser associated with IRAS 02455+6034.

surveys, particularly towards Southern Hemisphere objects, have been carried out by Schutte et al. (1993) and van der Walt et al. (1995). IRAS 02455+6034 is located in the [12–25–60] *IRAS* color-color plane (see Figure 4 in van der Walt et al. 1995) at the short wavelength end of the distribution typical for these sources. Hence, the maser associated with *IRAS* 02455+6034 appears to be a typical object of this class.

It is difficult to test the proposal of Ellingsen et al. (1996) regarding the location of the maser formation. There should be a correlation between the peak radio continuum emission and maser emission if the maser is produced in a disk around a massive star. If the maser is being produced in an outflow then it should be

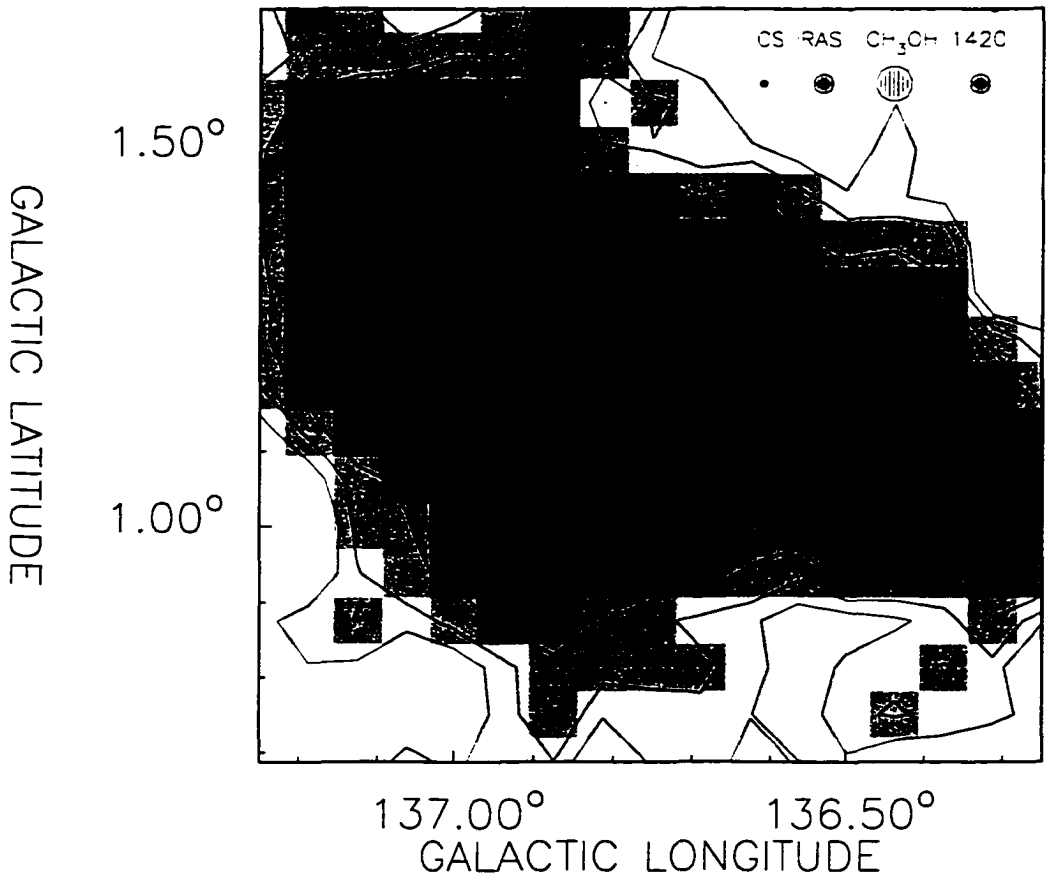

Figure 5.10 Positions of the methanol maser (open star), IRAS 02455+6034 (filled square), CS emission (open circle) and the only known radio-detected HII region, Lo2 (asterisk), superimposed on the associated CO emission. The contour intervals for the CO are the same as Figure 5.8.

distributed in a radial fashion about the peak radio emission along the axis of the outflow. A moderate resolution (9′), low sensitivity (130 mJy) radio continuum survey of the region at 1420 MHz (Kallas & Reich 1980) clearly shows a strong continuum feature (W5) which is very extensive and closely follows the CO emission. The peak radio emission of W5 is near the maser but the resolution and sensitivity are too poor to discern any radio emission features associated with the maser. The limitations of the 1420 MHz survey are clear when other well known masers are considered, such as Cep A which is a strong maser source (S_{peak} = 1420 Jy, Menten 1991) but shows only weak emission (5 - 10 mJy) at 20 cm (Hughes 1988). The only other radio continuum observation in the region, a 3 cm radio continuum observation at slightly higher resolution (3′), detected one HII region - Lo2 (Lockman 1989).

Figure 5.10 presents the updated position of the newly detected maser as well as the published position of IRAS 02455+6034 and the position of Lo2 overlaid on the associated CO emission (Di96). Given the resolution with which Lo2 was detected and the offset in position between Lo2 and both IRAS 02455+6034 and the maser, it is not likely that Lo2 is associated with the new methanol maser. Hence, the radio continuum source associated with the maser has not been properly identified to date, if it exists.

The only additional information on IRAS 02455+6034 available in the literature are some high resolution CS (2-1) observations by Bronfman *et al.* (1996). These observations of *IRAS* sources with UC HII colors show that IRAS 02455+6034 is a faint source in CS (T_{mb} = 0.25 K) but with one of the broadest lines in CS (Δv = 9.5 km s^{-1}) - there were 843 sources detected and IRAS 02455+6034 ranked 15th in linewidth. The peak velocities of the maser emission (-45.4 km s^{-1}) and CS emission (-39.8 km s^{-1}) do differ, but the CS emission may still be associated with the maser given the broad linewidth of the CS emission. Further work is required on the correlation of the linewidths in the CS sample with well studied maser regions before the significance of this ranking is understood.

5.4.4 Conclusions Regarding Methanol Masers

A recent survey with the DRAO 25.6m telescope has detected a new 5_1 - 6_0 A^+ methanol maser in the Perseus region associated with IRAS 02455+6034. A summary of the key points regarding this maser are:

1. It is of moderate strength ($\sim$ 35 Jy), spans a velocity range of -41 to -46 km s^{-1} and is located at $l = 136.^{\circ}786, b = +1.^{\circ}177$.
2. It does appear to be a typical Class II maser (Menten 1991) as it is closely associated with an UC HII region, as determined from its *IRAS* colors.
3. The central velocity of the maser is slightly offset from that of the CS emission feature.
4. Higher resolution radio and continuum observations with good sensitivity of the maser are required, in order to test the model of Ellingsen *et al.* (1996) as to whether the maser is being produced in a disk or outflow.

5.5 Molecular Outflows

5.5.1 Introduction

Molecular outflows were first detected in the late 1970's, and were quickly recognized as being a signature of a star very early in its formation. Indeed, the observation that the available force for accelerating the outflow from radiative pressure alone (L_*/c – the stellar luminosity divided by the speed of light) is always less than the required force, had been used as evidence that the source of energy for driving the outflow is due to the infall of material being accreted by the newly formed protostar and disk (Bally & Lada 1983). Observations of the brighter outflows were made in rapid succession after the nature of these objects was recognized: a list of $\sim$ 60 of these outflows was compiled by 1985 (Lada 1985). Fukui *et al.* (1993) extended this list to include $\sim$ 160 outflows, which number has been surpassed recently by Wu et al. (1996), who have compiled data for 264 outflows.

The observations presented here are of a new outflow, AFGL490-iki (Purton *et al.* 1995), serendipitously discovered during a recent CANFLEX (Canadian flexible high-frequency time allocation) observing run conducted in January 1995 with the James Clerk Maxwell Telescope (JCMT). [1] Part of those observations was of molecular clouds in the Cam OB1 region (Di96, see Chapter 2), and employed, for the first time in operational mode, the 'on-the-fly' raster-scan capability of the telescope. It was known at the time that there was a very energetic outflow, AFGL490 (Hasegawa 1986, Campbell et al. 1986, Mitchell et al. 1992, Mitchell et al. 1995), in the region, which appeared to be associated with multiple components of CO emission (Mitchell et al. 1992). These observations were undertaken to determine whether the multiplicity of such CO components existed throughout the parent cloud, or was restricted to the neighborhood of AFGL490. The observations reported here detected the presence of multiple CO emission only in the vicinity of AFGL490 and led to the discovery of AFGL490-iki. This supports the argument that star formation in the region is enhanced in the vicinity of AFGL490, and may have been prompted by the collision of two CO complexes (see Chapter 7).

[1] The JCMT is operated by the Royal Observatory, Edinburgh, for the Particle Physics and Astronomy Research Council, the National Research Council of Canada, and the Netherlands Organization for Pure Research.

Table 5.8

Summary of Outflow Survey Parameters

with the JCMT 15m Telescope

Observing Dates	Jan. 20 - 28, 1995
Observed Line	^{12}CO(2-1)
Observed Central Frequency	230.5380 GHz
Spectral Resolution	189 kHz (0.25 km s^{-1})
Channel Spacing	156 kHz (0.20 km s^{-1})
Observing Mode	'on-the-fly' Position Switching
Beamwidth (FWHM)	21″
T_{sys}	80 K
Integration Time/Spectra	5 sec.
$T_{R.rms}$/Channel	0.95 K
Off-Positions	
Position	l , b
A	142°.37, +2°.37
B[1]	141°.70, +1°.60
C	141°.40, +2°.70
D	142°.90, +1°.30
E	141°.80, +1°.80

1. The B off-position was observed to have some emission at -40 km s^{-1}, but it was free of emission over the velocity range of the quiescent CO gas in Cam OB1: $-5 \geq v_{LSR}/\mathrm{km\ s^{-1}} \geq -22$ (see Chapter 2).

5.5.2 Observations

Observations of the Cam OB1 region presented here were the first to use the 'on-the-fly' raster-scan technique. In this method, the telescope sweeps through a constant arc in the sky (usually in R.A.), integrating as it does so. A row of such observations is preceded and followed by observations at an off-position, while a grid of observations constitutes several rows offset in declination. For the observations presented here the total integration time for each position was 5 seconds, which resulted in a typical $T_{R,rms} \sim 0.95$ K. Position switching was used to linearize the response of the spectrometer, with off-positions sampled at the beginning and end of each row. The off-positions were selected at the beginning of the run after a check, via frequency-switching, of positions believed to be free of CO emission (Di96). Table 5.8 provides the relevant data for the outflow observations.

The time allotted allowed two passes through the region. In the first pass, a series of observations each comprising a 9×9 grid, with each grid point separated by 40″, were made. The central position for each grid was selected on the basis of either: a) a coincidence with an *IRAS* point source (Beichman et al. 1988) which had at least three moderate-quality flux measurements, which allows a preliminary classification as to its nature (Walker et al. 1989, see §5.3), or, b) the coincidence with CO emission (peaks and troughs) known to be in Cam OB1 (Di96, see Chapter 2). Table 5.9 lists the results of these observations. Figure 5.11 provides an overlay of the observed positions, *IRAS* positions and off-positions onto the CO emission. In the second pass, there was time to investigate further only the newly detected outflow, AFGL490-iki (Purton et al. 1995), which was labelled as Cam 4 in the first pass (Table 5.9). To this end, a 13×17 grid (17 rows, each consisting of 13 observations) was made, with the central position now coincident with AFGL490-iki, but with the grid points separated by 10″. Figure 5.12 shows the spectra for AFGL490-iki, from the second grid, while Figure 5.13 is an integrated map of the CO emission from AFGL490-iki made from these spectra, showing the red and blue lobes of CO emission.

Table 5.9
Positions Searched for Multiple-Peaked CO Emission

Name	l [deg]	b [deg]	Assoc. Source[a]	Ref. Off[b]	Comments
Cam 1	142.19+1.88	G142.1+1.8 12.3	Cam A		Peaked emission at -12 and -9 km s^{-1} which is broad ($\Delta v \sim 3-5$ km s^{-1}), and heavily blended, $T_{max} \sim 6$ K.
Cam 2	142.34+1.90	IRAS 03261+5829	Cam A		Double-peaked spectra throughout, as for Cam 1, $T_{max} \sim 8$ K.
Cam 3	142.22+1.65	G142.1+1.8-12.3	Cam B		As for Cam 1, $T_{max} \sim 8$ K.
					Third, narrow ($\Delta v \sim 2-3$ km s^{-1}), component at -18 km s^{-1}, $T_{max} \sim 3$ K.
Cam 4	141.92+1.91	IRAS 03234+5843	Cam B		AFGL490 – iki. Very broad wings ($\Delta v \sim \pm 30$ km s^{-1}), with central, quiescent clouds from -10 to -15 km s^{-1}, which are self-absorbed ($T_{max} \sim 8$ K, while neighboring position has $T_{max} \sim 12$ K).
					Double-peaked spectra, as for Cam 1, seen in NW part of field, $T_{max} \sim 8$ K.
Cam 5	142.09+1.74	G142.1+1.8 12.3	Cam B		As for Cam 1, with possible self-absorption.
					A third, narrow feature, at -22 km s^{-1}, $T_{max} \sim 8$ K.
Cam 6	141.81+2.66	G142.0+2.6-10.4	Cam C		Two narrow features at -10 and -13 km s^{-1}, $T_{max} \sim 6$ K.
Cam 7	141.80+2.12	G142.0+2.6-10.4	Cam B		Double-peaked spectra, as for Cam 1, $T_{max} \sim 6$ K.
Cam 8	141.16+2.23	G141.1+2.1-12.6	Cam A		Mostly single-peaked spectra at -9 km s^{-1}, $T_{max} \sim 3$ K.
					A few double-peaked spectra in W part of field, $T_{max} \sim 6$ K.
Cam 9	142.16+2.08	G142.1+1.8-12.3	Cam A		Narrow features at -9, -11 and -13 km s^{-1}, heavily blended in some places, $T_{max} \sim 6$ K. Some spectra very noisy.
Cam 10	142.49+1.33	G142.5+1.1-13.4	Cam D		Two broad features at -11 and -16 km s^{-1}. Both features possibly self-absorbed, $T_{max} \sim 5$ K.
Cam 11	142.64+1.13	G142.5+1.1-13.4	Cam D		Single, broad feature at -11 km s^{-1}, $T_{max} \sim 3$ K.
					Second weak peak at -13 km s^{-1} in E part of field, $T_{max} \sim 2$ K.
Cam 12	142.69+2.04	G142.5+1.1-13.4	Cam A		Double-peaked, narrow spectra at -9 and -11 km s^{-1}, in SW corner of field, $T_{max} \sim 6$ K.

Table 5.9 cont.
Positions Searched for Multiple-Peaked CO Emission

Name	l [deg]	b [deg]	Assoc. Source[a]	Ref. Off[b]	Comments
Cam 13	143.07	+1.70	G143.3+1.7 10.3	Cam D	Strong, broad feature at -9 km s^{-1}, which is possibly self-absorbed, $T_{max} \sim 7$ K. Two other narrow features seen at -11 km s^{-1} (NE corner, $T_{max} \sim 4$ K) and -16 km s^{-1} (SW corner, $T_{max} \sim 4$ K).
Cam 14	142.00	+0.87	G142.0+1.0 15.3	Cam E	Heavily-blended, very broad ($\Delta v \sim 8$ km s^{-1}) feature centered on -15 km s^{-1}, $T_{max} \sim 5$ K.
Cam 15	142.21	+0.67	G142.0+0.6 15.6	Cam E	As for Cam 14. $T_{max} \sim 4$ K. Weak feature at 0 km s^{-1}, $T_{max} \sim 2$ K.
Cam 16	142.21	+0.93	G142.0+1.0 15.3	Cam E	As for Cam 14, $T_{max} \sim 3$ K. Two peaks, well defined at -20 and -14 km s^{-1} in NW corner, $T_{max} \sim 4$ K.
Cam 17	142.82	+0.80	G142.5+1.1 13.4	Cam E	As for Cam 15.
Cam 18	142.71	+1.73	G143.3+1.7 10.3	Cam D	Double-peaked spectra with broad lines at -13 and -20 km s^{-1}, $T_{max} \sim 6$ K.
Cam 19	141.90	+0.60	G142.0+0.6 15.6	Cam E	Broad, self-absorbed feature at -14 km s^{-1}, $T_{max} \sim 7$ K.
Cam 20	142.65	+1.65	G142.5+1.1 13.4	Cam D	Weak emission at -11, -13 and -20 km s^{-1}. $T_{max} \sim 3$ K.
Cam 21	143.30	+1.65	G143.3+1.7 10.3	Cam D	Very broad, self-absorbed feature at -10 km s^{-1}. $T_{max} \sim 4$ K.
Cam 22	142.20	+2.67	G142.0+2.6 10.4	Cam A	Narrow feature at -10 km s^{-1}, $T_{max} \sim 5$ K. Some noisy spectra.
Cam 23	142.20	+2.08	G142.1+1.8 12.3	Cam A	Weak emission at -10 km s^{-1} in W half of field, $T_{max} \sim 5$ K.
Cam 24	142.20	+1.77	G142.1+1.8 12.3	Cam A	Broad, heavily blended double-peaked spectra centered at -8 and -10 km s^{-1}, $T_{max} \sim 8$ K.
Cam 25	142.20	+0.80	IRAS 03203+5740	Cam E	Weak emission features at 0, -10 and -13 km s^{-1}, $T_{max} \sim 4$ K.
Cam 26	141.15	+2.15	G141.1+2.1 12.6	Cam C	Weak emission feature at -15 km s^{-1}, $T_{max} \sim 3$ K.
Cam 27	140.10	+2.10	G139.8+1.7 13.6	Cam C	Weak emission feature at -11 km s^{-1}, $T_{max} \sim 3$ K.

a) Associated sources: IR – IRAS source (IRAS 1988), G – centroid (l, b, v) of CO emission from Lyder (1997).

b) Off-positions, as listed in Table 1, used during observation.

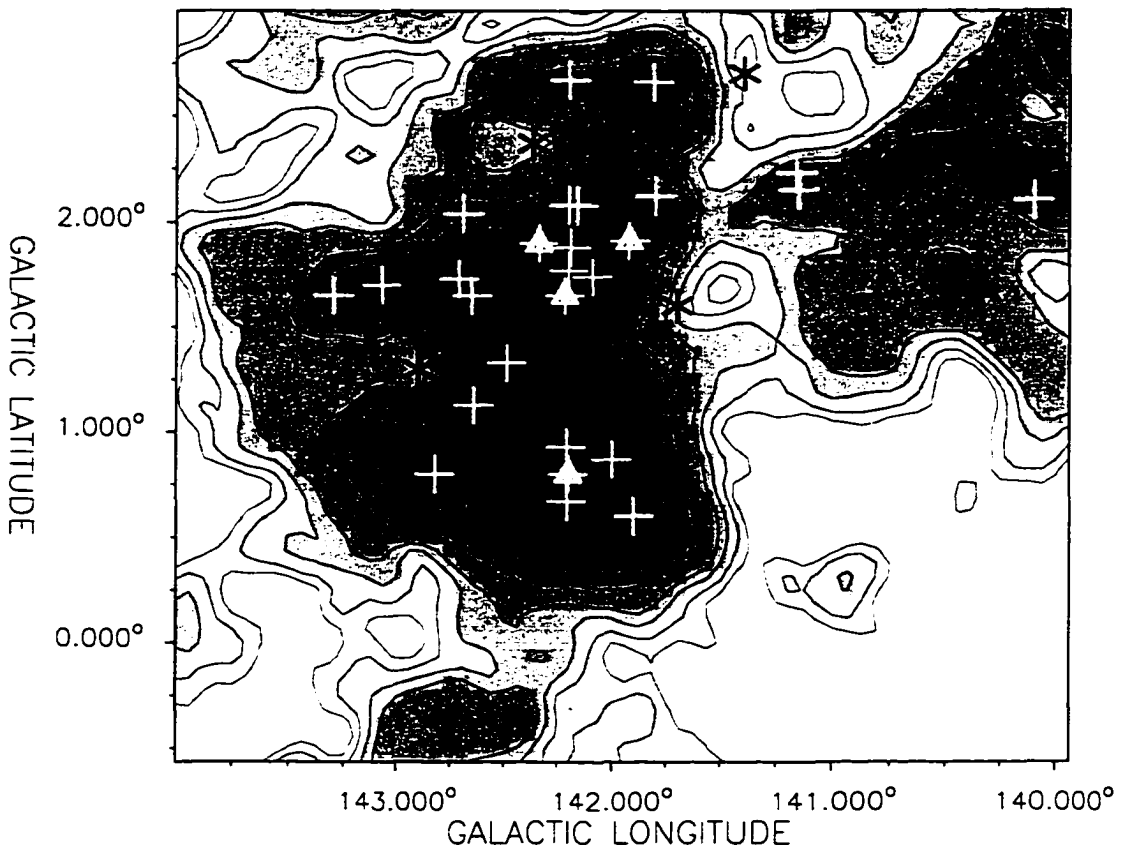

Figure 5.11 Overlay of observations onto integrated CO emission ($-5 \geq v_{LSR}/\mathrm{km\ s^{-1}} \geq -22$) in Cam OB1 region. The white crosses show all positions searched (Table 2), the white triangles show *IRAS* point sources (IRAS 1988) which have at least three moderate-quality flux measurements, and the black asterisks are the off-positions (Table 1). The contour levels for the CO emission are: 1.39 (3σ), 2.20, 3.48, 5.0, 10.0, 15.0, 20.0, 24.0, 28.0..... 54.0 K km s^{-1}.

5.5.3 Discussion

5.5.3.1 General Properties of the CO Spectra

It is possible to derive some statistics on the physical properties of the CO emission in Cam OB1 from the data in Table 5.9. Firstly, it would appear on the basis of Figure 5.11 that the CO emission can be separated into two spatial groups, emission lying to the north or to the south of $b \sim +1°.5$ (Figure 5.11; these correspond to Complexes F and G, respectively, in Chapter 7). The first group, the northern emission, has an estimated mean peak temperature, $T_{max} = 5.95 \pm 0.50$K,

while the southern emission is considerably colder, with an estimated mean peak temperature given by $T_{max} = 4.10 \pm 0.41$K. This is not surprising, as the northern emission (Complex F, Chapter 7) contains both AFGL490 and AFGL490-iki, which can act as internal heat sources. Furthermore, a number of late O- and early B-type stars, which are members of Cam OB1, are probably in close proximity to the northern emission (Humphreys 1978, see Chapter 6), and serve as an additional heat source to the ambient radiation field. Secondly, the spectra taken of the southern emission, for the most part, can be well fit by a single Gaussian profile whose peak emission lies in the velocity range ~ -13 to -16 km s^{-1}, while the spectra of the northern emission appears to be bimodal with peak velocities ~ -8 to -10 km s^{-1} or -11 to -13 km s^{-1}. Finally, all the spectra of the southern emission features have relatively broad lines ($\Delta v \sim 3 - 5$ km s^{-1}), while the spectra of the northern emission is made up of a mixture of emission features with narrow ($\Delta v \sim 2 - 3$ km s^{-1}) and broad lines.

Note that all the spectra of northern emission with narrow lines were taken from sites which are well away from the star forming region containing AFGL490-iki, and are associated with smaller CO emission features, e.g., the emission near $l = 140.^{\circ}10, b = +2.^{\circ}10$ and $l = 141.^{\circ}81, b = +2.^{\circ}66$. The remaining northern emission features, which are associated with AFGL490-iki, all have relatively broad lines. The difference in the linewidth of the spectra amongst the northern emission features can be attributed to a difference in the turbulence present (Larson 1981), i.e., the spectra with broader lines are probing larger, more turbulent features. The broad lines of the spectra taken from the southern emission features, which also belong to a large CO complex, can be explained in a similar manner.

5.5.3.2 AFGL490-iki

It can be seen from Figure 5.12 that AFGL490-iki is quite an energetic outflow, with a peak radiation temperature of $\sim 8 - 10$ K and a large velocity outflow $\sim \pm 40$ km s^{-1}. The outflow looks symmetric, and there are no apparent velocity features which could be construed as ejecta from the outflow (Mitchell et al. 1992). The observational grid did not cover all of the outflow emission but the general morphology of the outflow can be discerned.

Figure 5.13 shows an integrated map of the outflow emission. The blue-shifted emission (-37 to -16 km s^{-1}), shown by the solid contours, appears slightly larger

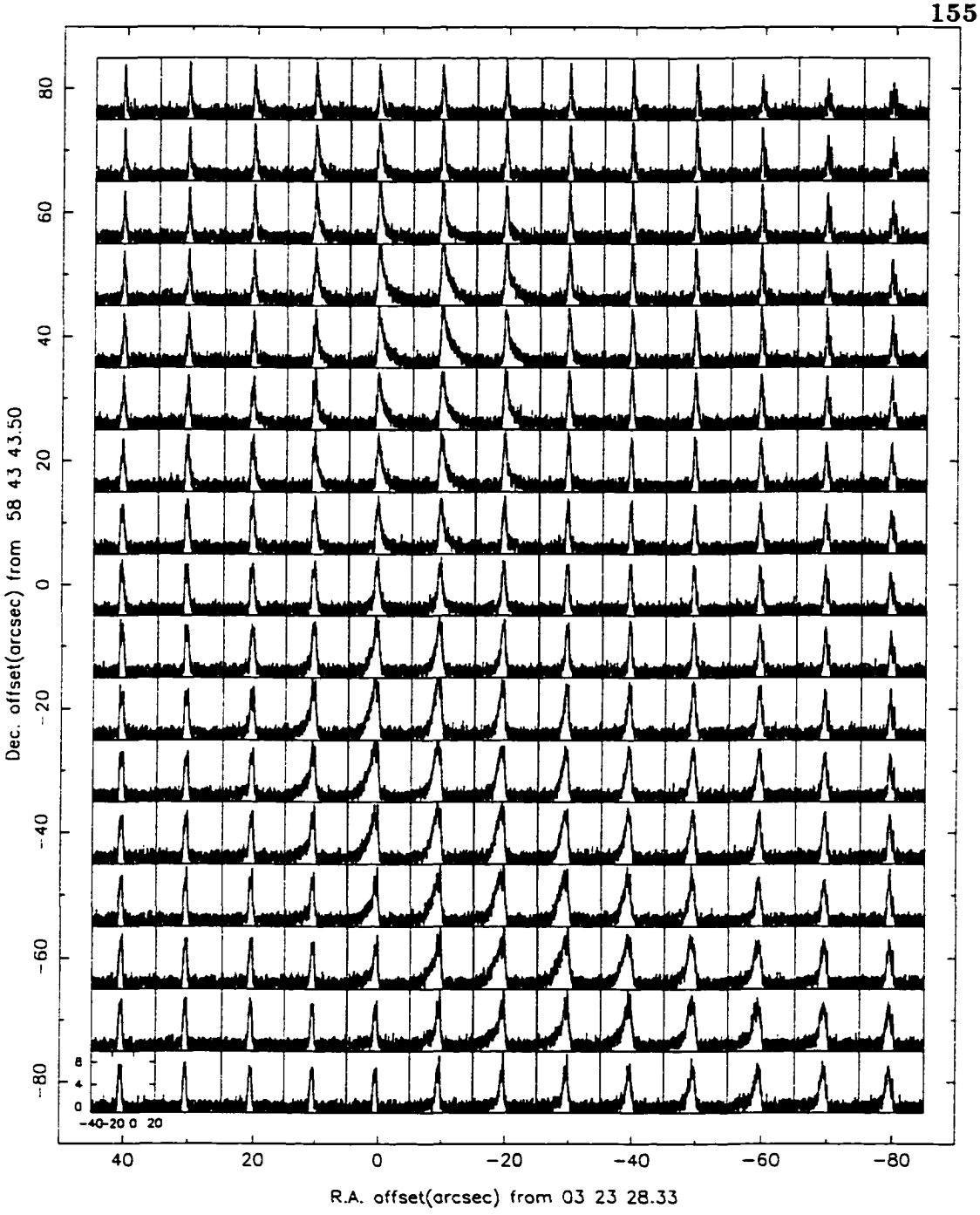

Figure 5.12 ^{12}CO(2-1) emission for AFGL490-iki centered on $l = 141.^{\circ}580, b = +1.^{\circ}475$. North is to the top and east is to the left. The positional offset between each spectrum is 10″ and $T_{R,rms} = 0.95$ K. The central velocity of the outflow is ~ -16 km s^{-1}, the red-shifted emission (upper left-hand corner) extends to 0 km s^{-1}, while the blue-shifted emission (lower middle to right-hand corner) extends to -30 km s^{-1}.

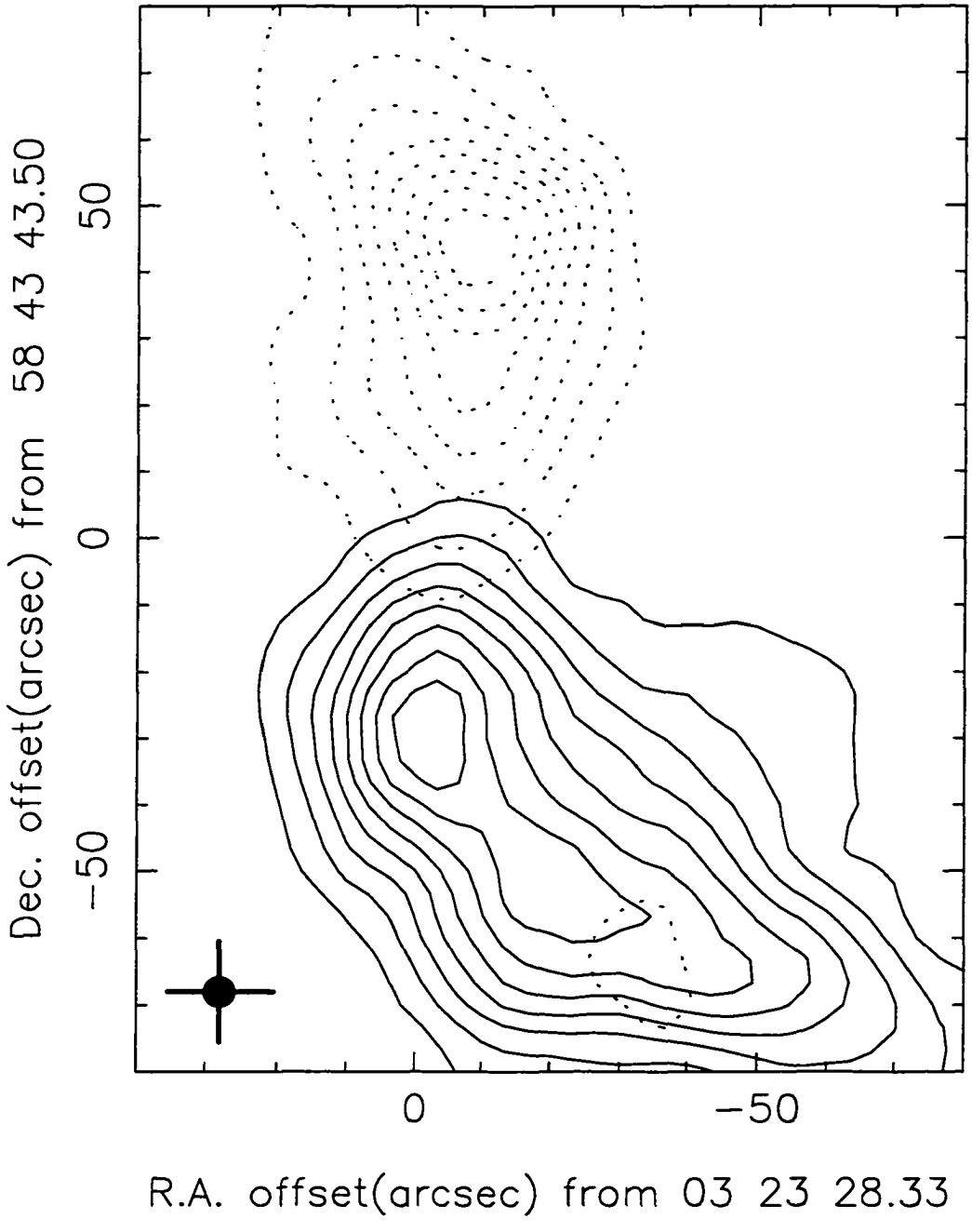

Figure 5.13 Average ^{12}CO(2-1) emission for AFGL490-iki, as shown in Figure 5.12, over the velocity range -37 to -16 km s^{-1} (solid-line, blue-shifted emission) and -10 to +11 km s^{-1} (dotted-line, red-shifted emission). Contours are at every 0.3 K. The resolution of the survey is indicated by the cross in the lower left-hand corner while the grid coordinates are in equatorial coordinates (B1950).

than the red-shifted emission (-10 to +11 km s^{-1}). Both lobes of the outflow appear to be elongated and have axial ratios of 1.8 (blue lobe) and 2.0 (red lobe). It is also clear from the map that the peaks of the emission for both lobes are well separated along the line-of-sight, which suggests the two lobes are inclined to the line-of-sight and that the angle of inclination to the line-of-sight, θ, is large. Furthermore, there is a small red-shifted emission feature near the southern tip of the blue-shifted lobe that has spilled over into the red-shifted velocity range which could occur if the inclination angle is high and the outflow broad. The amount of CO contained in each lobe, assuming optically thin gas, may be obtained from summing the total column density contained within each lobe. For ^{12}CO(2-1) the total column density is given by (Snell et al. 1984):

$$N_{total} = 1.04 \times 10^{13} T_{ex} e^{\frac{16.59}{T_{ex}}} \int T_R(2-1) dv, \quad [cm^{-2}] \tag{5.15}$$

where $T_R(2-1)$ is the detected radiation temperature, after correction for atmospheric attenuation and beam coupling, T_{ex} is the excitation temperature of the (2-1) transition, and dv is the increment of the velocity of the gas emission, i.e., 0.25 km s^{-1}. When the lobes are not aligned exactly with the line-of-sight to the observer, as is the case here, then dv is foreshortened by $cos\ \theta$ and hence, Eq. 5.15 must be divided by $cos\ \theta$. Assuming $T_{ex} \sim 15$ K, which is typical for these sources (Wu *et al.* 1996), an inclination angle of 45° and a distance of 975 pc (Chapter 4), then the mass contained in the wings of AFGL490-iki is 0.85 $M_\odot$ (red lobe) and 2.50 $M_\odot$ (blue lobe), suggesting a total ejection of $\sim$ 3.4 $M_\odot$. These values are a lower bound as they assume the gas is optically thin. Optically thick emission must be scaled by $\tau/(1-e^{-\tau})$ while assuming $T_{ex} = 20$ and 25 K scales all solutions by 1.02 and 1.07, respectively. Finally, the kinematic timescale of the outflow, assuming a smooth continuous flow of $\sim$ 15 km s^{-1}, is $\sim 2 \times 10^4$ yr, for both lobes, while the total kinetic energy of the outflow is $\sim 2.7 \times 10^{46}$ erg.

The driving source behind AFGL490-iki, IRAS 03234+5843, has *IRAS* colors suggestive of a pre-main sequence star (Walker et al. 1989, see §5.3). The luminosity of this source, based upon its *IRAS* fluxes (Carpenter et al. 1995, see Table 5.2), is $\sim$ 1100 $L_\odot$. If it is further assumed that the central star powering the outflow is close to the main sequence, then its mass may be found assuming $L_\odot = M_\odot^{3.6}$ (Casoli et al. 1986), i.e., the central star powering AFGL490-iki has a mass $\sim$ 7 $M_\odot$ (a B3 - B4 star).

In comparison to other outflows in the Galaxy (Fukui et al. 1993, Wu et al. 1996), it would appear that AFGL490-iki is typical for high-mass stars. It is more energetic than average (Fukui *et al.* 1993), but considerably less energetic than AFGL490 (Mitchell et al. 1992). Other outflows which agree very well with the above derived parameters for AFGL490-iki, e.g., mass in lobes, luminosity of source and outflow velocity, include NGC 2024/Ori B, LkHα198, IRAS 01133+6434, IRAS 00259+6510, NGC7129 FIR and NGC 23032+5937 (Wu et al. 1996).

It is interesting to note that if it is assumed that the large-scale Cam OB1 CO emission features at -9 and -11 km s^{-1} (see Chapter 7) are of depths comparable to their widths (say, one degree across or ~ 17 pc), and they are at the same distance, which is supported by both components being warmed, then the time scale possible for an interaction between the two would be of the order of a crossing time, i.e., $\sim 8 \times 10^6$ yr. The time scale for AFGL490-iki as an outflow, or as a pre-main sequence star (Palla & Stahler 1993) is considerably less than this. Hence, it cannot be ruled out from a consideration of time scales, that an interaction between the two CO complexes at -9 and -11 km s^{-1} (see Chapter 7) was responsible for triggering the formation of both AFGL490-iki and AFGL490. It will require more extensive observations of the region to determine whether the southern emission feature at -15 km s^{-1} could also possibly be intruding, and playing a role in the ongoing star formation.

5.5.4 Conclusion Regarding Outflows

A recent high-resolution survey carried out with the JCMT has detected a new outflow, AFGL490-iki, in the Cam OB1 region. The main results of this survey can be summarized as follows:

1. AFGL490-iki is a molecular outflow which has been active for $\sim 2 \times 10^4$ yr, and has ejected ~ 3.4 $M_\odot$, injecting $\sim 2.7 \times 10^{46}$ erg into the surrounding ISM. Additional observations of different molecular isotopes and transitions, e.g., ^{13}CO and ^{12}CO(3–2), are required to refine the solution further.
2. Molecular emission seen in the vicinity of AFGL490-iki shows multiple components at similar velocities to AFGL490-iki (at ~ -9, -11 and -15 km s^{-1}). AFGL490-iki and also AFGL490 may have been produced as a result of the interaction between these various molecular components. A more extensive mapping of the region is required to delineate the interface between these various

components.

3. The 'on-the-fly' mode of operation at JCMT is a very efficient method for mapping large areas containing bright emission features.

5.6 Conclusions Regarding ePIo in Cam OB1

In this chapter an investigation of candidate extreme Population I objects as selected on the basis of their *IRAS* colors, was carried out. From this study it can be concluded that:

1. There does appear to be an enhancement of infrared objects associated with the Cam OB1 emission.
2. The infrared objects selected as being associated with the Cam OB1 emission (66 objects) do appear to lie in different parts of the *IRAS* color-color planes from those in a nearby control region.
3. 19 of the selected infrared sources can be characterized on the basis of their *IRAS* colors: 16 of them are promising candidates to be ePIo while 3 are probably stars.
4. A search for methanol masers, associated with infrared sources in the survey field (Di96), led to the discovery of a new maser in the Perseus arm, associated with IRAS 02455+6034.
5. A search for molecular outflows in the Cam OB1 region led to the discovery of a new outflow, AFGL490-iki, associated with IRAS 03234+5843.

Chapter 6

On the Association of Cam OB1 Stars with Cam OB1 Molecular Gas

An investigation of the relationship between optically-identified stars in Cam OB1 and the Cam OB1 CO emission is presented. It is shown that HD 19820 is the principal source of Lyman-continuum photons for S202, the main HII region in Cam R1. It is also shown that a number of stars are physically related to Cam R1 CO emission via the warming of its associated dust.

6.1 Introduction

In Chapters 4 and 5, Cam OB1 stars identified by their optical emission and infrared emission, respectively, were assigned a distance of 975 ± 90 pc on the basis of main sequence fitting to the optically-identified stars. There was some discussion in Chapter 5 as to which stars could be associated with the Cam OB1 molecular gas on the basis of the ionization of this gas (see Table 5.3), or by the warming of the dust associated with the molecular and/or atomic gas by neighboring Cam OB1 stars (see Table 5.5). However, the data currently available on the interaction between Cam OB1 stars and associated gas are very limited. In order to understand the star forming history of the region, it is important to extend this analysis to the remaining stars in the region and establish, where possible, the association between the Cam OB1 optically-identified stars and the CO emission. There are two main ways to do this: a) on the basis of morphology, and b) from evidence of physical interaction between the stars and gas. In (a), the young, optically-identified stars should be nearly coincident with the CO emission in which they originated, although they may be heavily reddened and dimmed by the dust associated with foreground CO emission. In (b), evidence for physical interaction would include HII regions surrounding the stars with similar velocities and complementary morphology to the CO emission, or evidence of the dust having been warmed by the radiation from the stars. Furthermore, from an analysis of the physical interaction between the stars

and gas, it may be possible to place some constraints on the likelihood that the stars did indeed come from the neighboring gas on the basis of time-scales and energetics of the interactions.

The layout of this chapter will be as follows: In §6.2 morphological arguments, both spatial and kinematic, supporting the association of the molecular gas with the optically-identified stars will be presented. In §6.3 evidence for any physical interaction between the stars and molecular gas, on the basis of HII regions (§6.3.1), or warm dust (§6.3.2) will be discussed. §6.4 will provide a summary of the probability of the association of optically-identified stars with the molecular gas, and the likelihood that these stars originated in this gas.

6.2 Morphological Arguments

While it is not possible to associate the Cam OB1 CO emission unambiguously with optically-identified Cam OB1 stars solely on their spatial coincidence or similarity in radial velocities, a great deal can be learnt from such a comparison. Stars that are relatively young should be close to the CO cloud in which they formed, e.g., assuming a canonical value of 10 km s^{-1} for the velocity of separation of the newly formed star from its parent CO cloud (Leisawitz et al. 1989) then after 10^6 yr the star will lie at a distance of $\sim$ 10 pc from its birth site. For the Cam OB1 emission, at a distance of 975 pc, this translates into an angular separation of $\sim 0\overset{\circ}{.}5$ if all the motion is tangential to the observer.

Figure 6.1 shows a CO map of l vs. b, taken at different velocities, from the velocity range defining the Cam OB1 emission ($-5.5 \geq v_{LSR}/\mathrm{km\ s^{-1}} \geq -22$), which have been overlaid with the PIo selected in Chapter 4. For simplicity, stars in Figure 6.1 can be loosely assigned to three possible regions: a) most stars can be associated with the dominant star-forming region centered on $l = 140°$, $b = +3°$, which comprises Cam R1 N and Cam R1 S (see Figures 4.7 and 4.8), b) a second group of stars make up the compact cluster NGC 1502 at $l = 143\overset{\circ}{.}5$, $b = +7\overset{\circ}{.}5$, while, c) the remainder of the stars, which are primarily found at longitudes below $l = 138°$, are scattered throughout the field.

Of the group (c) field stars mentioned above, 9 lie at longitudes below $l = 138°$ and are randomly distributed throughout the field, with no strong coincidences with the Cam OB1 CO emission in this region. Several of the stars (HD 15000, LS I+59 136, BD+58 488, HD 17114 – see Table 4.4), may show some clustering around

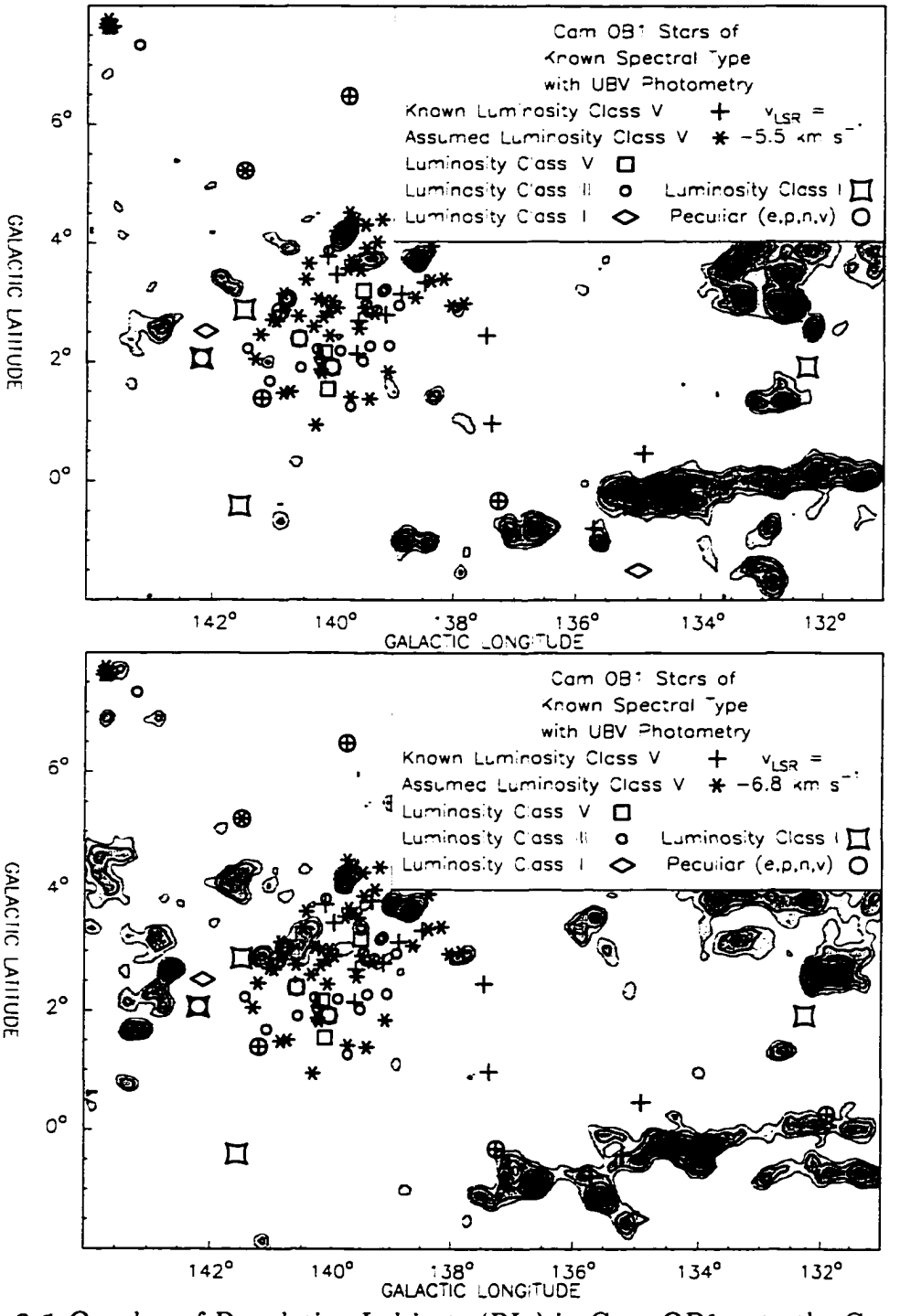

Figure 6.1 Overlay of Population I objects (PIo) in Cam OB1 onto the Cam OB1 CO emission. Every second velocity channel is shown with the first CO emission contour at 0.35 K (3 σ) and increasing by a factor of 1.58 for every contour thereafter.

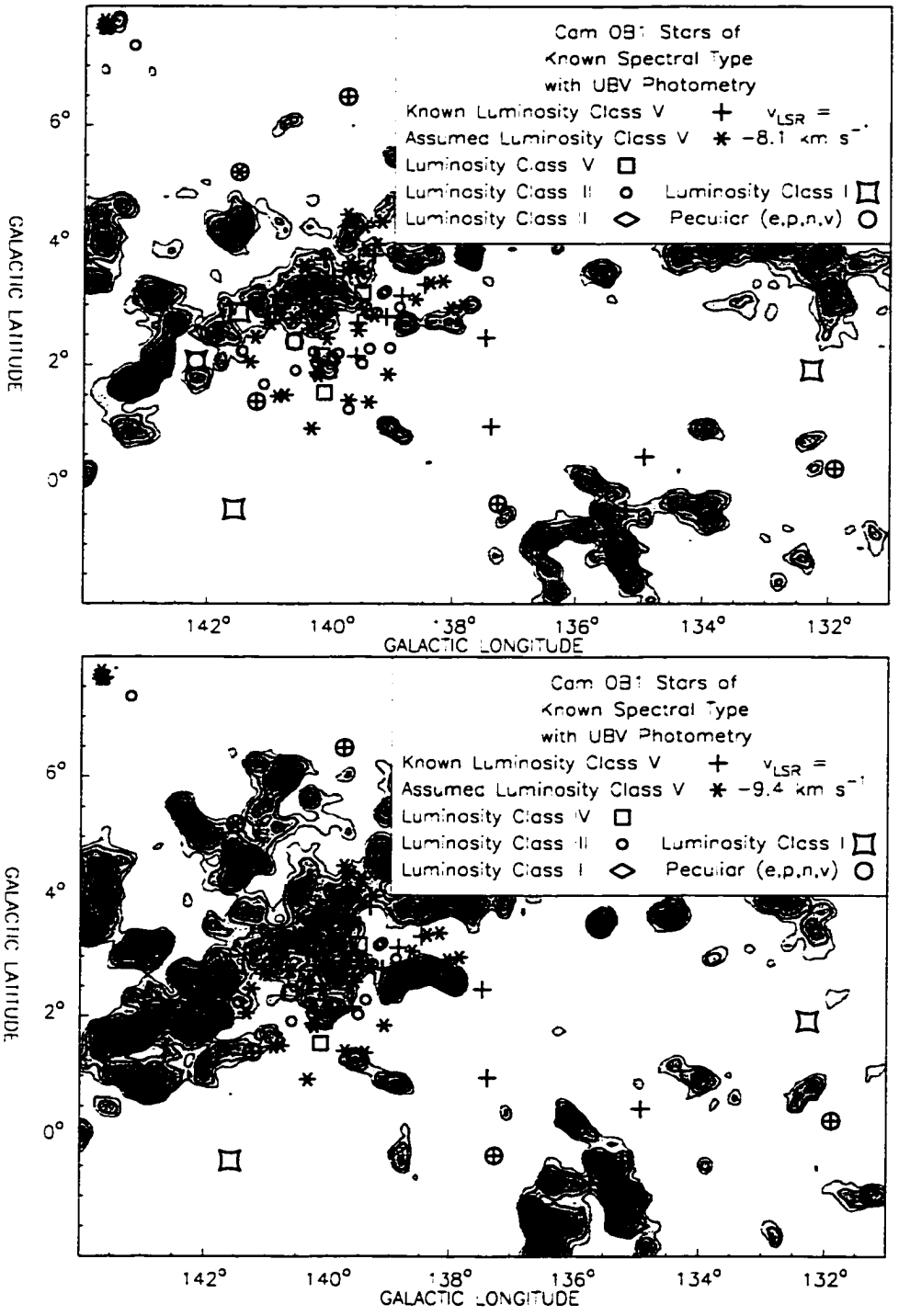

Figure 6.1 cont. Overlay of Cam OB1 stars on Cam OB1 CO emission at indicated velocity.

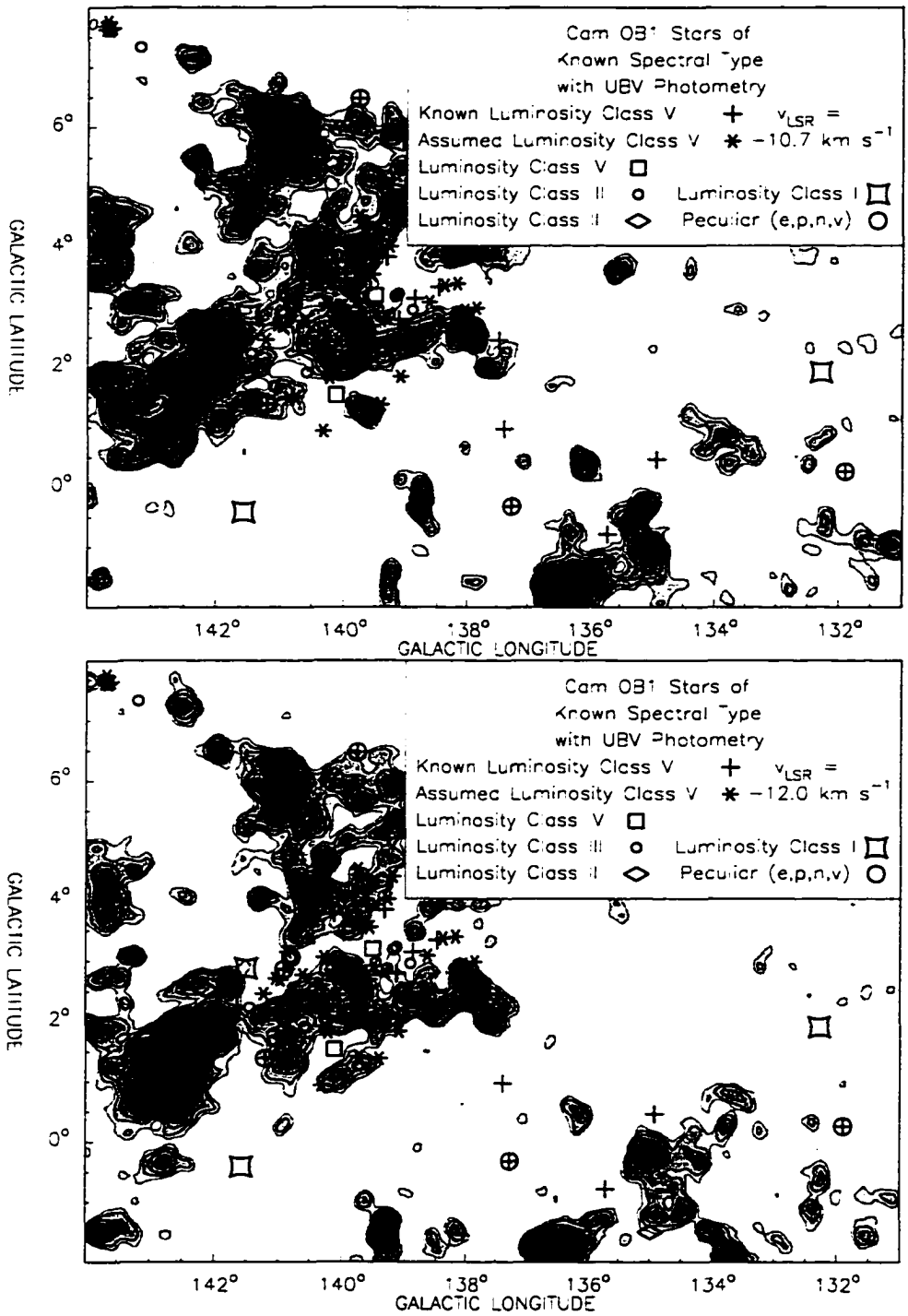

Figure 6.1 cont. Overlay of Cam OB1 stars on Cam OB1 CO emission at indicated velocity.

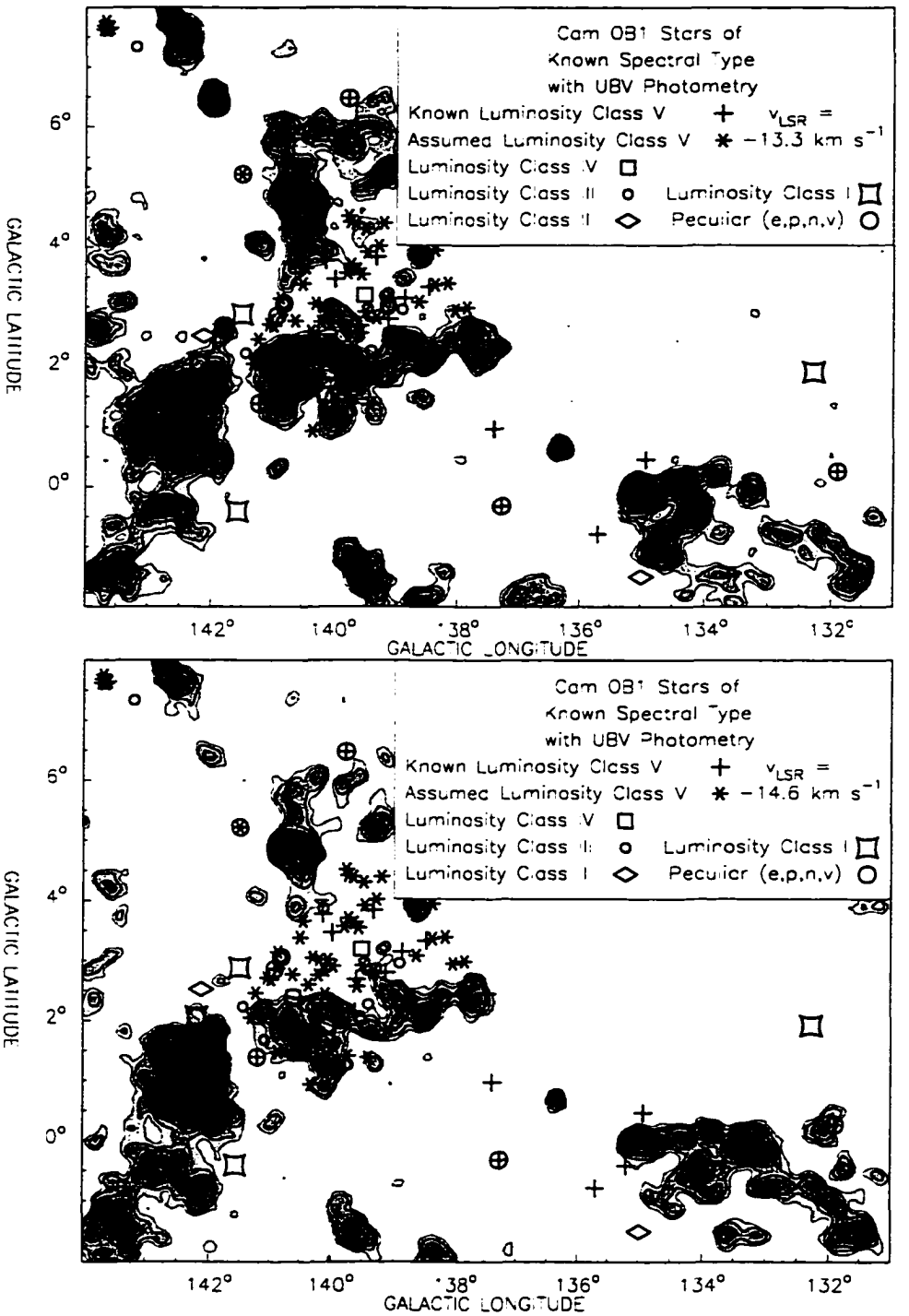

Figure 6.1 cont. Overlay of Cam OB1 stars on Cam OB1 CO emission at indicated velocity.

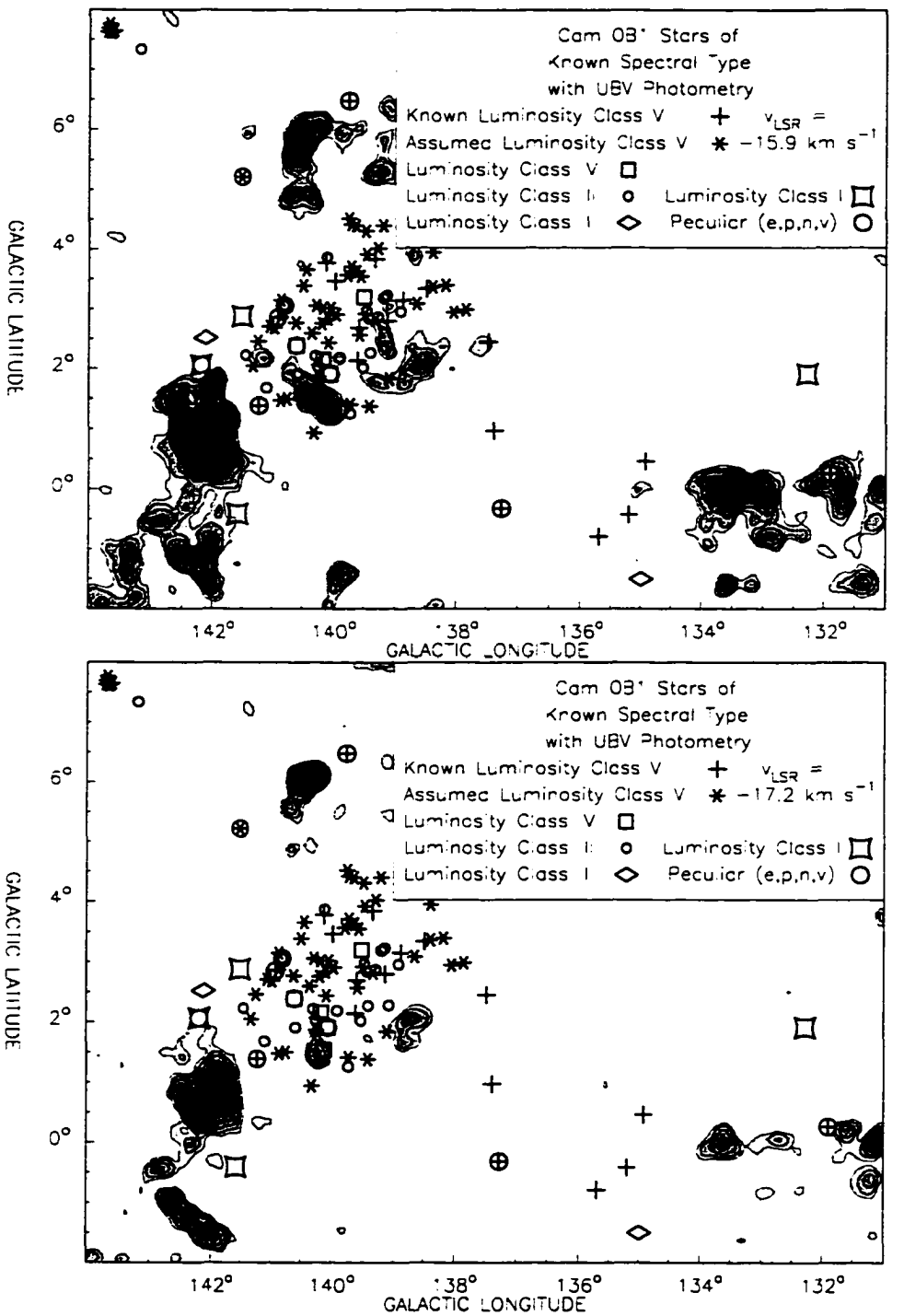

Figure 6.1 cont. Overlay of Cam OB1 stars on Cam OB1 CO emission at indicated velocity.

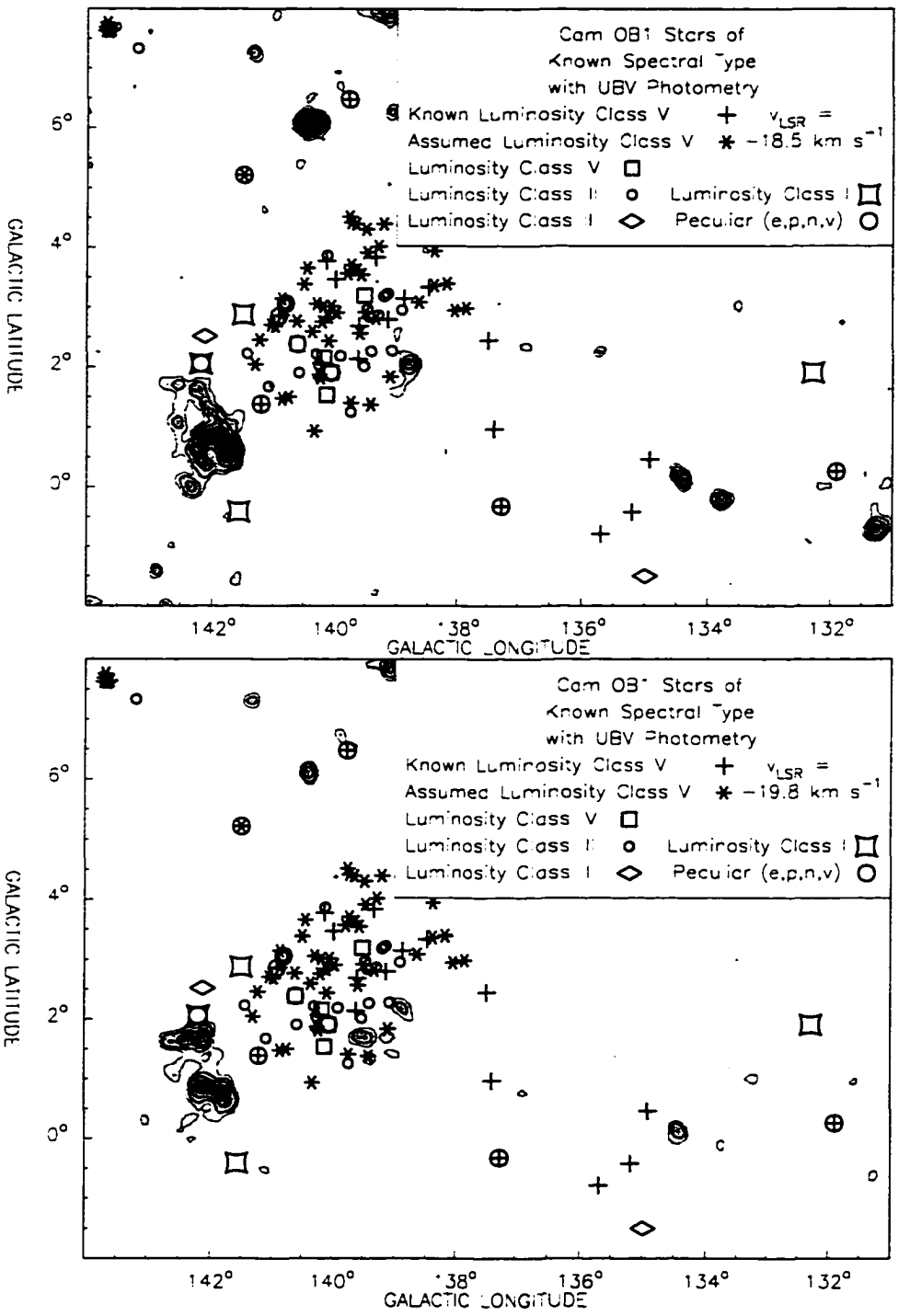

Figure 6.1 cont. Overlay of Cam OB1 stars on Cam OB1 CO emission at indicated velocity.

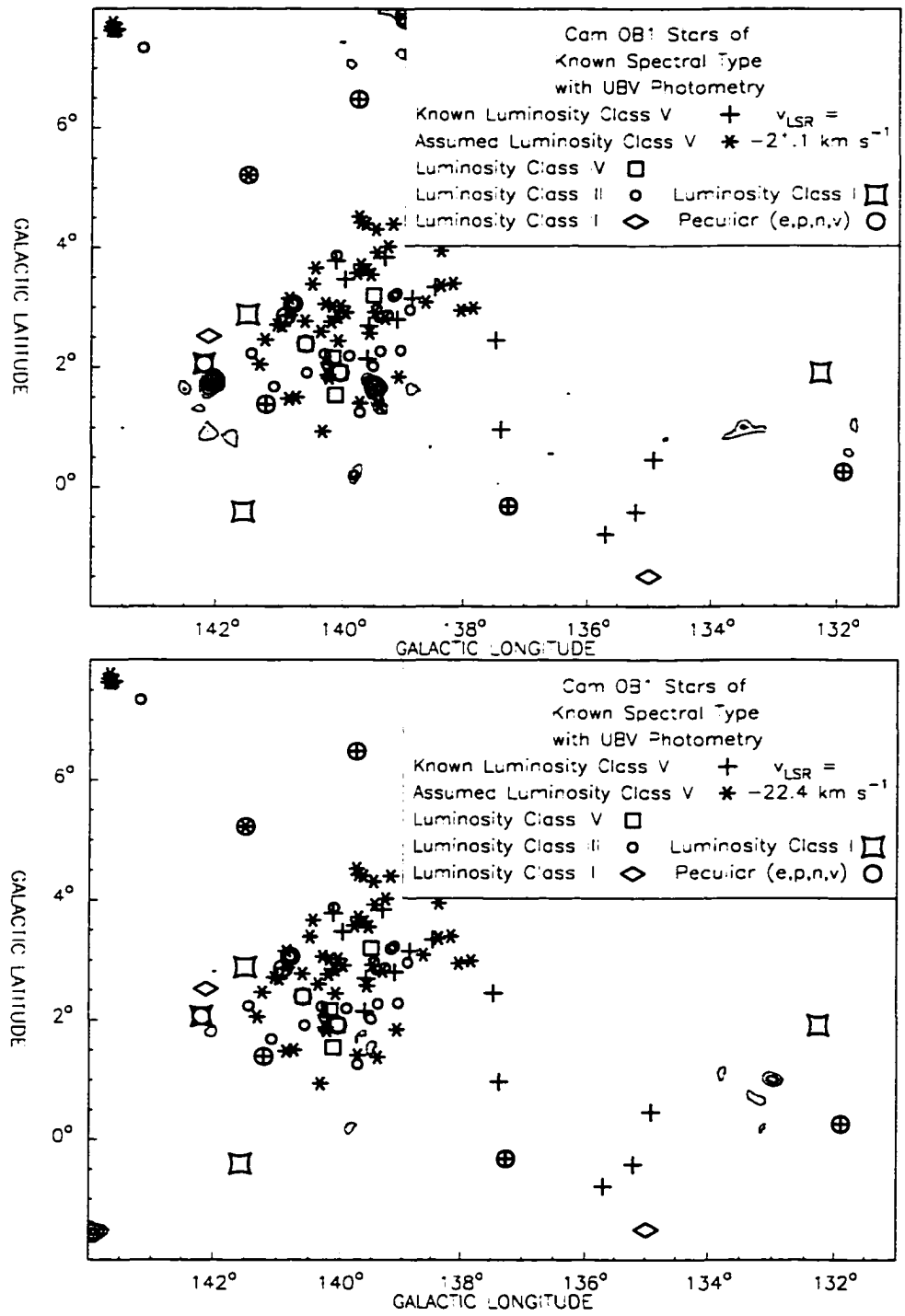

Figure 6.1 cont. Overlay of Cam OB1 stars on Cam OB1 CO emission at indicated velocity.

CO emission near $l = 135°, b = -1°$, but CO emission is also seen at very positive velocities, i.e., in the Local gas velocity range, as well as being present in the Cam OB1 velocity range. It is not possible on the basis of morphology alone to decide whether these stars are associated with the Local or Cam OB1 emission. Given the extinction is at least $\sim 1^m$ for most of these stars (see Table 4.4), they probably lie behind the Local emission but not behind the Cam OB1 emission. Unfortunately, very little additional radial velocity or proper motion information is available on these stars to help with this problem.

Other stars in the region (HD 13686 and HD 237015) do not appear to be strongly associated with either Local or Cam OB1 emission. Radial velocity measurements for these stars are not of much help. HD 237015 has a radial velocity, -15.0 km s^{-1}, consistent with that of the Cam OB1 emission, but it is sufficiently old, 98×10^6 yr (Table 4.4), that it could have travelled a considerable distance from its origin. HD 17114, the star with the most positive radial velocity, $+51$ km s^{-1}, in the field would have to be classified as a runaway star if it originated in Cam OB1 CO emission. Even given its relative youthfulness, 8×10^6 yr (Table 4.4), this star could have travelled a considerable distance from its origin. The remainder of the stars in this region have very little information to assist in their placement.

Hence, morphological, kinematic or time-scale arguments fail to provide any compelling evidence for the close association of Cam OB1 stars with the Cam OB1 CO emission below $l = 138°$.

There are three other 'field' stars which warrant some discussion. Firstly, HD 20041 is an early type supergiant ($l = 141°.57, b = -0°.41$) which has been previously identified as being associated with reflection nebulae in Cam OB1 (see Table 5.5). The strongest spatial correlation of HD 20041 with the CO emission occurs over the velocity range of -13.3 to -17.2 km s^{-1}. A velocity of -11.9 km s^{-1} for HD 20041 (a search of SIMBAD reveals a variation of only a few km s^{-1} in the radial velocity for this star) suggests that it is moving away from us, relative to the CO emission, at ~ 3 km s^{-1}. The relatively young age of this star, $\sim 15 \times 10^6$ yr (Table 4.4), also suggests that it should be close to its origin. It is intriguing that HD 20041 lies just below Cam R1 S, which has a number of stars of similar age, and it would have been possible for HD 20041 to have traversed the 30 to 40 pc separation in the plane of the sky, if it had a very small relative transverse velocity of ~ 2 km s^{-1} from Cam R1 S. Secondly, there are two early type stars which lie to the north of the

Cam R1 N and Cam R1 S complex, HD 21806 ($l = 139.^{\circ}76, b = +6.^{\circ}48$), and BD+61 623 ($l = 141.^{\circ}50, b = +5.^{\circ}22$), which may be associated with the CO emission. HD 21806 has a radial velocity of -22 km s^{-1} which would suggest it is moving toward us relative to the Cam OB1 CO emission, i.e., CO emission at ~ -12 km s^{-1}. An extinction of $1.^{m}8$ for this star suggests that it may be on the far side of this emission and given its relative motion, also be moving towards it. With an age of $\sim 8 \times 10^6$ yr it is also possible that HD 21806 originated in Cam R1. If this is the case, it would suggest that the CO emission lying in the northern half of the field is closer to us than the CO emission in the vicinity of Cam R1. BD+61 623 lies at a slightly lower latitude, closer to the Cam R1 region and it is sufficiently old ($\sim 5 \times 10^6$ yr), that it could have come from Cam R1. There are no radial velocity measurements available to determine its motion relative to the CO emission, but its extinction of $2.^{m}2$ suggests it is behind the Cam OB1 emission, as was the case for HD 21806.

Next, considering the group (b) stars, i.e., the open cluster NGC 1502, it is clear from Figure 6.1 that there are no striking positional coincidences of Cam OB1 CO emission with this cluster. The only CO emission of any consequence in the vicinity of NGC 1502 can be seen over the velocity range of -12.0 to -14.6 km s^{-1}, and lies at slightly lower longitude. The radial velocity measurements for stars assigned to NGC 1502 in the literature vary tremendously, e.g., HD 25090 has a radial velocity of -3.0 km s^{-1}, while UBV M 30864 has a radial velocity of -51.0 km s^{-1}, and BD+61 678, a known binary, has a radial velocity of -23.0 km s^{-1} (Table 4.4). The position of HD 25090 ($l = 143.^{\circ}19, b = +7.^{\circ}34$) is well away from NGC 1502 ($\sim l = 143.^{\circ}68, b = +7.^{\circ}65$), which suggests that it differs significantly in space motion from NGC 1502. In Figure 6.1, the only distinguishing characteristic of CO emission in the vicinity of NGC 1502 is that it has a slight curvature best seen at -13.3 km s^{-1}. Blaauw (1964) argued that NGC 1502 is the origin of the runaway star α Cam. If this is the case, then there was probably a supernova explosion in NGC 1502, which ejected α Cam from the cluster. Unfortunately, the morphology of the CO emission is really too nondescript to make any claims about the possible effect of the supernova on the neighboring CO emission.

Finally, the Cam R1 stars, group (a) above, show a strong spatial correlation with the Cam OB1 CO emission. At a velocity of -5.5 km s^{-1}, the stars are bounded by the CO emission to the north, which is just becoming visible. At more negative velocities, the spatial coincidence between the stars and CO emission

becomes more marked. For Cam R1 N, this coincidence is strongest at -8.1 km s^{-1} and $l = 140°, b = +3°$, as well as $l = 139°.5, b = +4°$. (This CO feature is referred to as Complex B in Chapter 7). The stars of Cam R1 S, which are mostly evolved, lie below this emission, and are almost perfectly spatially anti-correlated with it. The most northern members of Cam R1 S group (located near $l = 141°, b = +2°.75$) overlap with some Cam R1 N CO emission, but for the most part, are well confined by the CO emission coincident with the Cam R1 N stars.

It is interesting to note that an analysis of the radial velocities of B-type stars, which are presumably young and close to their origin, contained within the boundaries of Cam R1 N and Cam R1 S (Table 4.4 and Figure 4.7), shows that the Cam R1 N B-type stars (7 stars in total) have a mean radial velocity -5.1 ± 0.5 km s^{-1}, while the Cam R1 S B-type stars (3 stars in total) have a mean radial velocity of -11.2 ± 0.9 km s^{-1}. This suggests a real difference in the motion of the B-type stars for the two regions, which could indicate that they originated in different CO clouds.

At -9.4 km s^{-1}, there is a dramatic increase in the amount of CO emission associated with the Cam R1 S stars. This increased CO emission is composed of four main features:

At $l = 139°, b = +2°.5$, there is an elongated emission feature which breaks up into several smaller features at more negative velocities but it is best defined at $v_{LSR} = -9.4$ km s^{-1} (part of Complex B defined in Chapter 7). The stars in Cam OB1 skirt this feature but there are none visible in front of it (the one exception, BD+61 506, has a a radial velocity of 0.0 km s^{-1} [Table 4.4], which suggests a large motion relative to the main CO emission associated with Cam R1 N and Cam R1 S). This argues strongly that this particular feature actually consists of foreground emission relative to the Cam OB1 stars, both Cam R1 S and Cam R1 N.

At $l = 140°, b = +2°$, a second prominent CO feature which resembles a large triangular shape, is first identifiable (again, part of Complex B). The morphological connection between this feature and the Cam R1 S stars is particularly fascinating. At -9.4 km s^{-1} the stars in Cam R1 S skirt south of this feature, with this spatial anti-correlation relaxing at more negative velocities where the stars of Cam R1 S become spatially well mixed with the CO emission. The Cam R1 S stars forming the skirt are, for the most part, giants (Class III) stars and, if this classification holds true, represent more evolved stars in Cam R1. Hence, it would appear that

the more positive velocity component of this CO emission feature is in front of, and obscuring, most of the older stars in Cam R1 S.

The largest CO emission feature contained within the survey boundaries becomes visible first at -8.1 km s^{-1}, but is best seen at -10.7 km s^{-1} (part of Complex D defined in Chapter 7). The northern half of this complex resembles a large arc-like structure centered on $\sim l = 142°, b = +5°$. A large part of this complex has the same orientation as the other CO features which are coincident with Cam R1 S, indeed blending in with the previously mentioned CO emission. Components of this emission persist out to a velocity of -18.5 km s^{-1}.

The last CO feature to be considered is aligned at constant longitude along $l = 142.^{\circ}5$ centered on $\sim l = 142°, b = +1°$, and is best defined over the velocity range -12 to -14 km s^{-1} (part of Complex G in Chapter 7). This feature persists out to a velocity of -19.8 km s^{-1}. There are three evolved stars coincident with it, HD 21291 ($l = 141.^{\circ}50, b = +2.^{\circ}23$, Table 4.4), BD+58 611 ($l = 142.^{\circ}12, b = +2.^{\circ}52$, Table 4.4), and HD 21389 ($l = 142.^{\circ}19, b = +2.^{\circ}06$) - recall that HD 20041, a supergiant seen at the extreme southern end of the complex was not considered part of Cam R1. There are no obvious correlations between the CO emission and these stars. They do appear to be spatially coincident with CO emission over the velocity range -12 to -14.6 km s^{-1} but there are no remarkable spatial coincidences to speak of. The extinction for the supergiants is also comparable, $\sim 1.^{m}5$, while it is considerably higher for the bright giant, $\sim 3.^{m}4$. This would suggest that the supergiants are in front of the CO emission, while the bright giant probably lies behind it or is embedded in it. Furthermore, the available radial velocity measurements for the supergiants (none are known for the bright giant), with a mean value of ~ -6.5 km s^{-1}, would also suggest that the supergiants are moving towards the Cam OB1 CO emission.

6.3 Physical Interaction between the Cam OB1 CO Emission and Population I Objects

6.3.1 HII Regions

While the morphological arguments supporting the association of the selected Cam OB1 stars (Chapter 4) with the Cam OB1 CO emission (Chapter 2) are very interesting, a compelling case for their association may be made from evidence of their physical interaction. These arguments are based on the premise that the

presence of hot stars should quickly dissociate and ionize any nearby molecular gas to form HII regions (Spitzer 1978, Roger & Dewdney 1992), as well as warm any dust associated with the atomic and/or molecular gas (Leisawitz & Hauser 1988, Scoville & Good 1989). In Chapter 5 candidate HII regions, identified on the basis of their optical, infrared and radio continuum surveys, were presented. It remains now to demonstrate that these were formed as a result of the interaction with Cam OB1 stars.

In Tables 5.3, 5.4 and 5.5, and in Figure 5.7, details and positions of ePIo believed to lie in the Cam OB1 region are provided. What will be emphasized in the discussion provided here is S202. This very large, faint HII region, which dominates Cam R1, is clearly visible on the POSS plates as a large circular emission feature with a diameter of 170′ centered on $l = 140.^{\circ}59, b = +1.^{\circ}92$ (see Figure 5.7 for the outline of this feature). However, the nebula is not uniform in brightness, but shows a brightening towards the northern (S202 N) and southern (S202 S) edges.[1] From Table 4.4 it is possible to determine which optically identified stars could potentially fall inside the boundaries of S202, as seen in projection. Table 6.1 provides a summary of the relevant information for those candidate stars which have an appreciable Lyman-continuum flux.

A 1420 MHz radio continuum map for this region (Kallas & Reich 1980), presented in Figure 6.2, shows a weak continuum feature coincident with the position of S202, whose brightest emission is from regions to the south of the Cam OB1 CO emission near $l = 140.^{\circ}5, b = +1.^{\circ}0$ (S202 S) and coincident with the Cam OB1 CO emission near $l = 139.^{\circ}5, b = +2.^{\circ}5$ (S202 N).

S202 N covers an area of $\sim 1.2 \times 10^7$ arcsec^2 and, has a total flux density of ~ 25 Jy. The ion density producing this flux density may be found from (Genzel 1992),

$$S_\nu = 2.4 \times 10^{-9}\ T_4^{-0.35}\ \nu_{\rm GHz}^{-0.1}\ \theta^2_{\rm arcsec}\ {\rm EM} \quad [{\rm Jy}], \tag{6.1}$$

where T_4 is the excitation temperature of the nebula in 10^4 K (assumed to be 0.8, Osterbrock 1989), ν is the observed frequency in GHz (1.42), and θ^2 is the solid angle of the source in the sky in square arcsec. EM is the emission measure for the

[1] On the POSS plates S202 S is not as clear as the S202 N. This could be in part due to: a) vignetting, as S202 S is located near the bottom of the plate, and b) the lack of contrast with the background Perseus H_α emission which is enhanced in this region.

Table 6.1: Candidate Cam OB1 Stars with Significant Lyman Flux Associated with S202

Name	l [deg]	b [deg]	Sp. Type	v^a_{LSR} [km s^{-1}]	log N^b_L	L^c_{Bol} [10^3 $L_\odot$]
HD 19968	139.46	+2.97	B5III	-7.0(N)	42.79	1.8
BSD 9-1161	139.58	+2.57	B2		44.89	5.7
BD+60 648	139.59	+2.69	B5V		42.36	0.8
HD 19441	139.73	+1.26	B3III	-30.0(S)	44.30	5.0
HD 237090	140.05	+1.91	B0.5IV	-6.0(S)	46.65	60.0
HD 237091	140.06	+1.92	B1V	+7.6(S)	45.52	16.0
HD 19820	140.12	+1.54	O9IV	-4.2(S)	48.50	100.0
HD 20134	140.16	+2.16	B2.5IV-V	-12.5(N)	44.70	8.0
BD+59 624	140.21	+2.07	B5V		42.36	0.8
BD+58 574	140.32	+0.94	B1	-9.0(S)	45.52	14.0
HD 20295	140.58	+1.91	B5III	-32.0(S)	42.79	1.8
HD 20508	140.60	+2.39	B1.5IV	-28.0(N)	45.60	10.0
HD 20898	140.80	+3.06	B2III	-2.0(N)	45.25	17.0
LSI +58 119	140.86	+1.48	B5		42.36	0.8
HD 237134	140.91	+2.86	B5V		42.36	0.8
HD 20547	141.09	+1.68	B3III	-15.0(S)	44.30	5.0
HD 237121	141.21	+1.39	B0.5V	-12.0(S)	46.50	30.0
HD 20959	141.44	+2.23	B3III	-10.0(S)	44.30	5.0

a) Membership of the stars in Cam R1 N or Cam R1 S (see Figures 4.7 and 4.8) are indicated by (N) and (S) respectively.
b) N_L is the total number of ionizing photons s^{-1} as determined by Panagia (1973).
c) L_{Bol} is the stellar bolometric luminosity, as listed by Lang (1992).

nebula defined as

$$EM = \int n_e^2 \, dl \quad [cm^{-6} \, pc]. \tag{6.2}$$

where n_e is the electron density per cm^3, and the integration is performed over the length of the nebula, in pc, along the line-of-sight. If the nebula is assumed to be as deep as it is wide, then this depth is $\sim$ 22 pc, for an assumed distance of 975 pc to Cam OB1. Hence, it follows from Eq. 6.1 and 6.2 that, for S202 N, the EM is $\sim$ 830 cm^{-6} pc, and the electron density, $n_e \sim 6.1$ cm^{-3}. The calculated value for the EM of S202 N, and its appearance on the POSS plates, are in agreement with other well known HII regions, e.g., S187, IC5146, NGC281 and S142 (Roger & Dewdney 1992).

The number of Lyman-continuum photons which could be absorbed through

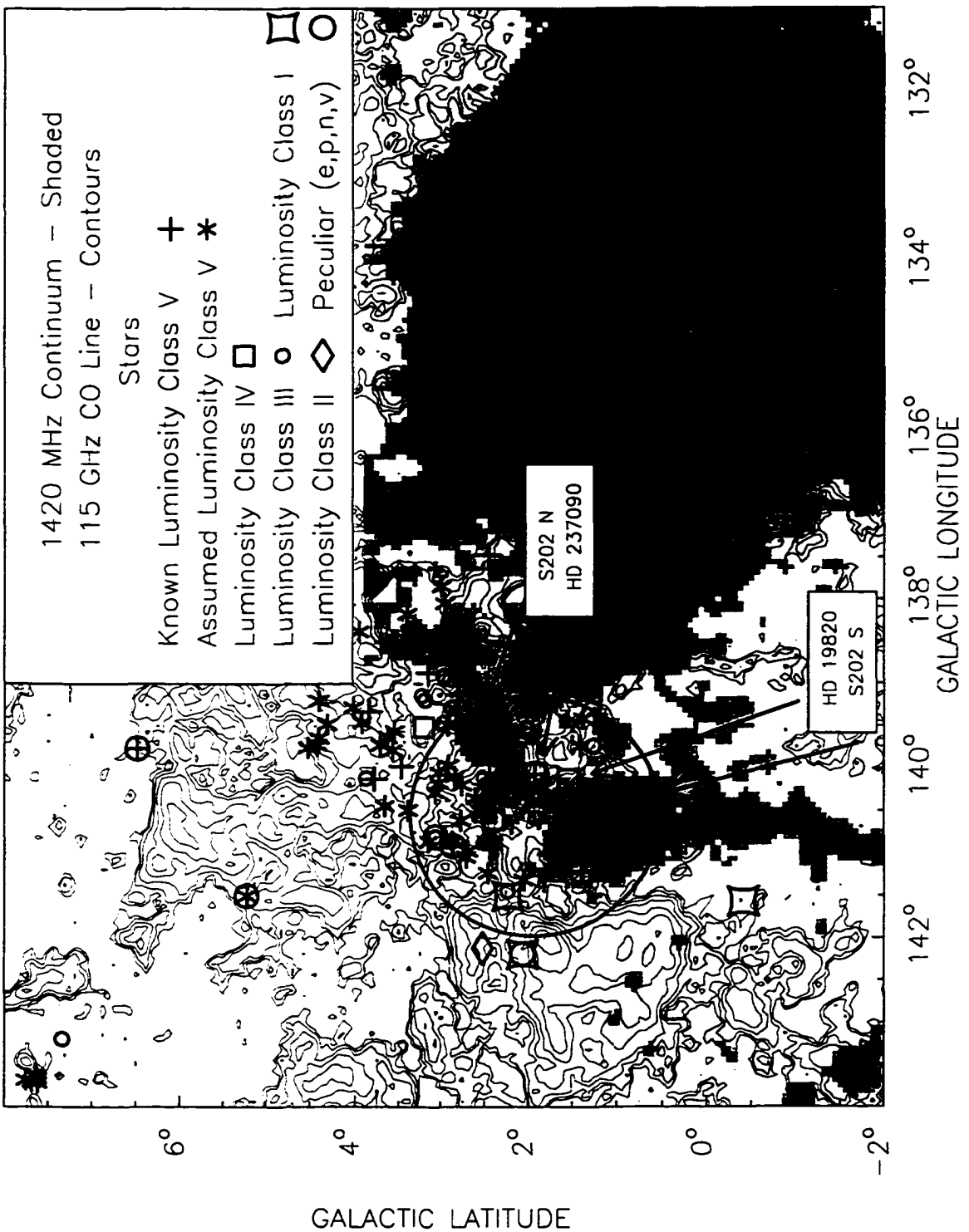

Figure 6.2 Overlay of CO emission (first contour at 3σ increasing by 1.58 thereafter) and Cam OB1 stars over the 1420 MHz continuum emission (Kallas & Reich 1980). A shading scheme for the radio continuum emission has been chosen to emphasize the S202 emission.

recombinations per second per unit volume (cm^{-3}) in an HII region is $3.4 \times 10^{-13}\ T_4^{-0.75}\ n_e^2$ (Osterbrock 1989). Hence, S202 N, with a volume of $\sim 1.7 \times 10^{59}$ cm^3 and $n_e = 6.1$ cm^{-3}, would absorb $\sim 2.5 \times 10^{48}$ Lyman-continuum photons s^{-1}. Several stars in Table 6.1 have considerable Lyman-continuum fluxes with HD 237090 being the closest to S202 N. However, the available ionizing flux from this star is several orders of magnitude less than what is required. HD 19820, the strongest source of ionizing photons could provide this flux if $\sim$ 80% of it went into ionizing S202 N. However, HD 19820 has a projected stand-off distance of $\sim$ 1°.2 or 21 pc at 975 pc which would limit the available flux which could energize S202 N to $\sim$ 10% of its total. Other stars in the Cam OB1 region, in particular HD 237090, probably could not alleviate this difficulty to the extent required. Nor are there any additional stars detected in Perseus (Appendix B) which could be contributing to the radio continuum emission. There are three sources of uncertainty in this calculation. Firstly, an error in the selection of the boundary of S202 N will affect both the estimate of the total flux in the nebula and the volume of the nebula. Secondly, the ionizing flux for HD 19820 may be underestimated, this is still open to debate and is an active area of research. Finally, the star's wind may have depleted the gas in its vicinity to some extent (Dorland et al. 1986).

Nevertheless, given the limitations of the mapping of S202 N and the absence of any other significant sources of ionizing photons, *HD 19820 must be the principal source of ionizing photons in S202 N.*

If the above analysis is applied to S202 S, it can be shown that the total flux density for the nebula is $\sim$ 212 Jy, extended over an area of $\sim 2.3 \times 10^7$ $arcsec^2$, which leads to an EM $\sim$ 2900 cm^{-6} pc. If it is assumed that S202 S is as deep as it is wide ($\sim$ 26 pc), then it follows its electron density is $\sim$ 11 cm^{-3}. Finally, the number of Lyman-continuum photons required to energize S202 S is $\sim 2.8 \times 10^{48}$ sec^{-1}, which is comparable to that of S 202 N. Furthermore, as is the case of S 202 N, S 202 S does not appear to have any other significant sources of Lyman-continuum photons than HD 19820. Hence, with the same caveats which were applied to the analysis of S 202 N it follows that *HD 19820 must be the principal source of ionizing photons in S202 S.*

6.3.2 Dust Warmed by the Cam OB1 Stars

As mentioned earlier, the warming effect of the Cam OB1 stars on the dust associated with the molecular gas is further evidence of their close proximity. Figure 6.3 presents a dust temperature map for the region, obtained by a comparison of the *IRAS* 60μm and 100μm emission. These maps are made from co-added HCON data from the *IRAS* survey (Laughlin 1991), which have more sensitivity than the original survey, but have the same resolution, i.e., typically the minimum detectable flux density decreased from 1 - 1.5 Jy to 0.8 Jy while the resolution remained at $\sim 4'$ at 60μm and $\sim 6'$ at 100μm. The dust temperature, obtained from a comparison of these two flux densities, may be found from (Evans 1980)

$$T_{(\frac{\lambda_1}{\lambda_2})} = \frac{\frac{hc}{k}(\frac{1}{\lambda_2} - \frac{1}{\lambda_1})}{(3+\beta)\ ln(\frac{\lambda_1}{\lambda_2}) + ln(\frac{S_\nu(\lambda_1)}{S_\nu(\lambda_2)})}. \tag{6.3}$$

where h, c and k are Planck's constant, the speed of light and Boltzmann's constant, respectively, $\lambda_1 = 60\mu$m and $\lambda_2 = 100\mu$m. β is a measure of the emissivity of the dust which is assumed to be 2, i.e., $Q(\lambda) \propto \lambda^{-2}$ with the flux density of the dust given by $S_\lambda = Q(\lambda) \times B(\lambda, T)$, where $B(\lambda, T)$ is the Planck function. In order to calculate the dust temperature as a function of position, as shown in Figure 6.3, two corrections need to be made to the data. Firstly, the 60μm emission must be convolved to match the resolution of the 100μm map and, secondly, both the 60μm and 100μm maps must be flat-fielded to remove the extraneous background emission. For the 60μm emission a constant background component of 7 MJy/sr, estimated by averaging several positions away from the region of interaction, was assumed. Similarly, for the 100μm emission a constant background of 45 MJy/sr was assumed. The effect of this removal can be seen in Figure 6.3 as 'white' pixels which appear at the edge of the emission, where the image has been cropped by the background subtraction. It should be noted that the very warm sources (very dark pixels) along the edges should not be given any weight as their implied temperatures are probably due to edge effects in one or both bands, i.e., when taking the ratio of two fluxes in a pixel near the edge, where the fluxes may be particularly sensitive to an improperly fit baseline, the calculated temperature may be erroneous.

In Figure 6.3, there are a number of sites where the stars of Cam OB1 appear to be warming the dust associated with the Cam OB1 CO gas. These sites are restricted to the region $l = 138°$ to $l = 144°$ and $b = -1°$ to $b = +4°$, i.e., the

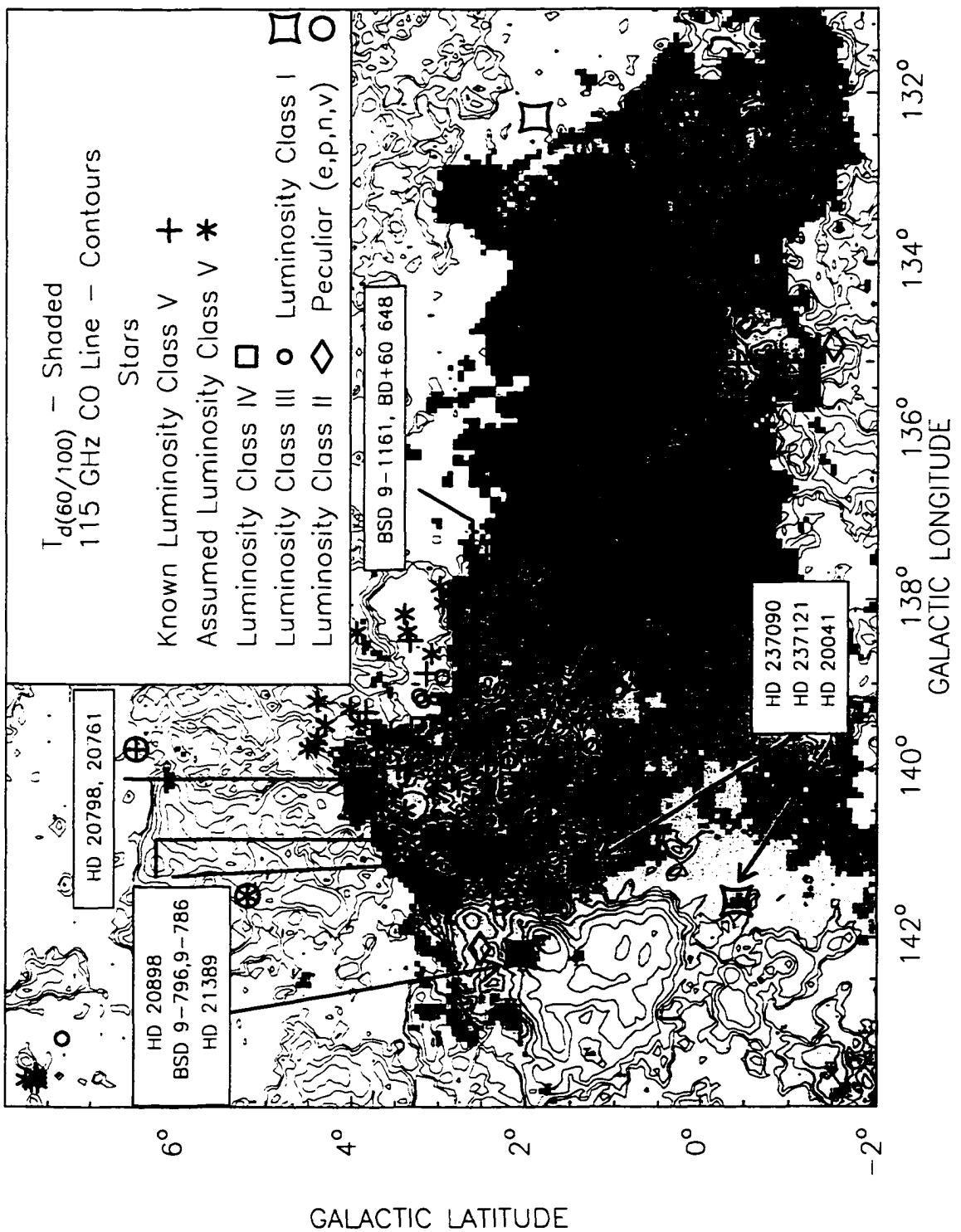

Figure 6.3 Overlay of CO emission (first contour at 3σ increasing by 1.58 thereafter) and Cam OB1 stars over a $T_{(\frac{60}{100})}$ dust temperature map constructed from the 60μm and 100μm emission. Empty pixels above and below the main dust emission represent 'subtracted' background emission.

Cam R1 region (see Figures 4.7 and 4.8), and slightly further south. In Figure 6.4, detailed maps of eight of these regions of interaction are presented. These particular regions have been selected as being typical, as well as providing a sampling across the entire spatial extent of the Cam R1 region. Accompanying each map is a plot of the dust temperature profile which has been obtained by azimuthally averaging around the central stellar position in bins $\sim$ one pixel wide ($\sim$ 1.06 pc at 975 pc). In order to determine the 'excess' warming that a star has on nearby dust, over the background radiation, $T_{(\frac{60}{100}),exc}$, the relationship (Leung 1975, Castelaz et al. 1987)

$$\frac{Q_{60}}{Q_{100}} = 16\ \pi\ \sigma\ T^4_{(\frac{60}{100}),exc}\ (\frac{r_s^2}{L_{Bol}}). \tag{6.4}$$

is used. The left hand side of Eq. 6.4 represents the ratio of emissivities of the dust at 60μm and 100μm, and has been set equal to 2100, i.e., similar to the dust seen in the vicinity of the Pleiades (Castelaz et al. 1987). σ is Stefan-Boltzman's constant and L_{Bol} is the bolometric luminosity of the star, as listed in Lang (1992). There are two parameters left to be fit to the data: $T_{(\frac{60}{100}),exc}$ represents the excess dust temperature due to the influence of the star, and the standoff distance, r_s, of the star from the dust in order for it to provide this additional flux. The expected dust temperature, $T_{(\frac{60}{100}),exp}$ is related to $T_{(\frac{60}{100}),exc}$ and the background dust temperature, $T_{(\frac{60}{100}),back}$, through the conservation of flux, i.e.,

$$T^4_{(\frac{60}{100}),exp} = T^4_{(\frac{60}{100}),exc} + T^4_{(\frac{60}{100}),back}. \tag{6.5}$$

In solving Eq. 6.5 the minimum standoff distance, $r_{s,0}$ is set to be the distance at which the dust is warmest, i.e., the closest point between star and dust. All other standoff distances, r_s, are calculated assuming the dust lies entirely in a plane, in which case,

$$r_s^2 = r_{s,0}^2 + r_F^2. \tag{6.6}$$

The Faceon Offset, r_F, is the displacement, seen in the plane of the sky, of the azimuthally averaged annuli from the center (warmest point) of dust emission.

A summary of the results of this analysis is provided in Table 6.2. while a brief discussion for each star(s) is provided below:

Table 6.2 Parameters for Cam OB1 Stars Warming Dust Associated with Cam OB1 CO Emission

Name	l [deg]	b [deg]	Sp. Type	L_{Bol} [10^3 $L_\odot$]	$T_{(\frac{60}{100}),exp}$ [K]	$r_{s,0}$ [pc]	$T_{(\frac{6}{100}),back}$ [K]	$T_{(\frac{60}{100}),exc}$ [K]
HD 21389	142.19	+2.06	A0Iab	35.0	35.8	3.1	27.3	32.4
HD 20041	141.57	-0.41	A0Ia	35.0	36.0	3.0	27.2	32.7
HD 237121	141.21	+1.39	B0.5V	30.0	35.9	3.1	30.8	29.6
BSD 9-796[a]	141.04	+2.71	B6	0.50	40.3	1.1	31.7	35.7
BSD 9-786[a]	140.97	+2.69	B8	0.18	40.3	1.1	31.7	35.7
HD 20898	140.80	+3.06	B2III	17.0	42.8	1.5	31.8	39.2
HD 20798[b]	140.11	+3.87	B2III-IV	17.0	37.3	2.2	30.4	32.2
HD 20761[b]	140.12	+3.78	B9V	0.10	37.3	2.2	30.4	32.2
HD 237090	140.05	+1.91	B0.5IV	60.0	32.5	8.2	30.5	22.6
BSD 9-1161[c]	139.58	+2.57	B2	5.70	34.1	2.1	31.0	25.6
BD+60 648[c]	139.59	+2.69	B5V	0.80	34.1	2.1	31.0	25.6

a) The luminosities of BSD 9–796 and BSD 9–786 were added together in the calculation of the standoff distance and excess flux at a point coincident with the more luminous of the two stars, BSD 9–796.

b) Similarly HD 20798 and HD 20761 are considered together.

c) Similarly BSD 9–1161 and BD+60 648 are considered together.

HD 21389 : This bright supergiant star lies at the east end of the Cam R1 region, and is warming the Cam OB1 dust. It is interesting that the radial profile for the 100μm emission shows a depletion of emission within the first $\sim$ 2 pc. This depletion is highly symmetric in appearance, as determined from an inspection of a 100μm emission map and is suggestive of a shell or bubble. Note: The bump in the radial distribution plots at $\sim$ 5 pc is due to the presence of the energetic outflows AFGL490 and AFGL490-iki (Chapter 5).

HD 20041 : This bright supergiant lies at the south-east end of Cam R1 and appears to be slightly offset from the Cam OB1 CO emission. However, the excellent fit to the temperature profile suggests that the simple model for warming the dust is essentially correct.

HD 237121 : This hot star is also almost certainly warming the dust associated with the Cam OB1 CO emission. Like HD 21389, there is a depletion of 100μm emission

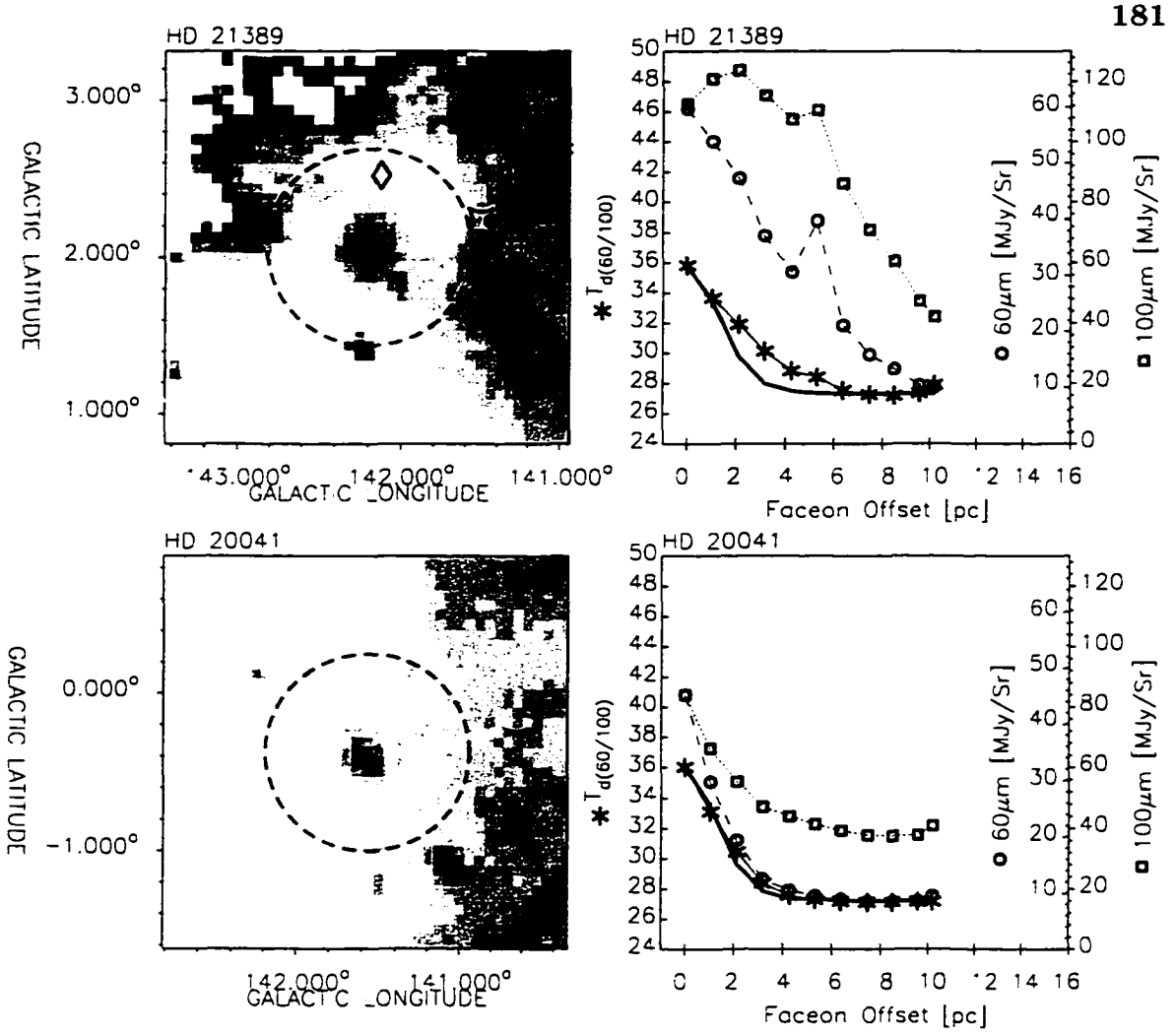

Figure 6.4 Selected Cam OB1 stars spatially coincident with warm dust associated with the Cam OB1 CO emission. The *IRAS* 60μm, 100μm emission and observed dust temperature, $T_{(\frac{60}{100})}$, are as indicated by open circles, open squares and asterisks, respectively. The expected dust temperature (Eq. 6.5), is indicated by the heavy solid line. The 'Faceon Offset' (or r_F) refers to the projected offset in the sky of the radial position of center of each azimuthally averaged bin, assuming a distance of 975 pc for the system. The dashed circle in each image is the position of the 10 pc limit of the azimuthal bins. Shading contours are set at 25.0, 27.0.....41.0, 50.0 K, with the cooler background dust ($T_{(\frac{60}{100}),back} \leq 25$ K) set to white.

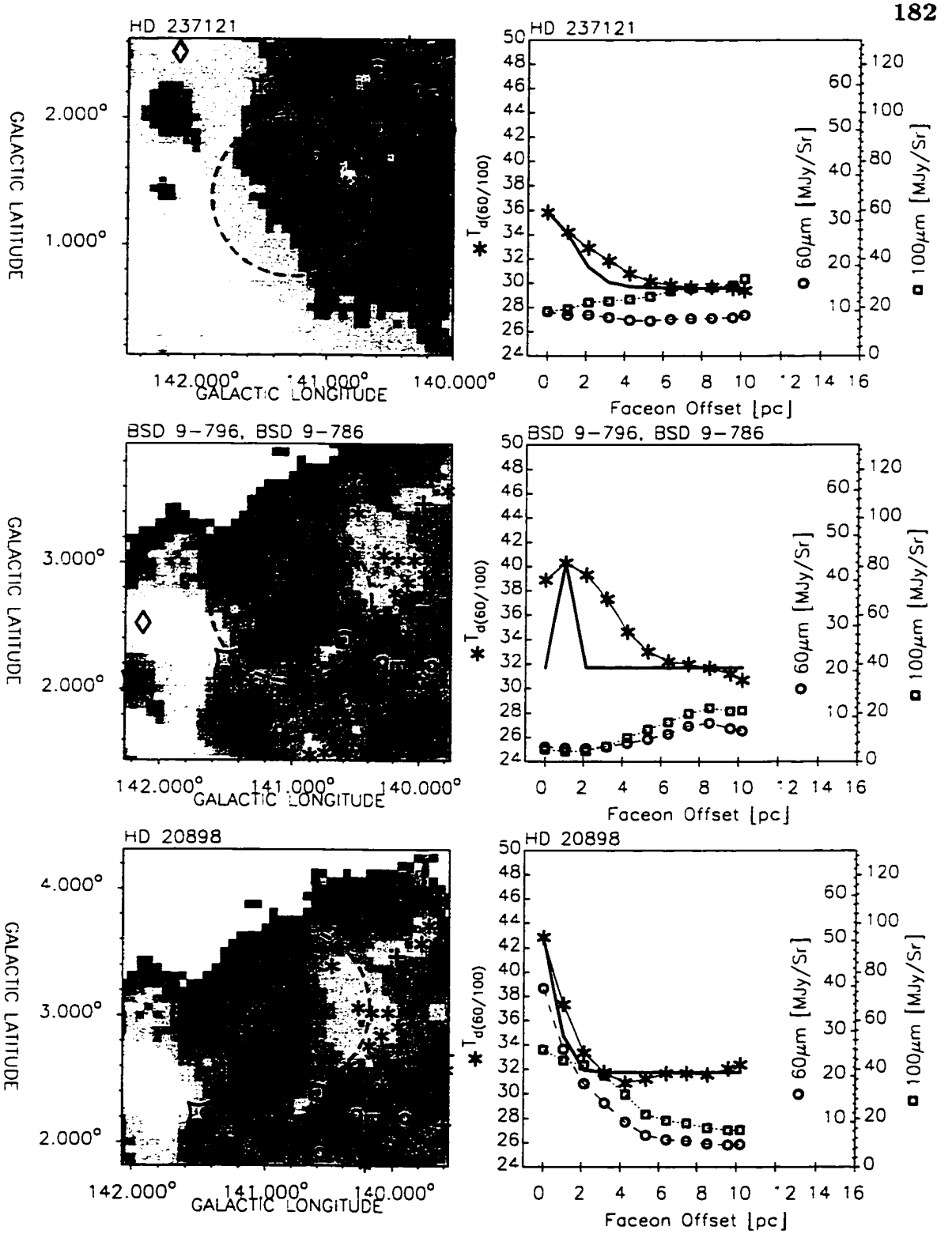

Figure 6.4 cont.

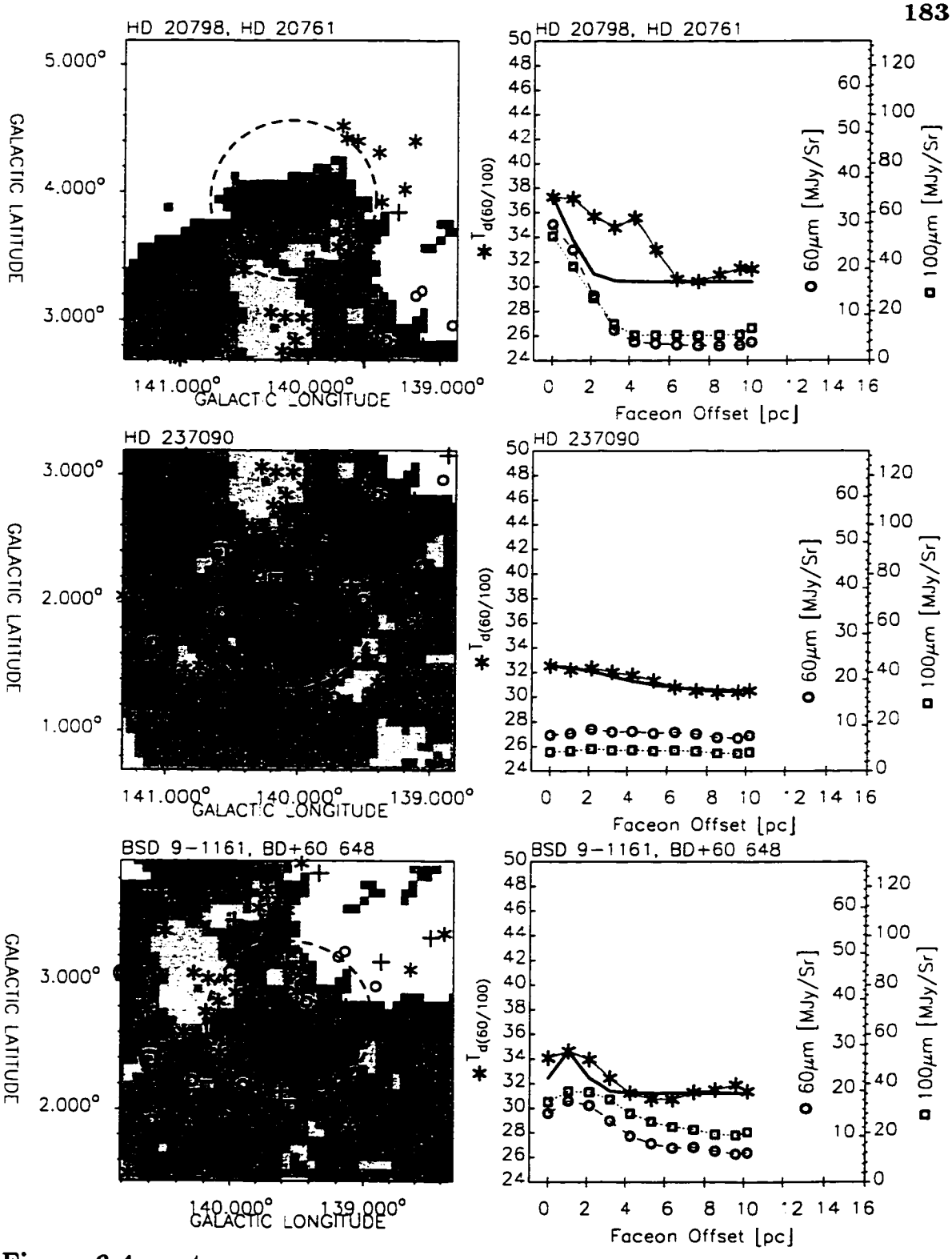

Figure 6.4 cont.

closer to the star, but in the case of HD 237121 this depletion appears to extend out to $\sim$ 4 pc. Given that HD 237121 (B0.5 V) is a much hotter star than HD 21389 (A0Iab), it may simply be that the dust grains in the vicinity of HD 237121 are being warmed out to a greater distance than in the vicinity of HD 21389.

BSD 9 – 796, BSD 9 – 786 : These two stars are superimposed upon the most extensive and warmest dust emission seen in the region. The dust could not have been warmed to the extent shown in Figure 6.4 by these stars alone, nor by all the additional Cam OB1 stars possibly associated with it (BSD 9–800, HD 237134 and BSD 9–780, Table 4.4). It is remarkable how symmetric the temperature profile is about the position of BSD 9–796 which argues against the presence of any additional heat source, either external and internal (embedded stars or proto-stars) being present. The solution to this dilemma may lie in the fact that the emission, both 60μm and 100μm, is very weak and may be sensitive to the correction for background emission. The symmetry of the dust temperature profile argues in favor of BSD 9-796 being the source of heat for warming the dust in this region, but a more careful analysis of the dust emission is required to confirm this.

HD 20898 : This hot giant lies to the north of the BSD 9-796, BSD 9-786 complex and appears to be warming the dust in Cam OB1 in a very predictable manner. As in the case of HD 21389 there is a decrease in the 100μm emission closer to HD 20898 but the drop off is shallower, and there is no apparent bright 100μm emission ridge encompassing it.

HD 20798, HD 20761 : Emission is peaked about the position of HD 20798 (HD 20761, a much cooler B9V star, almost certainly provides no additional warming), but the dust-temperature profile is very complicated. Within a few pc of HD 20798 the dust emission does diminish, but at a much slower rate than expected. At an offset position of $\sim$ 4 pc the dust temperature profile is severely affected by edge effects. There appear to be no other known sources in the field contributing to the warming of the dust and the coincidence of the warmest dust peak with HD 20798 does suggest it is responsible for warming the dust associated with Cam OB1.

HD 237090 : This very hot, luminous star appears to be adding a small amount of flux to the Cam OB1 dust. The fit to the dust temperature profile map is very good, suggesting the simple model of dust emission is essentially correct and that HD 237090 lies at a distance of 8.1 pc from the Cam OB1 dust. As was pointed out in §6.3.1, this star is probably not making a significant contribution to the ionizing

flux of S202 N, which lies slightly to the north-west at a distance of $\sim$ 17 pc. It is still curious that, given the ionizing flux of this star, no more radio continuum emission is observed in its immediate vicinity. The absence of such emission may be in part due to its close proximity to the CO emission where the attendant dust may serve to quench the flux of Lyman-continuum photons (Mathis 1986).

BSD 9 − 1161, BD + 60 648 : The emission for this region peaks at the position of BSD 9–1161, the hotter of the two stars. However, the radial profile of the dust emission does not diminish as rapidly as predicted by the simple model.

6.4 Conclusions

In this chapter it was shown that the optically identified Cam OB1 stars making up Cam R1 N and Cam R1 S are indeed associated with the Cam OB1 molecular gas seen along this line-of-sight. Evidence supporting this claim follows from:

1. Morphological arguments. There are two main stellar groups best seen in relation to the molecular gas at a radial velocity of -9.4 km s^{-1}. One group, which appears to be fairly young ($1 - 3 \times 10^6$ yr) is well correlated with a CO feature seen near $l = 140°, b = +3°$. A second, older ($3 - 50 \times 10^6$ yr) and more extended group appears to lie slightly to the south of the first group (centered on $l = 140°, b = +2°$). The absence of older stars in the first group suggests that the second group actually lies behind the CO emission containing the first group.
2. Physical arguments. The presence of HII regions coincident with the CO emission suggests they have been produced by hot Cam OB1 stars, primarily HD 19820. Furthermore, dust associated with the molecular gas in the Cam R1 region is clearly being warmed by the nearby Cam OB1 stars.
3. To the north or west of Cam R1 it is not possible to get any evidence of physical interaction between the stars and gas from radio or infrared emission, as these regions are either too confused with background emission or the data are not available.

Chapter 7

Star Formation in Cam OB1

Star formation in Cam OB1 is considered. It is shown that there are three distinct spatial and temporal star forming regions which appear to be restricted to the point of intersection of two, or possibly three, CO complexes. It is also shown that the structure of these CO complexes is similar to that of the newly formed stars, and that the star formation is relatively inefficient. It is proposed that star formation in the region has been triggered, either directly or indirectly, by a collision between the CO complexes.

7.1 Introduction

In the Introduction to this thesis, it was proposed that the star-forming process in the Galaxy could be considered in terms of three elements: a) the structural relationship between the newly formed stars and the molecular clouds from which they came, b) the temporal evolution of the molecular clouds leading to star formation, and c) the probability of star formation occurring at a given site. This chapter will consider the star formation in Cam OB1 and will attempt to assess the applicability of this analysis, within the limitations of the available data, to this region.

In regard to (a) above, the structural element of the star forming process, it was shown in Chapter 3 that the present CO survey (Digel et al. 1996, hereafter Di96) contained considerably more information about the structure of molecular clouds in the Cam OB1 region than previous CO surveys of the region (Dame et al. 1987). It was also shown that the distribution of CO emission followed a power-law similar to that found in the HI emission in the region (Green 1993). Finally, from an analysis of the structure of several of the CO complexes in this region using structure tree statistics (Houlahan & Scalo 1990, 1992), it was shown that the CO emission in these complexes appeared to have a hierarchical distribution suggestive of turbulence. In this chapter a comparison will be made of the distribution of CO cloud masses with the distribution of stellar masses in various regions of Cam OB1.

In regard to the second element of the star forming process, (b) the temporal evolution of the clouds, it was shown in Chapters 4, 5 and 6 that there are three spatially distinct groups of stars. In this chapter it will be established that there is a corresponding age difference for these groups, determined on the basis of HR diagrams constructed for two of the groups which are composed of optically-identified stars, or on the basis of the infrared emission from the third group of sources which suggests they are very young pre-main sequence stars still associated with their parental cocoons. Hence, the difference in the ages of these groups may be used to map out the evolution of the cloud complexes.

Finally, in regard to (c) above, the probability of the onset of star formation, it has been suggested by previous authors that the onset of star formation is triggered by the interaction between molecular cloud cores, which leads to the dissipation of their angular momentum and their subsequent collapse (Larson 1982, Evans et al. 1991, Bodenheimer et al. 1993). It is not possible, with the resolution of the CO data presently available (Di96), to consider the structure of the CO emission at scale-lengths $\leq$ 2.8 pc. However, circumstantial evidence, such as the low star forming efficiency (SFE), the preservation of the cloud structure over the course of star formation in the region, and the location of the star formation along the region of contact between two CO complexes, can be explained if the rate of favorable interactions, i.e., molecular core interactions which lead to the collapse of at least one core, is enhanced at the intersection of the colliding complexes.

The outline of this chapter will be as follows: §7.2 will identify and characterize the CO clouds and CO complexes in the Cam OB1 region. §7.3 will present an analysis of the star formation in terms of the three elements describing the star forming process, in each stellar group: §7.3.1 will consider Group I, §7.3.2 will consider Group II, and §7.3.3 will consider Group III. §7.4 will discuss the star forming mechanism(s) possibly active in the region. §7.5 will provide a summary of the analysis of star formation in the Cam OB1 region.

7.2 The Molecular Clouds and Cloud Complexes of Cam OB1

In Chapter 1 the idea that CO emission could be classified as being made up of a set of simple geometrical 'clouds' was introduced. The basis of this classification scheme was the assumption that a CO feature, say a 6σ peak which could be isolated from an integrated profile of the emission (see Figure 2.11) at some arbitrary noise level (3σ), in fact represented a physical entity. If this was the case, then these clouds could be characterized by a set of both measured and derived quantities. The measured quantities include Δv, the cloud's velocity dispersion, i.e., the $FWHM$ of a Gaussian fit to the velocity profile of the cloud, the radius of a cloud as fitted to the half-maximum of its integrated CO intensity, W_{CO}, and the centroid of the cloud in (l, b, v), while the derived quantities include the cloud's luminosity in the CO line (Eq. 1.47), the cloud's CO mass (Eq. 1.52) and the cloud's virial mass assuming it is spherical and uniform in density (Eq. 1.55). Details of the cloud selection procedure and an estimate of the uncertainty in the derived quantities for these clouds are given in Appendix A (in brief, these uncertainties are of the order of 10 - 25%, with the largest uncertainty for the smallest clouds).

Seventy-nine CO 'clouds' or emission features were selected in the Cam OB1 region which could be reasonably well modelled as spherical structures, with a Gaussian velocity profile. Clouds were rejected if they were too small, if it was too difficult to isolate one 6 σ peak, or if they could not be fitted by a simple Gaussian profile. Table 7.1 provides the results of this analysis and includes a cloud's central position (designation), whether or not it has been assigned to a complex (see below), the cloud's velocity dispersion, radius, CO luminosity, CO mass, virial mass, peak temperature and mean particle density. The last 3 columns of Table 7.1 provide the integration boundaries in (l, b, v) for each cloud. Note from the ultimate row in Table 7.1, which are the sums of the indicated quantities, that the total CO luminosity for the selected clouds is $\sim 42 \times 10^3$ K km s^{-1} pc^2, while the total luminosity for the surveyed region is $\sim 69 \times 10^3$ K km s^{-1} pc^2 (i.e., the total area of the survey, in pc, times the average of 2.43 K km s^{-1}). Hence, the sample of selected 'clouds' represents $\sim 61\%$ of the total CO emission in the region.

An additional classification scheme has been used to characterize the CO emission by placing the clouds into 'complexes', and in some cases, a collection of complexes. Clouds were considered part of a complex if they had similar mean velocities, and spatial positions. The strength of this claim was then checked by considering

Table 7.1: Physical Parameters for the Cam OB1 CO Clouds

No	Designation[a]	Complex[b]	Δv_{LSR}[c] [km s^{-1}]	r[d] [pc]	L_{CO}[e] [10^3 K km s^{-1} pc^2]	M_{CO}[f] [10^3 $M_\odot$]	M_{vir}[g] [10^3 $M_\odot$]	T_{max}[h] [K]	ρ[i] [H_2 cm^{-3}]	l[j] (min/max) [deg./deg.]	b[j] (min/max) [deg./deg.]	v[j] (min/max) [km s^{-1}/km s^{-1}]
1	G131.6-1.5-13.6		2.65	4.09	0.60	2.52	6.97	2.59	180	131.1250/132.0000	-1.8750/-01.1250	5.50/ 22.00
2	G131.6+2.5-9.2		1.53	2.90	0.02	0.08	1.65	1.44	160	131.3750/131.8125	+2.3125/+2.6875	5.50/ 22.00
3	G132.1+0.2-15.4		2.07	2.73	0.27	1.13	2.84	2.07	270	131.7500/132.4375	0.1250/+0.4375	10.66/ 22.00
4	G132.1+2.6-7.8		1.90	2.56	0.03	0.13	2.24	3.03	38	131.8750/132.3125	+2.3125/+2.8125	5.50/ 22.00
5	G132.2+0.8-10.2		2.80	2.39	0.11	0.46	4.54	1.49	160	131.9375/132.5000	+0.5625/+0.9375	5.50/ 22.00
6	G132.4-1.1-11.7		3.40	2.05	0.03	0.13	5.75	1.10	73	132.3125/132.5000	1.1875/ 0.9375	5.50/ 22.00
7	G132.9-0.8-14.1		3.50	3.24	0.24	1.01	9.62	2.14	140	132.6500/133.1875	1.0625/ 0.6250	9.36/ 22.00
8	G133.1-1.6-12.9		7.45	2.39	0.13	0.55	32.2	1.09	200	132.8750/133.2500	1.7500/ 1.3750	6.50/ 22.00
9	G133.1-1.6-11.8		1.65	2.73	0.15	0.63	1.80	1.42	150	132.8750/133.2500	1.7500/ 1.3750	6.11/ 22.00
10	G133.3-0.1-15.1		2.43	4.09	0.85	3.57	5.86	4.53	250	132.8125/133.6875	0.3125/+0.2500	8.71/ 22.00
11	G133.8-1.6-13.1		3.91	1.88	0.27	1.13	6.97	1.79	830	133.3750/134.1875	1.8125/ 1.3750	8.06/ 22.00
12	G133.8+0.2-14.3		4.63	2.39	0.19	0.80	12.4	2.60	290	133.6250/133.9375	+0.0625/+0.3125	9.36/ 22.00
13	G134.0-0.5-7.3		2.76	3.07	0.18	0.76	5.67	2.07	130	133.7500/134.2500	0.7500/ 0.3750	5.50/ 10.66
14	G134.0+0.9-11.2		3.64	3.41	0.32	1.34	11.0	1.43	160	133.6250/134.3125	+0.5625/+1.1875	5.50/ 22.00
15	G134.1-0.6-13.8		2.81	2.56	0.23	0.97	4.90	2.24	280	133.7500/134.2500	0.7500/ 0.3750	10.66/ 22.00
16	G134.3+3.8-9.2		2.71	3.07	0.06	0.25	5.47	2.03	42	134.0000/134.6250	+3.4375/+4.0000	5.50/ 22.00
17	G134.4-1.1-12.7		2.71	2.90	0.15	0.63	5.16	1.74	130	134.1875/134.6250	1.3125/ 0.9375	5.50/ 22.00
18	G134.4+0.1-14.4		1.88	2.22	0.30	1.26	1.90	2.97	560	134.1875/134.5625	0.1250/+0.3125	8.71/ 22.00
19	G135.1-1.2-9.8		4.03	5.97	0.93	3.91	23.5	3.28	89	134.8125/135.4375	1.6875/ 0.8125	5.50/ 22.00
20	G135.6+3.6-9.7		3.99	2.22	0.07	0.29	8.57	2.08	130	135.2500/135.8125	+3.3125/+3.8125	5.50/ 22.00
21	G135.9-0.8-8.3		3.61	2.90	0.25	1.05	9.16	2.27	210	135.6250/136.2500	1.0000/ 0.6250	5.50/ 22.00
22	G136.2+0.4-10.8		5.15	3.07	0.32	1.34	19.8	3.05	230	135.8125/136.5000	+0.0000/+0.9375	5.50/ 22.00
23	G136.4-1.7-10.6		3.20	5.63	1.47	6.17	14.0	3.72	170	135.8125/137.0000	2.0000/ 1.3125	5.50/ 22.00

Table 7.1 cont.: Physical Parameters for the Cam OB1 CO Clouds

No	Designation[a]	Complex[b]	Δv_{LSR}[c] [km s^{-1}]	r[d] [pc]	L_{CO}^{e} [10^3 K km s^{-1} pc^2]	M_{CO}^{f} [10^3 $M_\odot$]	M_{vir}^{g} [10^3 $M_\odot$]	T_{max}^{h} [K]	ρ^{i} [H_2 cm^{-3}]	$l^{j}_{(min/max)}$ [deg./deg.]	$b^{j}_{(min/max)}$ [deg./deg.]	$v^{j}_{(min/max)}$ [km s^{-1}/km s^{-1}]
24	G136.6-0.9-8.3		5.72	3.75	0.41	1.72	29.8	2.30	160	136.2500/136.8750	1.1250/ 0.6250	-5.50/-22.00
25	G137.3-1.2-9.5		2.03	1.88	0.05	0.21	1.88	0.94	150	137.1875/137.4375	-1.3125/-1.0000	-5.50/-22.00
26	G137.6+2.0-12.6	A	2.50	2.56	0.07	0.29	3.88	2.58	210	137.3750/137.8750	+1.8125/+2.1250	-5.50/-22.00
27	G137.8+2.5-12.3	A	4.72	3.92	0.48	2.02	21.2	3.29	160	137.3125/138.1875	+2.0625/+2.8125	-5.50/-22.00
28	G138.2-1.4-12.3		3.02	1.88	0.08	0.34	4.16	1.19	250	137.9375/138.3750	-1.5625/-1.2500	-5.50/-22.00
29	G138.3+3.8-10.0	B	3.66	3.57	0.94	3.95	11.6	3.03	420	137.3750/138.9375	+3.5000/+4.0000	-5.50/-22.00
30	G138.5-1.9-13.7		2.69	2.39	0.11	0.46	4.19	1.53	160	138.2500/138.7500	-2.0000/-1.6875	-5.50/-22.00
31	G138.8 0.4-10.5		1.43	3.41	0.20	0.84	1.69	2.14	100	138.5000/138.9375	-1.0000/+0.3125	-5.50/-22.00
32	G139.0+0.9-9.6		1.56	1.88	0.10	0.42	1.11	1.80	300	138.5625/139.1875	+0.6875/+1.0625	-5.50/-22.00
33	G139.2+4.6-10.8	B	2.97	3.74	0.43	1.81	8.00	2.67	170	139.0000/139.4375	+4.2500/+5.0000	-5.50/-22.00
34	G139.2+5.9-12.5	C	2.79	3.23	0.26	1.09	6.10	1.97	160	139.0000/139.3750	+5.6250/+6.1250	-5.50/-22.00
35	G139.2+6.3-13.5	C	7.48	3.23	0.18	0.76	43.8	0.95	110	139.0000/139.4375	+6.1250/+6.6250	-5.50/-22.00
36	G139.3+2.0-13.4	A	3.28	3.75	0.32	1.34	9.78	2.47	120	139.0625/139.5000	+1.6875/+2.1875	-5.50/-18.47
37	G139.3+5.3-12.6	C	6.00	2.72	0.65	2.73	23.8	2.76	650	139.0000/139.6875	+4.9375/+5.6250	-5.50/-22.00
38	G139.5-1.5-13.3		3.35	2.73	0.73	3.07	7.43	3.42	720	139.1250/140.1250	-2.0000/-0.9375	-5.50/-22.00
39	G139.6+1.3-12.9	A	4.20	2.56	0.28	0.88	11.0	2.92	250	139.1875/139.8125	+1.0625/+1.5000	-5.50/-22.00
40	G139.7+4.0-9.9	B	4.46	5.79	0.88	3.70	27.9	2.28	91	139.4375/140.0000	+3.4375/+4.5625	-5.50/-22.00
41	G139.7+6.0-12.6	C	5.71	2.21	0.23	0.97	17.5	1.29	430	139.4375/139.9375	+5.8125/+6.1250	-5.50/-22.00
42	G139.8+1.7-13.6	A	1.80	2.05	0.08	0.34	1.61	1.92	190	139.6250/139.9375	+1.5625/+1.8125	-5.50/-19.12
43	G139.8+5.7-12.6	C	2.48	3.23	0.19	0.80	4.82	2.89	110	139.5000/140.0000	+5.5000/+5.8125	-5.50/-22.00
44	G139.9+2.8-10.5	B	4.28	3.41	0.94	3.95	15.1	3.96	480	139.5000/140.3125	+2.5000/+3.1250	-5.50/-22.00
45	G140.0+2.2-12.1	A	4.73	4.27	1.15	4.83	23.2	3.58	300	139.5625/140.4375	+1.9375/+2.3750	-5.50/-22.00
46	G140.3+4.8-13.1	C	3.38	3.74	0.41	1.72	10.4	3.71	160	140.0625/140.4375	+4.5000/+5.0000	-5.50/-22.00

Table 7.1 cont.: Physical Parameters for the Cam OB1 CO Clouds

No	Designation[a]	Complex[b]	Δv_{LSR}[c] [km s^{-1}]	r[d] [pc]	L'_{CO} [10^3 K km s^{-1} pc^2]	M^f_{CO} [10^3 $M_\odot$]	M^g_{vir} [10^3 $M_\odot$]	T^h_{max} [K]	ρ^i [H_2 cm^{-3}]	$l^j_{(min/max)}$ [deg./deg.]	$b^j_{(min/max)}$ [deg./deg.]	$v^j_{(min/max)}$ [km s^{-1}/km s^{-1}]
47	G140.4+3.3-8.9	B	3.13	3.50	0.28	1.18	8.10	2.29	130	140.1875/140.5625	+3.0625/+3.4375	-5.50/-22.00
48	G140.5+1.5-13.9	A	3.98	5.97	1.26	5.29	22.4	3.61	120	139.9375/141.1250	+1.1250/+1.8125	5.50/ 22.00
49	G140.5+3.9-11.2	B	4.47	3.91	0.72	3.02	19.0	2.87	240	140.1875/140.8125	+3.6250/+4.1875	5.50/ 22.00
50	G140.7+2.2-12.7	A	2.87	3.75	0.48	2.02	7.49	3.56	180	140.5000/140.9375	+2.0000/+2.4375	5.50/ 22.00
51	G140.7+3.3-10.0	B	4.17	3.24	0.29	1.22	13.7	2.35	170	140.5625/140.9375	+3.1250/+3.5000	5.50/ 22.00
52	G140.7+4.9-13.3	C	2.40	3.57	0.56	2.35	4.99	4.31	250	140.5000/141.0000	+4.6250/+5.1250	5.50/ 22.00
53	G140.7+5.9-12.9	C	2.94	5.62	1.73	7.27	11.8	4.00	200	140.0625/141.1250	+5.5625/+6.1250	5.50/ 22.00
54	G141.1+2.1-12.6	A	4.31	2.56	0.32	1.34	11.5	2.60	380	140.9375/141.3750	+1.9375/+2.3750	5.50/ 22.00
55	G141.2+3.9-10.8	B	5.46	3.74	0.28	1.18	27.0	1.69	110	141.0000/141.3750	+3.5625/+4.2500	5.50/ 22.00
56	G141.2+5.4-10.9	D	1.85	2.55	0.25	1.05	2.12	3.92	300	141.0625/141.3750	+5.1875/+5.5650	5.50/ 22.00
57	G141.2+6.3-11.1	D	2.17	2.72	0.34	1.43	3.11	3.96	340	140.9375/141.4375	+6.1250/+6.5000	5.50/ 22.00
58	G141.4+2.0-11.5	G	2.07	1.71	0.08	0.34	1.78	2.05	330	141.3125/141.5625	+1.9375/+2.1250	-5.50/-22.00
59	G141.6+4.4-9.1	D	3.95	3.57	0.45	1.89	13.5	2.38	200	141.3750/141.8750	+4.0625/+4.6250	-5.50/-22.00
60	G141.9+6.5-12.2	C	3.91	2.38	0.31	1.30	8.82	2.92	460	141.5625/142.3750	+6.1875/+6.8125	5.50/ 22.00
61	G142.0+0.6-15.6	H	4.37	4.95	1.80	7.56	22.9	5.06	300	141.5000/142.3750	+0.3125/+0.7500	-5.50/-22.00
62	G142.0+1.0-15.3	H	3.64	5.12	1.82	7.64	16.5	5.67	270	141.6250/142.2500	+0.7500/+1.3125	-5.50/ 22.00
63	G142.0+2.6-10.4	F	2.84	3.58	1.40	5.88	7.00	5.18	610	141.4375/142.6875	+2.3125/+2.8750	5.50/-22.00
64	G142.1-1.5-17.7		1.95	2.90	0.12	0.50	2.67	2.00	100	141.4375/142.3125	2.0000/ 1.3750	5.50/ 22.00
65	G142.1+1.8-12.3	G	4.33	3.07	2.78	11.7	14.0	9.67	690	141.6250/142.3750	+1.5000/+2.1250	-5.50/-22.00
66	G142.2+5.2-9.6	D	1.40	4.08	0.32	1.34	1.94	3.17	94	141.8750/142.4375	+4.8125/+5.7500	5.50/-22.00
67	G142.4-1.1-15.2	H	2.62	4.44	0.41	1.72	7.39	2.27	94	141.9375/142.8750	1.3125/ 0.8125	5.50/ 22.00
68	G142.4-0.4-13.8	H	3.32	1.71	0.15	0.63	4.57	2.25	603	142.2500/142.5625	0.5000/ 0.1875	-5.50/-22.00
69	G142.4+4.0-11.2	B	3.78	1.87	0.07	0.29	6.48	0.95	210	142.1875/142.5000	+3.8750/+4.2500	-5.50/-22.00

Table 7.1 cont.: Physical Parameters for the Cam OB1 CO Clouds

No	Designation[a]	Complex[b]	Δv_{LSR}[c] [km s^{-1}]	r[d] [pc]	L'_{CO} [10^3 K km s^{-1} pc^2]	M^f_{CO} [10^3 $M_\odot$]	M^g_{vir} [10^3 $M_\odot$]	T^h_{max} [K]	ρ^i [H_2 cm^{-3}]	$l^j_{(min/max)}$ [deg./deg.]	$b^j_{(min/max)}$ [deg./deg.]	$v^j_{(min/max)}$ [km s^{-1}/km s^{-1}]
70	G142.5+1.1 13.4	G	4.52	5.46	2.10	8.82	27.1	6.08	180	142.3125/142.6875	+0.7500/+1.5000	5.50/-22.00
71	G142.5+7.5 13.8		2.64	3.74	0.62	2.60	6.32	3.54	160	141.9375/142.9375	+6.9375/+8.0000	5.50/ 22.00
72	G142.9-0.4 13.9	H	4.30	3.75	0.52	2.18	16.8	2.65	200	142.5625/143.1875	0.6875/ 0.1250	5.50/ 22.00
73	G143.0+0.9 11.6	G	4.29	4.95	1.60	6.72	22.1	4.09	270	142.6875/143.5000	+0.5000/+1.1250	5.50/ 22.00
74	G143.3+1.7 10.3	F	4.05	3.41	1.49	6.26	13.6	5.88	760	142.8750/143.8750	+1.3750/+1.9375	5.50/ 22.00
75	G143.3+4.6 10.8	E	5.81	2.72	0.19	0.80	22.3	1.41	190	143.0625/143.4375	+4.4375/+4.8125	5.50/ 22.00
76	G143.5-0.7 14.9	H	2.64	1.71	0.07	0.29	2.89	1.31	280	143.3125/143.6250	0.8125/ 0.4375	5.50/-22.00
77	G143.6 1.5 13.5	H	3.89	4.78	0.92	3.86	17.5	2.39	170	143.1250/144.0000	2.0000/ 0.9375	5.50/-22.00
78	G143.7+3.6 10.0	E	4.07	4.08	0.62	2.60	16.4	2.96	180	143.1875/144.0000	+3.1875/+3.8125	5.50/ 22.00
79	G143.7+4.3 10.2	E	5.52	5.28	1.14	4.79	39.0	2.24	160	143.3750/144.0000	+3.8125/+4.7500	5.50/ 22.00
	Total				41.8	175	914					

a) Mean position of emission feature in (l, b, v) coordinates.

b) Complex to which cloud has been assigned.

c) FWHM of the Gaussian fit. v_{LSR} is calculated assuming standard solar motion.

d) Cloud radius at the half-maximum contour of W_{CO}, corrected for beam size, and assuming D = 975 pc.

e) CO luminosity, integrated from the fit to the cloud's composite spectrum.

f) Cloud mass derived from L_{CO} on the assumption that $X = 1.9 \times 10^{-2}$ cm^{-2} (K km s^{-1})$^{-1}$ with an additional factor of 1.36 for helium.

g) Mass of a uniform, spherical cloud in virial equilibrium $M_{vir} = 5/(8\,G\,ln2)(4/3)^{1/2}\,r\,\Delta v^2$, where the factor $(4/3)^{1/2}$ corrects the half-maximum radius, r, to the full radius of a uniform, spherical cloud.

h) Peak T^*_R. Note: This peak cloud temperature does not necessarily occ ur at the cloud position suggested by its designation.

i) Equivalent mean H_2 particle density for cloud assuming $M_{H_2} = 3.32 \times 10^{-24}$ gm.

j) Boundaries of cloud in (l, b, v_{LSR}) coordinates used in calculating the cloud's composite spectrum.

the position of the various stellar groups identified in Chapters 4, 5 and 6 in relation to these complexes. As an example, all of the stars of Group I (older, more evolved stars - see §7.3.1) in the vicinity of Complex A, lie in front of this complex and are known to be interacting with it (see the discussion of Figure 6.1), which places all of the clouds in Complex A at the same distance and associated with one another. As another example, Complex C lies at more negative velocities than Complex B, and Complex C lies in front of Complex B, since there is a marked enhancement of Group II stars (younger, pre-main sequence stars - see §7.3.2), which are coincident with Complex B but obscured by Complex C. Finally, Complex B lies in front of Complex A, as the Group I stars associated with Complex A appear to be obscured by Complex B. The classification of complexes has been restricted to the clouds in the Cam R1 region.

The most detailed description of the CO cloud complexes is provided by the assignments given in Table 7.1. A simple schematic representation of these complexes is shown in Figure 7.1. The shading scheme and positional overlay of emission features, e.g., Complex C in front of Complex B, have been chosen to reflect the relative positions of the complexes.

In this representation of the data, and taking into account the similar velocities of some of the complexes, it would appear that the complexes may be organized into even larger CO structures. This is not easily seen in the map of the integrated CO emission (Figure 2.11), nor in the velocity-moment map (Figure 2.12). Figure 7.2 shows a histogram of the mean velocity distribution for the clouds in these larger CO structures.

One larger CO structure comprises the Complexes A, C and G, and has a centroid, weighted by mass, of ($141\overset{\circ}{.}1, +2\overset{\circ}{.}8, -12.7$ km s^{-1}) with a dispersion of ~ 0.6 km s^{-1}, and a mean radius of $2\overset{\circ}{.}1$ or ~ 37 pc. A second large CO structure, made up of Complexes B, D, E and F, has a centroid of ($141\overset{\circ}{.}6, +3\overset{\circ}{.}6, -10.3$ km s^{-1}), a dispersion in its velocity of ~ 0.3 km s^{-1}, and a mean radius of $1\overset{\circ}{.}9$ or ~ 33 pc.

The structure of Complex H is more difficult to understand given the paucity of clouds defining this complex. It may be that Complex H is either rotating, or possibly is made up of several different components at different velocities. A detailed survey of stars counts in this region may serve to distinguish between these two possible scenarios.

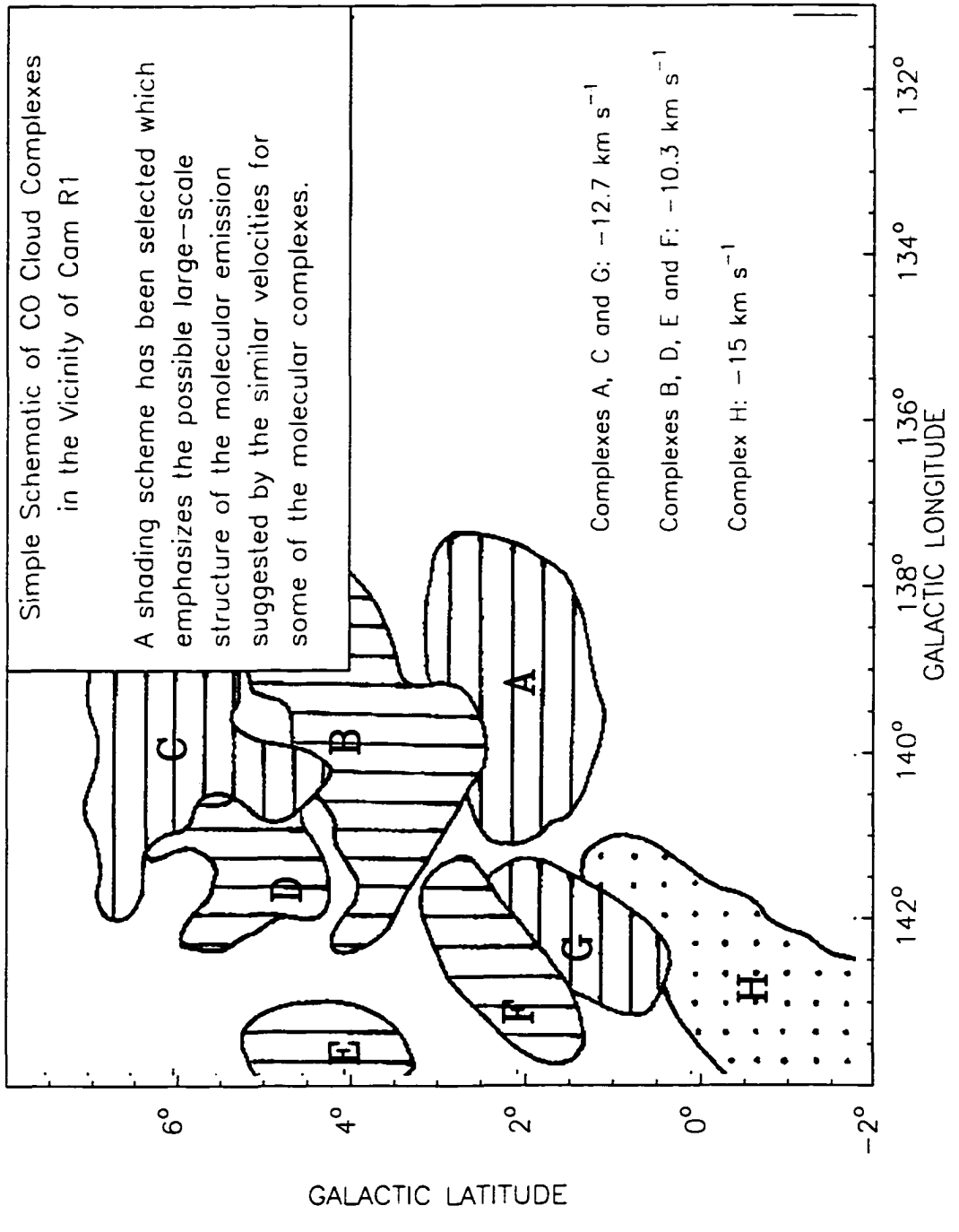

Figure 7.1 A simple schematic showing cloud complexes, selected on the basis of similar radial velocities and positions, in the Cam R1 region as listed in Table 7.1.

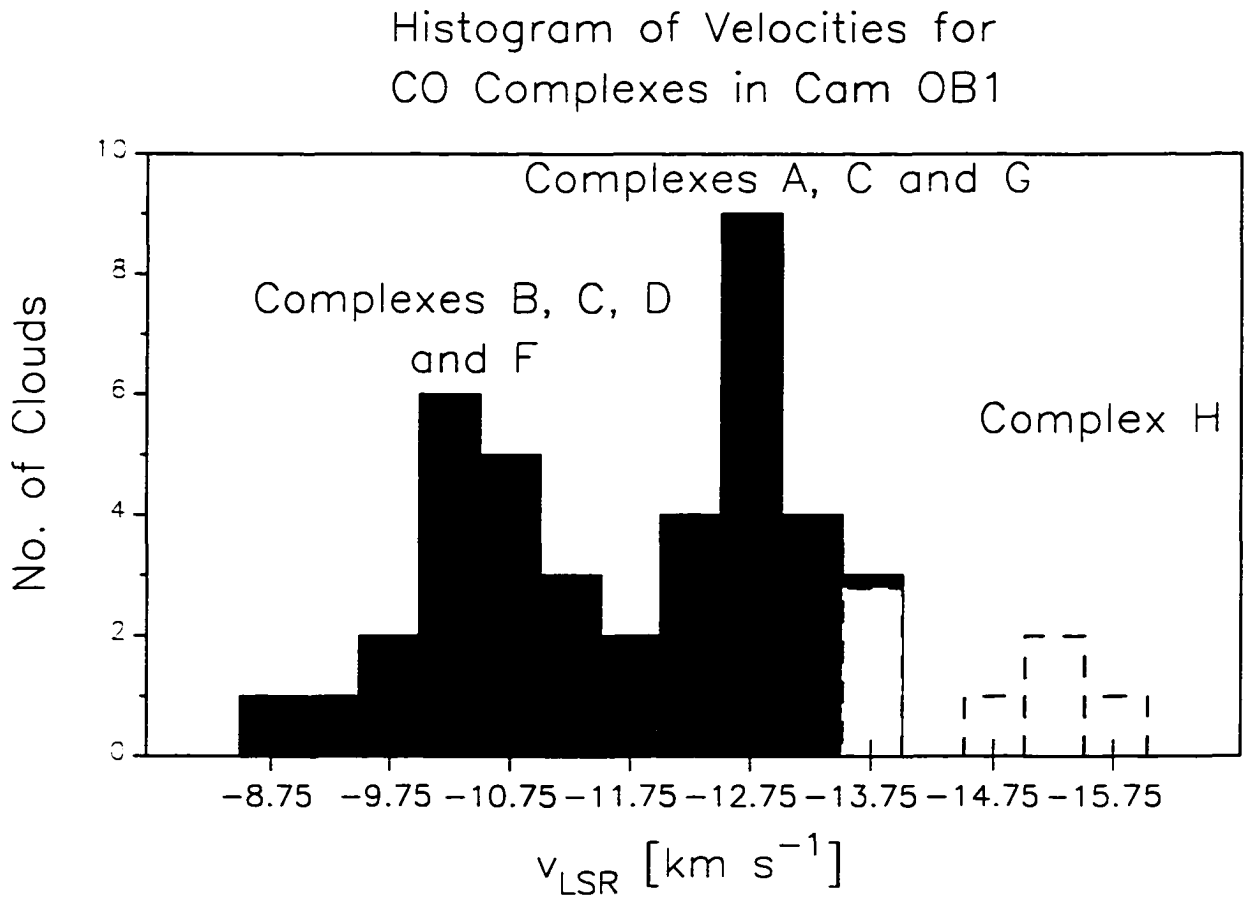

Figure 7.2 Histogram of mean velocities for the three main CO complexes seen in the Cam R1 region. Note that the height of the bin for the Complex H clouds at $v_{LSR} = -13.75$ km s^{-1} has been slightly reduced for clarity.

7.3 The Stellar Groups in Cam OB1

7.3.1 Group I

In Chapter 4, a description of the distribution of optically-identified stars associated with Cam R1 was made on the basis of age, which placed the stars in one of two groups, Cam R1 N or Cam R1 S, i.e., stars in Cam R1 N, on average, were appreciably younger than those in Cam R1 S (see Figures 4.7 and 4.8). It then became apparent in Chapter 6 (see discussion in §6.2) that the older population of stars that had been placed in Cam R1 N all appear at the edge of Complex B, and were probably located behind it. This suggested that these stars really are more typical of the stars in Cam R1 S, i.e., older and placed behind Complex B. Hence, a more meaningful description of the distribution of stars in Cam R1 would include the older stars of Cam R1 N with the stars of Cam R1 S. This group of older stars

will be designated as Group I. Figure 7.3 is an overlay of Group I over the CO emission seen at -9.4 km s^{-1}. This velocity cut has been chosen as it most clearly illustrates the position of the various Groups of stars relative to the CO complexes. An HR diagram is plotted in Figure 7.4 which shows the evolutionary status of the group. Stellar data for all of the figures are taken from Table 7.2.

In the model of star formation as a process characterized by three fundamental elements, i.e., structural, temporal and stochastic, there are several observations which can be made which demonstrate the role of these elements. For the Group I stars, these observations can be summarized as follows:

A. Temporal

1. Age Using the models of Palla & Stahler (1993) for pre-main sequence stars, and Garmany & Stencel (1992) for evolved stars, one can deduce from Figure 7.4 the ages for the individual stars for Group I. Figure 7.5 is a histogram of the age distribution for those Group I stars whose placement on the HR diagram, in terms of age, is unambiguous. There may be evidence from Figure 7.5 for a break in the frequency of star formation from 30 - 45 Myr. The reality of this break is difficult to estimate as it depends upon the uncertainty in the ages of the stars and relies on small number statistics. For a given star an uncertainty of $\sim$ 10% in its distance, an error in its photometry and reddening of $\sim 0^{m}.1$, plus an error in interpolating its position in the theoretical models of $\sim$ 10% would suggest an uncertainty of $\sim 20 - 30\%$. An uncertainty of this order would argue that the general distribution of stars is real but the gap may not be.

Stars older than 45 Myr represent the earliest epoch of star formation which can be seen in the Cam R1 region. The stars which did form prior to 45 Myr, and are still detectable, are all of intermediate mass $\sim 6 - 8$ $M_{\odot}$ (see Table 4.4). For stars younger than 30 Myr, there is a larger range in the masses, $\sim 3 - 30$ $M_{\odot}$. The star formation rate for these stars also appears to be steadily increasing since its onset. Hence, *it would appear that the Group I stars formed in a contemporaneous manner*, i.e., over a period of time, in agreement with current theoretical models of star formation (Stahler 1985, Palla & Stahler 1990, 1991), and with what is seen elsewhere in the Galaxy (Hillenbrand et al. 1993).

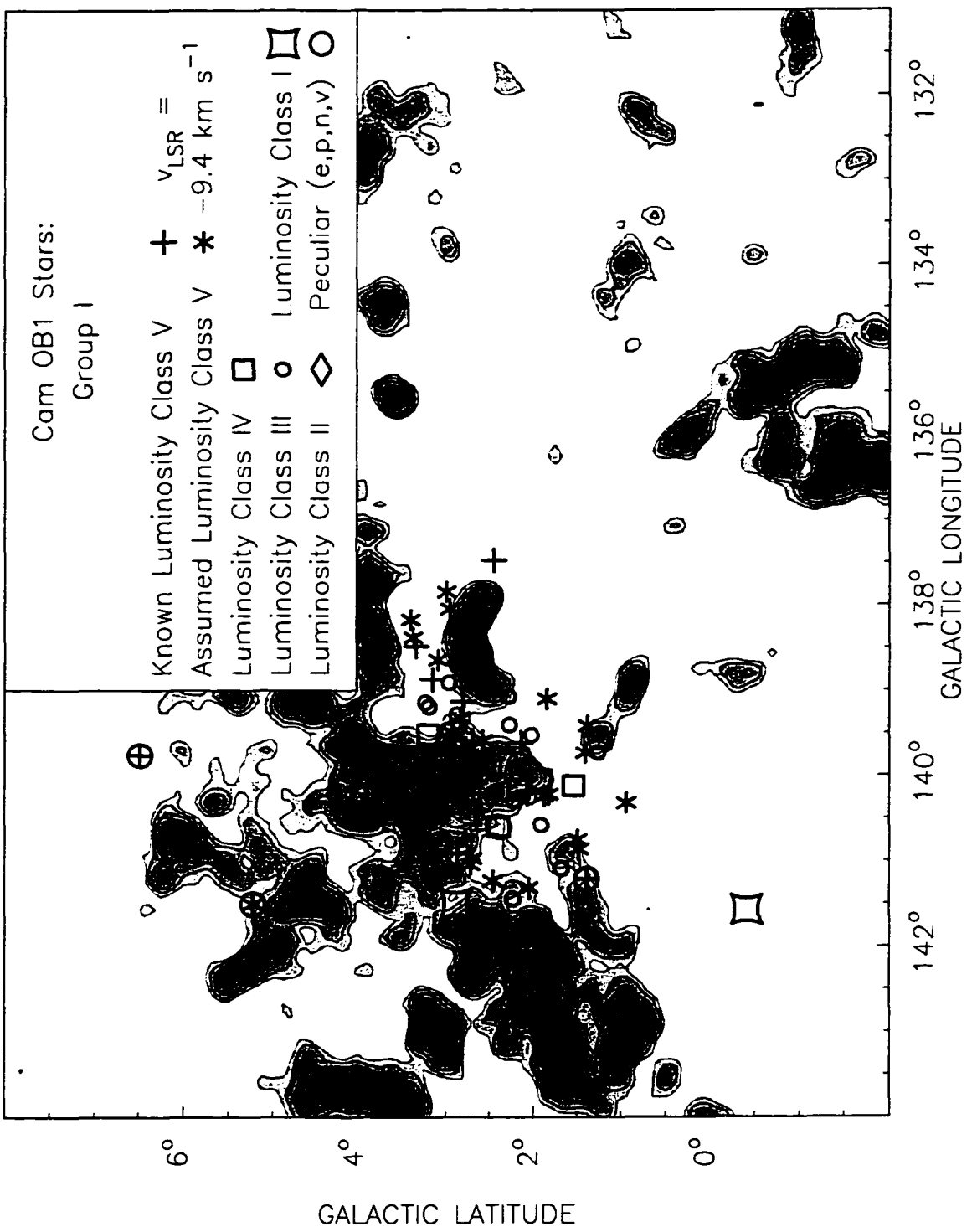

Figure 7.3 Overlay of Group I stars over CO emission at -9.4 km s^{-1}.

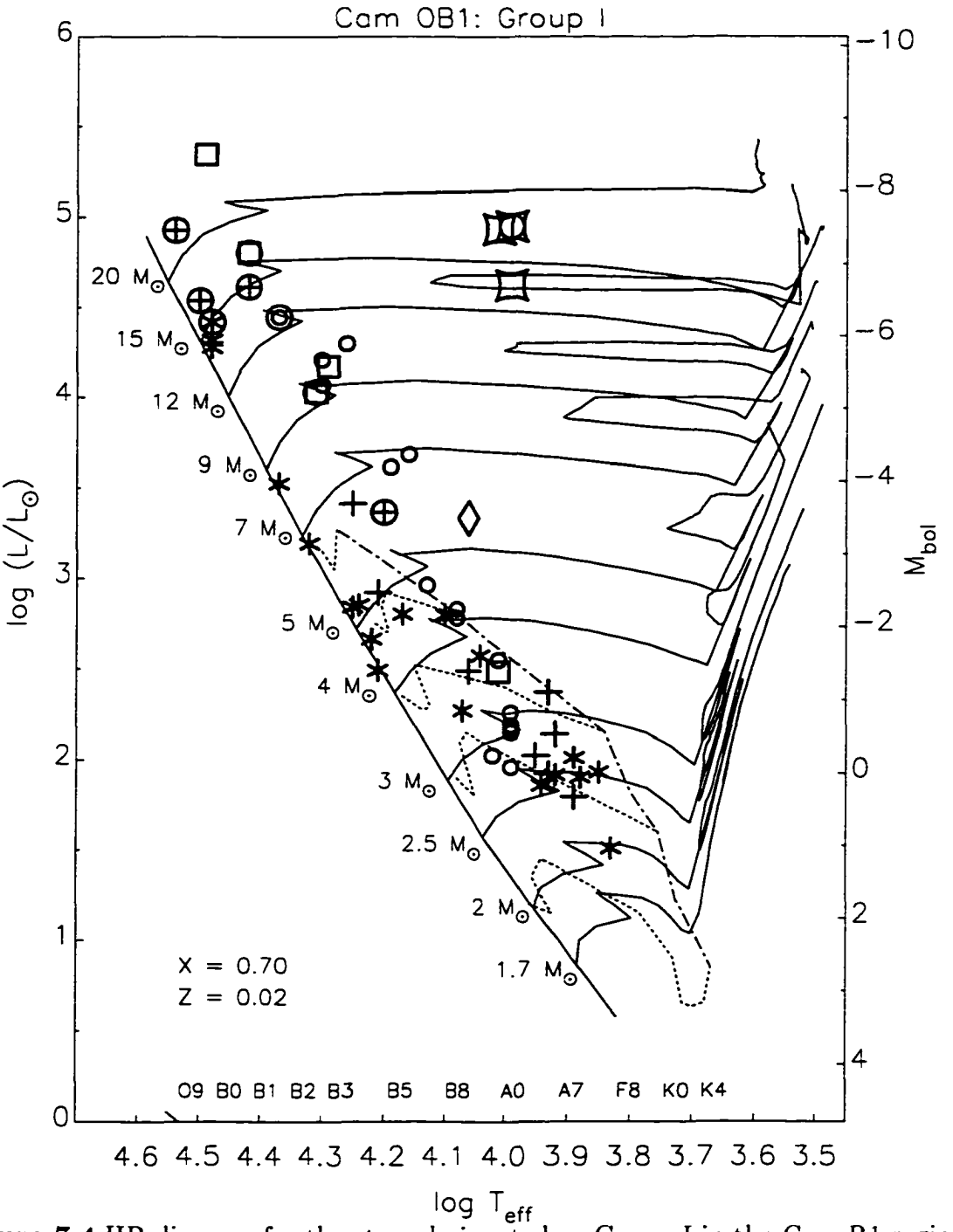

Figure 7.4 HR diagram for the stars designated as Group I in the Cam R1 region. The pre-main sequence tracks are taken from Palla & Stahler (1993) - dotted lines - as is the 'birthline' - dash-dot line - below which stars first become optically visible. An accretion rate, $d\mathrm{M}/dt = 1 \times 10^{-5}$ $\mathrm{M}_\odot$ yr^{-1} has been assumed in determining the position of the birthline on the HR diagram. A lower accretion rate will move the birthline to the right in the diagram (Stahler & Walter 1993). The post-main sequence evolutionary tracks - solid lines - are taken from Garmany & Stencel (1992) for the metallicity indicated.

Table 7.2: Cam OB1 - Stellar Group I

No.[a]	Name[b]	l^c [deg.]	b^c [deg.]	MK Des.[d]	v^c_{LSR} [km s^{-1}]	log T^f_{eff} [K]	M^g_{bol} [mag]	log M^h [$M/M_\odot$]	t_m/t^i_{pm} [10^6 yr]
9	BD+61 506	137.47	+2.45	B9V	+0.0	3.92	−0.54	0.54	/1
10	BSD 9-1528	137.84	+2.99	B6		4.17	−2.18	0.71	100/1
11	BSD 9-1541	138.04	+2.95	A0		3.85	−0.02	0.48	/1
12	BSD 9-1606	138.17	+3.40	B5		4.15	−2.53	0.75	100/1
13	BSD 9-1637	138.38	+3.37	B8		3.99	−0.34	0.52	300/2
14	BD+61 533	138.38	+3.95	B8		4.10	−2.17	0.71	170/1
15	BD+61 529	138.48	+3.34	B3V	−17.0	4.25	−3.70	0.87	75 /
16	BD+61 530	138.64	+3.09	B9		4.22	−1.84	0.67	87 /3
17	BD+61 534	138.87	+3.15	B8V	−3.0	3.95	−0.25	0.51	500/2
18	BD+60 635	138.91	+2.96	B7III	−36.0	4.08	−2.13	0.70	174/1
19	BSD 9-1042	139.07	+2.28	A0III		3.99	−0.57	0.54	400/2
20	BSD 9- 448	139.10	+1.84	B8		4.04	−1.61	0.65	/1
21	BSD 9-1102	139.13	+2.80	B9.5V		3.93	0.00	0.48	500/2
22	BD+60 645	139.14	+3.23	B8III		4.08	−2.25	0.72	174/1
23	BD+60 646	139.19	+3.19	B6III		4.13	−2.58	0.75	99 /
25	BSD 9-1134	139.28	+2.87	B9III		4.02	−0.25	0.51	450/3
27	BSD 9-1137	139.32	+2.82	A0		3.83	1.03	0.37	/3
29	BD+59 604	139.40	+2.27	B9III	+10.0	4.01	−1.55	0.64	200/1
30	BSD 9- 453	139.41	+1.38	B9		3.88	0.05	0.47	/1
31	BSD 9-1155	139.42	+2.84	A2III		3.99	−0.09	0.49	400/2
32	HD 19968	139.46	+2.97	B5III	−7.0 C	4.16	−4.37	0.94	47 /
35	BSD 9-1174	139.49	+2.92	B9		3.83	0.12	0.47	/1
36	BD+60 655	139.51	+3.20	B8IV	−29.0	4.01	−1.39	0.63	250/1
37	BD+59 603	139.52	+2.02	A0III		3.99	−0.83	0.57	500/2
39	BSD 9-1161	139.58	+2.57	B2		4.48	−5.95	1.10	8 /
40	BD+60 648	139.59	+2.69	B5V		4.21	−2.48	0.74	100/
41	BSD 9- 535	139.61	+2.14	A0V		3.89	0.32	0.45	/1
46	HD 19441	139.73	+1.26	B3III		4.30	−5.68	1.08	25 /
47	UBV 3031	139.73	+1.41	B9		3.89	−0.22	0.50	/1
49	HD 21806	139.76	+6.48	B1Vn..	−22.0 D	4.42	−6.69	1.18	8 /
51	BD+59 613	139.90	+2.19	A1III		3.99	−0.61	0.54	500/2
55	HD 237090	140.05	+1.91	B0.5IV:nnvar		4.42	−7.16	1.23	12 /
56	HD 237091	140.06	+1.92	B1:V:nnpe	+7.6 E	4.54	−7.47	1.26	4 /
60	HD 19820	140.12	+1.54	O9IV	−4.2 A	4.49	−8.50	1.37	7 /
62	HD 20134	140.16	+2.16	B2.5IV-V	−12.5 C	4.29	−5.59	1.07	25 /
65	BD+59 624	140.21	+2.07	B5V		4.06	−1.40	0.63	150/2
66	BSD 9- 600	140.22	+1.82	A0		3.92	0.02	0.48	/1
67	BSD 9- 614	140.24	+1.87	A0		3.94	0.16	0.46	500/3
68	BSD 9- 638	140.25	+2.04	A0III		3.99	−0.60	0.54	500/2
70	BSD 9- 660	140.29	+2.22	A1III		3.99	−0.66	0.55	500/2
71	BD+58 574	140.32	+0.94	B1	−9.0 E	4.48	−5.85	1.09	8 /
75	HD 20295	140.58	+1.91	B5III	−32.0 D	4.19	−4.20	0.92	47 /
76	HD 20508	140.60	+2.39	B1.5IVvar	−28.0 C	4.31	−5.23	1.03	28 /
78	BSD 9- 156	140.75	+1.50	B6		4.32	−3.15	0.81	22 /
79	HD 20898	140.80	+3.06	B2IIIvar	−2.0 D	4.37	−6.27	1.14	17 /
80	LS I +58 119	140.86	+1.48	B5		4.37	−3.98	0.90	15 /

Table 7.2 cont.: Cam OB1 - Stellar Group I

No.[a]	Name[b]	l^c [deg.]	b^c [deg.]	MK Des.[d]	v^e_{LSR} [km s^{-1}]	log T^f_{eff} [K]	M^g_{bol} [mag]	log M^h [$M/M_\odot$]	t_m/t^i_{pm} [10^6 yr]
83	HD 237134	140.91	+2.86	B5Ve		4.20	-3.58	0.86	60 /
84	BSD 9- 786	140.97	+2.69	B8		4.21	1.41	0.63	3 /3
85	BSD 9- 796	141.04	+2.71	B6		4.25	-2.28	0.72	50 /1
86	HD 20547	141.09	+1.68	B3III	-15.0 D	4.30	-5.33	1.04	25 /
87	HD 237121	141.21	+1.39	B0.5Vs	-12.0 C	4.50	-6.50	1.16	8 /
88	BSD 9- 800	141.23	+2.46	B8		4.07	-0.86	0.57	100/2
89	BSD 9- 778	141.31	+2.05	B6		4.24	-2.31	0.72	30 /1
90	HD 20959	141.44	+2.23	B3III	18.0 C	4.26	-5.90	1.10	17 /
91	HD 21291	141.50	+2.23	B9Ia	6.8 B	4.01	7.48	1.27	9 /
92	BD+61 623	141.50	+5.22	B2e		4.48	-6.20	1.13	5 /
93	HD 20041	141.57	-0.41	A0Ia	-11.9 B	3.99	-6.71	1.18	15 /
94	BD+58 611	142.12	+2.52	B8II		4.06	-3.50	0.85	80 /
95	HD 21389	142.19	+2.06	A0Iab:	-6.0 A	3.99	-7.52	1.27	11 /

a) Catalog entry for star as listed in Table 4.4

b) Catalog designation of star as given by, in order of preference, its HD, BD, LS I BSD or UBV entry.

c) Galactic coordinates of star.

d) MK classification of star.

e) Radial velocity for star, v_{LSR} (assuming standard solar motion).

f) Logarithm of the effective temperature of star.

g) Bolometric luminosity for star.

h) Logarithm of the mass of the star in solar units as determined from $log(M/M_\odot) = 0.48 - 0.105\ M_{bol}$ for stars with $-8 < M_{bol} < 10.5$ (McCluskey & Kondo 1972).

i) Lifetime of star if it is a main sequence star, t_m (Garmany & Stencel 1992), or a pre-main sequence star, t_{pm} (Palla & Stahler 1993).

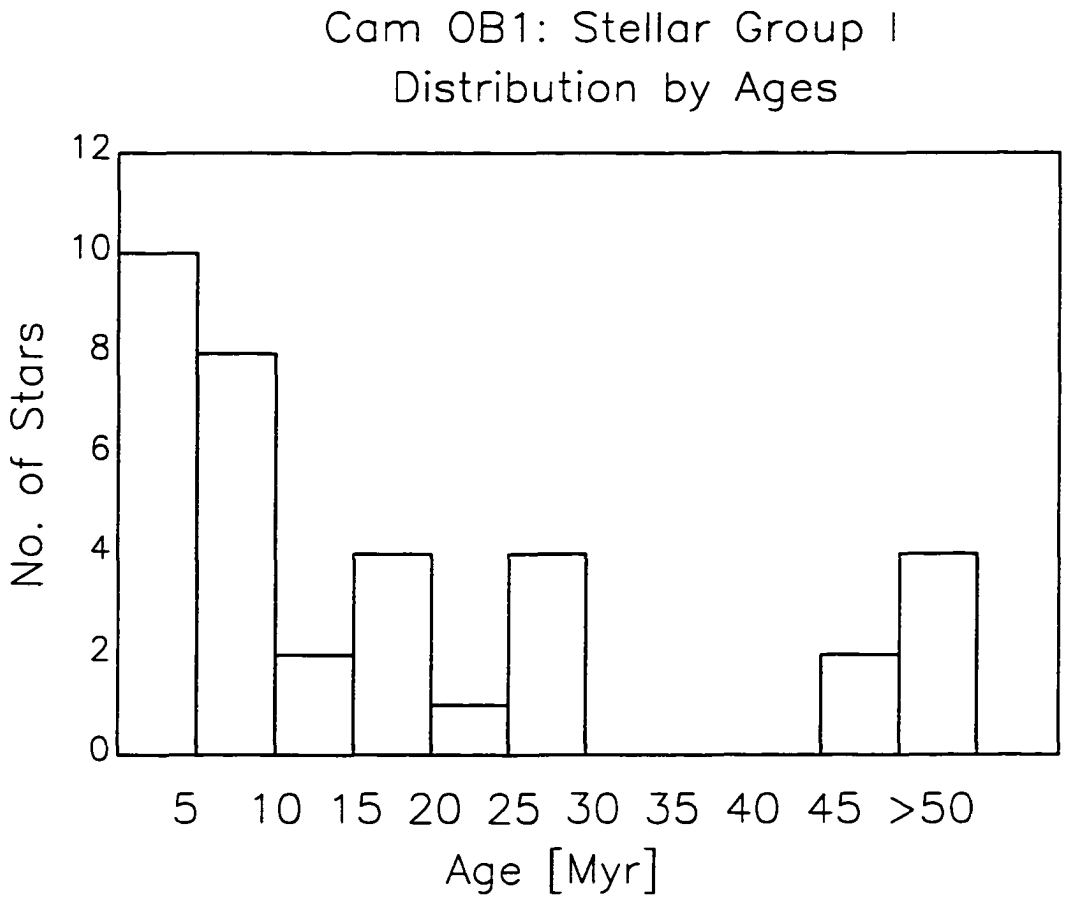

Figure 7.5 Age distribution of stars in Group I which can be assigned an age unambiguously.

B. Structure

1. Location From Figure 7.3 it is clear that, on average, the *Group I stars lie, both spatially and kinematically, between CO Complexes A and B.* This applies to all age groups of Group I stars. The centroid for the Group I stars, weighted by mass, is ($140.^{\circ}3, +2.^{\circ}2, -10.8$ km s^{-1}), and appears to lie between that of Complex A ($140.^{\circ}0, +2.^{\circ}0, -12.9$ km s^{-1}) and Complex B ($139.^{\circ}8, +3.^{\circ}7, -10.3$ km s^{-1}).

2. Stellar MF and Cloud Mass Spectrum Larson (1992) summarized the relationship between newly formed stars and the parent clouds from which they came by describing the clouds as large gravitational potential wells whose depth (mass) ultimately dictated the masses of the stars which formed from them. The local sites of star formation in the clouds, dense molecular cores, could have their initial masses moderated by turbulence (Larson 1982), magnetic fields (Shu et al. 1987) or rotation (Scalo 1990), but still the mass of the proto-stellar core and the mass of the

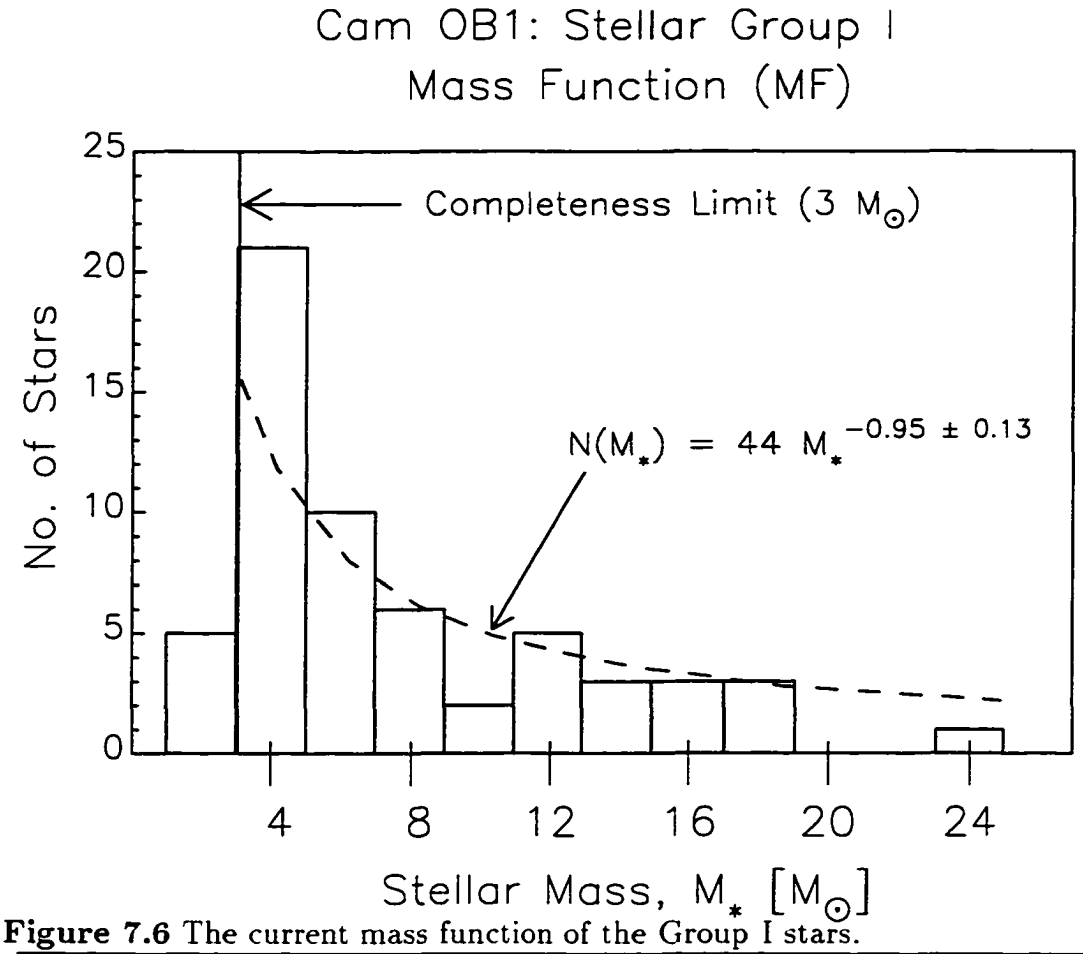

Figure 7.6 The current mass function of the Group I stars.

parent cloud are intimately related (Larson 1982, 1992).

Figure 7.6 is a plot of the current mass function (MF) of Group I stars. If there has been no significant mass loss from the stars, and the stars form a representative sample down to the observational limits, $M_V \sim 12\overset{m}{.}5$ (Schwassmann & van Rhijn, 1947), (i.e., stars which have dispersed from the association have been removed in a proportionate manner, weighted by their frequency, and that no significant number of massive stars have been removed via supernovae), then the MF and the IMF are identical. From the data in Table 7.2 and Figure 7.6 a completeness limit for the minimum mass is estimated to be ~ 3 $M_\odot$, or a B9 - A0 V star. To calculate the slope of the distribution of stars as a function of stellar mass, the method of Crawford et al. (1970) has been employed, which is independent of the choice of bin sizes. A fit to the equation of the form

$$N(M_*) \propto M_*^{-\alpha}, \tag{7.1}$$

for all of the Group I stars with $M_* \geq 3$ $M_\odot$ yields a value of $\alpha = -0.95 \pm 0.13$. The

choice of a power-law fit to the MF can be justified as it allows a direct comparison to the theoretical modelling for fragmentation of a molecular cloud in a single stage ($\alpha = -3$, Belresene 1970) or multiple stages (α is variable, Larson 1972), or allowing for the fragments to interact via collisions once they have formed (α is variable, Silk and Takahashi 1979). The complete solution to Eq. 7.1, given by an average fit over all of the bins, above the completeness limit, as presented in Figure 7.6, gives

$$N(M_*) = 44\ M_*^{-0.95\pm0.13}. \tag{7.2}$$

Hence, the rate of change of the number of stars per mass interval, the MF, follows as

$$\frac{dN(M_*)}{dM_*} = -(42 \pm 6)\ M_*^{-1.95\pm0.13}. \tag{7.3}$$

In fitting Eq. 7.1 to the data it has been assumed that the masses of the stars are exact, while in fact there is a possible error of up to $\sim$ 10% on any given stellar mass value, at least for the main sequence stars (Böhm-Vitense 1989). This uncertainty is less than the uncertainty in the exponent and smaller than the selected stellar mass bin sizes for the data shown in Figure 7.6, and hence, argues that the uncertainty in the exponent does reflect the quality of fit to the data.

Figure 7.7 is a plot of the CO cloud mass distribution for the clouds in Complexes A and B (see Table 7.1), the complexes involved in the formation of the Group I stars. A completeness limit for all the clouds in Cam OB1 has been estimated from a plot of the data in Table 7.1 (not shown) to be $\sim 1 \times 10^3$ $M_\odot$. The solution for the cloud mass function for the clouds of Complexes A and B was found to be:

$$\frac{dN(M_{cloud})}{dM_{cloud}} = -(9.4 \pm 2.5) \times 10^2 M_{cloud}^{-1.78\pm0.21}. \tag{7.4}$$

It can be seen from a comparison of Figures 7.6 and 7.7 that *the mass distribution for the stars in Group I is similar to that for the clouds in Complexes A and B.*

C.Stochastic

1. Star Forming Efficiency (SFE)

The SFE is defined as:

$$SFE = \left(\frac{M_*}{M_* + M_{CO}}\right). \tag{7.5}$$

Assuming that the Group I stars (total stellar mass 442 $M_\odot$) formed from Complexes A and B (total molecular mass 3.97×10^4 $M_\odot$), then *the SFE for the process which*

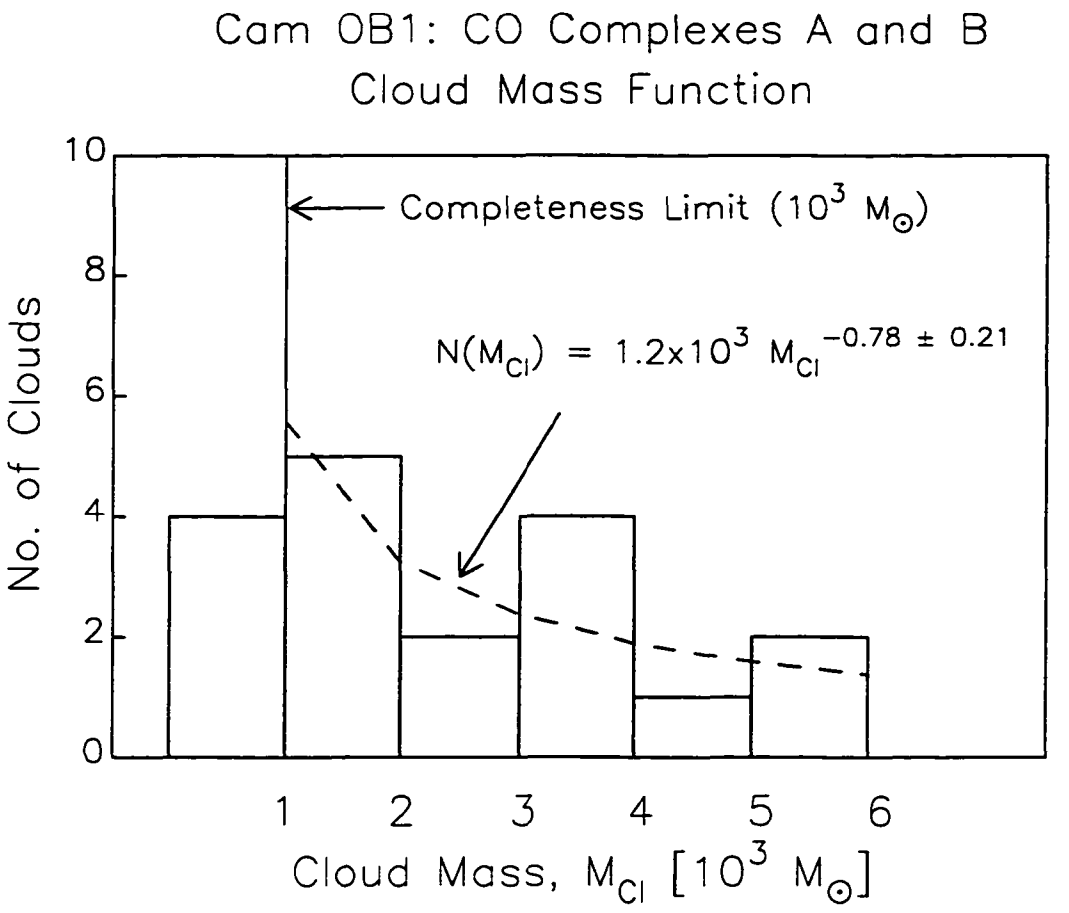

Figure 7.7 CO cloud mass function for the clouds making up Complexes A and B.

produced Group I, is $\sim 1\%$. This is a very low SFE, which is similar to that seen in low-mass star forming regions, e.g., Taurus (Larson 1982).

7.3.2 Group II

In Chapter 4, an initial model of the distribution of stars in the Cam R1 region placed the stars in one of two sub-regions, Cam R1 N or Cam R1 S. In §6.2, it was shown that many of the younger stars in Cam R1 N showed a strong positional coincidence with CO emission now termed Complex B. Hence, Group II stars are those stars which are relatively young, say ≤ 3 Myr, and appear to be spatially coincident with Complex B. Figures and tables for the Group II stars are organized in a similar manner to that for the Group I stars. Figure 7.8 shows the position of the Group II stars relative to the CO emission at -9.4 km s^{-1}. Figure 7.9 is an HR diagram showing the evolutionary state of the Group II stars, while the data for

all of the figures are provided in Table 7.3. The elements of star formation for this group of stars are given by:

A. Temporal

1. Age In the HR diagram for the Group II stars the two oldest and most massive stars assigned to this group, BD+61 566 and HD 20798, stand out as being the only two main sequence or evolved stars in the list. The relatively young age of the remainder of these stars supports the argument that they are probably members of Group I, and they are not included in any further analysis. The age distribution of the remainder of these stars is shown in Figure 7.10. From this figure, it would appear that *the Group II stars have been forming in Complex B for the last 3 Myr.*

B. Structure

1. Location One of the principal defining features of the Group II stars is that they are coincident with Complex B and appear to be distributed in a random fashion but there are two interesting spatial enhancements worth noting. Firstly, there is a group of stars near $l = 139.^{\circ}3, b = +4.^{\circ}2$, near the edge of the Complex B emission. If these stars are very young, it would appear that the star formation is enhanced in this region. Secondly, there is a cluster of stars (stars 53, 55, 59, 64, 65, 70, 78 and 82 in Table 7.3), centered on $l = 140.^{\circ}1, b = +2.^{\circ}8$, which is seen against the densest parts of the Complex B CO emission. In the HR diagram for Group II stars (Figure 7.9) these stars also form a relatively tight group of pre-main sequence stars. It is interesting to see the formation of such a cluster of stars, which has an age (1.6 ± 0.8 Myr) similar to that seen for the rest of the Group II stars (1.5 ± 0.8 Myr), but appears very compact spatially. More data on the velocity dispersion of these stars are required to determine whether this cluster is bound or not.

The stars with measured radial velocities in Group II suggest that Group II has a velocity of $\sim -4 \pm 18$ km s^{-1}, but there are too few stars (only 3 in total) to determine whether the difference in mean velocity between the Group I stars (-10.8 km s^{-1}) and the Group II stars is significant. However, the trend in the mean velocity to a more positive value is consistent with the stars originating in Complex B. Hence, with the exception of BD+61 566 and HD 20798, *Group II stars are all relatively young (less than 3 Myr) and are probably spatially and kinematically coincident with Complex B.*

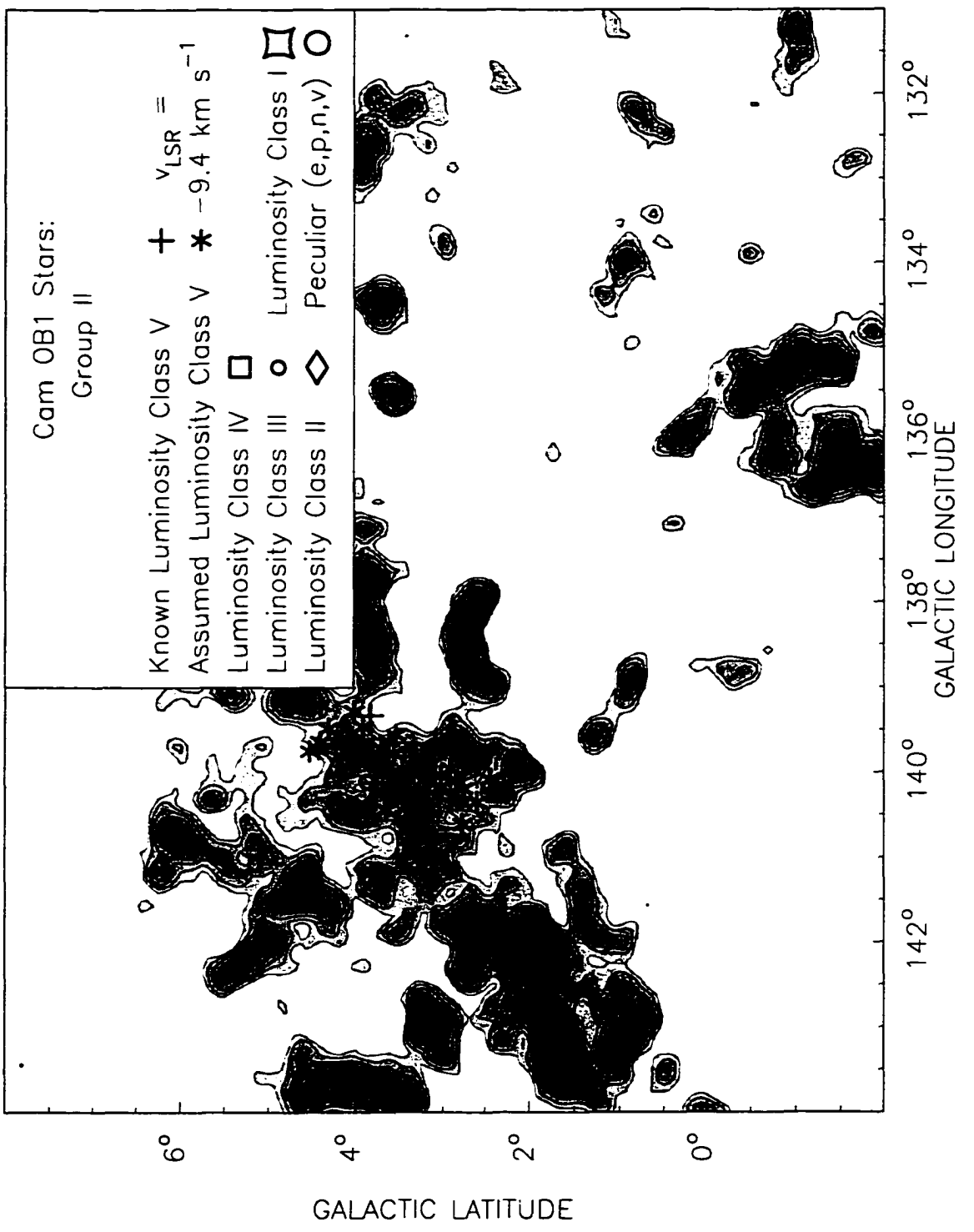

Figure 7.8 Overlay of Group II stars over CO emission at -9.4 km s^{-1}.

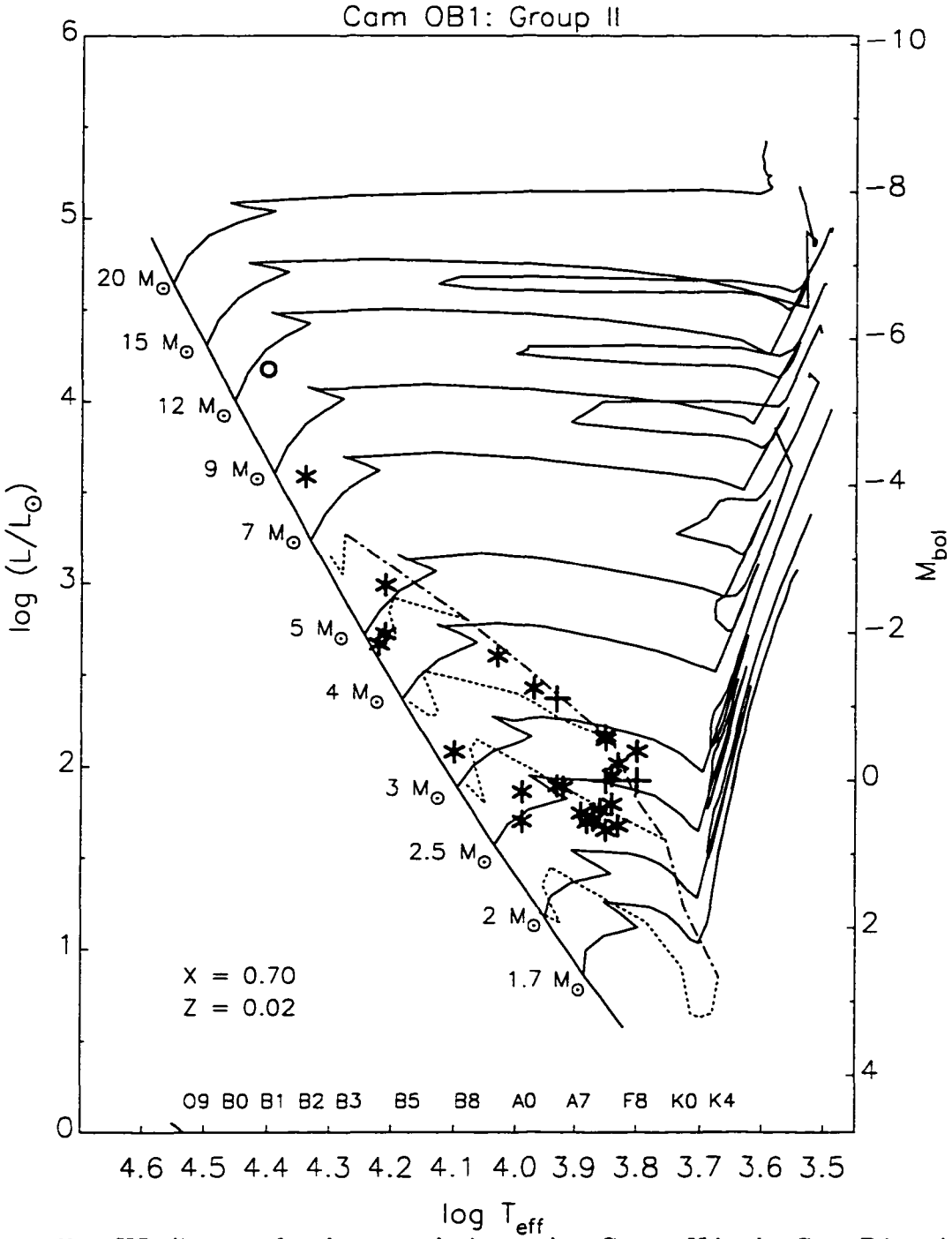

Figure 7.9 HR diagram for the stars designated as Group II in the Cam R1 region. The pre-main sequence tracks are taken from Palla & Stahler (1993) – dotted lines – as is the 'birthline' – dash-dot line – below which stars first become optically visible. An accretion rate, $dM/dt = 1 \times 10^{-5}$ $M_\odot$ yr^{-1} has been assumed in determining the position of the birthline on the HR diagram. A lower accretion rate will move the birthline to the right in the diagram (Stahler & Walter 1993). The post-main sequence evolutionary tracks – solid lines – are taken from Garmany & Stencel (1992) for the metallicity indicated.

Table 7.3: Cam OB1 - Stellar Group II

No.[a]	Name[b]	l^c [deg.]	b^c [deg.]	MK Des.[d]	v^e_{LSR} [km s^{-1}]	log T^f_{eff} [K]	M^g_{bol} [mag]	log M^h [$M/M_\odot$]	t_m/t^i_{pm} [10^6 yr]
24	BD+61 557	139.20	+4.40	B8		4.03	−1.69	0.65	200/1
26	BSD 9-1814	139.28	+4.02	B9		3.85	−0.56	0.54	/1
28	BD+61 549	139.33	+3.84	B5V	−26.0	3.93	−1.11	0.50	/1
33	BD+61 554	139.46	+3.92	B8		3.97	−1.25	0.61	/1
34	BSD 9-1856	139.48	+4.31	B5		4.21	−1.99	0.69	50 /3
38	BD+61 552	139.56	+3.55	B6		4.21	−2.65	0.76	30 /2
42	BSD 9-1829	139.63	+3.63	B9		3.89	0.44	0.43	/1
43	BD+61 566	139.64	+4.40	B5		4.34	−4.13	0.92	16 /
44	BSD 9-1842	139.72	+3.71	A0		3.84	0.32	0.45	/1
45	BSD 9-1891	139.72	+4.42	A0		3.81	0.65	0.41	/1
48	BSD 9-1904	139.75	+4.52	B9		3.84	−0.07	0.49	/1
50	BSD 9-1840	139.78	+3.57	B9		3.80	−0.40	0.52	/1
52	BSD 9-1262	139.96	+2.91	A0		3.83	0.61	0.42	/1
53	BSD 9-1315	139.97	+3.47	B9V	−6.0	3.80	−0.80	0.56	/1
54	BSD 9-1289	140.04	+3.02	B7		4.22	−1.85	0.67	50 /3
57	BSD 9- 645	140.08	+2.44	A0		3.88	0.56	0.42	700/2
58	BSD 9-1279	140.09	+2.84	A0		3.86	0.39	0.44	/1
59	HD 20798	140.11	+3.87	B2III-IV	−2.0 C	4.40	−5.60	1.07	25 /
61	HD 20761	140.12	+3.78	B9V	+19.0	3.85	−0.90	0.58	/1
63	BSD 9-1309	140.17	+3.02	A0		3.93	0.07	0.47	500/2
64	BSD 9-1286	140.19	+2.76	B9		3.85	−0.61	0.54	/1
69	BSD 9-1320	140.28	+3.06	A0		4.10	−0.39	0.52	200/3
72	BSD 9- 692	140.35	+2.60	B9		3.92	0.09	0.47	700/2
73	BSD 9-1377	140.44	+3.66	B9		3.83	−0.23	0.50	/1
74	BSD 9-1366	140.49	+3.39	A0		3.85	0.67	0.41	/1
77	BSD 9-1336	140.61	+2.77	A0		3.99	0.15	0.46	500/3
81	BSD 9- 780	140.86	+2.87	A0		3.99	0.55	0.42	500/3
82	BSD 9-1390	140.86	+3.15	A0		3.87	0.53	0.42	/1

a) Catalog entry for star as listed in Table 4.4

b) Catalog designation of star as given by, in order of preference, its HD, BD, LS I, BSD or UBV entry.

c) Galactic coordinates of star.

d) MK classification of star.

e) Radial velocity for star, v_{LSR} (assuming standard solar motion).

f) Logarithm of the effective temperature of star.

g) Bolometric luminosity for star.

h) Logarithm of the mass of the star in solar units as determined from $log(M/M_\odot) = 0.48 - 0.105\ M_{bol}$ for stars with $-8 < M_{bol} < 10.5$ (McCluskey & Kondo 1972).

i) Lifetime of star if it is a main sequence star, t_m (Garmany & Stencel 1992), or a pre-main sequence star, t_{pm} (Palla & Stahler 1993).

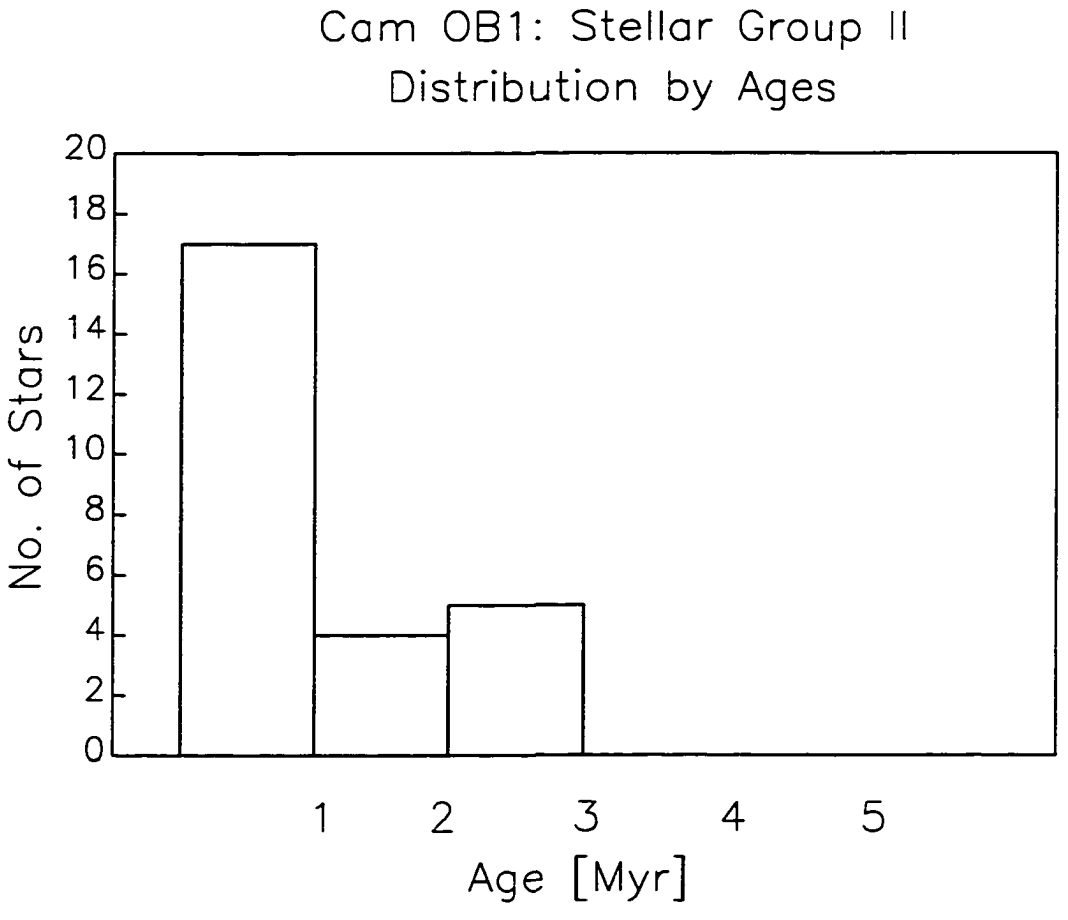

Figure 7.10 Age distribution of stars in Group I excluding BD+61 566 and HD 20798. In all cases the ages have been assumed to be those given by the pre-main sequence track (Palla & Stahler 1990). Note the difference in the scale from Figure 7.5.

2. Stellar MF and Cloud Mass Spectrum In an analogous manner to the Group I stars, Figure 7.11 shows the current mass function for the Group II stars. It is clear from this figure that there is not a large range in masses with which to fit a relationship for the number of stars at a given stellar mass. Nevertheless, assuming a completeness limit of 3 $M_\odot$ as was the case for the Group I stars (see Figure 7.6), it follows that an MF fit to the data shown in Figure 7.11 is given by

$$\frac{dN(M_*)}{dM_*} = -(15 \pm 4)\ M_*^{-2.13\pm0.30}. \tag{7.6}$$

This is in relatively good agreement with the MF found for the Group I stars. The larger uncertainty in the fit, compared to the Group I stars, reflects the limited mass

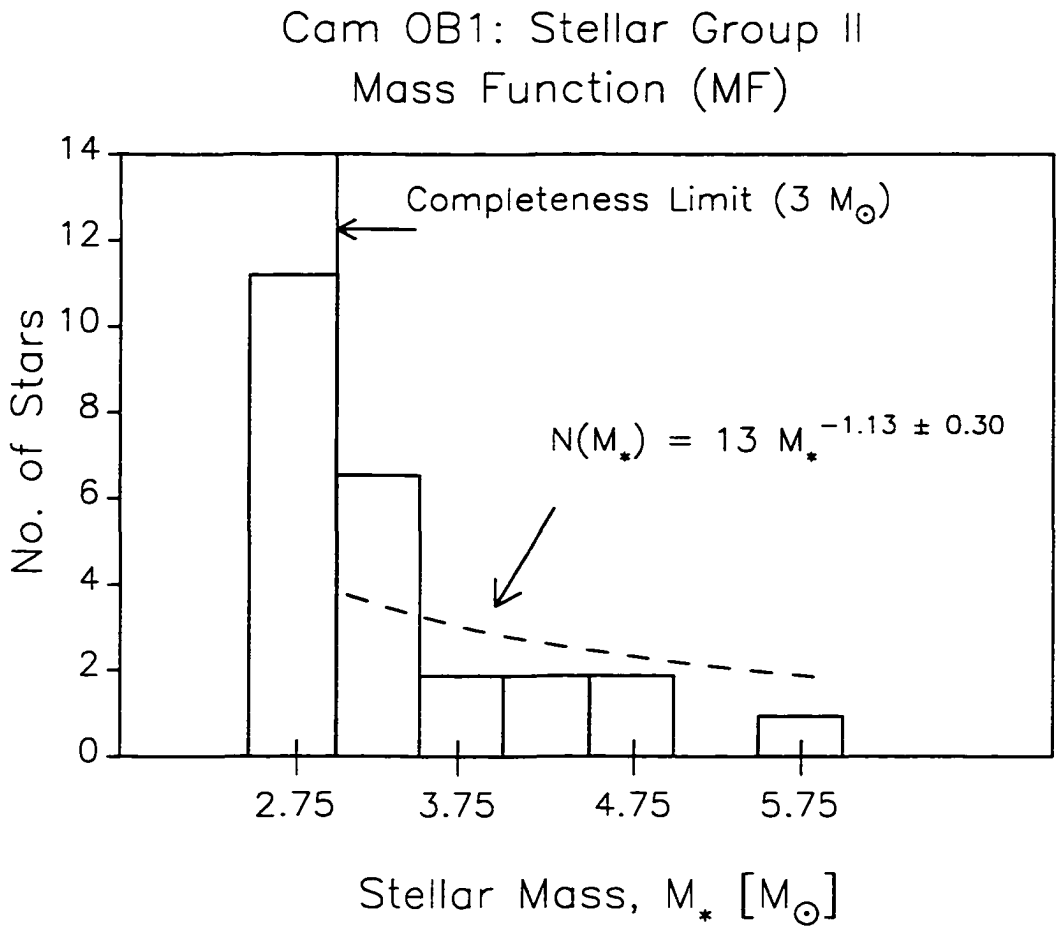

Figure 7.11 The current mass function of the Group II stars.

range and sample size.

The parent clouds of the Group II stars appear to have come only from Complex B. The distribution of masses for the clouds of Complex B is given in Figure 7.12. While it is possible to fit a power-law to this distribution, the limited range of masses and small number of clouds suggest caution be taken when interpreting it. The power-law fit to the Complex B clouds, as shown in Figure 7.12, is given by

$$\frac{dN(M_{cloud})}{dM_{cloud}} = -(3.6 \pm 1.5) \times 10^3 M_{cloud}^{-1.98 \pm 0.35}. \qquad (7.7)$$

Despite the large uncertainties in the fit to both the stellar masses for the Group II stars and CO masses for the associated CO clouds, it would still appear that *the mass distribution for the stars in Group II is similar to the mass distribution of molecular clouds in Complex B.* It should be noted that both of these distributions are consistent with the similar distributions calculated for the Group I objects.

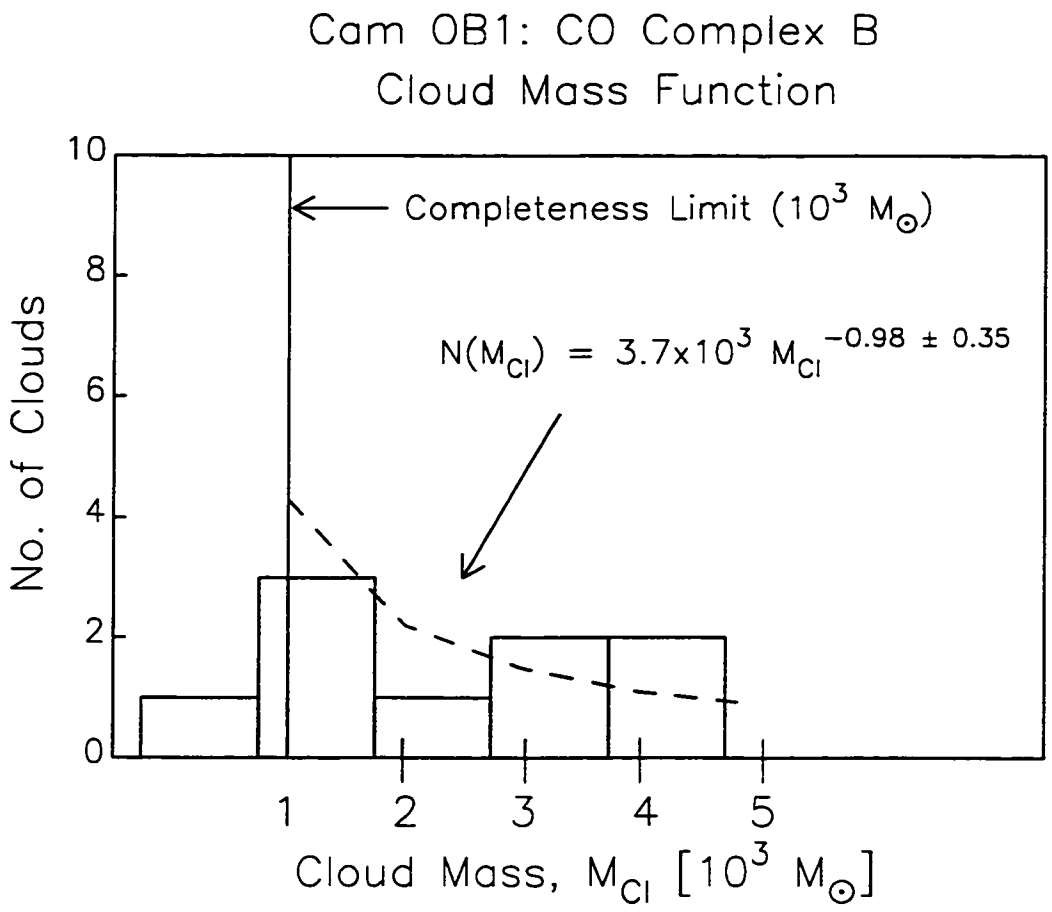

Figure 7.12 CO cloud mass function for the clouds making up Complex B.

C. Stochastic

1. Star Forming Efficiency (SFE) The total mass of stars in Group II, excluding BD+61 566 and HD 20798, is $\sim$ 86 $M_\odot$, and the sum of the masses of the CO clouds in the B Complex is 20.3×10^3 $M_\odot$. Hence, *the SFE for the Group II stars, if they formed from Complex B, is* $\sim$ 0.4%. This is lower than the Group I stars but not inconsistent with other regions in the Galaxy (Larson 1982).

7.3.3 Group III

The Group III objects, if they are stars, represent the youngest stars in the Cam R1 region. They are very different in nature to the Group I and II stars as they are emitting primarily at infrared wavelengths. The data for these objects have been taken from the *Infrared Astronomical Satellite*, *IRAS* (Beichman et al. 1988); details are provided in Chapter 5. The Group III objects listed in Table 7.4 have been taken from Table 5.2, excluding those objects listed in Table 5.2 which are known to have been produced by a Group I or II star, e.g., IRAS 03116+5951, a blue reflection nebula (BRN) associated with HD 237091.

It is not possible to construct an HR diagram for these objects, assuming they are embedded stars, without additional information on the temperature of the central source (McCutcheon et al. 1991). The masses of these objects have been derived from *IRAS* emission and hold true only if the source is an embedded star which is close to the main sequence (Casoli et al. 1986). The only two cases where this is known to hold true are for the outflows AFGL490 (Campbell et al. 1986), and AFGL490-iki, given its similar evolutionary state to AFGL490 (Chapter 5). Given this limitation the discussion regarding the Group III stars is more restricted.

Figure 7.13 shows the position of the Group III objects relative to the CO emission at -9.4 km s^{-1}. All of the relevant data for these stars are provided in Table 7.4. The elements of star formation for this group of stars are given by:

A. Temporal

1. Age If the Group III objects are proto-stellar objects then they are much younger than either the Group I or II stars. For proto-stellar objects the relevant time scales over which they can be observed are either the free-fall time, t_{ff}, for the very youngest objects, (i.e., molecular cloud cores), or the Kelvin-Helmholtz time, t_K, for the last stages of molecular core collapse when a proto-stellar core forms but nuclear burning has not yet commenced, e.g., during the outflow phase (Bally & Lada 1983). For molecular cores which produce OB stars such as the stars in Group III, $t_{ff} \sim 2 - 20 \times 10^4$ yr (Myers 1985). t_K for the more evolved cores may be found from $t_K \sim (M^2 G/RL)$ (Bowers & Deeming 1984), where M is the proto-stellar core mass, G is Newton's gravitational constant, R is the proto-stellar core radius and L the luminosity available from gravitational contraction. As an example, if AFGL490 has $M = 12$ $M_\odot$, $R = 5$ $R_\odot$ (a typical proto-stellar core radius, Shu et al. 1987) and

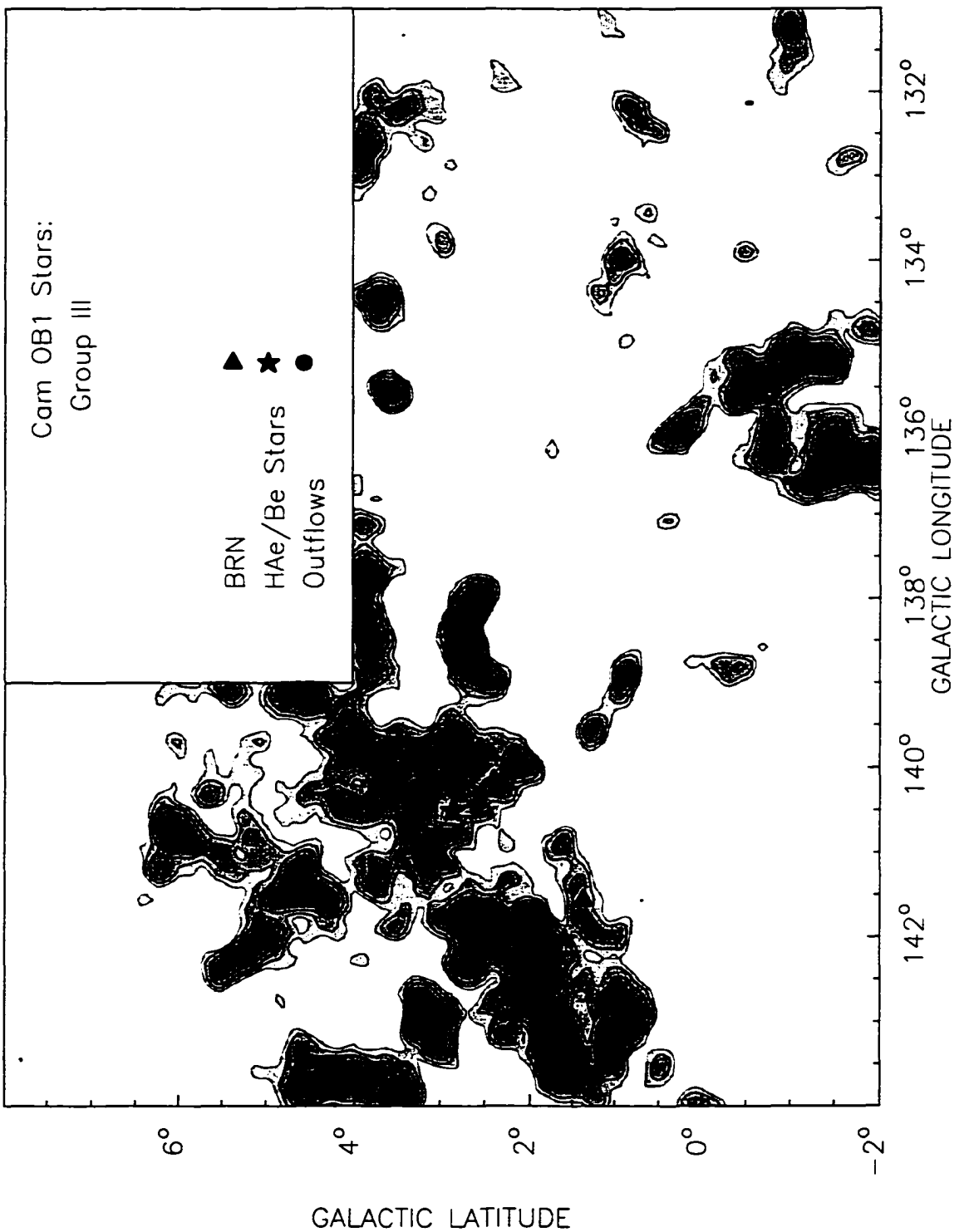

Figure 7.13 Overlay of Group III objects over CO emission at -9.4 km s^{-1}.

Table 7.4: Cam OB1 - Stellar Group III

No.	Name	l	b	12μm[a]	25μm[a]	60μm[a]	100μm[a]	[25 12][b]	[60 25][b]	[100 60][b]	OZ[c]	$L^{d}_{IR,L}$	$L^{d}_{IR,U}$	$L^{d}_{IR,Acc}$	M^{e}_{IR}	Identity:Associated Star
	[deg]	[deg]	[Jy]	[Jy]	[Jy]	[Jy]						[$L_{\odot}$]	[$L_{\odot}$]	[$M_{\odot}$]		
1	IRAS 03119+6025	139.77	+2.55	0.25L	0.22:	2.66	12.03	−0.06	1.08	0.66	f	8	45	45	2.9	BRN
2	IRAS 03119+6017	139.84	+2.44	0.46	0.67	10.36	24.65	0.16	1.19	0.38	f	39	107	107	3.7	BRN
3	IRAS 03139+6005	140.15	+2.40	0.30	0.40	5.26L	24.83	0.12	1.12	0.67	f	21	90	90	3.5	BRN
4	IRAS 03182+6017	140.51	+2.86	0.28L	0.18:	1.03:	10.24	−0.19	0.76	1.00	f,HAe/Be	8	36	36	2.7	HAe/Be
5	IRAS 03189+5828	141.56	+1.37	0.25L	0.26	3.08	10.09	0.02	1.07	0.52	f	13	66	66	3.2	BRN
6	IRAS 03234+5843	141.91	+1.91	0.50	1.81	5.66	784.90L	0.56	0.50	2.14	g,l,q,r,HII,HAe/Be	36	2200	1100	7.0	outflow:AFGL490-iki
7	IRAS 03236+5836	142.00	+1.82	82.39	278.40	716.70	784.90	0.53	0.41	0.04	g,l,q,r,HII,HAe/Be	5100	7300	7300	12	outflow:AFGL490
8	IRAS 03227+5824	142.02	+1.59	0.26L	0.30	2.31:	17.15	0.06	0.89	0.87	f,HAe/Be	12	59	59	3.1	HAe/Be
9	IRAS 03267+5855	142.16	+2.30	0.52	0.38	3.92:	42.57L	−0.14	1.01	1.04	?	20	137	79	3.4	BRN
10	IRAS 03243+5821	142.22	+1.65	0.69	1.42	2.74	38.82L	0.31	0.29	1.15	r,q,HAe/Be	27	134	81	3.4	HAe/Be
11	IRAS 03261+5829	142.34	+1.90	1.07	1.14	10.76	56.17	0.03	0.97	0.72	f	51	206	206	4.4	BRN

a) *IRAS* (Beichman *et al.* 1988) fluxes at 12, 25, 60 and 100 μm. A : following a flux value indicates a good quality flux measurement while a L represents an upper limit.
b) Colors from IRAS fluxes: [25 - 12] = $\log(F_{25}/F_{12})$, [60 - 25] = $\log(F_{60}/F_{25})$ and [100 - 60] = $\log(F_{100}/F_{60})$.
c) Occupation Zones as judged by Walker *et al.* (1989). See Table 5.1 for details. In summary the OZs are: a - bright stars, b - O-rich stars, c - optical stars, d - LRS C-rich stars, e - HII regions, f - blue refelction nebulae (BRN), g - red reflection nebulae, h - blue planetary nebulae, i - red planetary nebulae, j - blue galaxies, k - red galaxies, l - seyferts, m - quasars, o - T Tauri stars, o - LRS=3 stars, p - LRS=6 stars, q (author's designation) - Herbig Haro emission line stars, r (author's designation) - bipolar nebulae. Additional occupation zones are given for HII regions (Hughes & MacLeod 1989), UCHII regions (Wood & Churchwell 1989) and HAe/Be stars (Berrilli *et al.* 1992).
d) Luminosity of sources from IRAS emission. $L_{IR,L}$ has been calculated from the 12, 25 and 60 μm bands (Carpenter *et al.* 1995), $L_{IR,U}$ has been calculated in a similar manner from all four bands, $L_{IR,Acc}$ represents the accepted value of infrared luminosity in this paper. In the case of good 100 μm fluxes $L_{IR,U}$ and $L_{IR,Acc}$ are equivalent, while $L_{IR,Acc}$ is the mean of $L_{IR,U}$ and $L_{IR,L}$ when the 100 μm flux is an upper bound.
e) Mass of stars assuming the accepted infrared luminosity, $L_{IR,Acc}$, is equivalent to the bolometric luminosity and $L_{\odot} = M_{\odot}^{3.6}$ (Casoli *et al.* 1986).

L equivalent to its infrared luminosity (= 7300 $L_\odot$), then $t_K \sim 1.2 \times 10^5$ yr.

B. Structure

1. Location There are two clusters of infrared sources making up the Group III objects. The first, centered at $l = 139.^\circ84$, $b = +2.^\circ54$, is coincident with the southern end of molecular Complex B. This cluster of objects is composed mostly of low luminosity sources. The second cluster is centered at $l = 141.^\circ92$, $b = +1.^\circ82$, and is associated with the two known outflows in the region, AFGL490 and AFGL490-iki. The central velocity for both these objects is ~ -15 km s^{-1} (Mitchell et al. 1992; see also §5.5). This velocity is consistent with these objects being located in molecular Complex H but spatially they lie slightly above Complex H. However, the central velocity profiles are broad and it cannot be ruled out, on this basis, that the objects are actually associated with molecular Complexes F, G or a blend of these clouds. High resolution CO observations of this region may be able to delineate where the boundaries of these complexes are, and if they are related to the outflows in any interesting fashion, e.g., if the outflows are at the junction of two complexes.

2. Stellar MF and Cloud Mass Spectrum As stated earlier, it is not possible to derive the masses for the Group III objects with any reliability except, possibly, for AFGL490 and AFGL490-iki. Furthermore, the sample size for studying the mass distribution of these objects is small. Hence, no meaningful MF may be derived for the Group III objects from the present data. High-resolution observations of these objects at infrared and near infrared wavelengths may be able to help with this problem.

The study of the mass distribution for the molecular clouds associated with the Group III objects is also not possible with the current data. It is possible to identify the clouds associated with the Group III objects (Clouds no. 36, 42, 44, 45, 58, 62 and 65 in Table 7.1) but the clouds are heavily blended and the sample size is very small. There is evidence for an enhancement of low-mass clouds relative to the large-mass clouds in the region but the data are too sparse to conduct any meaningful analysis.

C. Stochastic

1. Star Forming Efficiency (SFE) If it is assumed that the masses for the Group III objects listed in Table 7.4 are close to the true proto-stellar masses then the

Table 7.5: Summary for Cam OB1: Cam R1 Stellar Groups

Group	Age [10^6 yr]	Sp. Type	(l, b, v) [°,°,km s^{-1}]	$\frac{dN}{dM_*}$ [$M_\odot^{-1}$]	$\frac{dN}{dM_{Cloud}}$ [$M_\odot^{-1}$]	SFE %
Group I	1 – 50	O9 – A0	(140.26,+2.19, 10.8)	$-(42 \pm 6)\ M^{-1.95 \pm 0.13}$	$-(9.4 \pm 2.5) \times 10^2\ M^{-1.78 \pm 0.21}$	1
Group II	1 – 3	B5 – A0	(140.07,+3.35, 4.0)	$-(15 \pm 4)\ M^{-2.13 \pm 0.30}$	$-(3.6 \pm 1.5) \times 10^3\ M^{-1.98 \pm 0.35}$	0.4
Group III	0.1 – 0.2	?	(139.84,+2.54,?)	?	?	≤ 0.2
			(141.92,+1.82, 12.0)			≤ 0.2

total stellar mass in Group III is ~ 50 $M_\odot$. The total molecular mass in the clouds associated with Group III is $\sim 3.0 \times 10^4$ $M_\odot$. Hence, the SFE for Group III is $\sim 0.2\%$. This SFE is low and may be an upper bound for the SFE given that some of the candidate sources in Table 7.4 may not be stellar objects. On the other hand, if star formation is ongoing in this region then the SFE should increase.

Table 7.5 summarizes the findings for the star formation in the Cam R1 region.

7.4 Discussion

It was suggested in the introduction that star formation could be considered in terms of three elements: the relationship between the structure of the parent molecular clouds and mass distribution of the newly formed stars, the evolution of the molecular clouds, and the probability of star formation occurring. With respect to the first element, Larson (1982, 1992) suggested that more massive stars should be produced by more massive clouds because the more massive clouds serve as deep potential wells which are successful in accreting material onto the proto-stellar cores. Two known examples of very young stars which are forming in the region, i.e., AFGL490 and AFGL490-iki, are massive stars which have formed from massive clouds, which is consistent with the proposed relationship. In addition, the results of the analyses of Groups I and II in the previous sections are also consistent with this scenario, but clearly the present data cannot provide evidence to confirm the causal relationship. The second element suggests that if a molecular cloud is left for sufficient time it will form some stars. If this holds, then the absence of any star formation in a GMC is the signature that the cloud is very young and may not have had enough time to form any stars, e.g., the GMC found by Maddalena et al. (1986). The last element, the probability of star formation occurring, is the most subtle of the three elements. In some cases, GMCs have formed molecular cores but have not produced any stars which may be indicative of their relatively young ages (Blitz 1993), or the absence of an efficient mechanism for removing angular momentum from the cores (Bodenheimer et al. 1993), or possibly the presence of magnetic fields also regulating the final collapse of the cores (Shu et al. 1987). If a molecular core does produce stars the SFE of the molecular core is quite high (Evans 1991). The element of the probability of star formation occurring really addresses the circumstances under which star formation is promoted at the molecular core level.

In comparison to other regions in the Galaxy, the cloud mass function for the Cam OB1 clouds, i.e., $dN/dM_{Cloud} \propto M_{Cloud}^{-(1.75\pm0.30)}$, is in good agreement with other surveys: e.g., Solomon et al. (1987) found a cloud mass function with exponent ~ 1.5 for 273 CO clouds in the first Galactic quadrant. Similarly, the MF determined for the Cam OB1 stars, excluding the Group III objects, i.e. $dN/dM_* \propto M_*^{-2.00\pm0.30}$, is also in agreement with studies of the IMF. Salpeter (1955) determined the IMF for stars between 1 - 10 $M_\odot$ in the solar neighborhood to be $dN/dM_* \propto M^{-2.33}$. More recent work by Miller & Scalo (1979) on field stars and cluster stars over a larger range of masses led to an IMF, $dN/dM_* \propto M^{-(1+log M)}$. If the stellar survey of the Cam OB1 region (Schwassmann & van Rhijn 1947) is incomplete then the MF derived for the Cam OB1 stars may be too flat due to missed low-mass stars in the survey. More sensitive imaging of the region is required in order to confirm the completeness limit of the original stellar survey, but it would seem to be an unusual coincidence for the mass distribution of clouds and stars in Cam OB1 to be similar if there was a serious underestimate of evolutionary effects and completeness for the stars. Hence, it follows that *the mass distribution of the Cam OB1 stars and the molecular clouds from which they form are similar.*

In the proposed model for star formation in Cam OB1, it has been argued that the evolution of these clouds into stars has been influenced by the collision of various molecular complexes in the region. If a cloud-cloud collision is responsible for triggering the star formation in Cam OB1, there must have been sufficient time for the collision to occur and the stars to form. In the case of the Group I stars, if it is assumed that the star formation initially began upon contact of Complexes A and B and if they are as deep as they are wide (~ 25 pc), and the relative velocity between the two complexes is $\sim 2 \pm 1$ km s^{-1}, then the duration for the collision is ~ 10 Myr, which is roughly in agreement with the ages of the Group I stars. Only a small increase in the depth of the interacting clouds or decrease in relative velocity is required in order to account for the full spread in ages, $\sim 1 - 30 \times 10^6$ yr, seen in the Group I stars.

In the case of the Group II stars, the star formation appears to be restricted to Complex B and there does not appear to be a second complex along the line-of-sight which could have triggered the star formation via a cloud-cloud collision. One explanation might be that the Group I stars, which are older than the Group II stars and positioned beside and behind the CO emission associated with the Group

II stars, may have induced the Group II star formation via enhanced ionization pressure or stellar winds. A model for this type of star formation has been termed 'sequential star formation' and has been seen elsewhere in the Galaxy (Blaauw 1964, Elmegreen & Lada 1977, Sargent 1977, 1979). It is interesting to note that the age difference between sub-groups in such a model is $\sim$ 4 Myr and the displacement between successive stellar groups is $\sim$ 20 pc. The ages of the Group I and II stars, and their relative displacement are consistent with this scenario of star formation. Details of how the ionization fronts from the Group I stars or their stellar winds could have induced the Group II star formation is beyond the scope of this thesis. One comment that may be made regarding this event is that it must have been sufficiently strong to be effective in triggering the star formation, while gentle enough to have preserved the structure of the molecular clouds associated with the Group II stars.

For the Group III stars (AFGL490 and AFGL490-iki), their young age ($\sim 1 - 2 \times 10^5$ yr) suggests that if a cloud-cloud collision were responsible for triggering their formation then these clouds should still be close at hand and the newly formed stars should have velocities similar to those of the interacting clouds. There is evidence for this being the case, as clouds from Complexes F, G and H as well as A and B, which are known to be in the immediate vicinity of the newly formed stars (on the basis of the gas in these complexes being warmed by nearby stars), have similar velocities. Higher resolution observations of the molecular emission in the region may help refine the model of this cloud-cloud collision. Nevertheless, it does appear that *collisions between molecular clouds in Cam OB1 may have influenced the evolution of these clouds and been the trigger for subsequent star formation.*

Finally, as mentioned earlier it is not possible to identify the molecular cores in the Cam OB1 clouds directly with the resolution of the present data, but there are several pieces of circumstantial evidence which indicate that they exist. It has been shown in §7.3 that the power-laws for the mass distribution of the parent molecular clouds and the newly formed stars are similar, while in Chapter 3 it was shown from structure tree statistics (Houlahan & Scalo 1990, 1992) for the clouds associated with the Group III stars that their density-size relationship, i.e., $\rho \propto r^{-2.2}$ where ρ is the volume density and r is the cloud radius, was self-similar and hierarchical. This analysis was conducted on clouds over the size range of $\sim 20 - 3$ pc, which is appreciably larger than the size of most cores, $\sim$ 0.3 pc. However, the density profiles of molecular cores seen elsewhere in the Galaxy have a similar density-size

relationship (Myers 1983) and, if the cores in Cam OB1 are not unusual, then the hierarchical self-similar relationship for the Cam OB1 clouds investigated here should persist down to the scale-lengths of their molecular cores. It is necessary to obtain high-resolution molecular observations of this region to test this hypothesis.

Similarly, the role that the molecular cores play in star formation in Cam OB1 also has to be inferred from the observations available. The low SFE for the molecular clouds does support the argument that the cores, which constitute only a small portion of the molecular clouds, are the regions of active star formation. Whether the star formation rate is regulated as a result of ambipolar diffusion (Shu et al. 1987) or core interactions (Bodenheimer et al. 1993) remains open to debate. However, the lack of alignment of the two known outflows in the region (see Chapter 5), which are relatively close together ($\sim$ 3 pc), suggests that ambipolar diffusion is not responsible for regulating the collapse of the parent molecular cores as this would also lead to some alignment of the outflow sources with the ambient magnetic field. Furthermore, the relatively low relative velocities between the molecular cores in the clouds which are colliding would be favorable circumstances for core-core interactions leading to their subsequent collapse (Habe & Ohta 1992, Kimura & Tosa 1996). Hence, the *observed star formation in Cam OB1 is consistent with the hypothesis that it has been regulated by the interaction of molecular cores.*

7.5 Conclusions

Observations of star formation in Cam OB1 were considered in terms of three elements: the structural relationship between molecular clouds and the stars which form from them, the evolution of the parent molecular clouds and the probability of star formation occurring. It was shown that this characterization of star formation is appropriate and useful in understanding the star forming process. Details of the results of this analysis are as follows:

1. There are a number of CO cloud complexes in the Cam R1 region which can be selected on the basis of their spatial position and mean velocities.
2. There are three distinct stellar groups: Group I is the oldest group and formed $1-30\times10^6$ yr ago from molecular Complexes A and B; Group II formed $1-3\times10^6$ yr ago from molecular Complex B; and Group III formed $1-2\times10^5$ yr ago from clouds in Complexes A, B, F, G and H.
3. The mass function of the molecular clouds from which the Cam OB1 stars

formed. i.e., $dN/dM_{Cloud} \propto M_{Cloud}^{-(1.75\pm0.30)}$, is similar to the stellar MF, i.e., $dN/dM_* \propto M_*^{-(2.00\pm0.30)}$.

4. Star formation in the region can be interpreted as being the direct result of cloud-cloud collisions for the Group I and III stars. The Group II stars probably formed as a result of ionization-shock fronts and/or stellar winds from the older Group I stars.
5. The lack of alignment of the molecular outflows in the Group III stars favors a collisionally enhanced star formation model over one using ambipolar diffusion to regulate the star formation rate in the region.

Chapter 8

On the Importance of Turbulence and Gravity to Molecular Cloud Structure in Cam OB1, Perseus and Elsewhere in the Galaxy

A study of the molecular clouds in the present survey (Digel et al 1996) is undertaken in order to determine whether these clouds are supported by turbulence and/or are in virial equilibrium. It is shown that all of the clouds are consistent with support by turbulence but some of the Cam OB1 clouds show a marked departure from virial equilibrium. A discussion of this result in terms of evolutionary and selection effects is presented.

8.1 Introduction

In the Introduction to the thesis Hoyle's model for the structure of HI in the Galaxy (Hoyle 1953) was briefly discussed. In this model, Hoyle proposed that gravity and turbulence combined to preserve any enhancements of material which occurred. With the realization that a large component of the ISM was in the form of molecular hydrogen, which could be traced out using the CO molecule (Wilson et al. 1970), this model was extended to the investigation of the molecular component of the ISM where it was found that the molecular component also appeared to be turbulent and followed a Kolmogorov prescription (Larson 1978, 1979, 1981). In Chapter 3 an analysis of the molecular clouds in Cam OB1 using structure tree statistics (Houlahan & Scalo 1990, 1992) led to the conclusion that they appeared to have a hierarchical element to their structure, also possibly due to turbulent support. In Chapter 7 it was shown that the power-law describing the structure of the clouds was similar to the IMF for the newly formed stars in Cam OB1 and that this power-law was similar to that elsewhere in the Galaxy. In this chapter the relative importance of gravity and turbulence in organizing molecular clouds in Cam OB1, Perseus and elsewhere in the Galaxy will be discussed.

Given the resolution of the current CO data set (Digel et al. 1996, hereafter Di96) it is not possible to analyze the structure of the CO emission in the region of

Perseus covered in Di96 using structure tree statistics. However, there is an alternative approach to the problem which does allow some estimation of the importance of gravity and turbulence in organizing molecular clouds. In the seminal work of Larson (1981, hereafter L81), parameters for estimating the influence of turbulence and gravity on the structure of molecular clouds were determined from the data then available in the literature for a large number of CO clouds throughout the Galaxy. The measure of turbulence for an ensemble of clouds is given by their *linewidth-size* relationship, i.e., the relationship between their three-dimensional velocity dispersion, σ_{3d}, and length, L, as measured along their longest axes. This relationship has the functional form:

$$\sigma_{3d} \propto L^{\alpha}. \tag{8.1}$$

For the same ensemble of clouds, the influence gravity has on their structure, as a function of cloud length L, was measured by the *Virial Parameter-size* relationship where the *Virial Parameter* is defined as the ratio of their potential energies, $\frac{2GM^2}{L}$, to twice their kinetic energies, $2\left(\frac{M\sigma_{3d}^2}{2}\right)$, where G is Newton's constant and M is the mass of the molecular clouds. The functional form of this relationship is:

$$\frac{2GM}{\sigma_{3d}^2 L} \propto L^{\beta}. \tag{8.2}$$

For clouds in or near virial equilibrium the ratio of the left-hand side of Eq. 8.2 should be approximately unity. If this condition holds over a large range of cloud sizes then $\beta \sim 0$.

There are four data sets which will be analyzed in this chapter: The Cam OB1 clouds *in situ* (see Chapter 7), the Cam OB1 clouds, if they were modified to give them the appearance that they would have at the distance of the Perseus clouds, the Perseus clouds, and the clouds in L81. The layout of this chapter will be as follows. In §8.2, details of the algorithm for transforming the Cam OB1 clouds to allow the direct comparison with the Perseus clouds will be provided. In §8.3, the modified Cam OB1 clouds and the Perseus clouds will be selected and qualitatively compared. In §8.4, the comparison of the *linewidth-size* relationship and the *Virial Parameter-size* relationship for the CO clouds in the present survey and in L81 will be discussed. In §8.5, a brief discussion of the results in light of Hoyle's hypothesis and L81's claim will be presented. Finally, in §8.6, the conclusions of the analysis will be presented.

8.2 'Moving' the Cam OB1 CO Clouds to Perseus

In order to modify the molecular clouds in Cam OB1 to make them appear as if they lie at the same distance as the Perseus clouds it is necessary to know the distance to both regions. In Chapter 4, a distance value of 2500 ± 200 pc was assigned to the Perseus emission on the basis of associated OB associations (Garmany & Stencel 1992), and a similar analysis of the stars in Cam OB1 led to a distance estimate for the Cam OB1 CO emission of 975±90 pc. Given the distances to the two regions, the general procedure for modifying the *in situ* Cam OB1 CO clouds to make them appear as if they lay at the distance of the Perseus emission is as follows:

1. Convolve with the appropriate beam (DRAO in-house software *convolve*) the original Cam OB1 map which has been integrated in velocity over the range -5 to -22 km s^{-1} (see Figure 2.11), which has a resolution of 10′. In the original data, all structure greater than ~ 2.84 pc can be resolved, i.e., 10′ at 975 pc, but if placed at 2500 pc only structure greater in size than ~ 7.27 pc (10′ at 2500 pc) would be resolved. Hence, the input map must be convolved with a beam such that output map can at best resolve ~ 7.27 pc features, i.e., an angular resolution of 25′.6. Assuming a Gaussian beam for the input and output maps, the width of the convolving beam can be found from:

$$25'.6_{\text{Final Beam}} = (10'^2 + \text{Convolving Beam}^2)^{1/2}. \qquad (8.3)$$

   which leads to a convolving beam of ~ 23′.6.
2. Place the modified map on the same grid as the original one (DRAO in-house software *mapconvrt*) keeping in mind the modified map has now been moved to a distance of 2500 pc. This entails re-gridding the modified map by assuming the input grid is really (975/2500) × 3′.75 apart, and then converting it to a new map with the pixels spaced 3′.75 apart. Such an operation is effectively a summation of the pixels within the final beam with a subsequent increase in the S/N given by (3.75/1.46) or ~ 2.5.

8.3 Cloud Selection in Cam OB1 and Perseus

8.3.1 The in situ and Modified Cam OB1 Clouds

Complete details of the selection of *in situ* Cam OB1 clouds may be found in Chapter 7, and the data used for the analysis presented here may be derived

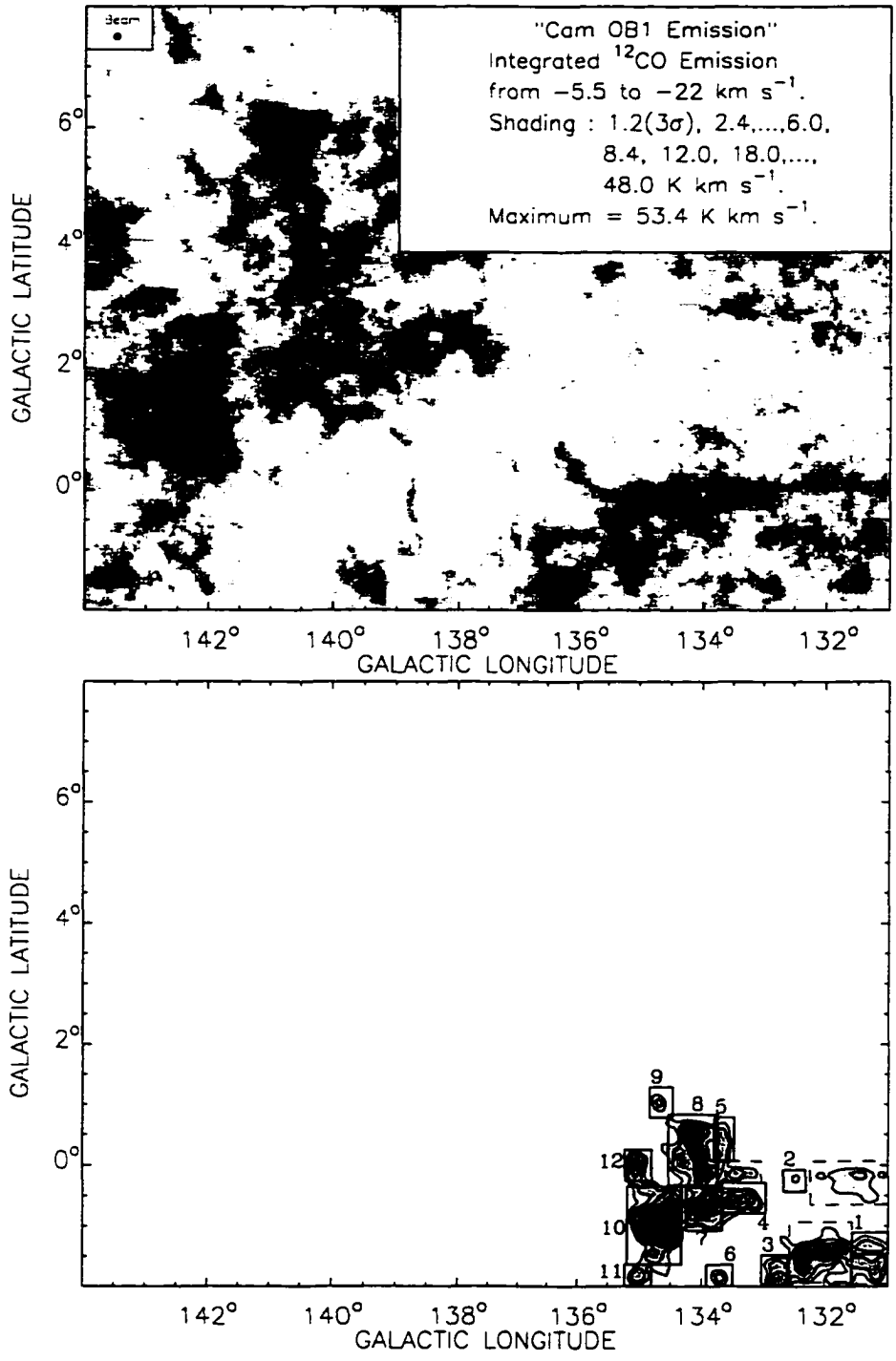

Figure 8.1 *In situ* Original Cam OB1 data (above) and modified Cam OB1 data (below). The contouring scheme for the modified data is 2.05, 3.23,... K km s^{-1}. Candidate Cam OB1 clouds (Table 8.1) are enclosed by a solid border while clouds blended with 'Local' emission are bounded by a broken border. Note that the velocity range of integration is −5 to −22 km s^{-1} for both maps. It should also be noted that the placement of the modified data in the lower right-hand corner is entirely arbitrary and a result of the modification procedure.

Table 8.1: Cam OB1 CO Clouds if They Were Located in the Perseus Arm

No	Designation	l^a [deg.]	b^a [deg.]	v_{LSR} [km s^{-1}]	Δv^b_{LSR} [km s^{-1}]	r^c [pc]	L^d_{CO} [10^3 K km s^{-1} pc^2]	M^e_{CO} [10^4 M$_\odot$]	$(\frac{2GM}{\Delta v^2 L})^f$	$l^g_{(min/max)}$ [deg./deg.]	$b^g_{(min/max)}$ [deg./deg.]	$v^g_{(min/max)}$ [km s^{-1}/km s^{-1}]
MC1	G131.3-1.3-17.7	131.2501	-1.3204	-17.70	2.51	7.85	0.25	0.16	0.14	131.0000/131.5000	-1.4375/-1.0625	-14.0/-23.00
MC2	G132.5-0.2-10.8*	132.4644	-0.2310	-10.78	4.40	3.49	0.10	0.06	0.04	132.4000/132.6000	-0.3500/ 0.1000	-5.50/-23.00
MC3	G132.7-1.8-11.5	132.7144	-1.8421	-11.49	3.44	5.67	0.80	0.49	0.31	132.5000/132.9375	-2.0000/-1.6875	-5.50/-23.00
MC4	G133.4-0.2-11.2	133.3745	-0.1451	-11.21	4.07	5.23	0.31	0.19	0.09	133.0625/133.6250	0.2500/ 0.0625	-5.50/-23.00
MC5	G133.6+0.4-13.7	133.6171	0.3809	-13.71	5.24	6.98	0.57	0.35	0.08	133.5000/133.6875	0.1250/ 0.6875	-5.50/-23.00
MC6	G133.7-1.9-14.1	133.6946	-1.8451	-14.10	3.14	4.36	0.31	0.19	0.19	133.5000/133.8750	2.0000/-1.6875	-5.50/-23.00
MC7	G134.0-0.7-13.5	133.9817	-0.6852	-13.48	5.32	11.78	3.35	2.07	0.27	133.6875/134.3125	1.0625/-0.3750	-5.50/-23.00
MC8	G134.1+0.2-12.9	134.1023	0.2249	-12.91	4.57	11.34	6.04	3.73	0.68	133.6875/134.6250	0.3125/ 0.9375	-5.50/-23.00
MC9	G134.7+1.0-15.2	134.6843	1.0309	-15.22	2.59	3.93	0.28	0.17	0.28	134.5000/134.8125	0.8750/ 1.2500	-5.50/-23.00
MC10	G134.7-0.9-14.0	134.6721	-0.9278	-13.95	6.96	9.59	10.96	6.77	0.63	134.3125/135.1250	1.6250/ 0.3125	-5.50/-23.00
MC11	G135.0-0.0-11.6	135.0218	-0.0269	-11.60	5.41	6.54	0.88	0.54	0.12	134.8750/135.1250	0.2500/ 0.2500	-5.50/-23.00
MC12	G135.0-1.8-14.9	134.9944	-1.8279	-14.88	3.82	5.23	0.48	0.29	0.16	134.8125/135.1875	2.0000/ 1.6875	-5.50/-23.00

a. For the MC OB1 clouds these coordinates are not real but are a result of the modification process. The relative position of the clouds and their appearance are correct but they could have been placed anywhere in the output grid.

b. FWHM velocity width, corrected for the 0.65 km s^{-1} channel size.

c. $r = (\text{Area}/\pi)^{1/2}$, where Area is the area of the cloud within the half-maximum contour of the intensity W_{CO}, corrected for the beam size of the telescope, at a distance D = 2.5 kpc.

d. CO luminosity, integrated from the fit to the cloud's composite spectrum.

e. $M_{CO} = 4.2(X/1.9)L_{CO}$ where $X = 1.9 \times 10^{20}$ cm^{-2} (K km s^{-1})$^{-1}$ (Strong et al. 1988), with an additional factor of 1.4 for helium.

f. Virial Parameter as defined by Larson (1981).

g. Boundary in (l, b, v) for cloud.

*. Not used in any analysis as cloud spectrum is questionable.

from the values listed in Table 7.1. Selection of the modified Cam OB1 (hereafter MC OB1) clouds followed essentially the same procedure but now starting with a modified map of integrated emission (see the lower panel of Figure 8.1). A summary of the physical parameters for the MC OB1 clouds is provided in Table 8.1. Some observations regarding particular MC OB1 clouds are as follows:

1. The brightest molecular clouds are almost certainly blended, e.g., MC10, but are included as all of their emission lies in the velocity range -5.5 to -22 km s^{-1}, and can be fitted well by a Gaussian profile.
2. Weaker features are generally not blended but reasonably well approximated by Gaussian profiles.
3. In the case of one very weak feature, MC2, blending of multiple kinematic components is apparent and severe. This feature is at the threshold level for selection and will not be included in any further analysis.

Figure 8.1 shows the MC OB1 CO emission and the *in situ* Cam OB1 CO emission. The effect of the modification is quite striking considering it is only a change in resolution by a factor of 3. As expected, fine details in the structure of the original emission are not visible in the modified image, but the trend in the large-scale structure, i.e., the CO emission being gathered into several bands which sweep from north to south with increasing longitude, is also lost in the modified image. It is interesting to note how well matched in appearance the MC OB1 emission is to the Perseus emission (see Figure 2.14), particularly the Perseus emission in the vicinity of $\sim l = 141°, b = 0°$. This suggests that from purely morphological considerations it would not be possible to distinguish between the Perseus clouds and MC OB1 clouds. However, the brighter features in Perseus have higher average peak temperatures than the MC OB1 counterparts, and tend to be composed of multiple-velocity components.

8.3.2 The Perseus Clouds

The selection strategy for Perseus clouds is very similar to that for the MC OB1 clouds. Extra care was taken in analyzing the most complicated regions, e.g., W3, and the cloud definition had to be relaxed slightly, in the sense that a cloud had to have a closed contour at least at the half-maximum emission level and, if possible, at the 3σ level. For the majority of complicated features in Perseus these two contour levels did not differ by much as the cloud profile tended to be very steep at the

cloud boundary. Finally, a visual inspection of Figure 2.14 was made to confirm that the cloud boundaries were representative and reasonable. Table 8.2 provides a summary of the CO clouds in Perseus covered by the present survey (Di96).

8.4 A Comparison of the Structure of Molecular Clouds in Cam OB1 and Perseus

In the introduction, two methods for estimating the significance of both turbulence via the *linewidth-size* relationship (Eq. 8.1), and gravity via the *Virial Parameter-size* relationship (Eq 8.2) were introduced. These methods may now be applied to the data for the MC OB1 clouds, the Cam OB1 clouds, the Perseus clouds and the clouds found in L81, and the results are discussed below.

8.4.1 The Turbulence Law.

In L81, an investigation of the relationship between the three-dimensional velocity dispersion, σ_{3d}, of the clouds and their maximum extent, L, was conducted. There were 46 clouds included in that study, and from a hand-fit curve to the data it was found that:

$$log\ (\sigma_{3d}) = 0.04 + 0.38\ log\ L. \tag{8.3}$$

where σ_{3d} is in km s^{-1} and L is in pc. Tables 7.1, 8.1 and 8.2 list the one-dimensional velocity dispersion, Δv, and radius for Cam OB1 clouds (79 clouds), MC OB1 clouds (11 clouds) and Perseus clouds (48 clouds), respectively. In order to make a direct comparison between L81 and these data, L81's result must be expressed in similar units. This is done by first assuming that:

1. all of the clouds are spherical, in which case the maximum extent of a cloud, L, is given by twice the cloud radius, $2r$, and
2. $\sigma_{3d} = (3/(8\ ln2))^{1/2}\Delta v$ (Myers 1985).

With the appropriate changes to the L81 data, a least-squares fit to his data gives: Larson (1981) :

$$log\ \Delta v = (0.19 \pm 0.03) + (0.36 \pm 0.03)\ log\ (2r), \tag{8.4}$$

where Δv is in km s^{-1} and r is in pc, with a correlation coefficient of ~ 0.89. The point of interest is the exponent, 0.36 ± 0.03, which is in good agreement with the clouds if they were supported by Kolmogorov turbulence, i.e., with an exponent of 0.33.

Table 8.2: Summary of Physical Parameters of Perseus Clouds

No	Designation	l^a [deg.]	b^a [deg.]	$v^a_{\rm LSR}$ [km s^{-1}]	$\Delta v^b_{\rm LSR}$ [km s^{-1}]	r^c [pc]	$L^d_{\rm CO}$ [10^3 K km s^{-1} pc^2]	$M^e_{\rm CO}$ [10^4 M$_\odot$]	$(\frac{2GM}{\Delta v^2 L})^f$	$l^g_{\rm (min/max)}$ [deg./deg.]	$b^g_{\rm (min/max)}$ [deg./deg.]	$v^g_{\rm (min/max)}$ [km s^{-1}/km s^{-1}]
P1	G131.4-1.1-34.5	131.3494	-1.1371	-34.54	1.70	4.35	0.23	0.14	0.48	131.1875/131.5625	1.3125/ 1.0000	-29.84/-44.80
P2	G131.8-0.7-53.5	131.8165	-0.6854	-53.45	3.69	3.50	0.64	0.39	0.35	131.6250/132.0000	0.8125/ 0.4375	-44.55/-64.55
P3	G132.2-0.9-54.8	132.2333	-0.8449	-54.81	2.63	9.15	1.09	0.67	0.45	132.0000/132.5000	1.1875/ 0.5000	-46.10/-66.25
P4	G132.6-1.5-38.1	132.5464	-1.5444	-38.10	2.70	3.05	0.66	0.41	0.79	132.1875/132.8750	1.8125/ 1.2500	-29.84/-46.10
P5	G132.7-0.4-50.3	132.6465	0.3937	-50.31	2.70	3.05	0.14	0.09	0.17	132.5000/132.8125	0.5000/ 0.2500	-40.90/-61.05
P6	G133.2+0.9-42.8	133.1893	0.9188	-42.76	4.67	10.90	9.06	5.59	1.01	132.1825/133.6250	0.6875/1.1250	-30.00/-70.00
P7	G133.2-1.1-37.9	133.1945	-1.1430	-37.89	2.54	4.35	0.15	0.09	0.14	133.0625/133.5000	1.2500/ 1.0000	-29.84/-42.20
P8	G133.3+2.1-42.6*	133.2469	2.0868	-42.57	4.08	0.87	0.13	0.08	N/A	133.0625/133.3750	2.0000/ 2.1875	-33.75/-53.25
P9	G133.3-1.3-38.5*	133.2849	-1.3198	-38.46	2.34	1.74	0.12	0.08	N/A	133.0625/133.5000	1.4375/ 1.2500	-29.84/-42.20
P10	G133.4+0.3-49.7	133.4271	0.2627	-49.65	4.17	7.85	3.63	2.24	0.70	133.1875/133.6250	0.0000/ 0.5000	-30.00/-70.00
P11	G133.7+1.2-41.2	133.6757	1.2298	-41.18	5.87	4.35	5.06	3.12	0.89	133.3125/133.9375	1.1250/ 1.3750	-30.00/-70.00
P12	G133.9+0.4-47.4	133.8890	0.4273	-47.35	5.80	9.6	5.89	3.63	0.48	133.6250/134.1250	0.1875/ 0.6250	-30.00/-70.00
P13	G133.9+1.1-44.3*	133.9242	1.0710	-44.29	8.10	4.35	2.21	1.37	N/A	133.8125/134.0625	0.9375/ 1.1875	-30.00/-70.00
P14	G134.1-0.9-39.4	134.0566	-0.9332	-39.41	2.36	4.35	0.20	0.12	0.21	133.7500/134.1875	1.1875/ 0.7500	-29.84/-50.00
P15	G134.1+0.8-48.2	134.1125	0.7619	-48.16	4.83	5.25	4.72	2.91	1.02	133.8750/134.3750	0.6250/ 0.9375	-30.00/-70.00
P16	G134.3-1.7-49.3	134.3219	-1.6891	-49.28	3.70	7.00	1.18	0.73	0.33	134.0000/134.6250	2.0000/ 1.3750	-36.35/-59.10
P17	G134.5+0.3-47.6	134.5147	0.2770	-47.58	3.31	5.65	0.39	0.24	0.17	134.3750/134.6875	0.0625/ 0.4375	-38.95/-56.50
P18	G134.6+1.9-37.2*	134.5858	1.8815	-37.16	2.52	1.74	0.19	0.12	N/A	134.4375/134.8125	1.7500/ 2.0000	-33.10/-42.85
P19	G134.7+2.2-40.5	134.6772	2.1540	-40.45	2.43	5.25	0.28	0.17	0.24	134.2500/134.8750	2.0000/ 2.4375	-34.40/-48.05
P20	G134.7-0.7-42.8	134.7377	-0.7003	-42.81	3.68	7.85	1.37	0.85	0.34	134.4375/135.0000	1.0000/ 0.5000	-33.10/-53.25
P21	G134.9+1.5-40.1	134.8558	1.5036	-40.11	4.51	3.5	0.93	0.57	0.35	134.6875/135.0000	1.1875/ 1.8125	-29.84/-50.00
P22	G134.8-0.0-44.8	134.8154	-0.0249	-44.76	3.56	4.35	0.34	0.21	0.16	134.6250/134.9375	0.1875/ 0.1875	-38.95/-58.95

Table 8.2 cont.: Summary of Physical Parameters of Perseus Clouds

No	Designation	l^a [deg.]	b^a [deg.]	$v^a_{\rm LSR}$ [km s^{-1}]	$\Delta v^b_{\rm LSR}$ [km s^{-1}]	r^c [pc]	$L^d_{\rm CO}$ [10^3 K km s^{-1} pc^2]	$M^e_{\rm CO}$ [10^4 M$_\odot$]	$(\frac{2GM}{\Delta v^2 L})^f$	$l^g_{\rm (min/max)}$ [deg./deg.]	$b^g_{\rm (min/max)}$ [deg./deg.]	$v^g_{\rm (min/max)}$ [km s^{-1}/km s^{-1}]
P23	G135.0-0.0-36.5	135.0374	-0.0321	-36.52	2.87	3.95	0.32	0.20	0.27	134.6250/135.2500	-0.1875/0.1875	-28.95/-38.95
P24	G135.1-0.0-44.2	135.1263	-0.0288	-44.24	3.45	4.35	0.66	0.41	0.34	134.9375/135.3125	0.1875/0.1875	-38.95/-58.95
P25	G135.3+1.1-44.7*	135.2762	1.0874	-44.71	4.54	2.18	1.14	0.79	N/A	135.0625/135.5000	0.8125/ 1.3750	-34.40/-54.55
P26	G135.6+0.2-36.9	135.5841	0.2267	-36.87	2.71	3.95	0.13	0.08	0.12	135.3750/135.7500	0.1250/ 0.3750	-29.84/-41.55
P27	G135.5+0.3-43.5	135.5089	0.2503	-43.47	2.24	3.05	0.23	0.14	0.39	135.3750/135.7500	0.1250/ 0.5000	-38.30/-52.60
P28	G135.7-0.2-38.7	135.7381	-0.2059	-38.65	5.27	5.65	0.61	0.38	0.10	135.5625/135.9375	0.4375/ 0.0625	-29.84/-50.00
P29	G136.1+2.1-45.2	136.1101	2.0890	-45.15	3.23	3.05	0.30	0.19	0.26	135.8750/136.3125	1.9375/ 2.3125	-36.35/-57.80
P30	G136.4+0.2-56.2	136.3735	0.2020	-56.17	3.55	4.35	0.44	0.27	0.21	136.1250/136.5625	0.0625/ 0.3750	-46.10/-66.25
P31	G136.5+1.2-37.4	136.4619	1.1743	-37.42	3.60	6.55	3.49	2.16	1.09	136.0000/136.7300	0.7500/ 1.7500	-29.84/-48.05
P32	G137.0+1.3-38.6	136.9560	1.2549	-38.58	6.13	5.25	8.80	5.43	1.19	136.7000/137.3750	0.7500/ 1.7500	-29.84/-48.05
P33	G137.3+2.7-45.2	137.2966	2.6684	-45.17	2.71	3.05	0.24	0.15	0.29	137.1875/137.4375	2.5000/ 2.8125	-35.05/-51.95
P34	G137.2+3.1-50.8	137.2288	3.0818	-50.81	1.86	3.05	0.25	0.15	0.61	136.8750/137.4375	2.9500/ 3.3750	-42.20/-61.70
P35	G137.7+1.5-39.1	137.7049	1.4702	-39.10	3.69	4.35	3.38	2.09	1.51	137.4375/138.0625	1.0625/ 1.7500	-29.84/-50.00
P36	G137.8-0.7-43.9	137.7464	-0.7117	-43.89	2.60	5.25	0.38	0.23	0.28	137.4375/137.9375	0.8750/ 0.4375	-41.55/-57.15
P37	G138.0+0.8-37.8	138.0020	0.8089	-37.78	2.90	4.35	0.77	0.47	0.55	137.7500/138.3125	0.5000/ 1.1250	-29.84/-48.05
P38	G138.5+1.6-38.7	138.4857	1.6419	-38.71	2.77	4.35	3.86	2.38	3.05	138.0625/139.0000	1.3750/ 1.9375	-28.84/-47.40
P39	G138.5+2.2-39.9	138.4607	2.1863	-39.89	2.50	5.65	0.54	0.34	0.41	138.1250/138.6250	2.0625/ 2.4375	-29.84/-50.00
P40	G138.4-0.8-37.0*	138.4260	-0.7819	-37.04	3.42	1.75	0.14	0.09	N/A	138.3000/138.6500	0.9000/ 0.6375	-29.84/-42.85
P41	G138.8+2.3-39.5	138.8156	2.3070	-39.52	2.60	5.65	0.42	0.26	0.29	138.6875/138.9375	2.0625/ 2.5625	-29.84/-47.40
P42	G139.2+0.4-39.8*	139.2280	0.4393	-39.83	1.91	2.18	0.31	0.19	N/A	138.9375/139.5000	0.2500/ 0.6250	-29.84/-50.00
P43	G139.2+1.1-39.3	139.2420	1.0463	-39.31	2.86	7.85	1.72	1.06	0.71	138.7500/139.6875	0.7500/ 1.3750	-29.84/-50.00
P44	G139.7-0.4-39.0	139.6448	-0.4393	-39.03	5.14	9.15	3.20	1.97	0.35	139.0000/140.2750	-1.0000/ 0.0000	-29.84/-50.00

Table 8.2 cont.: Summary of Physical Parameters of Perseus Clouds

No	Designation	l^a [deg.]	b^a [deg.]	$v^a_{\rm LSR}$ [km s^{-1}]	$\Delta v^b_{\rm LSR}$ [km s^{-1}]	r^c [pc]	$L^d_{\rm CO}$ [10^3 K km s^{-1} pc^2]	$M^e_{\rm CO}$ [10^4 M$_\odot$]	$(\frac{2GM}{\Delta v^2 L})^f$	$l^g_{\rm (min/max)}$ [deg./deg.]	$b^g_{\rm (min/max)}$ [deg./deg.]	$v^g_{\rm (min/max)}$ [km s^{-1}/km s^{-1}]
P45	G139.9+0.2-39.9*	139.9033	0.2086	-39.92	3.07	0.87	0.88	0.54	N/A	139.6250/140.1250	0.0000/ 0.4375	-29.84/ -50.65
P46	G139.9+2.6-51.5	139.9313	2.6279	-51.47	2.47	3.50	0.33	0.20	0.40	139.7500/140.3750	2.6000/ 2.8750	-40.25/ -59.75
P47	G140.6-0.2-39.6	140.5926	-0.1462	-39.64	4.08	6.1	2.65	1.64	0.69	140.2750/140.9275	-0.5625/ 0.2500	-29.84/ -50.00
P48	G140.6+0.7-37.9	140.6177	0.6725	-37.92	3.57	6.55	3.51	2.16	1.11	140.2125/141.0625	0.2500/ 1.2500	-29.84/ -50.00
P49	G140.9-1.1-40.8	140.8686	-1.0959	-40.82	4.05	6.55	5.28	3.26	1.31	140.4375/141.1875	-1.6250/ -0.5000	-31.14/ -50.65
P50	G141.5-1.2-41.1	141.5387	-1.1750	-41.06	2.63	3.95	3.00	1.85	2.92	141.2500/142.1250	-1.5000/ -0.6250	-31.14/ -50.65
P51	G141.8+1.6-47.7	141.7544	1.6240	-47.65	2.80	3.95	0.39	0.24	0.38	141.4375/142.0000	1.4375/ 1.8125	-36.35/ -57.15
P52	G142.2+1.4-44.8*	142.2032	1.4434	-44.77	2.84	1.74	0.25	0.16	N/A	142.0000/142.3750	1.3125/ 1.8125	-36.35/ -54.55
P53	G142.6+0.5-43.4	142.6387	0.5215	-43.25	3.42	3.05	0.76	0.47	0.56	142.4000/142.9375	0.3125/ 1.8125	-36.35/ -54.55
P54	G142.8-1.0-42.6	142.7475	-0.9884	-42.60	3.97	8.3	2.35	1.45	0.48	142.2500/143.1875	1.2500/ -0.5625	-31.79/ -50.65
P55	G143.4+1.0-38.0	143.4278	0.9526	-38.03	2.83	5.25	0.47	0.29	0.30	143.1875/143.7000	0.6875/ 1.1250	-29.84/ -50.00
P56	G143.6+0.2-34.5	143.5880	0.1850	-34.45	2.77	5.25	0.37	0.23	0.25	143.1250/144.0000	0.0625/ 0.3750	-27.89/ -37.00
P57	G143.9-1.5-30.7	143.8473	-1.4975	-30.65	2.51	5.7	1.60	0.99	1.19	143.5000/144.0000	-1.9000/ 1.0625	-27.89/ -48.70

a. Emission weighted mean values. $v_{\rm LSR}$ is measured relative to standard solar motion.

b. FWHM velocity width, corrected for the 0.65 km s^{-1} channel size.

c. $r = ({\rm Area}/\pi)^{1/2}$, where Area is the area of the cloud within the half-maximum contour of the intensity $W_{\rm CO}$, corrected for the beam size of the telescope, at a distance D = 2.5 kpc.

d. CO luminosity, integrated from the fit to the cloud's composite spectrum.

e. $M_{co} = 4.2(X/1.9)L_{co}$ where $X = 1.9 \times 10^{20}$ cm^{-2} (K km s^{-1})$^{-1}$ (Strong et al. 1988), with an additional factor of 1.4 for helium.

f. Virial Parameter as defined by Larson (1981).

g. Boundary in (l, b, v) for cloud.

*. Not used in any analysis as cloud spectrum is questionable.

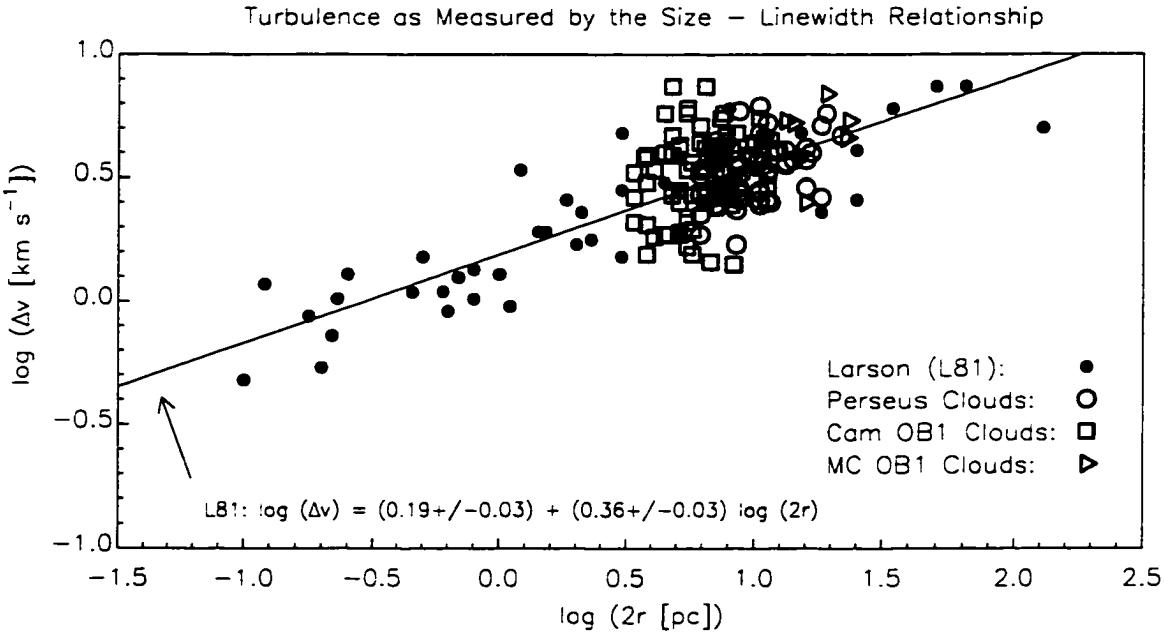

Figure 8.2 Comparison of the *linewidth-size* relationship as found by Larson (1981, 44 clouds) with the Cam OB1 clouds (79 clouds), modified Cam OB1 clouds (11 clouds) and Perseus clouds (48 clouds). More data, over a larger range in cloud radii, are required to find a complete solution to the data taken from the present survey (Di96).

Figure 8.2 shows an overlay of the data in the present work against that in L81. It would appear that the clouds from all samples fall onto the L81 linewidth-size relationship. However, the scatter in log (Δv) is large, particularly for the Cam OB1 clouds, and the range of cloud sizes is comparable to the scatter in log (Δv). Hence, without additional information on clouds spanning a larger range of sizes the only observation which can be made is that *the degrees of turbulence, as measured by the linewidth-size relationship, for molecular clouds taken from the present survey (Di96) have mean values which are consistent with L81.*

A summary of the key points regarding the influence of turbulence in supporting the clouds taken from the present survey, and those in L81, are:

1. The scatter in the *linewidth-size* relationship for the Cam OB1 clouds appears to be appreciably greater than that in L81 or for the other regions considered in the present survey.
2. Because of the small range of cloud sizes, it is not possible to test, in a statistical

sense, whether there is any difference between the *linewidth-size* relationship for the molecular clouds taken from the present survey and those of L81. However, the mean values for all of the populations considered in this work do agree with the results derived in L81.

8.4.2 Virial Equilibrium

In order to measure the degree to which clouds are in virial equilibrium, L81 suggested the use of a *Virial Parameter-size* relationship, i.e., Eq. 8.2. L81 found, from a hand-fit solution to his data, that the *Virial Parameter*, as a function of cloud size is given by:

$$log(\frac{2GM}{\sigma_{3d}^2 L}) = -0.04 + 0.14\ log\ (L[pc]). \tag{8.5}$$

A value greater than one for the Virial Parameter, $\frac{2GM/}{\sigma_{3d}^2 L}$, indicates that the system is gravitationally bound and susceptible to gravitational collapse provided that there are no other forces present, e.g., due to magnetic fields, or rotation. Converting this relationship to the quantities consistent with those presented in Tables 7.1, 8.1 and 8.2, and using the same assumptions as in §8.4.1, it follows that an unweighted least-squares solution to the L81 data, found by the author, is:
Larson (1981) :

$$log\Big(\frac{2GM}{\Delta v^2(2r)}\Big) = (0.00 \pm 0.07) + (0.07 \pm 0.08)\ log\ (2r[pc]). \tag{8.6}$$

In Figure 8.3 plots of the *Virial Parameter* for the three cloud samples, Perseus, Cam OB1 and MC OB1, together with the L81 data, and the least-squares relationship derived from the L81 data (Eq. 8.6), are presented. In order to quantify whether the data come from similar parent populations, a statistical analysis was undertaken to measure the absolute difference in the mean values for various combinations of the data as well as the deviation in the difference. Formally, the absolute difference in the mean of two populations, $\bar{Y}_1$ and $\bar{Y}_2$, is given by

$$D = |\bar{Y}_1 - \bar{Y}_2|, \tag{8.7}$$

which has a deviation given by

$$\sigma_D = \sqrt{\frac{\sigma_1^2}{n_1} + \frac{\sigma_2^2}{n_2}}, \tag{8.8}$$

where the σ_s and n_s refer to the standard deviation and sample size, respectively, of the two populations being compared (Mendenhall et al. 1981). The results of this comparison are presented in Table 8.3.

Table 8.3: Statistics for Comparison of Virial Parameter

	L81	Per	Cam OB1	MC OB1
	$D \pm \sigma_D$	$D \pm \sigma_D$	$D \pm \sigma_D$	$D \pm \sigma_D$
L81	N/A	0.06 ± 0.08	0.50 ± 0.07	0.39 ± 0.12
Per	0.06 ± 0.08	N/A	0.44 ± 0.07	0.33 ± 0.10
Cam OB1	0.50 ± 0.07	0.44 ± 0.07	N/A	0.11 ± 0.10
MC OB1	0.39 ± 0.12	0.33 ± 0.10	0.11 ± 0.10	N/A

There are several conclusions which can be drawn from the statistical results shown in Table 8.3 and from an examination of Figure 8.3. These include:

1. It is not possible to derive a formal solution for the *Virial Parameter* as a function of cloud size for the Perseus clouds (top panel, Figure 8.3) because of the limited range in cloud sizes studied. However, the mean value of the Perseus clouds' distribution and that of L81 are in agreement and would suggest that they came from the same parent population.
2. Again, owing to the limited range in cloud sizes sampled, it is not possible to obtain a formal solution for the *Virial Parameter-size* relationship for the MC OB1 clouds (middle panel, Figure 8.3). In the case of the MC OB1 clouds, the majority of them lie below the threshold to be self-gravitating (dashed line in Figure 8.3). The comparison between the MC OB1 mean and that of L81 and Perseus shows that the clouds do not come from the same parent population.
3. In the case of the *in situ* Cam OB1 clouds, the difficulty persists with the small range of cloud sizes. In this case, the difference between the two population means (D) from L81 and Per is even more pronounced than in the case of MC OB1.
4. The comparison of the MC OB1 clouds to the *in situ* Cam OB1 clouds shows that the difference in the means of the two populations is not significant. Furthermore, this suggests that the essential character of the *in situ* Cam OB1 clouds, as being clouds which have a mean *Virial Parameter* different from L81 or Perseus, has been preserved in the modification process to form the MC OB1

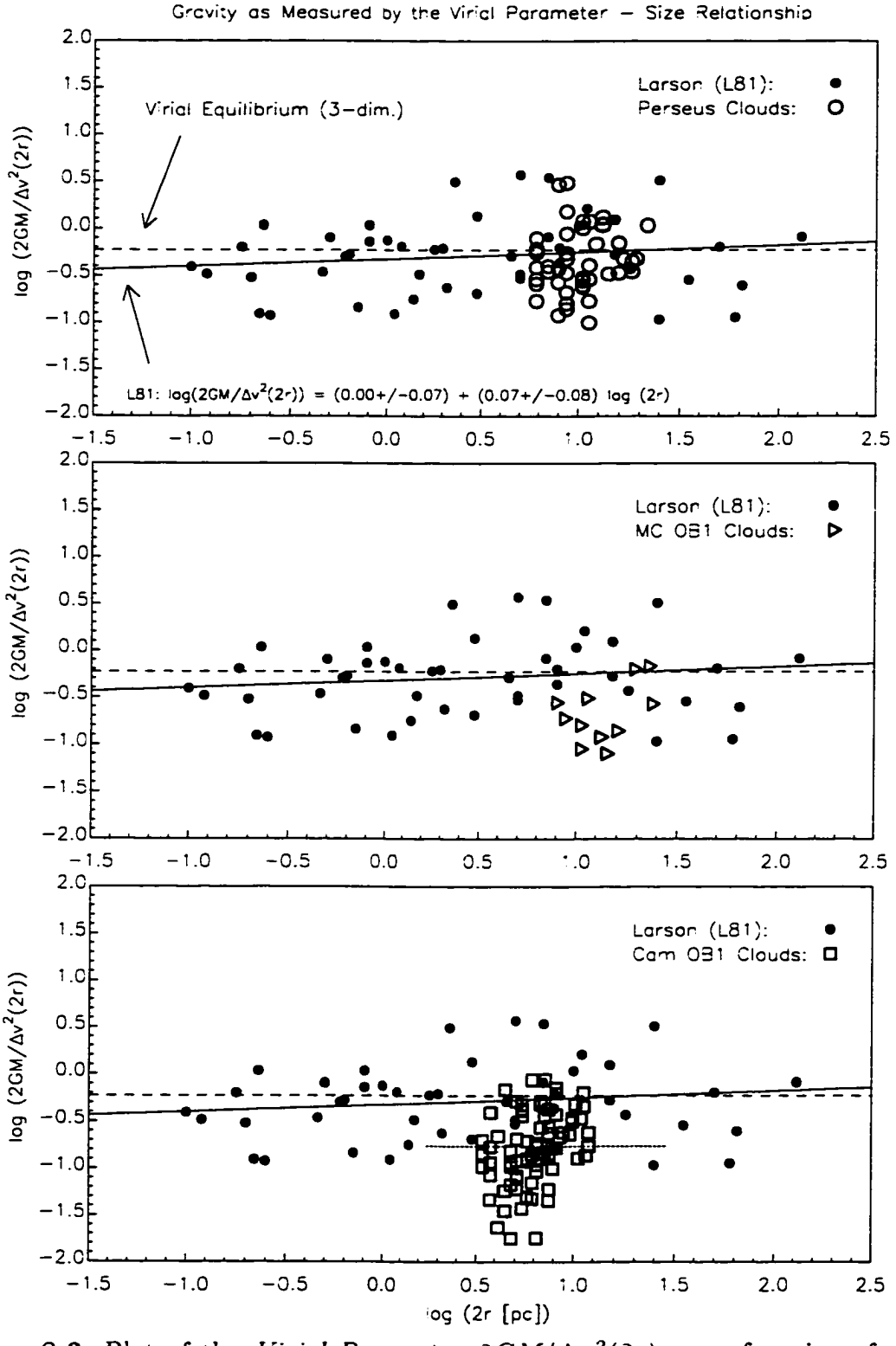

Figure 8.3 Plot of the *Virial Parameter*, $2GM/\Delta v^2(2r)$, as a function of cloud size. The condition for virial equilibrium is shown by the dashed line. For the Cam OB1 clouds (bottom panel) the mean in their distribution, as a function of the *Virial Parameter*, is shown by the dotted line.

clouds. Therefore, the *in situ* Cam OB1 clouds are essentially different from the L81 and Perseus clouds in the importance gravity has on regulating their structure.

In order to explore the cause of the large range in the *Virial Parameter* for the Cam OB1 clouds, an examination of the clouds making up the Cam OB1 data was undertaken. In this analysis, the Cam OB1 clouds were placed into one of two groups, depending on whether they are 'above' or 'below' the mean *Virial Parameter* for the Cam OB1 clouds (i.e., $log(2GM/\Delta v^2(2r)) = -0.77$, the dotted line shown in the lower panel of Figure 8.3). There are 40 clouds which lie above, and 39 clouds which lie below this dividing line. Table 8.4 provides a summary of this analysis. All of the values listed in Table 8.4 are mean values, with the error shown being the error in the mean.

Table 8.4: Physical Properties of Cam OB1 Clouds with Above- and Below-average Virial Parameters

Group	l [deg.]	b [deg.]	Δv [km s^{-1}]	r [pc]	M_{CO} [$\times 10^3$ M$_\odot$]	T_{max} [K]
Above	139.4 ± 0.5	1.8 ± 0.3	3.0 ± 0.2	3.7 ± 0.2	3.3 ± 0.4	3.5 ± 0.2
Below	138.1 ± 0.6	1.8 ± 0.4	4.0 ± 0.2	3.0 ± 0.1	1.1 ± 0.2	2.0 ± 0.1

The properties of the two groups of Cam OB1 clouds are quite different. There is an indication that the above-average *Virial Parameter* clouds may be preferentially located at higher longitudes but the difference in the mean longitude of the above- and below-average groups is only marginal and may not be significant. The clouds in the above-group also tend to have larger masses and narrower velocity linewidths than the below-group. Both of these tendencies will contribute to the placement of the above-group as being gravitationally bound and, conversely, for the below-group to be gravitationally unbound. The above-group clouds also tend to be warmer, which is expected for molecular clouds which are forming stars, i.e., molecular clouds associated with Cam R1.

8.5 Discussion

In Hoyle's model of HI (Hoyle 1953), now extended to molecular clouds, the permanence of a cloud in turbulent flow is due to the cohesive effects of gravity dominating over the dissipative force of turbulence. In principle, this permanence could be measured directly if there were some way of observing a cloud over its lifetime and confirming that the cloud was long-lived, persisting for at least the order of a dynamical time (Larson 1994). In practice, this is not possible, but the permanence of structure may be inferred in two ways: a) by the presence of star formation, in which case it is assumed that the clouds must have survived sufficiently long for stars to form, or b) by the distribution of cloud masses, i.e., if there is a large number of clouds present which exceed their virial masses.

The description of the balance between disruption and contraction of a molecular cloud is given by the virial equation, i.e.,

$$P - \Omega = 2T + B + 2L, \tag{8.9}$$

where P is energy due to external pressure, Ω is the potential energy of the system, T is the kinetic energy of the system due to thermal and turbulent motion, B is the energy due to magnetic pressure and L is now the energy due to rotation. Molecular clouds considered in this study are almost certainly turbulent, but the question of whether they are bound or not is more problematic. L81 claimed that all molecular clouds are gravitationally bound, over a large range of scale sizes. The Perseus clouds support this claim but not the *in situ* Cam OB1 clouds or the MC OB1 clouds. In fact, *the Cam OB1 clouds are a mixture, which vary in the degree to which their structures are regulated by gravity.* It has been argued that dramatic departures from conditions for being gravitationally bound have been seen in very vigorous star forming regions elsewhere in the Galaxy, e.g., Orion and Cep OB3 (Falgarone 1995), where an additional force to constrain those clouds is provided by external thermal pressure. In the case of Cam OB1, the star formation is not as vigorous and the clouds involved in the star formation tend to be gravitationally bound. It is the smaller clouds in Cam OB1, which are not active star forming regions, that appear to be out of virial equilibrium. Since these smaller clouds are not associated with any recent star forming activity and have not dispersed they may represent a young population of molecular clouds in Cam OB1.

8.6 Conclusions

In this chapter several aspects of the structure of molecular clouds in the present survey were considered. From this analysis it was possible to conclude that:

1. The appearance of the Cam OB1 molecular clouds would be similar to those of the Perseus clouds if they were placed at the same distance as the Perseus clouds.
2. All of the molecular clouds considered in the present survey are consistent with the linewidth-size relationship derived by Larson (1981). This relationship is suggestive of Kolmogorov-type turbulence.
3. The essential character of the *in situ* Cam OB1 clouds, as measured by their mean *Virial Parameter*, is preserved when they are scaled to appear as if they were at the same distance as the Perseus clouds.
4. Not all of the molecular clouds considered in the present survey are gravitationally bound. In particular, the *in situ* Cam OB1 and MC OB1 clouds show a strong departure from virial equilibrium. It is suggested that the clouds showing the strongest departure from being self-gravitating may be the youngest clouds in the field.

Chapter 9

Conclusions and Suggestions for Further Observations

A summary of the thesis in terms of the three elements of star formation is provided. Suggestions for further studies in the region are also given.

This thesis has attempted to examine the star formation in the Cam OB1 region, covered by a recent CO survey (Digel et al. 1996), in terms of three elements: a) the similarity of the structure of the molecular clouds from which stars form with the newly formed stars as measured by the cloud mass function and IMF, respectively; b) the temporal evolution of the molecular clouds, and c) the probability of star formation occurring. It has been shown that the CO emission in the Cam OB1 region appears to be hierarchical in structure and is probably supported against collapse by turbulence. It has also been shown in this thesis that the mechanism which governs the probability of star formation, in the case of Cam OB1, operates at the molecular core level and is probably a result of an enhanced number of core collisions in the region, leading to an enhanced number of core collapses and an increase in the subsequent star formation rate. The principle mechanism for this enhancement is the collision of molecular complexes in the region and ionization-shock fronts produced by the most massive stars in the region. It was also shown that the molecular clouds in Perseus have a similar structure to those seen in Cam OB1.

There are, of course, further observations which should be made of the Cam OB1 region in order to strengthen the arguments presented in this thesis. These include:

1. Extending the CO observations to the entire Cam OB1 region. The present observations cover only approximately half of the Cam OB1 region, as defined by the Cam OB1 association (Humphreys 1978), and it would be interesting to see if Cam R1 represents a unique region of contact for molecular material in Cam

OB1 or whether there are numerous such regions. It would also be interesting to see if the Cam OB1 emission can be separated from the Local emission over its entire extent, and whether or not there is any age differentiation of Cam OB1 stellar groups over this scale. Such a study may reveal whether Cam R1 is part of a larger shell-like structure where star formation is the result of expansion of molecular shells (Digel et al. 1996) or whether the molecular material is more fragmented and star formation is localized.

2. Infrared imaging of the regions of contact where the Group III stars are forming is badly needed. The *IRAS* data (Beichman et al. 1988) provides only an indication of the enhancement of infrared sources, above the background, in the surveyed field. An analysis of these sources based upon their infrared emission from better data is required in order to classify them and, in the cases of pre-main sequence stars, to determine their luminosity and possible stellar masses.
3. High-resolution observations, in various molecular transitions, of the molecular cloud interface in the vicinity of AFGL490 and AFGL490-iki could serve to improve the physical model of the outflow AFGL490-iki, as well as to determine exactly where in the cloud the outflows lie. It is also possible that abundance differences between the various complexes may be detected which would support the hypothesis that the colliding clouds are expanding shells.
4. Preliminary work on the Perseus clouds suggest that they have a similar structure to the Cam OB1 clouds. High-resolution observations of selected clouds in Perseus and a comparative study of the structure tree statistics for these clouds, and the entire Cam OB1 region, are required to confirm this result.
5. A comparison of the CO emission to the HI emission in the region (Gr 1993) showed that they followed similar power-laws. It would be interesting to analyze the HI data using structure tree statistics to see whether or not these statistics are also the same as those of the CO. This would provide more information on the structure of the ISM, and the interplay between various components of it, than is available from an FFT analysis alone.

Bibliography

Adams, F. C. and Fatuzzo, M. 1996. Astrophysical Journal, 464, 256.

Allen, C. 1973. Astrophysical Quantities, London: Athlone, 30.

Baade, W. 1944a. Astrophysical Journal, 100, 137.

Baade, W. 1944b. Astrophysical Journal, 100, 147.

Ball, J. A., Gottlieb, C. A., Lilley, A. E., and Radford, H. E. 1970. Astrophysical Journal, 162, L203.

Bally, J. and Lada, C. J. 1983. ApJ, 265, 824.

Barrett, A. H., Schwartz, P. R. and Waters, J. W. 1971. Astrophysical Journal, 16, L1.

Beichman, C. A., Myers, P. C., Emerson, J. P., Harris, S., Mathieu, R., Benson, P. J., and Jennings, R. E. 1986. Astrophysical Journal, 307, 337.

Beichman, C. A., Neugebauer, G., Habing, H. J., Clegg, P. E., and Chester, T. J. (eds.), 1988. *IRAS Explanatory Supplement*, NASA RP-1190, Washington, D.C.: GPO.

Belresene, E. P. 1970. Observatory, 90, 239.

Berrilli, F. Corciulo, G., Ingrosso, G., Lorenzetti, D., Nisini, B. and Strafella, F. 1992. Astrophysical Journal, 398, 254

Blaauw, A. 1963. In *Basic Astronomical Data*, ed. K. Aa. Strand, Chicago: University of Chicago Press, 383.

Blaauw, A. 1964. Annual Reviews in Astronomy and Astrophysics, 2, 213.

Blitz, L. 1993. In *Protostars and Planets III*, eds. Eugene H. Levy and Jonathan I. Lunine, Tucson: University of Arizona Press, 125.

Blitz, L. and Shu, F. H. 1980. Astrophysical Journal, 238, 148.

Blitz, L., Fich, M. and Stark, A. A. 1982. (BFS) Astrophysical Journal Supplement Series, 49, 183.

Bloemen, J. B. G. M., Caraveo, P. A., Hermsen, W. Lebrun, F. Maddalena, R. J., Strong, A. W., and Thaddeus, P. 1984. Astronomy and Astrophysics, 139, 37.

Bloemen, J. B. G. M., Strong, A. W., Blitz, L., Cohen, R. S., Dame, T. M., Grabelsky, D. A., Hermsen, W., Mayer-Hasselwander, H. A., and Thaddeus, P. 1986. Astronomy and Astrophysics, 154, 25.

Bloemen, J. B. G. M. 1989. Annual Reviews of Astronomy and Astrophysics, 27, 469.

Bodenheimer, P., Ruzmaikina, T. and Mathieu, R. D. 1993. In *Protostars and Planets III*, eds. Eugene. H. Levy and Jonathan I. Lunine, Tuscon: University of Arizona Press, 367.

Bohlin, R. C., Savage, B. D., and Drake, J. F. 1978. Astrophysical Journal, 224, 132.

Böhm-Vitense, E. 1989. Stellar Atmospheres, Vol. 2, Cambridge: Cambridge Univ. Press, 27.

Bonnor, W. B. 1956. Monthly Notices of the Royal Astronomical Society, 116, 351.

Bowers, R. and Deeming, T. 1984. Astrophysics I and II, Boston: Jones and Bartlett Pub., Inc.,

Brand, J. and Blitz, L. 1993. Astronomy and Astrophysics, 275, 67.

Brand, J., Cesaroni, R., Caselli, P., Catarzi, M., Codella, C., Comoret, G., Curioni, G. P., Di Franco, S., Felli, M., Giovanardi, C., Olmi, L., Palagi, F., Palla, F., Panella, D., Pareschi, G., Rossi, E., Speroni, N., and Tofani, G. 1994. Astronomy and Astrophysics Supplement Series, 103, 541.

Braunsfurth, E. 1983. Astronomy and Astrophysics, 117, 297.

Braunsfurth, E. and Reif, K. 1984. Astronomy and Astrophysics Supplement Series, 62, 365.

Bronfman, L., Cohen, R. S., Alvarez, H., May, J., and Thaddeus, P. 1988. Astrophysical Journal, 324, 248.

Bronfman, L., Nyman, L.-Å., and May, J. 1996. Astronomy and Astrophysics Supplement Series, 115, 81.

Burton, W. B. 1992. In *The Galactic Interstellar Medium*, eds. D. Pfenniger and P. Bartholdi, Berlin: Springer-Verlag, 1.

Campbell, B., Persson, S. E., and McGregor, P. J. 1986. Astrophysical Journal, 305, 336.

Carlberg, R. G. and Pudritz, R. E. 1990. Monthly Notices of the Royal Astronomical Society, 247, 353.

Carpenter, J. M., Snell, R. L., Schloerb, F. P., and Skrutskie, M. F. 1993. Astrophysical Journal, 407, 657.

Carpenter, J. M., Snell, R. L., and Schloerb, F. P. 1995. Astrophysical Journal, 450, 201.

Casoli, F., Dupraz, C., Gerin, M., Combes, F. and Boulanger, F. 1986. AA, 169, 281.

Castelaz, M. W., Sellgren, K. and M. W. Werner. 1987. Astrophysical Journal, 313, 853.

Cesaroni, R., Palagi, F., Felli, M., Catarzi, M., Comoretto, G., Di Franco, S., Giovanardi, C. and Palla, F. 1988. Astronomy and Astrophysics Supplement Series, 76, 445.

Chair, J. E., Kutner, M. L., Verter, F., and Leous, J. 1994. Astrophysical Journal, 431, 658.

Chan, G. and Fich, M. 1995. Astronomical Journal, 109, 2611.

Chandrasekhar, S. , and Lebovitz, N. R. 1962. Astrophysical Journal, 136, 1082.

Collins II, G. W. 1978. The Virial Theorem in Stellar Astrophysics, Tucson: Pachart Publishing House, 1.

Combes, F. 1991. Annual Review of Astronomy and Astrophysics, 29, 195.

Comoretto, G., Palagi, F., Cesaroni, R., Felli, M., Bettarini, A., Catarzi, M., Curioni, G. P., Curioni, P., Di Franco, S., Giovanardi, C., Massi, M., Palla, F., Panella, D., Rossi, E., Speroni, N. and Tofani, G. 1990. Astronomy and Astrophysics Supplement Series, 84, 179.

Crawford, D. F., Jauncey, D. L., and Murdoch, H. S. 1970. Astrophysical Journal, 162, 405.

Dame, T. 1983. Ph.D. Thesis, Columbia University.

Dame, T. M., and Thaddeus, P. 1985. Astrophysical Journal, 297, 751.

Dame, T. M., Ungerechts, H., Cohen, R. S., de Geus, E. J., Grenier, I. A., May, J., Murphy, D. C., Nyman, L.-Å, and Thaddeus, P. 1987. (Da87). Astrophysical Journal, 322, 706.

De Geus, E. 1990. In *Properties of Hot Luminous Stars*, ed. C. D. Garmany, Astronomical Society of the Pacific Conference Series, 7, 16.

de Jong, T., Dalgarno, A. and Boland, W. 1980. Astronomy and Astrophysics, 91, 68.

Dickman, R. L. 1988. In *Molecular Clouds in the Milky Way and External Galaxies*, eds. R. L. Dickman, R. L. Snell, and J. S. Young, Berlin: Springer-Verlag, 55.

Digel, S. W. 1991. Ph. D. Thesis, Harvard University.

Digel, S. W., Bally, J., and Thaddeus, P. 1990. Astrophysical Journal, 357, L29.

Digel, S. W., Lyder, D. A., Philbrick, A. J., Puche, D. and Thaddeus, P. 1996 (Di96). Astrophysical Journal, 458, 561.

Dixon, R. S. and Sonneborn, G. 1980. In *A Master List of Nonstellar Optical Astronomical Objects*, Ohio: Ohio State University Press.

Dobashi, K., Yonekura, Y., Mizuno, A., and Fukui, Y. 1992. Astronomical Journal, 104, 1525.

Dorland, H., Montmerle, T. and Doom, C. 1986. Astronomy and Astrophysics, 160, 1.

DRAO. 1996. Reduction notes for Super Synthesis Telescope data, Dominion Radio Astrophysical Observatory.

Dubout-Crillon, R. 1976. Astronomy and Astrophysics Supplement Series, 25, 25.

Ebert, R. 1955. Z. Astrophys., 37, 222.

Elias, J. H. 1978. Astrophysical Journal, 224, 453.

Ellingsen, S. P., Norris, R. P. and McCulloch, P. M. 1996. Monthly Notices of the Royal Astronomical Society, 279, 101.

Elmegreen, B. G. 1985. In *Protostars and Planets II*, eds., D. C. Black and M. S. Mathews, Tuscon: University of Arizona Press, 33.

Elmegreen, B. G. 1987. In *Interstellar Processes*, eds. D. J. Hollenbach and H. A. Thronson Jr., Dordrecht: D. Reidel, 259.

Elmegreen, B. G. 1993. In *Protostars and Planets III*, eds. Eugene H. Levy and Jonathan I. Lunine, Tucson: University of Arizona Press, 97.

Elmegreen, B. G. and Lada, C. J. 1977. Astrophysical Journal, 214, 725.

Elmegreen, B. G. and Wang, M. 1988. In *Molecular Clouds in the Milky Way and External Galaxies*, eds. R. L. Dickman, R. L. Snell and J. S. Young, Berlin: Springer-Verlag, 240.

Evans II, N. J. 1980. In IAU 87, *Interstellar Molecules*, ed. B.H. Andrews (Dordrecht: D. Reidel), 1.

Evans, N. J., II. 1991. In *Frontiers in Stellar Evolution*, San Francisco, CA: Astronomical Society of the Pacific, 45.

Falgarone, E. 1995. In *The Physics and Chemistry of Molecular Clouds*, eds. G. Winnewisser and G.C. Pelz, Berlin: Springer-Verlag, 100.

Felli, M., Palagi, F., and Tofani, G. 1992. Astronomy and Astrophysics, 248, 453.

Fich, M., Dahl, G. P., and Treffers, R. R. 1990. Astronomical Journal, 99, 622.

Field, G. B. and Saslaw, W. C. 1965. Astrophysical Journal, 142, 568.

Finkenzeller, U. and Mundt, R. 1984. Astronomy and Astrophysics Supplement Series, 55, 109.

FitzGerald, M. P. 1970. Astronomy and Astrophysics, 4, 234.

Fitzpatrick, E. L. and Garmany, C. D. 1990. Astrophysical Journal, 363, 119.

Flower, P. J. 1977. Astronomy and Astrophysics, 54, 31.

Fukui, Y. 1989. In *ESO Workshop on Low Mass Star Formation and Pre-Main Sequence Objects*, ed. B. Reipurth, Garching: European Southern Observatories, 95.

Fukui, Y., Iwata, T., Mizuno, A., Bally, J., and Lane, A. P. 1993. In *Protostars and Planets III*, eds., Eugene H. Levy and Jonathan I. Lunine, University of Arizona: University of Arizona Press, 603.

Garmany, C. D. 1994. Publications of the Astronomical Society of the Pacific, 106, 25.

Garmany, C. D. and Stencel, R. E. 1992 (GS92). Astronomy and Astrophysics Supplement Series, 94, 211.

Gaze, V. F., and Shajn, G. A. 1953. Izv. Krym. Astrofiz. Obs., 9, 52.

Gaze, V. F., and Shajn, G. A. 1954. Izv. Krym. Astrofiz. Obs., 11, 39.

Gaze, V. F., and Shajn, G. A. 1955. Izv. Krym. Astrofiz. Obs., 15, 11.

Genzel, R. 1991. In *The Physics of Star Formation and Early Stellar Evolution*, eds. Charles J. Lada and Nikolaos D. Kylafis, Dordrecht: Kluwer Academic Press, 155.

Genzel, R. 1992. In *The Galactic Interstellar Medium*, Saas-Fee Advanced Course 21, Lecture Notes 1991, Swiss Society for Astrophysics and Astronomy, eds. D. Pfenniger and P. Bartholdi, Berlin: Springer-Verlag, 282.

Genzel, R. and Downes, D. 1979. Astronomy and Astrophysics, 72, 234.

Georgelin, Y. M. and Georgelin, Y. P. 1976. Astronomy and Astrophysics, 49, 57.

Goodman, A. A., Bastien, P., Myers, P. C. and Menard, P. C. 1990. Astrophysical Journal, 359, 363.

Green, D. A. 1989. Astronomical Journal, 98, 2210.

Green, D. A. 1993 (Gr93). Monthly Notices of the Astronomical Society, 262, 327.

Habe, A. and Ohta, K. 1992. Publications of the Society of Japan, 44, 203.

Hartmann, L. and MacGregor, K. B. 1982. Astrophysical Journal, 259, 180.

Hasegawa, T. 1986. Astrophysics and Space Science, 118, 421.

Haug, U. 1970. Astronomy and Astrophysics Supplement Series, 1, 35.

Heeschen, D. S. 1951. Astrophysical Journal, 114, 132.

Heiles, C., Goodman, A. A., McKee, C. F. and Zweibel, E. G. 1993. In *Protostars and Planets III*, eds. Eugene H. Levy and Jonathan I. Lunine, Tucson: University of Arizona Press, 279.

Henriksen, R. N. 1991. In *Fragmentation of Molecular Clouds and Star Formation*, IAU Symposium 147, eds. E. Falgarone, F. Boulanger and G. Duvert, Dordrecht: Kluwer Academic Press, 83.

Herbig, G. H. 1960. Astrophysical Journal Supplement Series, 4, 337.

Herbig, G. H. 1985. Astrophysical Journal, 289, 269.

Herbst, W. 1975. Astronomical Journal, 80, 503.

Hirshfeld, A. and Sinnott, R. W. (eds.). *Sky Catalogue 2000.0: Volume I*, 1985, Cambridge, MA: Sky Publishing Co. 274.

Hillenbrand, L. A., Massey, P., Strom, S. E. and Merrill, K. M. 1993. Astronomical Journal, 106, 1906.

Houlahan, P. and Scalo, J. 1990. Astrophysical Journal Supplement Series, 72, 133.

Houlahan, P. and Scalo, J. 1992. Astrophysical Journal, 393, 172.

Hoyle, F. 1953. Astrophysical Journal, 118, 513.

Hughes, V. A. 1988. ApJ, 333, 788.

Hughes, V. A., and MacLeod, G. C. 1989. Astronomical Journal, 97, 786.

Humphreys, R., M. 1978. Astrophysical Journal Supplement Series, 38, 309.

Jaschek, C and Jaschek, M. 1987. *The Classification of Stars*, Cambridge: Cambridge, University Press.

Johnson, H. L. 1958. Lowell Observatory Bulletin, 90, 37.

Jonas, D. 1971. Astronomy and Astrophysics, 11, 123.

Kallas, E. and Reich, W. 1980. Astronomy and Astrophysics Supplement Series, 42, 227.

Kawabe, R., Ogawa, H., Fukui, Y, Takano, T., Takaba, H., Fujimoto, Y., Sugitani, K. and Fujimoto, M. 1984. Astrophysical Journal, 282, L73.

Kerr, F. J., Bowers, P. F., Jackson, P. D., and Kerr, M. 1986. Astronomy and Astrophysics Supplement Series, 66, 373.

Kimura, T. and Tosa, M. 1996. Astronomy and Astrophysics, 308, 979.

Kolmogorov, A. N. 1941. Reprinted in 1961 in *Turbulence: Classic Papers on Statistical Theory*, eds. S. K. Friedland and L. Topper, New York: Interscience.

Kraus, J. D. 1986. *Radio Astronomy, 2nd ed.*, Ohio: Cygnus-Quasar Books, 1.

Kutner, M. L. 1978. Astrophysical Journal Letters, 19, 81.

Kutner, M. L., and Ulich, B. L. 1981. Astrophysical Journal, 250, 341.

Lada, C. J. 1985. Annual Reviews of Astronomy and Astrophysics, 23, 267.

Lada, C. J., Elmegreen, B. G., Cong, H.-I., and Thaddeus, P. 1978. Astrophysical Journal, 226, L39.

Lada, E. A., Strom, K. M., and Myers, P. C. 1993. In *Protostars and Planets III*, eds. Eugene H. Levy and Jonathan I. Lunine, Tucson: University of Arizona Press, 245.

Lang, K. R. 1980. *Astrophysical Formulae*, New York: Springer-Verlag.

Lang, K. R. 1992. *Astrophysical Data: Planets and Stars*, New York: Springer-Verlag.

Larson, R. B. 1972. Nature, 236, 21.

Larson, R. B. 1978. Monthly Notices of the Royal Astronomical Society, 184, 69.

Larson, R. B. 1979. Monthly Notices of the Royal Astronomical Society, 194, 69.

Larson, R. B. 1981 (L81). Monthly Notices of the Royal Astronomical Society, 194, 809.

Larson, R. B. 1982. Monthly Notices of the Royal Astronomical Society, 200, 159.

Larson, R. B. 1991. In *Fragmentation of Molecular Clouds and Star Formation*, eds. E. Falgarone, F. Boulanger and G. Duvet, Dordrecht: Kluwer Academic Press, 261.

Larson, R. B. 1992. Monthly Notices of the Royal Astronomical Society, 256, 641.

Larson, R. B. 1994. In *The Structure and Content of Molecular Clouds*, eds. Thomas L. Wilson and Kenneth J. Johnston, Berlin: Springer-Verlag, 13.

Laughlin, G. 1991. IPAC User's Guide, JPL D-2416, Pasadena, CA: California Institute of Technology.

Lebrun, F., Bennett, K., Bignami, G. F., Bloemen, J. B. G. M., Buccheri, R., Caraveo, P. A., Gottwald, M., Hermsen, W., Kanbach, G., Mayer-Hasselwander, H. A., Montmerle, T., Paul, J. A., Sacco, B., Strong, A. W., Wills, R. D., Dame, T. M., Cohen, R. S., and Thaddeus, P. 1983. Astrophysical Journal, 274, 231.

Leinert, C. 1994. In *Star Formation and Techniques in Infrared and mm-Wave Astronomy*, eds. T. P. Ray and S. V. W. Beckwith, Berlin: Springer-Verlag, 215.

Leisawitz, D. and Hauser, M. G. 1988. Astrophysical Journal, 332, 954.

Leisawitz, D., Bash, F. N., and Thaddeus, P. 1989. Astrophysical Journal Supplement Series, 70, 731.

Leung, C. M. 1975, Astrophysical Journal, 199, 340.

Leung, H. O. and Thaddeus, P. 1991. Astrophysical Journal Supplement Series, 81, 267.

Lockman, F. J. 1989. Astrophysical Journal Supplement Series, 71, 469.

Lyder, D. A. and Galt, J. 1997. Astronomical Journal, 113, 131.

Lynds, B. T. 1962. Astrophysical Journal Supplement Series, 7, 1.

Maddalena, R. J., Morris, M. Moscowitz, J., and Thaddeus, P. 1986. Astrophysical Journal, 303, 375.

Maeder, A. and Meynet, G. 1988. Astronomy and Astrophysics Supplement Series, 76, 411.

Mathis, J. S. 1986. Publications of the Society of the Pacific, 98, 995.

McCluskey, G. E. and Kondo, Y. 1972. Astrophysics and Space Science, 17, 134.

McCutcheon, W. H., Dewdney, P. E., Purton, C. R. and Sato, T. 1991. Astronomical Journal, 101, 1435.

Mendenhall, W., Scheaffer, R. L. and Wackerly, D. D. 1981. Mathematical Statistics with Applications, 2nd Ed., Boston, Mass: Duxbury Press, 488.

Menten, K. M. 1991. Astrophysical Journal, 380, L75.

Mermilliod, J. C. 1981. Astronomy and Astrophysics, 97, 235.

Mihalas, D. and Binney, J. 1981. Galactic Astronomy, 2nd ed., San Francisco: W. H. Freeman & Co.

Miller, G. E. and Scalo, J. M. 1979. Astrophysical Journal Supplement series, 41, 513.

Mitchell, G. F., Hasegawa, T. I., and Schella, J. 1992. ApJ, 386, 604.

Mitchell, G.F., Lee, S. W., Maillard, J.-P., Mathews, H., Hasegawa, T. and Harris, A. I. 1995. Astrophysical Journal, 438, 794.

Mouschovias, T. Ch. 1991. In *The Physics of Star Formation and Early Stellar Evolution*, eds. C. J. Lada and N. D. Kylafis, Dordrecht: Kluwer Press, 449.

Myers, P. C. 1983. Astrophysical Journal, 270, 105.

Myers, P. C. 1985. In *Protostars and Planets II*, eds., D. C. Black and M. S. Mathews, Tuscon: University of Arizona Press, 81.

Myers, P. C. 1991. In *Fragmentation of Molecular Clouds and Star Formation*, eds. E. Falgarone, F. Boulanger and G. Duvet, Dordrecht: Kluwer Academic Press, 221.

Myers, P. C. and Benson, P. J. 1983. Astrophysical Journal, 266, 309.

Myers, P. C., Fuller, G. A., Goodman, A. A. and Benson, P. J. 1991. Astrophysical Journal, 376, 561.

Nakano, T. 1976. Publications of the Society of Japan, 28, 355.

Nakano, T. 1977. Publications of the Society of Japan, 29, 197.

Ochsenbein, F. 1974. Astronomy and Astrophysics Supplement Series, 15, 215.

Odenwald, S. F. and Schwartz, P. R. 1993. Astrophysical Journal, 405, 706.

Oort, J. H. 1954. Bulletin of the Astronomical Institute of the Netherlands, 12, 177.

Osterbrock, D. E. 1989. In *Astrophysics of Gaseous Nebulae and Active Galactic Nuclei*, (Mills Valley, CA: University Science Books), 17.

Palla, F. and Stahler, S. W. 1990. Astrophysical Journal, 360, L47.

Palla, F. and Stahler, S. W. 1991. Astrophysical Journal, 375, 288.

Palla, F. and Stahler, S. W. 1993. Astrophysical Journal, 418, 414.

Palmer, E. S. 1993. Observatory communication.

Panagia, N. 1973. Astronomical Journal, 78, 929.

Parker, R. A. R., Gull, T. R. and Kirschner, R. P. 1979. NASA SP-434, Washington, D.C.: GPO.

Peters, W. L. & Bash, F. N. 1987. Astrophysical Journal, 317, 646.

Press, W. H., Flannery, B. P., Teukolsky, S. A. and Vetterling, W. T. 1989. *Numerical Recipes*, Cambridge: Cambridge University Press, 449.

Prusti, T. J. 1992. Ph.D. Thesis, Rijksuniversiteit Groningen.

Puche, D. 1993. Observatory communication.

Purton, C. R., Lyder, D. A., Gower, A. C. and Belton, D. S. 1995. Bulletin of the American Astronomical Society, 187, 2112.

Racine, R. 1968. Astronomical Journal, 73, 233.

Reifenstein, E. C., Wilson, T. L., Burke, B. F. Mezger, P. G. and Altenhoff, W. F. 1970. Astronomy and Astrophysics, 4, 357.

Roberts, W. W. 1972. Astrophysical Journal, 173, 259.

Roger, R. S. and Dewdney, P. E. 1992. Astrophysical Journal, 385, 536.

Rucinski, S. M. 1985. Astronomical Journal, 90, 2321.

Rybicki, G. B. and Lightman, A. P. 1979. In *Radiative Processes in Astrophysics*, New York: John Wiley & Sons, 8.

Salpeter, E. E. 1955. Astrophysical Journal, 121, 161.

Sanders, D. B., Solomon, P. M., and Scoville, N. Z. 1984. Astrophysical Journal, 276, 182.

Sanders, D. B., Scoville, N. Z., and Solomon, P. M. 1985. Astrophysical Journal, 289, 373.

Sargent, A. I. 1977. Astrophysical Journal, 218, 736.

Sargent, A. I. 1979. Astrophysical Journal, 233, 163.

Savage, B. D., Bohlin, R. C., Drake, J. F., and Budich, W. 1977. Astrophysical Journal, 216, 291.

Scalo, J. M. 1985. In *Protostars and Planets II*, eds. D. C. Black and M. S. Mathews, Tuscon: Univ. of Arizona Press, 201.

Scalo, J. M. 1987. In *Interstellar Processes*, eds. D. J. Hollenbach and H. A. Thronson Jr., Dordrecht: Kluwer, 349.

Scalo, J. M. 1988. In *Molecular Clouds in the Milky Way and External Galaxies*, eds. R. L. Dickman, R. L. Snell and J. S. Young, New York: Springer-Verlag, 201.

Scalo, J. M. 1990. In *Physical Processes in Fragmentation and Star Formation*, eds. R. Capuzzo-Dolcetta, C. Chiosi and A. Di Fazio, Dordrecht: Kluwer Press, 151.

Scheffler, H. and Elsässer, H. 1987. In *Physics of the Galaxy and Interstellar Matter*, eds. Martin Harwit, Rudolf Kippenhahn and Jean-Paul Zahn, Berlin: Springer-Verlag, 241.

Schmidt-Kaler, T. H. 1982. In *Landolt-Bornstein New Series, Volume 2b, Astronomy and Astrophysics - Stars and Star Clusters*, eds. K. Schaifers and H. H. Voigt, New York: Springer-Verlag.

Schutte, A. J., van der Walt, D. J., Gaylard, M. J., and MacLeod, G. C. 1993. Monthly Notices of the Royal Astronomical Society, 261, 783.

Schwassmann, A. and van Rhijn, P. J. 1947. In *Bergedorfer Spektral-Durchmusterung*. Bergedorf:NP, 1947.

Scoville, N. Z. and Sanders, B. 1987. In *Interstellar Processes*, eds. D. J. Hollenbach and H. A. Thronson Jr., Dordrecht: Reidel, 23.

Scoville, N. Z. and Good, J. C. 1989. Astrophysical Journal, 339, 149.

Sellgren K. 1984. Astrophysical Journal, 277, 623.

Shajn, G. A. and Gaze, V. F. 1951. Izv. Krym. Astrofiz. Obs., 7, 93.

Sharpless, S. 1959. Astrophysical Journal Supplement Series, 4, 257.

Sharpless, S. 1962. Astrophysical Journal, 136, 767.

Shu, F. H., Adams, F. C. and Lizano, S. 1987. Annual Reviews of Astronomy and Astrophysics, 25, 23.

Silk, J. I. and Takahashi, T. 1979. Astrophysical Journal, 229, 242.

Snell, R. L., Scoville, N. Z., Sanders, D. B., and Erickson, N. R. 1984. Astrophysical Journal, 284, 176.

Solomon, P. M., Rivolo, A. R., Barrett, J., and Yahil, A. 1987. Astrophysical Journal, 319, 730.

Spitzer, L. 1978. In *Physical Processes in the Interstellar Medium*, (New York: Wiley), 23.

Stahler, S. W. 1985. Astrophysical Journal, 293, 207.

Stahler, S. W. and Walter, F. M. 1993. In *Protostars and Planets III*, eds. Eugene H. Levy and Jonathan I. Lunine, Tucson: University of Arizona Press, 405.
Stahler, S. W. and Walter, F. M. 1993.

Strom, K. M., Strom, S. E., Kenyon, S. J., and Hartmann, L. 1988. Astronomical Journal, 95, 534.

Strom, K. M., Newton, G., Strom, S. E., Seaman, R. L., Carrasco, L., Cruz-Gonzalez, I., Serrano, A. and Grasdalen, G. L. 1989. Astrophysical Journal Supplement Series, 71, 183.

Strong, A. W., Bloemen, J. B. G. M., Dame, T. M., Grenier, I. A., Hermsen, W., Lebrun, F., Nyman, L.-Å, Pollock, A. M. T., and Thaddeus, P. 1988. Astronomy and Astrophysics, 207, 1.

Struck-Marcell, C. Scalo, J. M. 1984. Astrophysical Journal, 277, 132.

Tenorio-Tagle, G. and Bodenheimer, P. 1989. Annual Reviews of Astronomy and Astrophysics, 26, 145.

Tereby, S., Fich, M., Blitz, L., and Henkel, C. 1986. Astrophysical Journal, 308, 357.

Vallée, J. P. and Bastien, P. 1996. The JCMT Newsletter, 7, 19.

van den Bergh, S. 1966. Astronomical Journal, 71, 990.

van den Bergh, S. and Herbst, W. 1975. Astronomical Journal, 80, 208.

van der Walt, D. J., Gaylard, M. J. and MacLeod, G. C. 1995. Astronomy and Astrophysics Supplement Series, 110, 81.

von Weizäcker, C. F. 1951. Astrophysical Journal, 114, 165.

Walker, H. J. and Cohen, M. 1988. Astronomical Journal, 95, 1801.

Walker, H. J., Cohen, M., Volk, K., Wainscoat, R. J., and Schwartz, D. E. 1989. (W89). Astronomical Journal, 98, 2163.

Weaver, H. F. and Williams, D. R. W. 1973. Astronomy and Astrophysics Supplement Series, 8, 1.

Weintraub, D. 1990. Astrophysical Journal Supplement Series, 74, 575.

Wilking, B. A., Greene, T. P., Lada, C. J., Meyer, M. R., and Young, E. T. 1992. Astrophysical Journal, 397, 520.

Wilson, R. W., Jefferts, K. B., and Penzias, A. A. 1970. Astrophysical Journal, 161, L43.

Wood, D. O. S. and Churchwell, E. 1989. Astrophysical Journal Supplement Series, 69, 831.

Wouterloot, J. G. A. and Brand, J. 1989. Astronomy and Astrophysics Supplement Series, 80, 149.

Wouterloot, J. G. A., Brand, J., and Fiegle, K. 1993. Astronomy and Astrophysics Supplement Series, 98, 589.

Wu, Y., Huang, M. and He, J. 1996. AASS, 115, 283.

Zinnecker, H. 1984. Astrophysical Space Science, 99, 41.

Appendix A

A.1 The Uncertainty in the Measured and Derived Quantities Used to Characterize Molecular Clouds

In Chapter 1, the measured and derived physical quantities used to characterize molecular clouds were introduced. In brief, the measured quantities are the $FWHM$ of the velocity profile of a cloud as fitted by a Gaussian profile, the radius of a cloud as fitted to the half-maximum of its integrated CO intensity, W_{CO}, and the centroid of the cloud in l, b and v. The derived quantities consist of the cloud's luminosity in the CO line (Eq. 1.47), the cloud's CO mass (Eq. 1.52) and the cloud's virial mass assuming the cloud is spherical and uniform in density (Eq. 1.55).

In practice, determination of these quantities is a multi-step process. Cloud candidates are initially selected from an integrated map, e.g., the Cam OB1 emission shown in Figure 2.11, by first identifying simple closed '3σ' features which contain only one '6σ' peak. Boundaries for the candidate clouds are then set as a simple box so as to include all of the emission associated with the feature. Ideally the cloud boundary should terminate near enough to the feature to include only the feature but far enough away to include important contributions from any extended features. A detailed analysis of the effect that cloud boundary selection has on the derived cloud parameters is included at the end of this section. More complicated regions, i.e., cloud candidates with more than one 6σ peak, are broken into separate features if there is some suggestion from their morphology that such distinct features are easily identifiable.

Given the initial list of cloud candidates, or more correctly cloud candidate boundaries, each candidate cloud is then analyzed using a software package, *cloud_find*, written by the author to determine whether it was possible to obtain a closed half-maximum radius and a simple, single-peaked spectrum fitted well by a Gaussian. For the cases where there are multiple peaks that could be kinematically isolated, i.e., more than one $FWHM$ apart in velocity, multiple clouds were obtained with the same longitude and latitude boundaries but with the velocity ranges reset appropriately. If a spatially well defined feature is well fit by a Gaussian but a second velocity feature appears in the wings of the first's velocity profile,

then the velocity boundary between the two was deemed acceptable. For the most complicated emission features the brightest one is examined first as the primary cloud and half-maximum radius discriminator. The brightest emission feature is then removed and considered counted, after which the next brightest feature is examined in a similar fashion, and so forth until the complicated emission feature has been completely analyzed.

It is also necessary to estimate the effect that the cloud selection process has on the measured physical parameters of the clouds. Obviously, if the box boundaries are set to be too broad in all dimensions then many features will be encompassed, while a too-narrow boundary will fall within the cloud and possibly cut the half-maximum contour. In order to quantify the uncertainty introduced in estimating a cloud boundary, an experiment whereby the effect of varying the cloud boundary by one pixel in each spatial coordinate was computed for two clouds, one representing large clouds of at least several beamwidths in radius (testone), and one representative of small clouds comparable to a beamwidth in radius (testtwo). The guiding principle to know when the choice of a cloud boundary is appropriate for a cloud is to consider the range of boundaries possible for which a relatively steady cloud half-maximum radius is obtained. The mean and range over which the cloud half-maximum radius is slowly varying serve as measures of the mean and uncertainty in the cloud radius. The values of the physical quantities of interest, e.g., virial mass, etc., and their associated uncertainties, are found commensurately. Results of this experiment are presented in Table A.1. In the majority of cases, the errors in the derived quantities, i.e. the cloud's luminosity, CO mass and virial mass, are typically 10 – 25% with a larger relative uncertainty associated with the smaller clouds.

Table A.1: Summary of Typical Cloud Uncertainties

Case	Δv_{LSR} [km s^{-1}]	Radius,r [pc]	L_{CO} [10^3 K km $^{-1}$ pc^2]	M_{CO} [$10^3 M_\odot$]	M_{vir} [$10^3 M_\odot$]
testone	$4.79\pm^{0.04}_{0.22}$	$4.43\pm^{0.34}_{0.28}$	$9.42\pm^{1.25}_{2.11}$	$8.85\pm^{1.20}_{1.87}$	$24.6\pm^{1.9}_{1.6}$
testtwo	$2.72\pm^{0.30}_{0.13}$	$1.54\pm^{0.34}_{0.11}$	$0.47\pm^{0.11}_{0.07}$	$0.44\pm^{0.11}_{0.08}$	$2.76\pm^{0.75}_{0.19}$

There is one last source of uncertainty, which has the potential to produce very large uncertainties in the determined physical quantities of small clouds. In Chapter

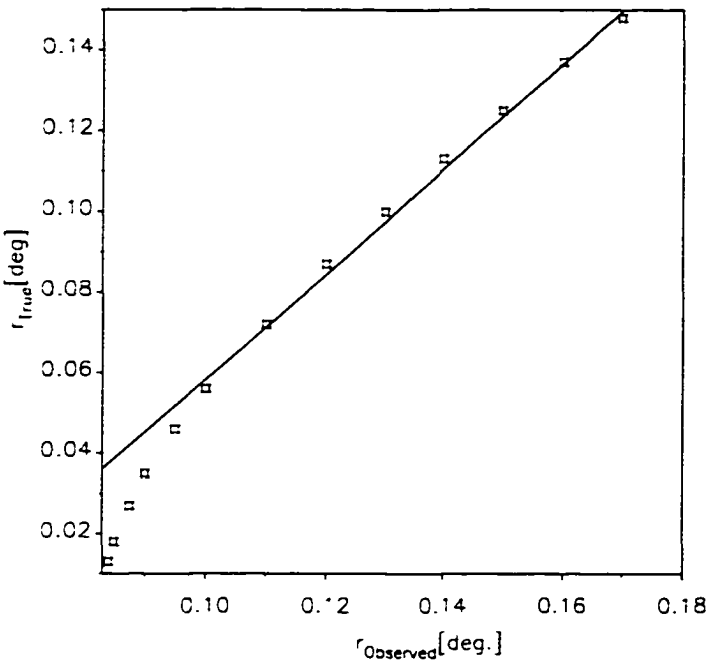

Figure A.1 Effect of the finite resolution of the beam on the measurement of cloud radii. A turnover in the relationship between r_{True} and $r_{Observed}$, defined by equation 1.31 (in degrees), i.e. $r_{True} = (r^2_{Observed} - 0.083^2)^{1/2}$, takes place in the vicinity of $r_{Observed} \sim 0.1$ deg. At this point a small change in $r_{Observed} \sim 10\%$ leads to a change of $\sim 50\%$ in r_{True}.

1 it was shown to be necessary to convert the observed cloud radius to a 'true' cloud radius (Eq. 1.42), which involved taking the square of the difference between the squares of the observed radius and the survey beam size. A small error in the observed cloud radius can produce a larger uncertainty in the true cloud radius for a cloud comparable in observed radius to the survey beam size. Hence, clouds with observed radii of this magnitude or smaller should not be included in any analysis. Figure A.1 illustrates this point.

Appendix B

B.1 Per OB1 and Cas OB6

In Chapter 4, the distance to the Perseus CO clouds is stated to be 2500 ± 200 pc on the basis of main sequence fitting to the B stars in the associations Per OB1 and Cas OB6 (GS92). Tables B1 and B2 provide details taken from GS92 useful in characterizing the two associations. In the last column in both tables are the distances to the stars, Dist 1, derived on the basis of their distance modulus, while the penultimate column lists the radial velocities for the stars, when available. Proper motions are not included, even though some are listed in SIMBAD, as the uncertainties exceed their quoted values.

Making use of the values of Dist 1 and the radial velocity listed in Tables B1 and B2 it is possible to derive the mean and associated error in the mean for both of these quantities. In general, for some quantity, x, these values are obtained from (Taylor 1982):

$$x = \overline{x} \pm \delta_x. \tag{B.1}$$

where $x = \overline{x}$ is the mean of the sample of xs and $\delta_x = \sigma_x/\sqrt{N}$. For a sample size, N, the standard deviation in the distribution, σ_x, is given by:

$$\sigma_x = \sqrt{\frac{\Sigma_{i=1}^{N}(x_i - \overline{x})^2}{N-1}}. \tag{B.2}$$

For the Cas OB6 and Per OB1 stars it follows that:

Cas OB 6

Stars:	B Main Sequence	All B	All Stars
$N_{\text{Dist 1}}$:	14	24	42
Dist 1 [kpc]:	2.26 ± 0.10	2.69 ± 0.18	2.70 ± 0.16
$N_{v_{\text{LSR}}}$:	1	6	15
v_{LSR} [km s^{-1}]:	−40.0±?	−33.8 ± 13.8	−42.4 ± 10.9

Per OB1

Stars:	B Main Sequence	All B	All Stars
$N_{\text{Dist 1}}$:	2	17	26
Dist 1 [kpc]:	1.83 ± 0.17	2.52 ± 0.18	2.89 ± 0.32
$N_{v_{\text{LSR}}}$:	0	8	15
v_{LSR} [km s^{-1}]:	?±?	−42.0 ± 1.3	−44.1 ± 2.0

Table B1: Cas OB6

No.	Object Name[a]	l^b [deg.]	b^b [deg.]	MK Des.[c]	B[d] [mags]	V[d] [mags]	v^e_{LSR} [km s^{-1}]	Dist. [f] [kpc]
1	BD+60 470	133.883	-0.075	O8Vvar	10.58	9.88		2.24
2	BD+62 411	133.883	+2.700	B1Ib-II	8.78	8.46	-52.9	3.47
3	BD+62 419	134.169	+2.999	B0:V:	10.08	9.72		2.23
4	BD+60 478	134.417	-0.034	M1Ib	14.02	10.77		1.36
5	IC 1805 23	134.470	+0.552	B1V	12.31	11.47		1.87
6	BD+60 496 (IC 1805 104)	134.582	+1.035	O6V	9.36	8.79	-50.3	2.08
7	IC 1805 111	134.594	+1.070	B2V	12.04	11.55		2.30
8	BD+60 496 (IC 1805 103)	134.608	+0.965	B0V	11.03	10.53		2.67
9	BD+60 493 (IC 1805 70)	134.623	+0.583	B0.5Ia	9.22	8.43	-39.6	2.43
10	BD+60 498 (IC 1805 112)	134.629	+0.990	O9V	10.45	9.92		2.40
11	BD+60 499 (IC 1805 118)	134.640	+0.995	O9.5V	10.80	10.26		2.48
12	IC 1805 161	134.673	+1.112	B1.5V	11.31	10.85		2.01
13	IC 1805 136	134.683	+0.995	B1V	11.62	11.01		2.07
14	IC 1805 113	134.693	+0.819	O9Ve	11.80	10.92		2.34
15	BD+60 501 (IC 1805 138)	134.706	+0.937	O6.5V	10.05	9.59	-47.0 E	3.34
16	HD 15558 (IC 1805 148)	134.724	+0.925	O5III(f)	8.35	7.86	-50.0 C	2.22
17	IC 1805 174	134.764	+0.956	B2V	12.06	11.56		2.28
18	BD+60 506B (IC 1805 185)	134.778	+0.949	B2V	12.15	11.61		2.21
19	BD+60 596 (IC 1805 183)	134.780	+0.941	B1II	11.74	11.15		6.31
20	IC 1805 169	134.790	+0.859	B2IV	12.39	11.71		2.57
21	IC 1805 211	134.843	+0.953	B1V	11.47	10.89		2.05
22	BD+60 513 (IC 1805 232)	134.898	+0.922	O9V	9.90	9.41		2.00
23	IC 1805 260	134.907	+1.051	B2V	11.97	11.51		2.36
24	IC 1805 221	134.929	+0.772	B8II-III	12.12	11.57		3.50
25	IC 1805 308	134.960	+1.235	G5Ib-II	12.46	10.93		6.14
26	IC 1805 288	134.975	+1.043	B1.5V	11.58	11.11		2.29
27	BD+59 497	134.994	-0.693	B0V:	11.21	10.47		3.39
28	HD 15785	135.306	+0.188	B1Iab	8.91	8.34	-37.0 D	3.10
29	BD+59 510	135.439	-0.331	B1III	10.84	10.28		2.76
30	HD 16429	135.678	+1.146	O9.5III	8.29	7.67	-62.0 D	1.09
31	HD 16778	136.634	-0.023	A2Ia	8.61	7.71	-36.0 C	2.88
32	HD 237007 (IC 1848 3)	137.136	+0.858	B0V	9.76	9.43	-10.0 E	2.03
33	HD 17520 (IC 1848 2)	137.216	+0.880	O9V	8.54	8.24	-52.0	1.52
34	LS I +59 153	137.376	+0.194	O9.5V	11.72	11.10		3.27
35	HD 18409	137.119	+3.460	O9Ib	8.78	8.36	-42.3 C	3.10
36	BD+60 594	137.379	+2.119	O9V	9.66	9.30		2.28
37	BD+60 586	137.420	+1.279	O8III	8.76	8.46	-42.3	3.06
38	HD 17971	137.727	+1.147	F5Ia	8.82	7.75	-51.0	4.94
39	LS I +59 154	138.138	+0.091	B1V	11.23	10.66		1.87
40	HD 18076	138.437	+0.046	B0II-III	9.64	9.06	-59.0 D	2.69
41	BD+58 547	138.848	+0.552	B3II-III	10.05	9.61	+26.0	3.15
42	UBV 2842	139.098	-0.723	B1II-III	10.84	10.04		2.83

a. Catalog designation of star as given by, in order of preference, its HD, BD, LS I, BSD or UBV entry.

b. Galactic co-ordinates of star.

c. MK classification of star, as listed in GS92.

d. B and V photometric indices.

e. Radial velocity of star corrected to Local Standard of Rest assuming standard solar motion. The letter index, when listed in SIMBAD, gives the quality of the spectra: A - excellent to E - poor.

f. Distance from $m_v - M_v = 5\,log(d) - 5 + A_v$, assuming the intrinsic colors and abolute magnitude-color relationship of Schmidt-Kaler (1982) as given in Lang (1992), and R = 3.1 (Fitzpatrick & Garmany 1990). The distance claimed by GS92 for Cas OB6 is 2.40 kpc.

Table B2: Per OB1

No.	Object Name[a]	l^b [deg.]	b^b [deg.]	MK Des.[c]	B[d] [mags]	V[d] [mags]	v^e_{LSR} [km s^{-1}]	Dist. [f] [kpc]
1	BD+59 372	131.304	-1.506	K5Ia	11.57	9.29	-59.7	8.91
2	BD+60 416	131.336	-0.666	B0.5III	10.23	9.56		2.01
3	BD+59 387	131.704	-1.574	B3II	10.22	9.59		2.09
4	BD+59 388	131.732	-1.675	B3II	10.21	9.61		2.20
5	HD 13036 (Stock 2 1)	132.678	-1.763	B0.5:III	9.08	8.55	-39.0 D	1.49
6	LS I+59 112	132.938	-1.385	O9V	12.00	11.03		2.05
7	HD 13402 (Stock 2 31)	133.105	-1.713	B0.5Ib	8.66	8.07	-39.0 C	2.08
8	BD+59 451 (Stock 2 115)	133.445	-1.445	B1II	9.99	9.30		2.34
9	BD+59 456 (Stock 2 146)	133.651	-1.250	B0.5V	10.43	9.88		1.58
10	BD+59 461 (Stock 2 158)	133.811	-1.274	B1II	10.60	10.09		4.33
11	HD 14242 (AG+59 258)	133.950	-1.284	M2Iab	10.79	8.36	-34.2	2.23
12	HD 14442	134.206	-1.321	O5.5N(f)p	9.62	9.21		3.19
13	HD 14142 (BD+58 439)	134.067	-1.997	M2Iab	10.86	8.52	-43.0	2.79
14	BD+58 451A	134.154	-1.456	B1III:	10.59	10.07		2.65
15	BD+58 453	134.264	-1.549	B1V	10.98	10.53		2.07
16	HD 236960	134.592	-1.520	B0.5III	10.21	9.76	-45.0 C	3.05
17	HD 14947	134.995	-1.745	O5IF+	8.46	8.01	-54.0 C	1.73
18	BD+57 586	135.902	-1.679	B1II	10.72	10.11		3.80
19	HD 15752 (AG+58 273)	136.064	-1.821	B0III	9.23	8.74	-44.0 E	1.98
20	BD+58 501 (AG+59 284)	136.261	-0.439	M2Iab	12.22	9.37	-51.3	2.04
21	HD 16808	137.287	-1.369	B0.5Ib	9.16	8.60	-36.6 C	2.77
22	HD 236995	137.305	-1.113	A0Ia	9.15	8.63	-52.0 C	7.01
23	HD 16779	137.440	-1.847	B2Ib	9.59	8.85	-49.0 D	2.28
24	HD 17088	137.868	-1.751	B9Ia	8.32	7.50	-40.5 B	2.68
25	HD 17145	137.959	-1.771	B8Ia	8.98	8.15	-43.0 C	3.48
26	HD 237010 (BD+57 647)	138.320	-1.396	M2Iab	12.11	9.38	-39.0	2.42

a. Catalog designation of star as given by, in order of preference, its HD, BD, LS I, BSD or UBV entry.

b. Galactic co-ordinates of star.

c. MK classification of star as listed in GS92.

d. B and V photometric indices.

e. Radial velocity of star corrected to Local Standard of Rest assuming standard solar motion. The letter index, when listed in SIMBAD, gives the quality of the spectra: A - excellent to E - poor.

f. Distance from $m_\epsilon - M_\epsilon = 5\,log(d) - 5 + A_\epsilon$, assuming the intrinsic colors and abolute magnitude-color relationship of Schmidt-Kaler (1982) as given in Lang (1992), and R = 3.1 (Fitzpatrick & Garmany 1990). The distance claimed by GS92 for Per OB1 is 2.30 kpc.

B.2 Candidate Perseus Arm Stars

There were stars rejected as being outside the Cam OB1 region which were not listed in GS92. In some cases, these stars were known to lie in the Perseus arm. Most of these stars have been identified as Perseus objects in SIMBAD from the work of Haug (1970). There was also a third group of stars rejected, as not being associated with Cam OB1, on the basis of their position in the observer's HR diagram for Cam OB1 (§4.2.3). It has not been established in this work that these stars are Perseus objects but they do appear to lie beyond Cam OB1. In Table B.3 the stellar data for both the known and possible Perseus objects are presented. An indication in the comments column of membership in Perseus is taken from SIMBAD.

Table B.3: Other Candidate Perseus Stars

No.	Object Name[a]	l^b [deg.]	b^b [deg.]	MK Des.[c]	U[d] [mag]	B[d] [mag]	V[d] [mag]	v^e_{LSR} [km s^{-1}]	Dist [f] [kpc]	Comments
1	LS I +60 209	131.08	-1.17	B1Vpe	10.53	10.89	10.15	-38.0	1.11	Be star. Perseus
2	HD 12302	131.81	-1.95	B1:V:pe	7.82	8.31	8.05	+7.0 C	0.84	Be star. Perseus
3	HD 13590	131.95	+2.63	B2IIIe	7.84	8.25	7.90	-32.0 C	1.04	Perseus
4	BD+58 458	134.57	-1.81	B1pe	9.75	10.34	9.80		1.26	Perseus
5	BD+60 562	136.21	+1.31	B9	10.91	11.05	10.79	+9.0	0.74	Variable
6	BSD 9-1401	137.41	+2.08	B9	11.39	11.14	10.76		0.68	
7	BSD 9-1426	137.41	+2.38	B8	11.72	11.76	11.30		0.90	
8	BSD 9- 838	137.55	+2.02	A0	12.84	12.57	12.12		1.01	
9	BSD 9- 861	137.72	+1.96	B9	11.70	11.67	11.09		0.59	
10	BD+60 598	137.84	+1.44	B6	9.76	10.29	9.96		0.75	S199. Perseus
11	BSD 9- 915	137.86	+2.28	B8	11.08	11.28	10.89		0.83	
12	BSD 9- 863	137.92	+1.63	A0	13.50	13.16	12.53		0.94	S199. Perseus
13	BSD 9- 893	137.93	+1.86	A0	13.30	12.84	12.15		0.72	S199. Perseus
14	BSD 9- 908	137.93	+2.07	B9	11.44	11.09	10.69		0.64	
15	BSD 9- 933	137.98	+2.30	B9	11.29	11.02	10.72		0.74	
16	LS I +60 287	138.00	+1.29	B9e	11.06	11.40	11.04		0.79	S199. Perseus
17	BD+60 606	138.01	+1.52	B0e	9.48	10.04	9.45		1.37	S199. Perseus
18	BSD 9- 879	138.05	+1.51	B5	12.04	12.26	11.67		1.27	S199. Perseus
19	BSD 9- 868	138.08	+1.38	B8	10.43	10.27	9.98		0.63	S199. Perseus
20	BSD 9- 862	138.09	+1.34	A0	12.57	12.25	11.76		0.81	S199. Perseus
21	BSD 9- 874	138.12	+1.34	A0	13.28	12.83	12.31		0.99	S199. Perseus
22	BSD 9- 878	138.12	+1.40	B4	10.70	11.17	10.82		1.28	S199. Perseus
23	BSD 9- 943	138.14	+2.26	B9	11.70	11.79	11.42		0.93	
24	BSD 9- 247	138.36	+0.66	A0	13.13	12.80	12.27		0.96	S198. Perseus
25	BSD 9- 11	138.44	+0.78	A0	13.76	13.36	12.45		0.61	S198. Perseus
26	BSD 9- 342	138.56	+1.39	B9	11.86	11.46	10.97		0.64	
27	LS I +59 162	138.61	+0.56	B4	10.89	11.16	10.53	-44.0 D	0.75	S198. Perseus
28	BSD 9- 12	138.67	+0.37	A0	12.92	12.40	11.76		0.65	S198. Perseus
29	BSD 9- 344	138.88	+0.84	A0	12.82	12.52	12.04		0.93	S198. Perseus
30	BSD 9- 341	138.89	+0.81	B9	11.74	11.45	11.05		0.75	S198. Perseus
31	BSD 9- 360	138.93	+0.94	B9	12.38	12.10	11.68		0.98	S198. Perseus
32	BSD 9- 365	139.00	+0.85	B9	12.09	11.81	11.26		0.67	S198. Perseus
33	BSD 9- 399	139.04	+1.25	B9	12.27	11.90	11.35		0.70	
34	BD+58 554B	139.13	+0.82	B9	12.02	11.81	11.37		0.82	
35	BD+59 591	139.19	+1.11	B8III	10.98	10.78	10.48		1.21	
36	BSD 9- 37	139.21	+0.70	B9	11.73	11.49	10.98		0.62	S198. Perseus
37	HD 237052	139.36	-0.33	B3	8.50	8.82	8.45	-21.0 C	0.69	
38	BSD 9- 46	139.46	+0.78	B9	12.66	12.16	11.52		0.66	S198. Perseus
39	LS I +59 168	139.69	+0.95	B5	12.26	12.41	11.73		1.15	Perseus
40	LS I +58 115	139.72	+0.86	B5e	12.35	12.48	11.57		0.77	Be star. Perseus
41	HD 237056	139.80	-0.90	B0.5:V:pe	8.86	9.34	8.66	-22.0 C	0.72	Be star. Perseus
42	LS I +59 172	139.90	+1.64	B5e	12.59	12.71	11.77		0.81	Be star. Perseus
43	BSD 9- 69	139.91	+0.63	B5III	10.96	10.91	10.32		1.34	

a. Catalog designation of star as given by, in order of preference, its HD, BD, LS I, BSD or UBV entry.

b. Galactic co-ordinates of star.

c. MK classification of star as listed in GS92.

d. UBV photometric indices.

e. Radial velocity of star corrected to Local Standard of Rest assuming standard solar motion. The letter index, when listed in SIMBAD, gives the quality of the spectra: A - excellent to E - poor.

f. Distance from $m_v - M_v = 5\,log(d) - 5 + A_v$, assuming the intrinsic colors and abolute magnitude-color relationship of Schmidt-Kaler (1982) as given in Lang (1992), and R = 3.1 (Fitzpatrick & Garmany 1990).